THE UNIVERSITY OF CHICAGO

COMPUTATIONAL TECHNIQUES FOR INVESTIGATING NEMATIC LIQUID CRYSTALS: CHIRALITY, CONFINEMENT, AND COLLOIDAL SELF-ASSEMBLY

A DISSERTATION SUBMITTED TO
THE FACULTY OF THE PRITZKER SCHOOL OF MOLECULAR ENGINEERING
IN CANDIDACY FOR THE DEGREE OF
DOCTOR OF PHILOSOPHY

BY
VIVIANA PALACIO BETANCUR

CHICAGO, ILLINOIS
AUGUST 2023

To my parents, Ara and Leo,

for teaching me how to learn

Luck is not chance –
It's toil –
Fortune's expensive smile
Is earned –
The Father of the Mine
Is that old-fashioned Coin
We spurned –

— Emily Dickinson

Table of Contents

List of Figures

List of Tables

Abstract

In this dissertation, an exploration of nematic liquid crystal (LC) systems is conducted, encompassing various conditions such as confinement, chirality, and colloidal interactions. Employing a mean-field approach and innovative simulation techniques, the research aims to unravel the intricate interplay between elasticity, confining geometries, and computational efficiency in the realm of soft matter materials. To efficiently navigate the vast parameter space, a rigorous framework augmented with stochastic elements is employed.

The initial part of the dissertation delves into the fascinating realm of geometrical frustration in LC systems. Through meticulous investigation, it unveils the emergence of hybrid morphologies resulting from the delicate interplay between chirality and confinement. Notably, the pivotal role of surface defects in stabilizing equilibrium configurations is elucidated. Furthermore, the deformation of LC spheroids is examined, shedding light on its profound influence on the growth and thermal stability of blue phases. Analogous effects are observed in cylindrical and toroidal confinement, leading to the discovery of tunable chiral ribbon-like defects.

The subsequent section of this work centers around the intriguing interaction between liquid crystals and colloidal particles. The research uncovers the formation of stable configurations characterized by intricate defect structures at interfaces, thereby offering exciting prospects for the design of stimuli-responsive emulsions. Moreover, it investigates the assembly of nanoparticle clusters on bipolar droplets, revealing the presence of kinetic traps through the application of advanced simulation techniques. To simplify the complex energy landscape, a novel simplified model is developed based on mean-field results, providing valuable insights into the construction of the free energy surface.

The final study within this dissertation focuses on the optimization of phenomenological parameters in continuum simulations through comparisons with experimental microscopy images. The research showcases an efficient simulation methodology capable of accurately capturing the complexities of intricate geometries and nonlinear behavior. The integration of stochastic elements prevents configurations from becoming trapped in local minima, while Bayesian optimization facilitates thorough exploration of the parameter space.

In summary, this dissertation presents a comprehensive investigation into soft matter materials, merging conventional continuum methods with molecular simulation elements. It highlights the profound impact of geometric effects, particularly the role of frustration, in engineering unique defect morphologies and driving colloidal assembly. The findings of this research open up exciting possibilities for the design and manipulation of soft matter materials, paving the way for future advancements in the field.

Acknowledgments

My time in Chicago has been an incredible adventure that took me to places and discoveries beyond what I could Imagine when I was admitted to the Molecular Engineering program in 2016. These have been the most intellectually stimulating and personally satisfying years of my life, and I am extremely grateful to have had the fortune of spending them at this university with all its history and in this department with all its energizing and innovative pursuits. This thesis has a single author, but none of it had been possible without the support and teachings of an entire community that embraced me throughout the past seven years.

First and foremost, I give thanks to my advisor Professor Juan J. de Pablo for his mentorship and dedication during my tenure in the group. His enthusiasm for scientific discovery and breadth of scholarship are only matched by his generosity and unwavering optimism in the face of challenge. My experience under Juan's wing taught me how to cultivate a nurturing academic community and to lead with kindness. It has been an honor and a joyful experience to work with Juan on developing creative ways to tackle diverse and interesting questions. The path to my doctoral studies was built on the efforts and guidance of Professor Juan P. Hernández-Ortiz at *Universidad Nacional de Colombia*. I am extremely fortunate to count on him as a mentor, collaborator, and friend. His attention to detail and perseverance in pushing the boundaries of Chemical Engineering in Colombia left an imprint on me of what education and research can accomplish, despite his Thermodynamics and Statistical Mechanics class being scheduled at 6 AM. I also wish to thank Professor Julio C. Armas-Pérez at *Universidad de Guanajuato*, whose creativity and passion for computational methods were fundamental and inspiring in addressing the challenges of my research. I am deeply indebted to all three for their continued support,

both academic and professional.

I am also grateful to have been able to meet, collaborate with, and learn from many wonderful scientists. To my committee members, Professors Paul Nealey and Vincenzo Vitelli who also evaluated my candidacy proposal, with their questions fueled my interest in broadening the impact of the research and methods I developed. Many thanks to Dr. Stiven Villada-Gil, whose patience and rigor made it possible to extend my research to non-equilibrium systems. I would also like to acknowledge my experimental collaborators for their contributions to the research reported in this thesis, mainly Professor Nicholas Abbott and his students Yu Yang and Xin Wang at Cornell University, Professor Sanaz Sadati and her student Sepideh Norouzi at University of South Carolina, Professor Emmanuelle Lacaze and Dr. Haifa Jeridi at UPMC–Sorbonne, Professor Teresa López-León and her student Guillaume Durey at ESPCI Paris.

As I reflect on my time as a doctoral student, I realize the great fortune it was to be in the research group at the same time as Professors Nick Jackson, Mike Webb, and Josh Lequieu. It was not only that I got a front-row seat to their research, but also to realize their impact on my own by the fact that they raised the standard and encouraged everyone by doing so. Many thanks to Professor Andrew Ferguson who has been a constant source of inspiration and encouragement during the past years.

One of my great passions is teaching, and I was privileged to have the opportunity of honing my teaching skills and be of support to fantastic lecturers. Professors David Venerus, Eric S. G. Shaqfeh, and Andrew Ferguson taught me the intricacies of Transport Phenomena, Rheology, and Molecular Modeling, and more importantly how to teach it. Their enthusiasm for their field stays with me as I endeavor to expand my own knowledge.

I offer thanks to the Fulbright Commission in Colombia and COLCIENCIAS for their support during the first half of my doctoral studies. Thanks to the Eiffel scholarship and

the Chateaubriand fellowship program for supporting my research stay in Paris.

I would like to thank the administrators of the PME, specifically Rovana Popoff, Novia Pagone, David Taylor, Hayley Huffman, Lisa Abston-Leftridge, Laura Rico-Beck, Maria Rubio, Janet Boland, Sandra Marijan, Heather Crews, and Lisa Vonesh for their patience and unrelenting work behind the scenes.

Many thanks to my dear friends and their families Johnny Alfaro-Pérez (Kelechi, Beatriz, Mónica, Johnny), Lucas Antony, Alec Bowen, Ashley Guo, Cody Bezik (Amanda and Faye), Emre Sevgen (Anna), Jenni Antane (Alejandro), Nick Jackson (Caroline, Gabe, Freja), Phil Rauscher (Rachel, Gus, Tom, Minnie), Ruben Waldman, Moshe Dolejsi (Victoria and David), Viktor Rozsa (Hannah, János, Éva), Pablo Zubieta Rico, Regina Sánchez and Chuqiao Chen. They have made Chicago a place of comfort and joy. I also want to thank everyone from the de Pablo group, past and present, for being an exceptional group of colleagues. My experience was greatly enhanced by the many conversations and discussions with them, including Sumi Hur, Jian Qin, Yamil Colón, Grant Garner, Adrián Martínez-Gonzalez, Ye Zhou, Ali Mozaffari, Rui Zhang, Hadi Ramezani-Dakhel, Marat Andreev, Liza Lee, Jiyuan Li, Gustavo Pérez-Lemus, Walter Alvarado, Fabian Byléhn, Chuting Deng, Yiheng Wu, Tadej Emersic, María Ley, Joán Montes de Oca, Cintia Menéndez, Riccardo Alessandri, Heyi Liang, and Jonathan Salmerón.

Finally, I thank my family. My parents ingrained in my brother and me a sense of responsibility, passion for academia, and love for work and each other that keeps us propelling forward. My grandparents sacrificed more than any of us can imagine to ensure that future generations had access to a good education; the culmination of this thesis goes beyond any of their wildest dreams. It is thanks to them, and my extended family, that I keep my feet on the ground. Last, but certainly not least, my infinite thanks and love to Josh Moller (Toro), his compassion and encouragement have sustained me through the highs and lows of my graduate career. I can't wait to see what the future holds.

Chapter 1

Introduction

Materials-based applications rely on harnessing properties that originate at the molecular scale for their response at the macroscale. While functional hard materials with static properties have been the primary focus of technological advances, soft materials offer dynamic properties that open up unique opportunities for the fabrication of advanced and smart materials. Among these soft materials, liquid crystals (LCs) occupy an intermediate state of matter. They exhibit long-range orientational order but lack long-range translational order, which allows them to flow relatively easily and respond to various external stimuli such as electric fields, magnetic fields, heat, light, and mechanical forces. The molecular anisotropy of LCs gives rise to several fascinating properties, including birefringence, dielectric anisotropy, viscosity, elasticity, flexo- and ferroelectricity.

The discovery and development of liquid crystals have a rich historical background. In the late 19th century, Friedrich Reinitzer, an Austrian botanist, observed that a substance derived from cholesterol exhibited peculiar optical properties as it transformed from a solid to a cloudy liquid and eventually into a clear liquid. This substance, later named "cholesteric liquid crystal", was the first identified form of liquid crystal material. Around the same time, Otto Lehmann, a German physicist, further investigated liquid crystals and introduced the term "liquid crystal" to describe their dual liquid-like and crystal-like nature.

In the early 20th century, liquid crystal research remained relatively dormant until the 1960s when significant advancements were made in understanding their properties and potential applications. It was during this period that the first practical liquid crystal

displays (LCDs) were developed. In 1968, George Heilmeier and his team at RCA Laboratories demonstrated the first operational LCD, which utilized the twisted nematic (TN) effect to control the passage of light through a liquid crystal bulk. This breakthrough paved the way for the development of flat panel LC display devices, revolutionizing the field of visual technology and leading to the widespread adoption of LCD screens in televisions, computer monitors, and mobile devices.

Since then, liquid crystal-based applications have expanded beyond display technology. Researchers and engineers have recognized the unique properties and versatility of liquid crystals, leading to the exploration of new and innovative applications. The ability of liquid crystals to form defect structures and respond to external stimuli has opened doors to various fields, including biosensors, self-healing materials, elastomers, and active matter. By leveraging the defects and dynamic properties of liquid crystals, researchers have been able to design advanced materials with programmable properties, enabling applications in fields such as photonics, optoelectronics, and soft robotics.

To understand the behavior of liquid crystals and explore their potential applications, the development of simulations as a tool in materials science has played a crucial role. Simulations allow researchers to investigate and predict the behavior of materials at different length scales and timescales, providing insights that complement experimental observations. To delve into the molecular-level mechanisms and understand the intricate interplay between various factors that govern the behavior of liquid crystals, researchers can choose appropriate computational tools that resolve the relevant phenomena.

One powerful tool for investigating the role of chemical identity and molecular-level specificity, selectivity, and precision is molecular simulations. Molecular simulations provide a detailed atomistic description of the system, allowing researchers to study the interactions and dynamics of individual molecules within the liquid crystal. These simulations can vary in the level of description, ranging from atomistic simulations that capture

the behavior of each atom to united atom or coarse-grained simulations that provide a more computationally efficient representation of the system. In all of these simulations, the anisotropy of the material is specified by means of the geometry of the LC mesogen, enabling a comprehensive understanding of the structural and dynamic properties of liquid crystals.

In this work, we adopt a mean-field approach with the central role played by Landau theory. This theory disregards the microscopic structure of matter and instead utilizes considerations of symmetry and smoothness of functions to predict phase transitions and energetic penalties for distortions. The free energy is expressed in terms of order parameters, and the richness of phase diagrams emerges from the various ways these order parameters can be combined to formulate the free energy functional.

Finding equilibrium configurations at this length scale requires the use of variational calculus since the free energy function depends on the local order parameter and its derivatives, which are themselves functions. While simple systems may allow for analytical solutions through the minimization of the free energy, the systems we are exploring pose analytical challenges. Therefore, we employ numerical methods to resolve complex geometries and capture non-linear behavior.

The focus of this thesis is on the effects of chirality, confinement, and inclusions in equilibrium configurations of thermotropic nematic liquid crystals at the continuum scale. By leveraging the advancements in simulations and computational resources, we can accurately represent and explore these systems, bridging the gap between theoretical predictions and experimental observations. Through this research, we aim to gain insights into the intricate behavior of LCs and contribute to the understanding and development of advanced materials and devices.

Chirality refers to the inherent twist that induces molecules to spontaneously align in a helical path. Experimentally, chirality can be controlled through the addition of a chiral

dopant to an achiral liquid crystal. Chirality can be frustrated by confinement, leading to a competition between the elasticity of the material, and the preferred orientation at the boundaries. In order to investigate this effect, several studies were performed. Firstly, a computational exploration of geometrical frustration is done in which a LC is confined in spheroids of different aspect ratios (chapter 3). The geometry imposes topological constraints at equilibrium, and the curvature truncates the natural development of double-twist domains. Specifically, in the high chirality regime, the stability of Blue Phases shifts by the effect of curvature, and the results provide a path forward to expanding the applicability of defect networks with cuboidal symmetry.

Experimental realizations of these predictions are presented in chapter 4. A method based on light scattering is developed to characterize phase transitions of LCs confined in nanoemulsions. The results indicate that the Blue Phase-Cholesteric transition can be suppressed by controlling the balance between chiral elasticity and surface tension. Finally, in chapter 5 we make use of non-uniform Gaussian curvature to engineer novel morphologies of cholesteric textures. In this instance, cylindrical capillaries and toroidal geometries are used to confine the LC, and since the curvature is comparable to the characteristic dimensions of the system, it can be harnessed to mold the soft defect regions.

When considering inclusions, particles in the colloidal regime interact with the background nematic order field by alleviating local distortions. Additionally, multiple colloids interact and self-assemble mediated by the elasticity of the LC. This is the ruling principle for the design of metamaterials. In chapter 6 we explore the role of tilted-alignment at the interface with the core of a nematic shell. The optical response indicates the emergence of quadrupolar and dipolar symmetry. The perfluoroalkane-nematic two-phase systems provide new opportunities to design stimuli-responsive emulsions, and platforms to study the role of elastic moduli on the optical texture perceived in the visible range.

The assembly of nematic colloids has been explored vastly, whether it happens in bulk or using patterned surfaces. However, a versatile platform is using LC droplets that exhibit surface defects. These sites offer locations that attract nanoparticles, and is the functional principle of many biosensing devices. In chapter 7 we develop a new method that allows us to unveil kinetically-trapped states when multiple nanoparticles assemble at the poles of the LC droplet. In the past, experimental studies have presented the variability of goemetrical packing, and previous simulations reveal that these states are metastable. However, the conventional mean-field approach provides a deterministic view whereas this new method involves the consideration of different assembly pathways.

Finally, in chapter 8 we present a methodology that allows future *in silico* explorations to follow a guided path, based on the similarity between simulated optical textures and those provided by experimental observations. The proof of concept is given in the form of being able to capture the dependence of uniaxial-radial droplet transition as a function of anchoring strength, as well as the optimization of the colloidal shape that captures the stable assembly of non-spherical nematic inclusions.

By delving into the behavior of liquid crystals and exploring different regions of configuration space, we can gain insights into their fundamental properties and their potential for application in various fields. Through this research, we aim to contribute to the understanding and development of advanced materials and devices based on liquid crystal systems.

1.1 Outline

Chapter 2 is devoted to the fundamental and relevant background information for the description of liquid crystalline order at the continuum scale, and the different numerical techniques that were implemented throughout the studies in this thesis.

The following chapters stand as distinct studies, deriving from the following publica-

tions, either fully or partially.

- Viviana Palacio-Betancur, Julio C. Armas-Pérez, Stiven Villada-Gil, Nicholas L. Abbott, Juan P. Hernández-Ortiz, and Juan J. de Pablo, "Cuboidal liquid crystal phases under multiaxial geometrical frustration" *Soft Matter* **16**, 4, 870–880 (2020).
  Chapter 3

- Yu Yang*, Viviana Palacio-Betancur*, Xin Wang, Juan J. de Pablo, Nicholas L. Abbott, "Strongly Chiral Liquid Crystals in Nanoemulsions" *Small* **18**, 10, 2105835 (2022).
  Chapter 4

- Viviana Palacio-Betancur, Julio C. Armas-Pérez, Juan P. Hernández-Ortiz, and Juan J. de Pablo, "Curvature and Confinement Effects on Chiral Liquid Crystal Morphologies" *Soft Matter* **In Press** (2023).
  Chapter 5

- Xin Wang, Ye Zhou, Viviana Palacio-Betancur, Young-Ki Kim, Lily Delalande, Michael Tsuei, Yu Yang, Juan J. de Pablo, Nicholas L. Abbott, "Reconfigurable multi-compartment emulsion drops formed by nematic liquid crystals and immiscible perfluorocarbon oils", *Langmuir* **35**, 49, 16312–16323 (2019).
  Chapter 6

- Viviana Palacio-Betancur, Julio C. Armas-Pérez, Juan P. Hernández-Ortiz, and Juan J. de Pablo, "Topological dereliction in liquid crystal mediated nano-particle assembly on spherical droplets" (In preparation 2023)
  Chapter 7

- Viviana Palacio-Betancur, Chuqiao Chen, Monirosadat Sadati, William Irvine and Juan J. de Pablo, "Exploring LC parameter space with experimentally-informed Bayesian optimization" (In preparation 2023).
  Chapter 8

- Stiven Villada-Gil*, Viviana Palacio-Betancur*, Julio C. Armas-Pérez, Juan P. Hernández-Ortiz, and Juan J. de Pablo, "Directing the far-from-equilibrium assembly of nanoparticles in confined liquid crystals by hydrodynamic fields" *Soft Matter*, **17**, 12, 3463–3472 (2021).

  Chapter 9

Chapter 2

Modeling nematic liquid crystals

The ordering quality of LCs is given by the shape of its molecules, which are classified in three categories: rod-like, disk-like and bent-core. The two first categories are the most common and are often found in biological systems, *e.g.* the lipids in cell membranes are rod-like molecules and the cholesterol is disc-like. A representation of both types is shown in Figure 2.1 with molecules of 5CB (rod-like) and triphenylene (disc-like). The alignment of these molecules is responsible for their optical activity.

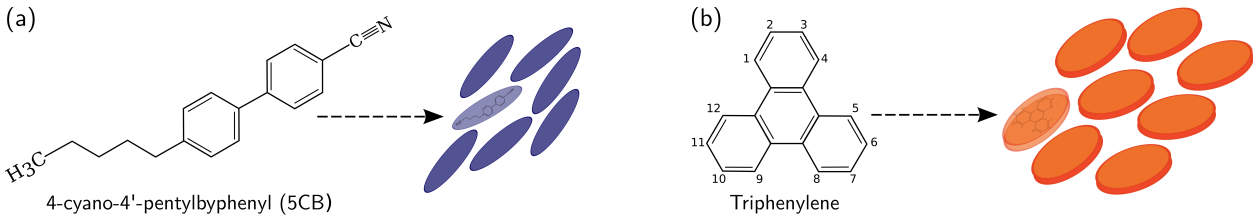

Figure 2.1: Representation of (a) a rod-like molecule of 5CB and (b) disk-like molecule of triphenylene.

Liquid crystals can also be classified as *(i)* thermotropic, *(ii)* lyotropic or *(iii)* metallotropic. Thermotropic liquid crystals are those whose ordering can be altered by heating or cooling of the material. For lyotropic LCs to be observed, it is necessary to reach a critical concentration and it depends on the length and diameter of the molecules. Metallotropic LCs are a mixture of inorganic and organic materials with dependence of temperature. Our main interest is focused on thermotropic liquid crystals, which exist in a specific range of temperature. Any LC system is a collection of distinct mesomorphous phases, or mesophases, each with a specific type of ordering. The order is defined by the uniformity of the orientation within the domain. In thermotropic LCs the phases range from nematic to smectics as function of the temperature as shown in Figure 2.2.

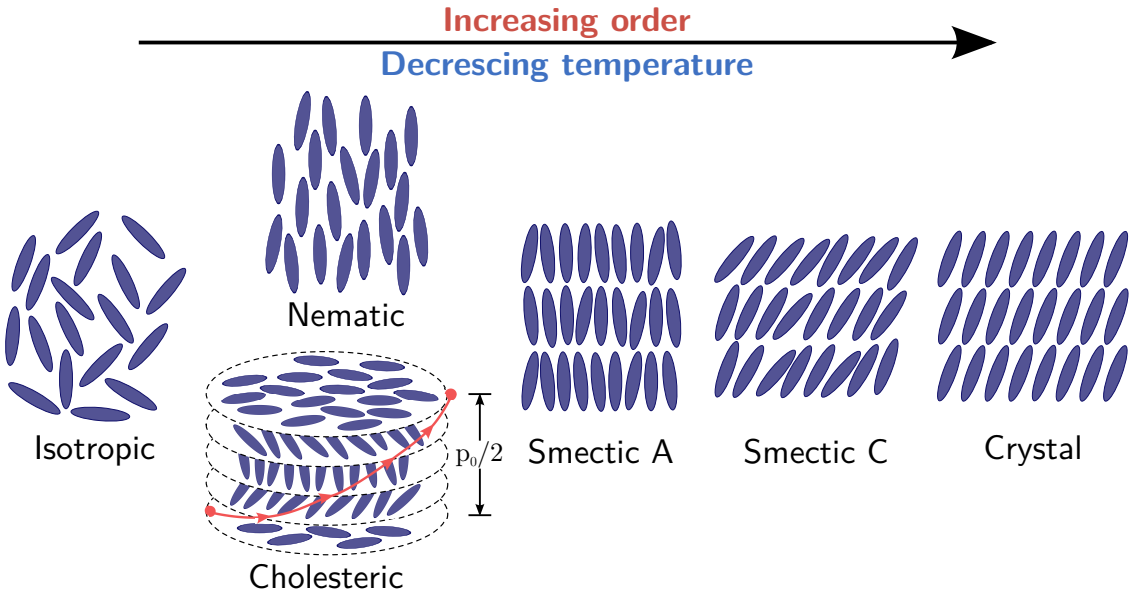

Figure 2.2: Different phases for thermotropic uniaxial liquid crystals as temperature decreases.

After transitioning from the isotropic state we found the nematic phase, which is characterized by long range orientational order along the average molecular orientation, but no positional order. Cholesterics are a special case of nematics in which there is also a supermolecular structure related to a helical rotation of the director, it can be interpreted as nematic layers stacked and the local orientation of each layer rotates respect to the previous one. By decreasing temperature furthermore, we transition to smectic phases, which exhibit positional and orientational molecular order, it is the phase that resembles the most to a crystal before reaching crystallization.

Besides their relationship with temperature, LCs behavior is also influenced by the presence of foreign substances, confinement, or applied external fields. The interaction between the LC molecules and any surface is called anchoring and it dictates the preferred orientation at the surface, the most common ones are homeotropic and planar anchoring.

When molecules realign to match boundary conditions, conflicting directions may arise and the director field becomes singular at some points, thus forming defects. Defects vary in shape, size and location depending on the imposed boundary conditions,

geometry and physical properties of the material. Defects are often characterized by their topological charge, which counts how many times the director rotates around the discontinuity in multiples of π and obeys a conservation law; it is zero in a flat surface and when enclosed in a sphere it must be 2 as required by the Poincaré-Hopf theorem [100].

The frustration, this is the competition between different influences on a physical system, is resolved when there is balance between the elastic energy that penalizes deformations, the interface interaction that promotes a preferred orientation, and the geometry restrictions [85]. For simplicity, the equilibrium configurations of the director field will be called phases.

A comprehensive description of liquid crystalline behavior must be able to capture the variations on the orientation of the molecules in a free domain as well as when confinement or interaction with foreign particles forces a specific orientation. Besides the description of the molecular ordering, free energies penalties exist to determine the most stable configuration of a LC system. This chapter introduces the mathematical tools needed for the modeling of uniaxial nematic liquid crystals. First, we dedicate a section to the definition of different order parameters. Then, the free energy description is presented as the result of three different contributions: bulk, elastic, and surface free energies. A brief description of the formation of topological defects is shown, as well as a general depiction of nematic and cholesteric phases.

2.1 Physics of nematic phases

2.1.1 Order description

The first attempt to quantify the ordering of a LC system consisted of a scalar parameter indicating the degree of isotropy. The definition comes from averaging the molecular

orientations and measuring the angle between molecules, θ.

$$S \equiv \frac{1}{2}\langle 3\cos^2\theta - 1\rangle. \tag{2.1}$$

This description is macroscopic and does not capture the minutia in the range of the molecular scale. The next step would be to obtain information of the direction of the molecular alignment **u**, thus obtaining the director fields **n** and **n′** where the latter only arises for biaxial molecules. This is depicted in figure 2.3. Recall that for uniaxial molecules, **n** is equivalent to **n′**.

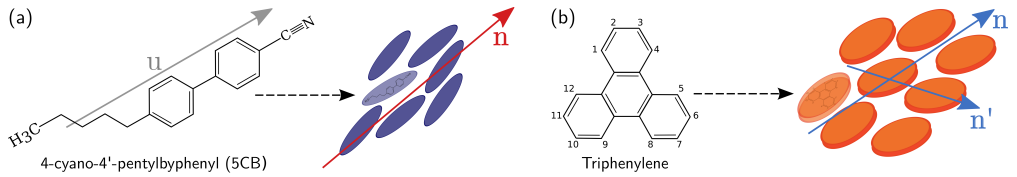

Figure 2.3: Molecular orientation for (a) uniaxial and (b) biaxial molecules. The vector **u** indicates the orientation of a single molecule, and **n**, **n′** are the director vectors.

As mentioned before, the use of liquid crystals is appealing because of the optical particularities that arise from defects. These defects are, by definition, regions where the molecular orientations diverge so any calculations for said region based on vectorial descriptions is not appropriate. To circumvent this issue, the description is taken to the next level with the formulation of a traceless and symmetric tensor, **Q**. It is defined by the director field and the probability distribution function $\psi_{(\mathbf{n},\mathbf{x},t)}$ of molecular orientations:

$$\mathbf{Q} = \int \mathbf{nn}\psi(\mathbf{n},\mathbf{x},t)\mathrm{d}\mathbf{n} - \frac{\boldsymbol{\delta}}{3}, \tag{2.2}$$

where $\boldsymbol{\delta}$ is the 3×3 identity matrix. Tensor **Q** may be written in terms of its eigenvalues

in a diagonal form as follows,

$$\mathbf{Q} = \begin{pmatrix} \frac{2}{3}S & & \\ & \eta - \frac{1}{3}S & \\ & & -\eta - \frac{1}{3}S \end{pmatrix} \tag{2.3}$$

According to this representation, tensor $\mathbf{Q}$ can also be written in terms of its eigenvalues [214, 15],

$$\mathbf{Q} = S\left(\mathbf{nn} - \frac{\delta}{3}\right) + \eta\left[\mathbf{n'n'} - \left(\mathbf{n}\times\mathbf{n'}\right)\left(\mathbf{n}\times\mathbf{n'}\right)\right], \tag{2.4}$$

where $S(\mathbf{x})$ is the scalar order parameter, related to the maximum eigenvalue. The biaxiality $\eta(\mathbf{x})$ is related to the other two eigenvalues. The order parameters are bounded by $S \in [-1/2, 1]$, and $\eta \in [-1/3(1-S), 1/3(1-S)]$. The eigenvectors, $\mathbf{n}$ and $\mathbf{n'}$, define an orthonormal basis $\{\mathbf{n}, \mathbf{n'}, (\mathbf{n}\times\mathbf{n'})\}$ for the LC orientation.

This definition of an order parameter allows for a continuous representation of the molecular ordering, and a precise description of regions with defects. The $\mathbf{Q}$ tensor contains all the information for an accurate thermodynamic description of the system, whether the system is in a LC state or during the transitions between these states.

2.1.2 Free energy description

The expressions at static equilibrium that describe this type of material, typically lead to the Helmholtz free energy taking the form of a polynomial expression in $\mathbf{Q}$ or in S as originally presented by Landau in 1936 [122], and later adapted to liquid crystals by de Gennes in 1969 [46]. Alternatives for the static description include de Maier-Saupe theory [143], and the Onsager theory [177]. For the non-homogeneity of nematic phases, the Oseen theory [179] and later reformulated by Frank [65] is very popular since it includes different modes of deformation that carries energetic penalties. More realistic situations

include confinement conditions, for which we present different functionals that impose a preferred orientation of the molecules as a boundary condition.

Joining these contributions, the free energy functional is calculated as,

$$F(\mathbf{Q}) = \int \mathrm{d}^3\mathbf{x}\,[f_L(\mathbf{Q}) + f_E(\mathbf{Q}, \nabla\mathbf{Q})] + \oint \mathrm{d}^2\mathbf{x} f_S(\mathbf{Q}) \tag{2.5}$$

where f_L is the Landau–de Gennes free energy, f_E is the elastic free energy, and f_S is the surface free energy. In the following sections each contribution will be explained in more detail.

Landau–de Gennes free energy

For the description of the bulk free energy we use a phenomenological approach that serves to characterize the internal structure of the medium. The free energy density is described by a truncated polynomial expansion of the tensor order parameter's invariants [46, 122, 47, 76, 229].

$$f_L(\mathbf{Q}) = \frac{1}{2}A(T)\mathrm{tr}(\mathbf{Q}^2) + \frac{1}{3}B\mathrm{tr}(\mathbf{Q}^3) + \frac{1}{4}C\mathrm{tr}(\mathbf{Q}^2)^2,$$

where $A(T), B$, and C are phenomenological coefficients, $\mathrm{tr}\,(\mathbf{M})$ is the trace of the matrix $\mathbf{M}$ and $\mathbf{Q}^2 = Q_{ij}Q_{jk}$. The free energy density in eq. (2.6) predicts a phase transition at a temperature that forces A to vanish. Therefore, it is assumed that A has the form,

$$A(T) = a\,(T - T^*)\,, \tag{2.6}$$

where a is positive and constant, T is the temperature and T^* is a temperature close to the NI transition temperature, T_{NI}.

Through this functional it is possible to study the transition from the isotropic state to the nematic, by differentiating four different temperature regimes. At high temperatures,

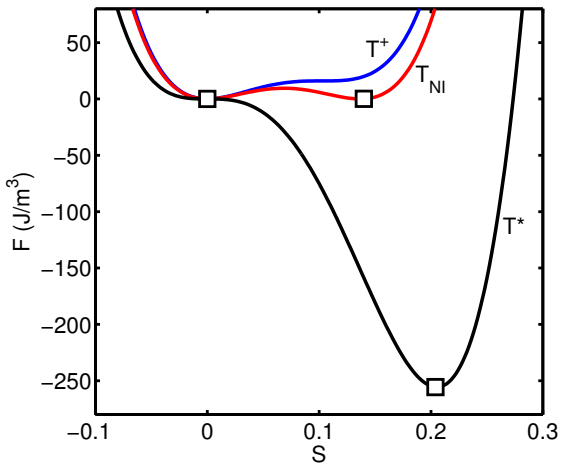

Figure 2.4: Free energy density of the 5CB as a function of the uniaxial order parameter at three different temperatures: T^+, T_{NI}, and T^*. The phenomenological coefficients are: $a = 0.13 \times 10^6 J/m^3 K, B = -1.6 \times 10^6 J/m^3, C = 3.9 \times 10^6 J/m^3$, and $T^* = 307.15K$ from [41]. The squares indicate the equilibrium values of the order parameter. This diagram is valid only for $B < 0$.

$T > T^+$, there is a single minimum in the free energy that corresponds to a stable isotropic phase; F has only one minimum at $S = 0$. For $T_{NI} < T < T^+$, the isotropic phase is still the stable state, but there is an additional local minimum in the free energy at

$$S = -\frac{B}{4C}\left\{1 + \left[1 - 24\frac{aC}{B^2}(T - T^*)\right]^{1/2}\right\}, \tag{2.7}$$

that corresponds to a metastable nematic phase. On the contrary, for $T^* < T < T_{NI}$ the stable state is the nematic phase, while the isotropic phase is the local free energy minimum. Finally, at $T < T^*$ there is a unique nematic stable phase. At $T = T_{NI}$ the two minima are equivalent, thereby defining the NI transition. Note that this transition shows a discontinuity in the order parameter, ergo it is a first-order transition. This is explained by the odd-order powers of tr($\mathbf{Q}$) in the free energy functional.

The form of the free energy density in eq. (2.6) provides additional characteristics and properties for the transitions and phases. For instance, the free energy density is non-linear thus allowing the isotropic phase. The first term drives the NI transition. The

inclusion of a third order term causes the NI transition to be first order. It also ensures asymmetry with respect to $\mathbf{Q} \leftrightarrow -\mathbf{Q}$.

From the Doi theory [50], the free energy functional from eq. (2.4) is expressed in terms of another set of phenomenological coefficients. The set consists on A_i coefficients that control the energy scale of the model, and an adimensional parameter U that controls the scalar order parameter S. The free energy functional is rewritten as,

$$f_L(\mathbf{Q}) = \frac{1}{2}A_1\left(1 - \frac{U}{3}\right)\mathrm{tr}(\mathbf{Q}^2) - \frac{1}{3}A_2 U\,\mathrm{tr}(\mathbf{Q}^3) + \frac{1}{4}A_3 U\,\mathrm{tr}(\mathbf{Q}^2)^2, \tag{2.8}$$

For a system without boundary restrictions, the order parameter is related to U through the following expression,

$$S_{bulk} = \frac{1}{4} + \frac{3}{4}\sqrt{1 - \frac{8}{3U}} \tag{2.9}$$

To transform the free energy functional from eq. (2.6) to the Doi notation in eq. (2.8) it is necessary to apply the following equivalences,

$$A = A_1\left(1 - \frac{U}{3}\right) \tag{2.10}$$

$$B = -A_2 U \tag{2.11}$$

$$C = A_3 U \tag{2.12}$$

Following the same analysis for the phase transition lines, values for U analogous to those of T_{NI} and T^+ can be found by assuming a unique value for A_i.

Elastic energy: Frank–Oseen theory

The origin of the Frank–Oseen theory lies on an analogy to solid elasticity. When the director field is inhomogeneous, spatial distortions of the molecular orientations caused by the presence of non-zero curvature that later result in a higher free energy. considers

that all deformations are a result of three independent modes of variation of **n**: splay, twist, and bend, using three elastic non-vanishing moduli, k_{11}, k_{22}, and k_{33} as illustrated in figure 2.5.

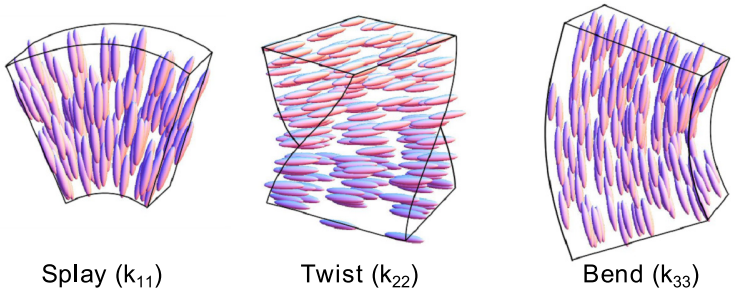

Figure 2.5: Elastic deformation moduli. Figure adapted from [36].

The formulation of this theory in terms of the director field is,

$$f_E = \frac{1}{2}k_{11}\left(\nabla \cdot \mathbf{n}\right)^2 + \frac{1}{2}k_{22}\left(\mathbf{n} \cdot \nabla \times \mathbf{n}\right)^2 + \frac{1}{2}k_{33}|\mathbf{n} \times \left(\nabla \times \mathbf{n}\right)|^2 \tag{2.13}$$

The elastic constants must be positive so the homogeneous state corresponds to a minimum of the elastic free energy. As mentioned before, the use of a phenomenological formulation in terms of vector order parameters is limited to continuous variations of the molecular orientations. The mapping from **n** to **Q** is only valid for uniaxial molecules and results in the following expression,

$$f_E = \frac{L_1}{2}\frac{\partial Q_{ij}}{\partial x_k}\frac{\partial Q_{ij}}{\partial x_k} + \frac{L_2}{2}\frac{\partial Q_{jk}}{\partial x_k}\frac{\partial Q_{jl}}{\partial x_l} + \frac{L_3}{2}Q_{ij}\frac{\partial Q_{kl}}{\partial x_i}\frac{\partial Q_{kl}}{\partial x_j} \tag{2.14}$$

with the elastic constants L_i related to the elastic moduli by,

$$L_1 = \frac{1}{6S_{bulk}^2}(k_{33} - k_{11} + 3k_{22}) \tag{2.15}$$

$$L_2 = \frac{1}{S_{bulk}^2}(k_{11} - k_{22}) \tag{2.16}$$

$$L_3 = \frac{1}{2S_{bulk}^2}(k_{33} - k_{11}) \tag{2.17}$$

Additional terms might be added to eq. (2.14) in order to describe additional spatial distortions. This is the case for saddle–splay deformations and chirality. Traditionally, the k_{24} constant, corresponding to a saddle-splay deformation, has been neglected because its value is difficult to determine. In curved surfaces or inhomogeneous boundary conditions, the presence of spatial distortion is evident and so, the saddle-splay elastic constant must be included in the free energy [231]. The additional term is:

$$\frac{L_4}{2}\frac{\partial Q_{jk}}{\partial x_l}\frac{\partial Q_{jl}}{\partial x_k}, \tag{2.18}$$

with $L_4 = k_{24}/S_{bulk}^2$ being the elastic constant. The saddle-splay moduli, k_{24}, is bounded by the following two inequalities,

$$-k_{22} \leq k_{24} \leq \min(2k_{11} - k_{22}, k_{22}) \tag{2.19}$$

The first measurements of the saddle–splay elasticity were done by Ondris–Crawford *et al.*[175] for a confined nematic phase. One of the substantial remarks is that curvature effects add difficulty to determine the value of k_{24}, especially when confinement is in the submicron scale; for supramicron droplets, a stability diagram was obtained for two different configurations of the droplet [57] but it only provided qualitative appreciations since combined elastic effects (*e.g.* saddle–splay, mixed splay-bend) were neglected due

to lack of information.

When treating chiral materials, there is an inherent twist of the director vector of each nematic layer caused by the enantiomeric character of the molecules, as illustrated in figure 2.2. The director field follows a helical fashion and completes one revolution in a distance p_0, called the pitch of the material. A material with chirality will not present this type of rotation only if the mixture is racemic. The term that describes this behavior is:

$$\frac{1}{2}L_5\epsilon_{ikl}Q_{ij}\frac{\partial Q_{lj}}{\partial x_k}, \tag{2.20}$$

with ϵ_{ikl} being the Levi–Civita tensor, and L_5 is the elastic constant related to the twist deformation mode k_{22} and the chirality of the system $q_0 = 2\pi/p_0$, by $L_5 = {}^{2}/_{S^2_{bulk}} q_0 k_{22}$. Note that since there is only one gradient that contributes to this type of deformation, the free energy is minimized as the twisting is more frequent.

The one-elastic constant approximation is a common consideration for systems sufficiently large. Due to its simplicity ($k_{11} = k_{22} = k_{33}$), it has been proven appropriate if the geometry has no dramatic changes in curvature [176, 3].

Surface free energy

The imposition of a molecular alignement at the surface influences the behavior of the medium so the director takes a compatible orientation that minimizes the free energy, as illustrated in fiugre 2.6. For the homeotropic (perpendicular) anchoring, the second order Rapini–Papoular potential is used [185]:

$$f_S(\mathbf{Q}) = \frac{1}{2}W\left(\mathbf{Q} - \mathbf{Q^o}\right)^2, \tag{2.21}$$

where W represents the anchoring strength and $\mathbf{Q^o}$ is the preferred tensor order parameter at the surface. For degenerate-planar anchoring, the 4th order Fournier–Galatola

potential is used [63],

$$f_S(\mathbf{Q}) = \frac{W}{2}(\mathbf{Q} - \mathbf{Q}_\perp)^2 + \frac{W}{4}\left(\mathbf{Q} : \mathbf{Q} - S^2\right)^2, \tag{2.22}$$

where $\bar{Q}_{ij} = Q_{ij} + S\delta_{ij}/3$, $\mathbf{Q}_\perp = \mathbf{pQp}$, $p_{ij} = \delta_{ij} - \nu_i\nu_j$ and ν is the unit vector normal to the surface.

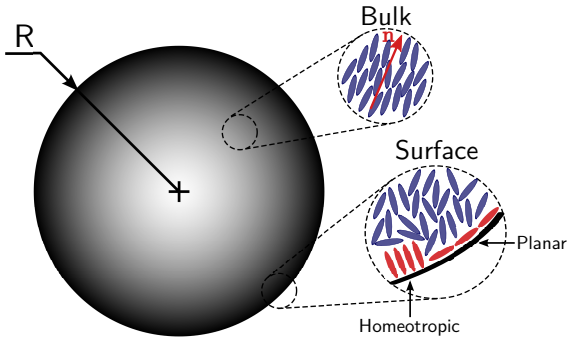

Figure 2.6: Schematic representation of different anchoring conditions for a confined liquid crystal.

2.1.3 Topological defects

When conflicting orientations are present in a LC system, a region where the order is destroyed and the rotational symmetry is broken. That region is called a topological defect, or disclinations, and can also be seen as a singularity of the director field. These defects polarize light [111] and represent regions with higher free energy that is attractive to colloids [202, 156, 183]. It is precisely the ability of LCs to form defects by design, that makes them attractive for technological applications.

Every system that is confined exhibits a competition between the surface orientation and the bulk uniformity, and depending on the anchoring strength it is possible to induce phase transitions [85]. With sufficiently strong anchoring, well defined defects can be differentiated. For achiral LCs, when the anchoring is homeotropic the radial phase is recognized by one defect centered in the bulk where the director field diverges, whether

with the tangential anchoring the bipolar phase is observed with two diametrically opposed boojum defects located on the surface. As the anchoring strength decreases, the phases are degenerated and more weakly defined phases are observed, as the twisted radial and the escaped radial (pre-radial) phases. The axial and uniaxial configurations are observed when the anchoring is weak and thus the imposed orientation is easily modified by the elastic forces. These phases are illustrated in figure 2.7.

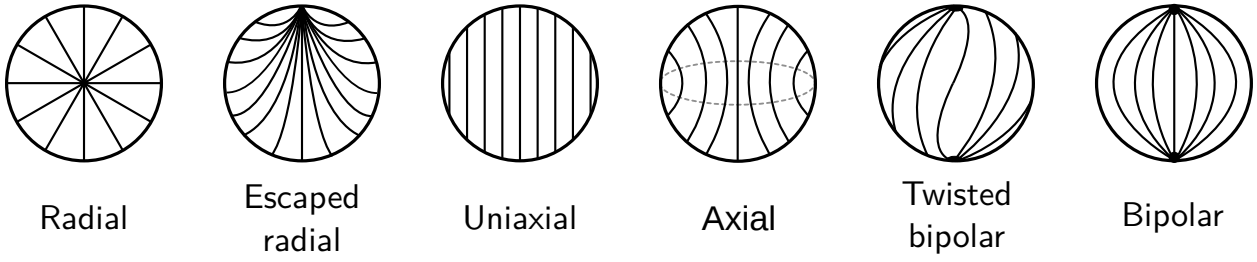

Figure 2.7: Director field configurations for different phases induced by the anchoring conditions in a droplet of nematic liquid crystals.

As chirality is introduced, two regimes define the type of defects. For low chirality, the material is cholesteric and the director field rotates continuously. There are regions with topological charge but not with an abrupt change of the scalar order parameter S. Some of these anormalities are shown in figure 2.8.

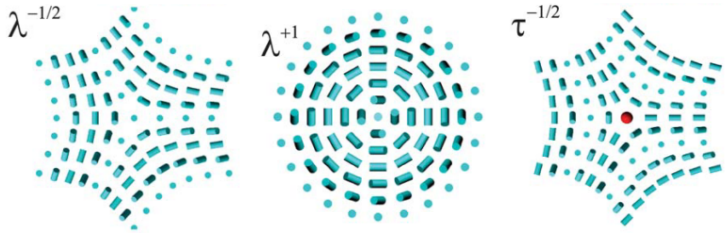

Figure 2.8: Schematic representation of three different cholesteric defects. Adapted from [215].

For materials with high chirality, the director rotates more frequently and regions with double twists join to form defect lines in the bulk, or disclinations. These arrays of defects follow a cubic symmetry of the O^8 type, seen in the body centered cubic structure and

called Blue Phase I (BPI), and the O^2 type is called Blue Phase II (BPII) seen in the simple cubic structure.

2.2 Free energy minimization

2.2.1 Ginzburg–Landau relaxation

Inspired by time-dependent relaxations, the most popular method in the literature is the Ginzburg-Landau isothermal (iso-entropic) relaxation. A detailed description of a Finite Difference discretization of this type of relaxation is presented by Ravnik and Zumer [201]. The evolution equation for the $\mathbf{Q}$ tensor follows,

$$\frac{\partial \mathbf{Q}}{\partial t} = -\frac{1}{\gamma}\left(\frac{\delta F}{\delta \mathbf{Q}}\right)^{ST}, \tag{2.23}$$

where γ is a rotational viscosity (or diffusion) coefficient and $(\cdot)^{ST}$ is a projector operator that ensures the symmetric and traceless character of the operand, in this case the Volterra derivatives from equation (**??**). This set of equations can be rewritten explicitly as,

$$\begin{aligned} \frac{\partial \mathbf{Q}}{\partial t} &= \nabla^2 \mathbf{Q} + \mathbf{f}'\left(\mathbf{Q}, \nabla \mathbf{Q}\right), \qquad \mathbf{x} \in \boldsymbol{\Omega} \\ \frac{\partial \mathbf{Q}}{\partial \mathbf{x}} \cdot \boldsymbol{\nu} &= \mathbf{f}''\left(\mathbf{Q}\right), \qquad \mathbf{x} \in \partial\boldsymbol{\Omega}, \end{aligned} \tag{2.24}$$

where $\mathbf{f}'$ contains the Volterra derivatives that have nonlinear terms such as the Landau–de Gennes contribution and all elastic contributions except that from the L_1 mode. For the boundaries, the term $\mathbf{f}''$ contains the Volterra derivatives for the surface potentials and the surface projections of the elastic deformations.

This method, albeit more robust than a pure numerical minimization, often relaxes the system into a local minimum and is unable to escape it in search of a more stable configuration. It is befitting of systems that are far away from any transition between

mesophases. Near a transition, the system will have at least two minima of comparable free energy separated by a significant barrier. Once the method relaxes into one of the minima, there is no driving force that enables the rearranging of $\mathbf{Q}$ in a significant way such that the system overcomes the barrier. In this way, the use of this method becomes cumbersome when exploring mesophases and structural transitions since there is no certainty of whether the configuration represents the most stable state. Common practice resorts to implementing *ansatz* and comparisons of final free energies in order to determine the most stable structure.

2.2.2 Theoretically-informed Monte Carlo relaxation

An alternative to classical methods is inspired by implementations in the field of polymer science, where a coarse grained model informs a sequence of Monte Carlo moves. In this case, as presented in [9, 7], the continuum free energy functional defined in section **??** is calculated for each trial move and the Metropolis criteria is implemented to accept or reject the new configuration. A similar approach was used recently by Parrinello *et al.*[92]. The pioneers on stochastic sampling of orientational fields showed the first implementations using the director formulation for a 2D lattice system including multiple elastic constants and interaction with a spherical particle [77, 206].

As a first consideration, the relaxation of the $\mathbf{Q}$ field is constrained by the bounds set for its eigenvalues, thus restricting its eigenvectors. In order to ensure a uniform sampling over the 5 independent components of $\mathbf{Q}$, we map the order tensor to an orthonormal tensor basis previously introduced by Hess *et al.*[98],

$$\mathbf{Q} = \sum_{\nu=1}^{5} a_\nu \left(\mathbf{x}\right) \mathbf{T}^\nu, \tag{2.25}$$

where the five scalar components a_ν are projections. The basis are defined by,

$$\begin{gathered}\mathbf{T}^1 = \sqrt{3/2}\,[\mathbf{zz}]^{ST}\,, \quad \mathbf{T}^2 = \sqrt{2}\,[\mathbf{xy}]^{ST}\,, \quad \mathbf{T}^3 = \sqrt{2}\,[\mathbf{xz}]^{ST}\,, \\ \mathbf{T}^4 = \sqrt{1/2}\,(\mathbf{xx} - \mathbf{yy})\,, \quad \mathbf{T}^5 = \sqrt{2}\,[\mathbf{yz}]^{ST}\,.\end{gathered} \tag{2.26}$$

Here, $[A]^{ST}$ is the symmetric-traceless projection operator, $\mathbf{x}$, $\mathbf{y}$, and $\mathbf{z}$ are the canonical $\mathfrak{R}^3$ basis, and δ_{ij} is the Kronecker delta. In this way, the sampling will be done on the 5 coefficients of the new basis which are free to take any real value and at the end of the MC run we can map any result back to $\mathbf{Q}$–space by using the following rules,

$$\begin{gathered}Q_{11} = -\frac{a_1}{\sqrt{6}} + \frac{a_4}{\sqrt{2}}, \quad Q_{12} = \frac{a_2}{\sqrt{2}}, \quad Q_{13} = \frac{a_3}{\sqrt{2}} \\ Q_{22} = -\frac{a_1}{\sqrt{6}} - \frac{a_4}{\sqrt{2}}, \quad Q_{23} = \frac{a_5}{\sqrt{2}}.\end{gathered} \tag{2.27}$$

Once we transfrom to a-space, the sampling is done by randomly selecting a point in the domain $\mathbf{x_i}$, and then attempting to randomly displace $\mathbf{a}\,(\mathbf{x})$ according to,

$$a_{\mu,new}\,(\mathbf{x}) = a_{\mu,old}\,(\mathbf{x}) + \bar{\delta}_\mu\,(\zeta - 0.5)\,, \tag{2.28}$$

where μ is an integer random number from 1 to 5 that selects which component we displace, $\zeta \in [0, 1]$ is a random number uniformly distributed, and $\bar{\delta}_\mu$ is the maximum allowed displacement. The sequence of trial moves that are accepted form a Markov chain of configurations, each transition is accepted with probability,

$$P_{acc}\,(o \to n) = \min\left[1, \exp\left(-\beta \Delta F\right)\right], \tag{2.29}$$

where $\beta^{-1} = k_B \hat{T}$ with k_B is the Boltzmann constant and $\hat{T}$ is an artificial temperature that is not related to the real temperature of the system; $\Delta F = F\,(\mathbf{Q}_n) - F\,(\mathbf{Q}_o)$ is the change in the free energy due to an alteration in the old configuration. Numerical integration is

implemented to calculate the free energy before and after each trial move. In order to minimize the free energy, an annealing scheme is set in place where $\hat{T}$ is reduced periodically and controls $\bar{\delta}_{\mu}$.

Although unconventional, this method has shown great potential for identifying a great variety of mesophases under distinct conditions, and more importantly it often finds the configuration with the lowest free energy. Given the fact that it does not make use of the Volterra derivatives, additional terms of the free energy functional are easier to implement than with the Ginzburg-Landau relaxation method in section 2.2.1. This has been of particular use in two cases: implementation of other elastic deformation modes, and the complete formulation of planar degenerate anchoring. The downside to this method is related to the artificial temperature for the annealing that seems to be system-dependent, and the computational efficiency due to large memory requirements for systems of larger size than 2μm.

2.3 Numerical methods

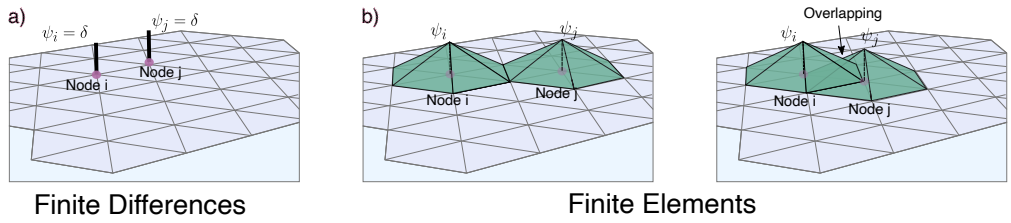

Figure 2.9: Graphical representation of the basis functions used for integration in the (a) Finite Differences Method and (b) Finite Elements Method.

2.3.1 Finite difference discretization

The finite difference method is a numerical technique commonly used to solve partial differential equations (PDEs) by approximating derivatives with discrete differences. It

involves dividing the spatial and temporal domains into a grid of points and expressing the derivatives at each point in terms of the function values at neighboring grid points. By discretizing the domain, the continuous PDE problem is transformed into a system of algebraic equations that can be solved using standard linear algebra techniques. The accuracy of the solution depends on the size of the grid and the order of the finite difference approximation. The finite difference method is widely applicable and has been successfully used to solve a variety of PDEs in various fields of science and engineering.

When applying the finite difference method to solve PDEs, the choice of appropriate boundary conditions and initial conditions is crucial. Boundary conditions specify the values or behavior of the solution at the boundaries of the domain, while initial conditions determine the solution at the initial time or starting point. These conditions are incorporated into the finite difference equations, allowing for an accurate approximation of the solution throughout the domain and over the desired time interval. The choice of boundary and initial conditions should reflect the physical problem being modeled and ensure a well-posed mathematical formulation.

In the study of liquid crystals, an anisotropic phase of matter with properties between those of liquids and solids, the choice of basis functions for the finite difference method is important to accurately capture the behavior of the material. Liquid crystals exhibit orientational order and exhibit complex director field patterns. Basis functions that can adequately represent these patterns are needed for an effective simulation. One common choice is to use tensor spherical harmonics as the basis functions, which allow for the description of the orientational order in terms of spherical harmonics while also capturing the anisotropic nature of the liquid crystal. These basis functions provide a convenient representation of the director field and enable the accurate computation of material properties and dynamics in liquid crystal systems. However, the choice of basis functions may vary depending on the specific characteristics and symmetries of the system under study.

2.3.2 Gaussian quadrature with Finite Element discretization

The Finite Element Method (FEM) is a numerical technique widely used to solve partial differential equations (PDEs) by dividing the domain into smaller, simpler regions called finite elements. Each finite element represents a small portion of the domain and is defined by a set of nodes and shape functions. The basic idea of FEM is to approximate the solution to the PDE by expressing it as a linear combination of these shape functions within each element. The governing equations are then transformed into a set of algebraic equations by applying the principle of weighted residuals, such as the Galerkin approach. The Galerkin method involves multiplying the PDE by a weight function and integrating over the domain, resulting in a set of equations that can be solved using linear algebra techniques. The FEM provides a flexible framework for solving complex PDE problems in various fields, including structural analysis, fluid dynamics, and electromagnetics.

The Galerkin approach is a key concept within the Finite Element Method, where a suitable weight function is chosen to form a weighted residual. The weight function satisfies certain properties, such as being continuous and differentiable, and is typically selected to have similar properties as the shape functions used to approximate the solution. By multiplying the PDE by the weight function and integrating over the domain, the resulting weighted residual is minimized to obtain a system of equations that approximate the original PDE. This approach ensures that the solution satisfies the PDE in a weak sense, meaning it holds in an integrated or averaged sense over each finite element. The Galerkin approach is a fundamental principle in FEM and provides a systematic way to construct the algebraic equations that approximate the PDE solution.

Gaussian quadrature is a numerical integration technique commonly used in the Finite Element Method to efficiently compute the integrals arising from the Galerkin approach. When solving PDEs using FEM, various integrals over the domain and element boundaries need to be evaluated. Gaussian quadrature approximates these integrals by

choosing a set of points and weights that accurately capture the integrand's behavior. The key idea is to approximate the integral as a weighted sum of function evaluations at these specific points, where the weights are chosen to minimize the error. Gaussian quadrature is particularly useful as it provides accurate results using a minimal number of evaluation points, making it computationally efficient. The number of quadrature points used depends on the order of accuracy desired, with higher-order quadrature formulas providing more accurate results. Gaussian quadrature is widely employed in FEM to efficiently handle the integration requirements and enable the solution of complex PDEs in a practical manner.

The integration is done using Gauss-Legendre quadrature over linear and quadratic tetrahedral elements, of the form:

$$I = \int \int \int_T f(x, y, z) \mathrm{d}x \mathrm{d}y \mathrm{d}z \approx \sum_{i=1}^{N} c_m f(x_m, y_m, z_m), \tag{2.30}$$

where T is the tetrahedral element, x, y, z are the coordinates, N is the number of Gauss points or pivotal points, f is the function to be integrated, and c_m are the weights on each point. For the integration we isoparametrize the elements for easier and faster calculation.

The Finite Element-based meshing allows us to capture the nuance of the geometries to perfection and is done using third–party software provided by Argonne National Laboratory [121, 109].

Chapter 3

Cuboidal liquid crystal phases under multiaxial geometrical frustration

3.1 Introduction

Blue phases arise spontaneously in chiral liquid crystals. they consist of networks of defect lines that organize themselves into space filling lattices with cubic symmetry. [52] Technological applications include low–energy consumption displays, [104] optical sensors, [21, 134, 207] and photonic crystals. [59, 30, 135, 156] Blue phases (BPs) have attracted attention for their fast response to external stimuli, [84, 242] but their narrow range of thermal stability poses challenges to their use. Past efforts to stabilize BPs have focused on addition of dopants to nematic phases, [33, 202, 49, 66, 82, 198, 265, 218] and little work has been devoted to the study of geometrical confinement as a means to manipulate their structure.

Geometrical frustration can be used to generate new families of defect configurations. More specifically, one can engineer the balance between the surface and elastic contributions to the free energy, [100] and favor anchoring driven transitions over bulk morphologies. For instance, cholesteric liquid crystals (ChLCs) confined in channels form structures similar to skyrmions, [67, 68, 149, 2] and the orientation of the cholesteric can be changed through surface functionalization. [146, 126**?**] Under spherical confinement, BPs reproduce their lattice order and may be manipulated to take advantage of the intrinsic topology of the chiral nematics to form knots or to braid nanopar-

ticles. [11, 267, 215, 102, 216, 146, 183, 178]

A phase diagram for micron-sized droplets of chiral LCs has been reported previously by Martínez-González et al. [146]. In that work, the stability of each region was determined by minimizing the total free energy using a Ginzburg–Landau relaxation from initial *ansatze* configurations. A wide variety of configurations was reported, including twisted cylinders (TC), radial spherical structures (RSS), and blue phases one (BPI) and two (BPII). Some regions of the phase diagram correspond to the phases formed in bulk [53, 241], and others do not.

Particle-based molecular simulations have shown that a freely suspended LC droplet adopts a prolate geometry due to the elongated shape of the molecules [252]. The formation of non–spherical droplets has also been reported in lyotropic liquid crystals [101, 246, 106, 191]. The anisotropy of these shapes induces chiral morphologies with a certain range of stability. For instance, mechanical deformation of a BPI has been used to tune optical response through an applied strain [35, 32], providing options for the fabrication of low–voltage electro–optical devices. More recently, cellulose nanocrystal suspensions have been shown to form chiral nematic tactoids, which offer the possibility to reach greater lengths and higher aspect ratios, and can aid in separation processes for nanoparticles [258, 259]. Building on these past studies, the central questions that we address here are whether it is possible to stabilize BPs by means of an external asymmetric physical constraint, as opposed to a chemical alteration, and whether the resulting phases undergo significant changes that may alter their optical properties.

A model chiral LC is confined into spheroids of different aspect ratios. We consider oblate, spherical, and prolate geometries. The reference geometry is a sphere with a radius of 500 nm; its axes are stretched to obtain isochoric geometries with different aspect ratios $\varphi = c/a$, where c and a are the lengths of the semi-principal axes aligned with the z and x Cartesian axes, respectively. An oblate is described by $\varphi < 1$, while a prolate is

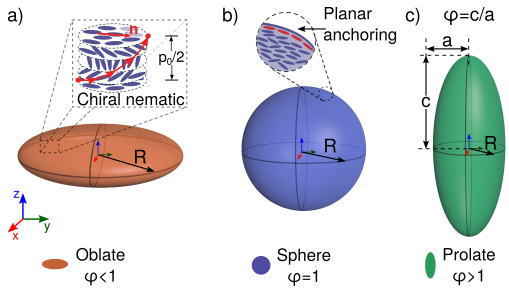

Figure 3.1: Schematic of the types of tactoids. (a) Oblate, $\varphi < 1$. The insert shows an schematic of the behavior of a chiral nematic, where p_0 is the cholesteric pitch and $\mathbf{n}$ is the mean molecular orientation or director vector. (b) Sphere, $\varphi = 1$. The insert shows the planar alignment of the molecules at the surface. (c) Prolate, $\varphi > 1$. The aspect ratio φ is defined by the lengths c and a which are aligned with the Cartesian directions z and y. The cartoons next to each spheroid will be used throughout this paper to represent the geometry.

described by $\varphi > 1$. Accordingly, a sphere corresponds to $\varphi = 1$. Figure 3.1 shows the three type of spheroids and the orientation of the axes. The surface imposes a degenerate planar orientation on the LC material, and the pitch p_0 is defined in terms of N, which denotes the number of π–turns along the major axis. Note that for all geometries the cross section parallel to the xy-plane is a circle of radius R.

3.2 Results

The chiral liquid crystal's nematic coherence length is $\xi_N = \sqrt{L_1/A} = 10$ nm; the elastic constant is $k_{11} = 16$ pN. The surfaces impose degenerate planar anchoring; we consider high ($W = 1 \times 10^{-3} J/m^2$), intermediate ($W = 1 \times 10^{-4} J/m^2$), and low ($W = 1 \times 10^{-5} J/m^2$) anchoring strengths. The chirality is controlled through the dimensionless parameter $N = 4R/p_0$, indicating the number of π–turns the director makes along a distance R. In order to build consistent phase diagrams for all geometries, we calculate the pitch necessary to keep N constant as φ varies. The phase diagrams are built in terms of the inverse reduced temperature $\tau = 9\,(3 - U)\,/U$ and the chirality parameter N.

3.2.1 Free energy analysis

We begin by examining different contributions to the free energy functional as the aspect ratio is changed. We restrict this analysis to the strong anchoring conditions, $W = 1 \times 10^{-3} J/m^2$, and $U = 2.9$. Moderate and weak anchoring as well as lower temperatures follow similar trends. The consequences of changing W, U and N are reflected the phase diagrams, which are discussed in the following sections.

Figure 3.2 shows the total free energy as a function of the aspect ratio for different values of N. At first sight it appears that the free energy decreases monotonically as the aspect ratio increases; note, however, that as φ increases the chirality also increases. Recall that the chiral contribution to the free energy is negative, implying that the formation of defects stabilizes the system as L_5 increases. The behavior of the total free energy in Fig. 3.2 helps explain the effects of N: for $N < 2$ the dependence of the free energy on φ is less than when $N > 3$, and $N = 3$ serves to delineate different morphologies, where the strong decrease of the total free energy is accompanied by a change of the nature of the underlying defect structure.

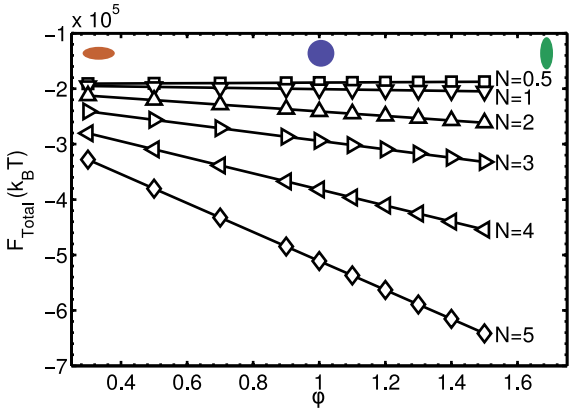

Figure 3.2: Total free energy as a function of the aspect ratio, φ and different chiral systems distinguished by N. The free energy is calculated for strong anchoring conditions with $W = 1 \times 10^{-3} J/m^2$ and $U = 2.9$. The cartoons in the top of the figure indicate the type of spheroid.

Figures 3.3 and 3.4 show the different contributions to the free energy density as a

function of φ for different values of N. According to Fig. 3.3, the Landau and surface free energy densities follow the same trend when the chirality and φ are modified. The monotonic behavior of these contributions as the chirality increases (purple arrow in Fig. 3.3) is a consequence of the formation of defects. Note that for all cases with $N < 2$, where the pitch values vary between 850 nm and 6 μm, these contributions are almost constant. Therefore, the system exhibits a nematic–like morphology, free of inner defects, or a cholesteric configuration, identified by the continuous twist of the director field; i.e. the distribution of the scalar order parameter in the bulk is uniform. For highly chiral systems, $N > 3$, the defect density increases dramatically and the local nematic order changes abruptly. The effect of φ (blue arrow in Fig. 3.3) translates into an increase in the tactoid axes along the z-direction, resulting in more space for nematic defects and increasing the Landau energy. The surface free energy penalties when $N < 2$ come from the surface boojums. For shorter pitches, the network of disclination lines is distributed throughout the bulk and touches the surface, forming a texture or patterns composed of various $\lambda^{-1/2}$ and λ^{+1} rotations of the director field, which are related to half skyrmions. The number of regions where there are surface penalties is therefore greater. The inset in Fig. 3.3 shows the surface area as a function of φ. Note that the surface area is minimized when $\varphi = 1$, and even though the oblate has the maximum surface area, it also exhibits larger patterns when compared to the prolate, contributing in a lesser manner to the energy penalties at the surface.

The total elastic free energy and the gradients of the chiral term are shown in Fig. 3.4. The decreasing character of this contribution is caused by the dominance of the chiral term, quantified by the elastic constant L_5. The elastic constant L_5 is proportional to the inverse pitch q_0, so smaller values of the pitch contribute to a decrease in the free energy by generating elastic deformations. The chiral term is therefore more dominant in prolates than oblates. Similar to the Landau and surface contributions, for high vales

of N the distortions are stronger, resulting in higher contributions to the total free energy. In Fig. 3.4(Bottom) we show the contribution of the chiral elastic term normalized by the value of L_5, i.e. the effect of the pitch is removed. As φ increases these elastic gradients reach a plateau. Therefore, after removing the changing value of p_0, there is a specific aspect ratio, according to the value of N, where the contribution of the elastic free energy density does not change considerably. This behavior is an indication that freely suspended chiral droplets would not increase their aspect ratio indefinitely, and instead the final shape will be determined by the balance between elasticity and confinement, and additional contributions from the surface tension.

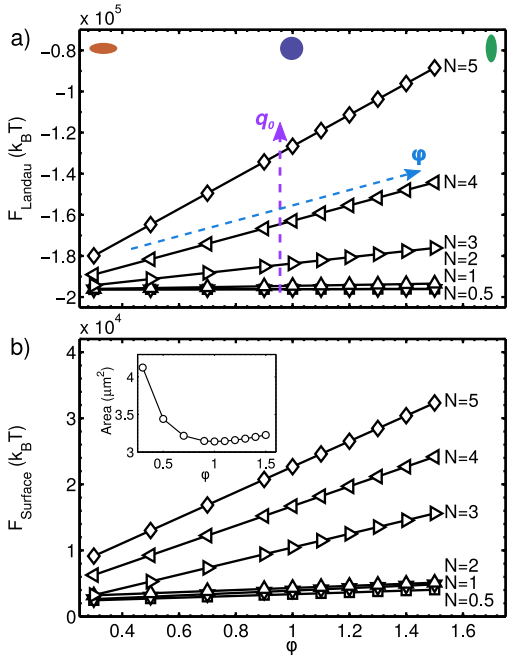

Figure 3.3: (a) Landau and (b) surface free energy contributions as a function of the aspect ratio, φ, for different chiralities, N, under strong anchoring conditions, $W = 1\times10^{-3} J/m^2$, and $U = 2.9$. The cartoons on the top indicate the type of confining geometry. The arrows in (a) serve as guide for increasing aspect ratio (blue) and increasing q_0 (purple). The insert in (b) shows the surface area for the tactoids.

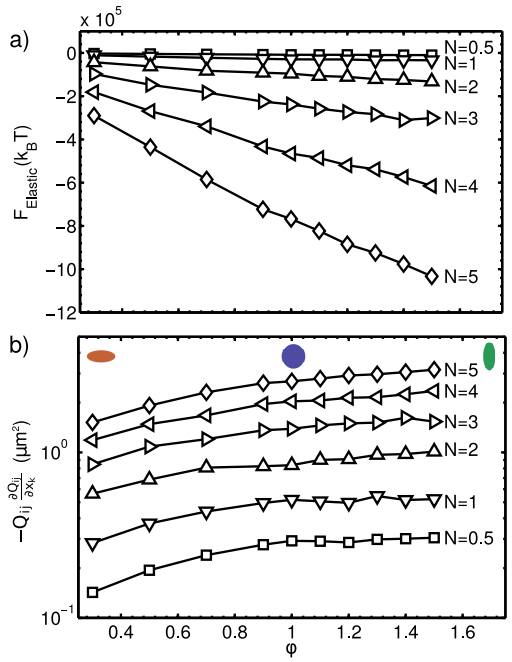

Figure 3.4: (a) Elastic free energy and (b) chiral gradients as a function of the aspect ratio, φ, for different chiral system distinguished by N under strong anchoring $W = 1{\times}10^{-3} J/m^2$ and $U = 2.9$.

3.2.2 Phase diagrams

Three sets of diagrams are presented for $\varphi = 1$ (droplet), $\varphi > 1$ (prolate) and $\varphi < 1$ (oblate). The diagrams include strong anchoring conditions with $W = 1 \times 10^{-3} J/m^2$ and moderate with $W = 1{\times}10^{-4} J/m^2$. The morphologies for weaker anchoring strengths $W < 1{\times}10^{-4} J/m^2$ are similar to those for moderate conditions. As the geometry and anchoring are modified, some phases persist and others rearrange, leading to an expanded family of possible configurations. Figure 3.5 shows the phase diagram for a chiral LC in a spherical droplet as a function of τ and N. Strong anchoring conditions are used for Figure 3.5A, while moderate anchoring conditions are used for Fig. 3.5B. On the right of the diagrams we depict the characteristic morphologies corresponding to each region.

One can observe two families of phases: one dictated by the surface ordering and the other governed by the bulk elasticity. When the surface dominates, Bipolar (B), Twisted Bipolar (TwBs), and Radial Spherical Structures (RSS) are observed. On the other hand,

blue phases (BPI and BPII) are observed when the bulk dominates over the surface, thereby forming defect structures within the droplet. Surface anchoring and N serve as the control variables for the interplay between surface and bulk free energy contributions. Phase diagrams for blue phase droplets with strong anchoring conditions have been reported by Martínez-González *et al.* [131]. The morphologies presented there coincide with our results in figure 3.5A. Additionally, they introduce the idea of controlling and expanding the stability of the blue phase through spherical confinement and corroborated with experimental information. As we will show, this phenomena is not exclusive to droplets and in turn deforming the droplet results in interesting new features in the family of chiral tactoids.

For strong anchoring conditions, in the absence of chirality, the bipolar phase is observed with its two characteristic surface boojums. With increasing chirality, the boojums remain in the opposite poles as the director field twists inside the droplet following a helical pathway: this phase is the TwBs. As chirality increases at low temperature, the boojums approach each other in order to satisfy the high induced twist of the director field. They are not located in opposite poles and eventually merge to form one single surface defect, which ties a knot defect similar to the Frank-Prize structure. This phase is the RSS.

For high chirality and temperature ($\tau > 0$), the LC morphologies are characterized by a network of disclination lines. These are the BPs. For non-confined systems, the defect networks form cubic lattices (BPII with a O_2 symmetry and BPI with O_8 symmetry). For confined systems, the periodicity of the BP structures is interrupted, and the defect lines bend and deform to conform with the geometry. We identify the BPII when the defect lines merge in the center of the cell (blue highlights in the red morphologies in Fig. 3.5). On the other hand, the BPI defect network is such that they don't interact with each other (green defect lines in Fig. 3.5). For the rest of the manuscript, BPII is shown in red and

blue colors, while the BPI is colored in green. Although the BP defects are highly bent, the surface structure forms a regular hexagonal pattern with penta–hepta defects composed of an array of $\lambda^{-1/2}$ and λ^{+1} disclinations. These surface structures are typical of cholesteric phases where there is no abrupt change in the molecular orientations. The pattern is better defined for a narrow interval of temperatures that coincide with the stability region of the BPII. At lower temperatures, more regions obey the planar anchoring conditions, thereby narrowing the surface pattern and presenting more red regions, where molecules satisfy the planar anchoring conditions.

For moderate and weak anchoring conditions (Fig. 3.5B), the surface-dominated morphologies are only found in the low chirality regime. For non-chiral systems, the bipolar phase transforms into a Uniaxial (U) phase, where the two surface boojums no longer exist. At low chirality, the director field twists and forms a Twisted Cylinder (TC) structure. The TC morphology can be interpreted as a stack of layers, each with a λ^{+1} disclination, which is discussed in more detail later on. For intermediate chirality ($N = 2, 3$), the resulting phases are precursors of fully developed BPs. At low temperatures, we find a τ–Cholesteric phase (τ-Ch) that exhibits a single $\tau^{-1/2}$ defect across the bulk and a trefoil pattern on the surface. On the other hand, at higher temperatures, defects across the bulk become unstable, leading to formation of two u-shaped defects in what we call a pre-BPI morphology. The location and orientation of these line defects are similar to a defective joint on a BPII; however, the pitch values and temperature range of this morphology are more fitting of a BPI. At high chirality we encounter BPs. While the stability region for the BPII is not altered, once the anchoring is decreased, the BPI is now stable for a wider interval of temperatures and chiralities. The regular periodic structure in the bulk is only found at temperatures near the isotropic transition. The defect lines at low temperatures show a propensity to form tangles and knotts, thus creating highly deformed lattice cells.

The prolate is formed by "pulling" two opposite poles of the droplet. The surface

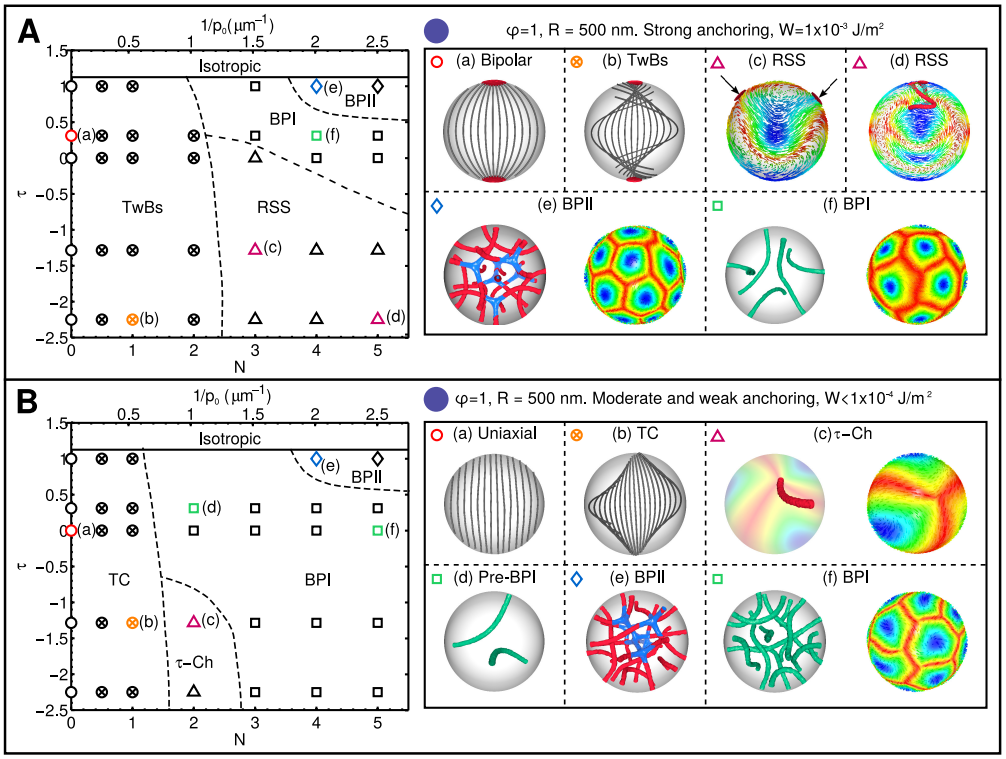

Figure 3.5: Phase diagrams with the corresponding stable morphologies for a chiral LC **droplet** under (A) strong surface anchoring $W = 1 \times 10^{-3} J/m^2$ and (B) moderate anchoring $W = 1 \times 10^{-4} J/m^2$ conditions. On the left we present the phase diagrams in terms of $\tau = 9(3-U)/U$ and N, and representative configurations are shown on the right. Bipolar, Twisted Bipolar (TwBs), Radial Spherical Structure (RSS), Blue Phase II (BPII), and Blue Phase I (BPI) are shown for strong anchoring and Uniaxial, Twisted Cylinder (TC), τ–Cholesteric (τ-Ch), Blue Phase II (BPII) and Blue Phase I (BPI) for moderate anchoring. Iso-surfaces of the scalar order parameter are shown in red, blue and green. Streamlines of the director field are represented by the gray lines. The surface colormaps indicate the orientation of the LC molecules with respect to the surface: red for parallel and blue for perpendicular alignment.

area and curvature are changed and the boundaries within the droplet phase diagram move according to the value of φ. The prolate phase diagrams are shown in Fig. 3.6 for $1.1 < \varphi < 1.5$. As a general trend, the morphologies are similar to those from Fig. 3.5.

For strong anchoring conditions, Fig. 3.6A, the BPI phase is stabilized and the regions for the TwBS and the RSS phases shrink as φ increases. For the TwBs, the boojums are now located at the ends of the major axis of the spheroid and the director twists in the same helical pathway from the spherical case. The attraction of the boojums in the RSS morphology occurs in the region with higher curvature. Consequently, the surface-induced morphologies are stable at lower temperatures. For instance, we show how the RSS morphology that is observed for $\varphi = 1$ turns into a well defined BPI for $\varphi = 1.1$ under the same conditions of τ and N.

The destabilization of the droplet morphologies is more evident as the anchoring is weakened, Fig. 3.6B. For low chirality, the bipolar phase becomes a uniform phase that is oriented along the major axis, while the TwBs becomes a TC. The RSS structure is not observed and the τ-Ch phase appears, where the trefoil pattern covers the surface with parallel orientation domains that avoid the high-curvature regions. This phase is destabilized as φ increases, and is replaced by a BPI.

An interesting effect is observed in the region where the BPII is usually found. As the droplet is stretched, a combination of the two BP defect structures is generated. The tetrahedral structure of the BPII defects is kept and stretched, and long disclination lines, characteristic of a BPI, cross the lattice along the newly opened spaces. The BP hexagonal pattern on the surface is not altered. We call these phases hybridized BP (hBP). They are shown using red, blue, and green colors for the defect morphologies in the figure.

An oblate is formed by pressing down on two opposite points of the droplet. The oblate phase diagrams are shown in Fig. 3.7 for $0.5 < \varphi < 0.9$. Under strong anchoring conditions, Fig. 3.7A, the only destabilization occurs in the transition from TwBs to RSS,

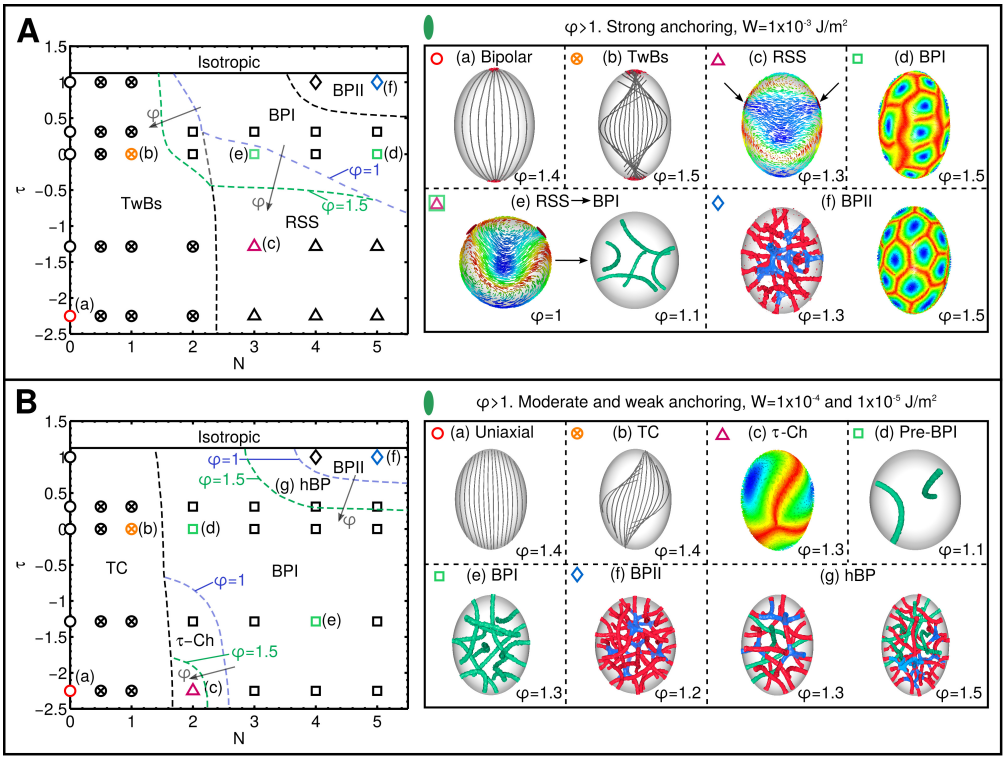

Figure 3.6: Phase diagrams with the corresponding stable morphologies for a chiral LC **prolate** under (A) strong surface anchoring $W = 1\times10^{-3}J/m^2$ and (B) moderate anchoring $W = 1\times10^{-4}J/m^2$ conditions. On the left we present the phase diagrams in terms of τ vs. N, while representative configurations are shown on the right. Shaded regions correspond to changes in the phase diagram with respect to $\varphi = 1$. Bipolar, Twisted Bipolar (TwBs), Radial Spherical Structure (RSS), Blue Phase II (BPII), and Blue Phase I (BPI) are shown for strong anchoring and Uniaxial, Twisted Cylinder (TC), τ–Cholesteric (τ-Ch), Blue Phase II (BPII) and Blue Phase I (BPI) for moderate (low) anchoring. Iso-surfaces of the scalar order parameter are shown in red, blue and green. Streamlines of the director field are represented by the gray lines. The surface colormaps indicate the orientation of the LC molecules with respect to the surface: red for parallel and blue for perpendicular alignment.

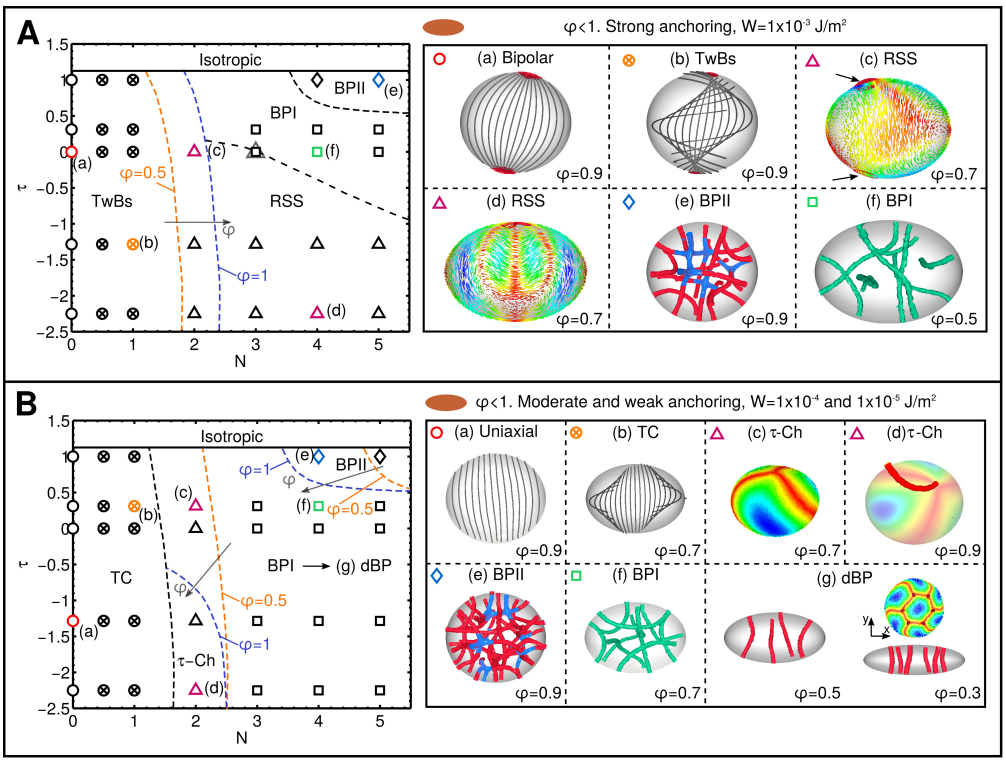

Figure 3.7: Phase diagrams that summarize stable morphologies for a chiral LC **oblate** under (A) strong surface anchoring $W = 1 \times 10^{-3} J/m^2$ and (B) moderate anchoring $W = 1 \times 10^{-4} J/m^2$ conditions. On the left we present the phase diagrams τ vs. N, while on the right representative configurations are highlighted for completeness. Shaded regions correspond to changes in the phase diagram with respect to $\varphi = 1$. Bipolar, Twisted Bipolar (TwBs), Radial Spherical Structure (RSS), Blue Phase II (BPII), and Blue Phase I (BPI) are shown for strong anchoring and Uniaxial, Twisted Cylinder (TC), τ–Cholesteric (τ-Ch), Blue Phase II (BPII) and Blue Phase I (BPI) for moderate (low) anchoring. Iso-surfaces of the scalar order parameter are shown in red, blue and green. Streamlines of the director field are represented by the gray lines. The surface colormaps indicate the orientation of the LC molecules with respect to the surface: red for parallel and blue for perpendicular alignment.

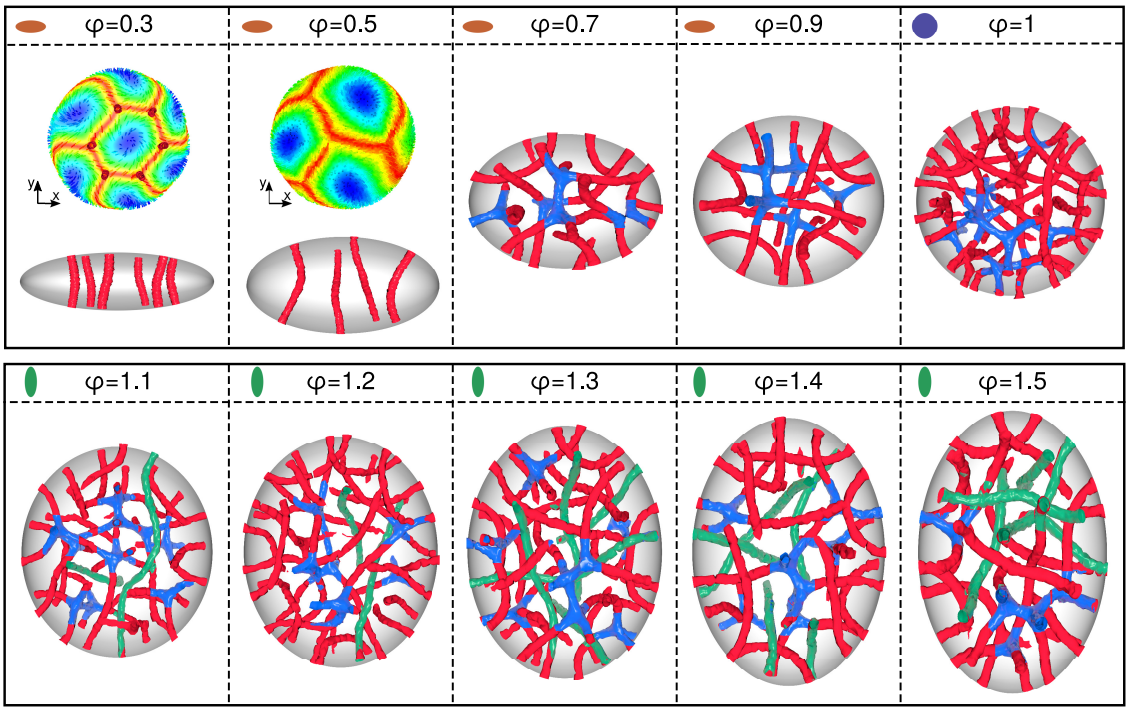

Figure 3.8: Progression of blue phases as φ increases for high temperature and moderate anchoring conditions. Derived blue phases (dBP) are observed for oblates with $\varphi < 0.5$. Defect lines join and form BPII structures as the geometry resembles a droplet. For $\varphi > 1$ the hybridization of BPs occur. The defect structure is colored in red, tetrahedral joints are highlighted in blue and defect lines typical of BPI are colored in green. Surface patterns are colored according to the director orientation with respect to the imposed boundary conditions, red signifies parallel and blue is perpendicular alignment. For clarity we only show a section of the bulk defect structure.

when φ is lowered. The bipolar and TwBS phases show the two surface boojums aligned with the minor axis of the geometry when $\varphi < 0.7$. If the sphericity is not strongly altered, the boojums are displaced from the z-axis towards the region with higher curvature and are not necessarily antipodal. This predisposes the TwBS to form the RSS. The BPs are stable in the same temperature and chirality intervals than in the spherical droplet.

For moderate and weak anchoring conditions, Fig. 3.7B, the τ-Ch phase is stabilized as a precursor of the BPI. The stable region for the BPII moves to higher chirality as φ decreases. The original BP morphologies are deformed to create defect structures without an identifiable symmetry; we call these new phases derived BP (dBP). The disclination lines cross through the oblate and touch the surface. They form hexagonal patterns of λ disclinations similar to the half-skyrmion structures observed in nanochannels.

3.2.3 Additional discussion on chiral tactoids

The are three particular phenomena that merit additional discussion: (i) the progression of BP morphologies as φ is modified from 0.3 to 1.5, (ii) the specifics of the Twisted cylinder structure, and (iii) the multiple orientations of the cholesteric phases.

As can be seen in the phase diagrams, Figs. 3.5–3.7, the regions of stability are affected by the confining geometry. However, simulations show that cholesteric morphologies are not modified drastically by geometrical frustration. At the other end of the chirality spectrum, we find an intriguing behavior at high temperatures. We consider tactoids under moderate and low anchoring with $N = 4, 5$ and $\tau \in [0.5, 1]$. In Figure 3.8, we delineate how the BP changes from the dBP to the hBP as φ is increased from 0.3 to 1.5. For oblates ($\varphi < 1$), the formation of a BP is hindered by the narrow space along the z-direction. This causes an interruption in the symmetry and periodicity of the defect network, which makes it impossible to distinguish between BPII and BPI. The defects are tubes that touch the surface of the oblate and, together, they form structures similar to

those found in nanochannels, namely 2D skyrmions shown in [68]. As the oblate loses its eccentricity ($\varphi \rightarrow 0.7$), the defects join and form a precursor for BPII which later develops in a spherical geometry (droplet, $\varphi = 1$).

As the droplet is stretched ($\varphi > 1$), we observe a hybridization of the blue phases. The defect structure exhibits tetrahedral junctures typical of BPII (in blue) and long disconnected defect lines characteristic of BPI (in green). As the geometry starts resembling a spindle, more BPI-like disclination lines appear, thus obtaining a heavily populated bulk. When defects reach the boundary of the prolate, they imprint the hexagonal pattern of surface defects characteristic of confined BPs. In practice, the heavily populated bulk implies a change in the lattice parameter, which affects the color of the sample that ensues from Bragg's law. Simulations for prolate systems that start from the ansatz for BPI and BPII show higher energies than the Hybrid Blue Phase identified here in MC simulations. However, it has only been possible to observe this new morphology by starting from an initial random orientation. This suggests that hBPs are stable but rare.

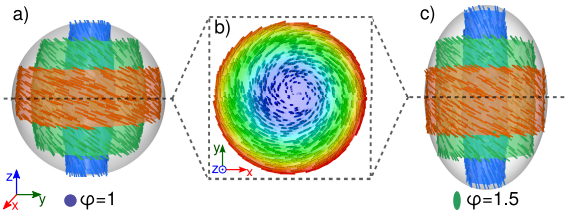

Figure 3.9: Twisted cylinder structure in (a) a droplet ($\varphi = 1$) and (c) a prolate (φ) with $N = 1$ and $W = 1 \times 10^{-4} J/m^2$. Three concentric cylindrical shells indicating different orientations of the director field. (b) Cross section view of the director field at $z = 0$. The color map indicates the molecular orientation relative to the z-axis: blue is parallel and red is perpendicular.

Although cholesteric morphologies do not undergo severe transformations, we would like to expand on the nature of the Twisted cylinder structure. The TC is stable in all geometries for low chiralities and under moderate to weak surface anchoring. This phase is a derivative of the TwBs when the director field is virtually unbounded. Notice that for both phases, TwBs and TC, the director follows a helical trajectory. However, the crucial

difference lies in the presence of boojums. From these features, the TC is better described as consisting of concentric cylindrical shells with unique orientations of the director with respect to the major axis of the geometry. The TC is shown in Fig. 3.9 for a droplet and a prolate, illustrating how the cylindrical shells are stretched along the z-direction as φ increases. A cross-sectional view of the morphology shows how the outer shell follows the surface alignment, while the director twists gradually until it is parallel to the z-axis at the core of the geometry.

For systems with $\varphi \neq 1$, the cholesteric axis may adopt a tilt without a particular preferred angle. We discovered this behavior by realizing that out of multiple simulations, all started from random isotropic phases, the final cholesteric morphology was oriented in different angles with respect to the major axis.

To expand and explain this behavior, we studied systems with two chiralities $N = 0.5, 1$ and four different aspect ratios, $\varphi = 0.5,\ 1.1,\ 1.3,\ 1.5$. We used two different initial configurations: uniaxial and TC, both oriented at an angle θ with respect to the z-axis. Figure 3.10 shows the total free energy as a function of θ for a prolate with $\varphi = 1.5$ for $N = 0.5$ and 1. This free energy plot is representative of the other geometries. Note that the total free energy is practically independent of the orientation of the cholesteric. Figure 3.10 also includes the cholesteric morphologies, and shows surface orientation contours and the director field inside the prolate. The only energetic resistance to reorientation of the cholesteric along a particular direction is the surface free energy; however, the penalties from $\theta = 0$ to $\pi/2$ are of order 200 k_BT, which can be neglected given the magnitude of the elastic free energy. Although there is no difference from the energetic point of view, there is a distortion of the TC as the cholesteric aligns with the minor axis of the geometry. This is evidenced by the torsion of the region parallel to the surface (red color) of the prolate as θ approaches $\pi/2$, similar to a lemniscate. These patterns of the surface contours are typical of a cholesteric phase as reported in [9]. On the other hand,

for $\theta = 0$, the parallel regions form a perfect ring along the equator of the geometry.

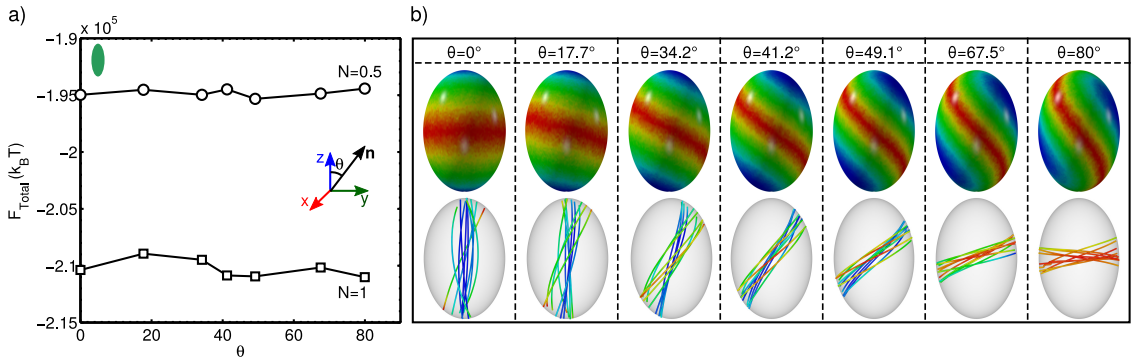

Figure 3.10: Rotated TC in a prolate. (a) Total free energy versus inclination of the cholesteric rotation axis for $N = 0.5$ and $N = 1$ on a prolate ($\varphi = 1.5$) with moderate anchoring $W = 1 \times 10^{-4} J/m^2$. (b) Final configurations of tilted cholesterics at an angle θ respect to the z-axis. The top row shows the orientation of the molecules respect to the surface, red indicates parallel orientation and blue is perpendicular. The bottom row shows streamlines of the director field in the bulk of the prolate.

3.3 Conclusions

A systematic study of chiral nematics in spheroids has been carried out by resorting to a continuum description of the free energy. Simulations were implemented by minimizing the free energy through a theoretically informed Monte Carlo relaxation and a finite element discretization. The corresponding phase diagrams were determined in terms of temperature and chirality for three families of spheroids under strong, moderate and low anchoring conditions. The droplet phase diagram was consistent with those reported in the literature. As the anchoring is weakened, some phases transform into precursors to the BPs in the intermediate chirality regime, a feature that had not been appreciated in the past.

Geometric frustration helps stabilize and engender new BP-like morphologies. The main consequence on changing the geometry is the widening or narrowing of some regions in the phase diagram. The high curvature on the spheroid becomes a region where

surface defects are most stable, and facilitates the formation of structures like the RSS. The constriction in one dimension hinders the formation of symmetric defect networks, and lead to structures similar to those reported for BPs confined in nanochannels. As the spheroid takes a more spherical shape, the truncated BP transforms into a BPII. In the prolate shape, the bulk is highly populated by defects typical of BPI. The hybridization of both BPs provides a new region that has a distinct optical response, and serves to stabilize the BPs over wider ranges of temperature.

Chapter 4

Strongly Chiral Liquid Crystals in Nanoemulsions

Liquid crystal (LC) emulsions represent a class of confined soft matter that exhibit exotic internal organizations and size-dependent properties, including responses to chemical and physical stimuli. Past studies have explored micrometer-scale LC emulsion droplets but little is known about LC ordering within submicrometer-sized droplets. This paper reports experiments and simulations that unmask the consequences of confinement in nanoemulsions on strongly chiral LCs that form bulk cholesteric and blue phases (BPs). A method based on light scattering is developed to characterize phase transitions of LCs within the nanodroplets. For droplets with a radius to the pitch ratio (R_v/p_0) as small as 2/3, the BP-to-cholesteric transition is substantially suppressed, leading to a threefold increase of the BP temperature interval relative to bulk behavior. Complementary simulations align with experimental findings and reveal the dominant role of chiral elastic energy. For $R_v/p_0 \sim 1/3$, a single LC phase forms below the clearing point, with simulations revealing the new configuration to contain a $\tau^{-1/2}$ disclination that extends across the nanodroplet. These findings are discussed in the context of mechanisms by which polymer networks stabilize BPs and, more broadly, for the design of nanoconfined soft matter.

All experiments and synthesis were performed by Dr.Yu Yang and Dr. Xin Wang and the computational studies were all developed and performed by me.

4.1 Introduction

Nanoscale confinement can endow materials with properties that differ substantially from those of their bulk state. [145, 103, 226] For example, the crystallization temperature of water in nanodroplets of radius 3.2 nm is suppressed to 202 K; [145] suspensions of noble metal nanoparticles possess size-dependent optical absorption spectra due to surface plasmon resonances; [103] and the elastic moduli of polystyrene polymer films decrease substantially below 40 nm. [226] These examples highlight how nanoscopic confinement provides an important route for expanding the palette of materials structures and properties. Of particular relevance to the study reported in this paper, liquid crystals (LCs) are known to be strongly influenced by confinement. [279, 26, 57] For example, confinement of LCs can lead to changes to topological defects present in a sample, [279] alteration of optical properties [26] and changes to the way in which LCs respond to external fields (e.g., electric fields). [57] The majority of past studies, however, have focused on confinement of LCs on the micrometer-scale with fewer studies exploring the submicrometer-scale. [74, 90, 91, 4, 268, 245, 119, 144, 192, 80, 281, 244, 19]

The majority of past studies of LCs in submicrometer-scale confinement have involved the use of droplets of nematic LCs. [268, 245, 119, 144, 192, 80, 281, 244, 19] These studies have reported internal LC configurations that depend on droplet size and the chemistry of the confining surfaces. Gupta et al. [80] observed that nematic droplets confined within multilayered polyelectrolyte shells of poly(styrene sulfonate) and poly(allylamine hydrochloride) changed from a bipolar configuration to a radial configuration as the diameter decreased from 3μm to 700 nm. An additional study by Zou et al. [281] found that a confinement-induced bipolar-to-radial configuration transition in nematic droplets occurred when the LC was in contact with an adsorbed layer of poly(styrenesulfonic acid) but not poly(styrenesulfonate sodium), suggesting that the effects of confinement are modulated by surface interactions. In contrast, Peng et al. [192] have reported that

nematic nanodroplets confined in SiO_2 capsules assumed a uniform internal alignment as the droplet diameter decreased to 200 nm, regardless of the LCs used that have either a tangential or homeotropic anchoring with the capsules. In addition to changes in internal structure, phase transitions from isotropic to nematic phases have been reported to occur at temperatures that increase, decrease, or are invariant with nanodroplet size. [245, 192] These conflicting observations likely arise from differences in interfacial chemistry and/or LC elastic properties. More broadly, however, they both highlight the opportunity that exists to tune LC properties via nanoconfinement but also pinpoint the need for additional studies of LC nanodroplets, including investigations of the effects of confinement on nanodroplets formed from LCs other than nematics.

Limits on the resolution of far-field optical microscopy also make studies of LC droplets on the submicrometer-scale more challenging than larger droplets. To address this challenge, past studies have resorted to differential scanning calorimetry (DSC), [268, 119, 245] dynamic light scattering (DLS), [245, 19] and ultrasonic studies [144] to investigate the influence of confinement on nematic-to-isotropic phase transitions. Nevertheless, most existing experimental methods are not effective at characterizing phase transitions between two LC phases, in particular for phases with complex supramolecular organizations. For example, DSC can be used to identify phase transitions from isotropic phases to LC phases, but it is limited in utility when characterizing phases with similar thermal properties such as two chiral LC phases. [5] Our preliminary efforts (discussed below) conducted using DSC at the outset of this study were able to identify the blue phase (BP) to isotropic phase transition in nanoemulsions (mean diameter $\sim$ 450 nm) but not detect the cholesteric to BP transition. Additional methods are needed to facilitate characterization of phase transitions between chiral LCs phase in nanoconfinement.

Here we report the use of nanoemulsions to study the confinement of strongly chiral LCs. Nanoemulsions represent a simple but attractive approach for studying the con-

finement of LCs on the submicrometer-scale because nanodroplets are kinetically stable for long times. [5, 79, 237] In particular, past studies [237] have predicted that steric repulsion between droplets is stronger in nanoemulsions than macroemulsions, thus inhibiting flocculation of nanoemulsions. Additionally, the high stability and large specific surface areas of nanodroplets appear promising for applications such as sensing and drug delivery. [187] Motivated by these considerations, here we report on investigation of nanoscale LC droplets.

The LCs used in the study reported in this paper are strongly chiral LCs that form bulk cholesteric and BPs. [23, 184] The cholesteric phase possesses a director that twists along the helical axis, with a 2π twisting length called the pitch (Figure 4.1a). When chirality is sufficiently strong, BPs appear between the cholesteric phase and the isotropic phase, with a three-dimensional structure comprised of double twist cylinders (Figure 4.1a). Most BPs possess a cubic lattice structure that enables Bragg reflection in the visible spectrum. BPs have attracted attention for their potential application in photonic or electro-optic devices. [42, 34, 87, 270] However, the disclination network that spontaneously forms within BPs (due to topological constraints) causes BPs to be stable over a narrow temperature interval, a fact that has limited their utility. A number of studies have reported strategies to enhance the thermal stability of BPs, including replacement of the defect cores with colloids or polymers [104] and optimization of LC elastic properties. [42] It has also been reported that BPs can be supercooled into long-lived metastable states when confined within pores of polymer networks, while the expansion of BP temperature interval was not observed with heating. [173, 168]

Past theoretical and experimental studies have revealed that chiral nematic LC films form a range of exotic structures under nanoconfinement when the film thickness is less than the pitch. [68, 171] In contrast to ultrathin films, prior studies have not explored nanodroplets (only micrometer-scale droplets [215, 279, 23, 146**?** , 210]). Inspired by the

diversity of structures formed in nanoconfined thin films, here we report on how confinement in nanoscale droplets impacts the phase behavior of strongly chiral LCs. First, we describe methods that permit the preparation of kinetically stable nanodroplets of strongly chiral LC with identical surface chemistry and then develop a method based on light scattering to study phase transitions between strongly chiral phases within nanodroplets. We sought to determine whether or not new configurations emerge in analogy to the thin film studies reported above. [68, 171] Our approach combines both experiment and computer simulations, with the latter used to dissect the energetics that gives rise to the substantial effects of nanoconfinement that we discovered via experiments. We conclude by placing our results into the context of past studies of the stabilization of BPs within polymerized networks. [39, 83]

4.2 Results

4.2.1 Preparation of Nanoemulsions of Strongly Chiral LCs

Prior to investigating the effects of confinement on chiral LC nanodroplets, we first determined the bulk phase behavior of the two LC compositions used in our study. For these experiments, we used microdroplets and LCs with chiral dopant (S-811) concentrations of 29.9 wt% and 37.4 wt% (the pitches of the cholesteric phases formed by the LCs are p_0 = 330 nm and 280 nm, respectively [184]). Figure 4.1b-i shows optical micrographs of LC microdroplets with radii of about 20 μm between crossed polars in reflection mode. At 27.0 °C , the droplets prepared from both mixtures exhibit a cholesteric phase with an optical texture that is similar to that of nematic droplets with radial configurations (Figure 4.1b, c, f). This arises because the apparent optic axis of the cholesteric phase with a short pitch ($p_0 \leq$ visible wavelength) coincides with the helix axis, not the local director, such that the optic axis appears uniformly aligned in the radial direction in the droplets [267]. When

observed in transmission mode, however, the cholesteric phase is identified by a disclination formed along the droplet radius (Figure S1, Supporting Information), which is often termed a radial spherical structure (RSS, the director field of the structure forms concentric spherical shells with the normal in the radial direction). [215, 25] Upon heating the droplets containing 29.9 wt% S-811 to 49.0 °C , we observed the droplets to display pink and blue platelet domains (Figure 4.1d), a characteristic texture of BPI. Upon further heating to 52.0 °C , the droplets appeared dark, indicating a phase transition to the isotropic phase (Figure 4.1e). Figure 4.1g shows that the cholesteric-BPI transition for droplets containing 37.4 wt% S-811 occurred at 39.0 °C , as indicated by the appearance of green platelet domains. The green color results from the diffraction of light from the 255 nm lattice spacing of BPI ([110] plane). [23] Upon further heating of the microdroplets to 40.0 °C , the color of the reflected light changed from green to dark blue (Figure 4.1h), indicating a phase transition to BPII with a 150 nm lattice spacing. [23] The dark blue domains in Figure 4.1h arise from the [100] plane of the BPII lattice. Finally, we observed the BPII-isotropic transition at 42.5 °C (Figure 4.1i). Overall, the bulk phase behavior of LCs with chiral dopant (S-811) concentrations of 29.9 wt% (p_0 = 330 nm) and 37.4 wt% (p_0 = 280 nm) are: Cholesteric $\xrightarrow{48.8\pm0.1°C}$ BPI $\xrightarrow{52.0\pm0.2°C}$ Isotropic, and Cholesteric $\xrightarrow{38.8\pm0.1°C}$ BPI $\xrightarrow{39.6\pm0.1°C}$ BPII $\xrightarrow{41.8\pm0.1°C}$ Isotropic, respectively. These results show that a higher concentration of the chiral dopant lowered the clearing point of the mixture and resulted in the appearance of BPII.

We prepared LC nanoemulsions by vortexing the mixtures described above in aqueous PVA and then ultrasonicating them at different power levels scale [245, 79] (see Experimental Section). Figure 4.1j and 1k show the volume-mean-radii (R_v) of nanodroplets of the LC mixtures containing 29.9 wt% and 37.4 wt% S-811 (additional information on the size distributions is provided in Figure S2, Supporting Information). We note that nanoemulsions with volume-mean-radii (R_v) larger than 150 nm were prepared with

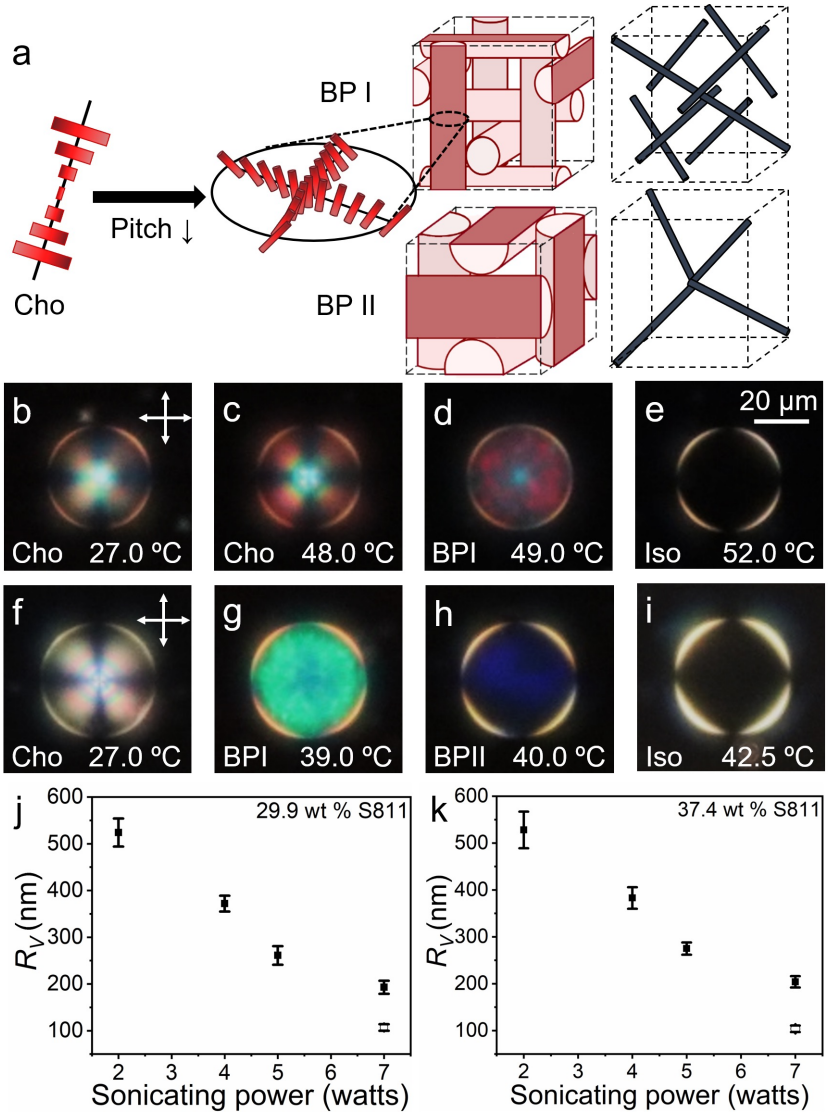

Figure 4.1: (a) Schematic illustration of the structure of the bulk cholesteric phase and BPs. Short rods represent the director of the LC; Cylinders represent the double twist cylinder structures; Black lines represent the disclinations.; (b-i) Micrographs of micrometer-scale droplets between crossed polars in reflection mode as a function of temperature for LC droplets containing: (b-e) 29.9 wt%, (f-i) 37.4 wt% S-811. The scale bar is 20 μm. (Cho: cholesteric, Iso: isotropic). The droplets were stabilized at each temperature for 10 min; (j-k) Volume-mean-radii (R_v) as a function of ultrasonic power for LC droplets containing (j) 29.9 wt%, (k) 37.4 wt% S-811 in aqueous phase of (solid points) PVA (MW 31000 g mol^{-1}, 86.7-88.7% hydrolysis) or (open symbol) PVA (MW 9000~10000 g mol^{-1}, 80 % hydrolysis). Error bars represent standard deviations of the volume mean radii and $n \geq 3$ for each point.

aqueous PVA (MW 31000 g mol^{-1}, 86.7-88.7% hydrolysis), while nanoemulsions with R_v smaller than 150 nm were prepared using aqueous PVA (MW 9000~10000 g mol^{-1}, 80% hydrolysis). Inspection of Figure 4.1j and 1k reveals that, independent of the composition of the LC, the values of R_v decreased from 528±39 nm to 204±12 nm with increasing the ultrasonic power, and further decreased to 108±5 nm when using aqueous PVA with the lower molecular weight and smaller hydrolysis degree. The latter result is consistent with prior observations that the interfacial tensions of aqueous-oil interfaces decorated with PVA decrease with PVA molecular weight and hydrolysis degree. [27, 38] We note that the smallest radii of the droplets obtained are smaller than half the pitch of the cholesteric LC ($p_0/2$= 140 nm for 37.4 wt% S-811 and 165 nm for 29.9 wt% S-811). The polydispersity indices (PDI) of the nanoemulsions ranged from 0.35±0.06 to 0.15±0.01 with the general trend that the PDI decreased with a decrease in R_v. We found that the LC nanoemulsions were kinetically stable for more than 10 days (Figure S3, Supporting Information). We also demonstrated that aqueous PVA with different molecular weights and hydrolysis degrees do not influence the phase behavior of the LC in nanodroplets (see below).

4.2.2 Characterization of the Phase Behavior in the Nanoemulsions

Our initial attempts to characterize the phase behavior of the LCs in the nanodroplets used DSC (Figure S4, Supporting Information). While DSC allowed us to identify the clearing point (formation of isotropic phase), we were not able to identify the transition temperature corresponding to the cholesteric-to-BP phase transition due to the smaller latent heat of the phase transition (18±1 J mol^{-1} for cholesteryl nonanoate) relative to that of BP to isotropic transition (170 ± 25 J mol $^{-1}$ for cholesteryl nonanoate). [240] The scattering of light, however, has been used previously to characterize the LC-to-isotropic phase transitions, [19, 245] and hence we sought to determine if a comparable approach could be used to identify the transition between cholesteric and BPs within nanodroplets.

Specifically, we measured the temperature-dependence of the intensity of light reflected and transmitted from emulsions of nanodroplets when using crossed polars. The normalized intensity i is calculated as $i = (I/I_{min} - 1)^{1/2}$, where I is the intensity measured from optical images, I_{min} is the minimum measured intensity (we note that I_{min} will change with droplet size and measurement of reflected versus transmitted light). [19] We performed these measurements upon heating to avoid potentially incorrect assignment of equilibrium phase boundaries due to supercooling (suppression of the BP-to-cholesteric transition temperature is commonly observed during cooling of bulk phases [173]).

Here we illustrate our light scattering method using nanodroplets with $R_v = 528 \pm 39$ nm (the error is the standard deviation of the volume mean radii, and the PDI is 0.35 ± 0.06), the smallest droplets with optical textures that we could, for purposes of validation, directly image with our microscope (see Figure S5 for experimental setup and emulsions with larger droplets, Supporting Information). Figure 4.2a shows the intensity of light reflected from the sample (back scattering) as a function of temperature. The intensity (i) initially decreased with increasing temperature from 25.0°C to 39.5°C , (ii) was invariant from 39.5°C to 40.5°C , (iii) decreased rapidly to near zero from 40.°C to 43.°C , and (iv) finally changed little after 43.0°C . We interpreted the temperature-dependence of the intensity of reflected light by simultaneously recording micrographs of the droplets (see inset in Figure 4.2a, and Figure S5, Supporting Information). From 25.0°C to 39.5°C , the droplets showed a cross-type texture characteristic of the cholesteric phase (see Figure 4.1 and associated text). From 39.5°C to 40.5°C , the droplets displayed green colors of BPI, and from 40.5°C to 43.0°C , the droplets displayed blue colors of BPII. At temperatures greater than 43.0°C , the droplets were dark, indicating the formation of the isotropic phase. By comparing the temperature-dependent reflected intensity plots and the corresponding micrographs, we were able to correlate changes in the reflected intensity (from 25.0°C to 43.0°C) with the presence of the cholesteric phase, BPs, and isotropic phase.

We propose that several factors underlie this correlation. First, the scattered intensity of reflected light between cross polars is proportional to the scalar order parameter of the LC, [19] which decreases with increasing temperature and turns zero in the isotropic phase. Accordingly, we observed the intensity of reflected light to generally decrease with an increase in temperature. Second, Bragg reflection of light occurs in cholesteric and BPs, and thus we observe a much higher intensity of reflected light in chiral LC phases than the isotropic phase. A third feature was the plateau or slight increase (see also Figure S5 (b), Supporting Information) in the intensity of reflected light from 39.5°C to 40.5°C , which was assigned to BPI. This plateau appears to arise from two competing effects. On the one hand, a red-shift in the peak of the reflected light intensity from BPI (relative to the cholesteric phase which has a peak in reflection intensity in the violet region (pitch $p_0 \sim$ 280 nm, wavelength $\lambda \sim$440 nm) leads to a greater intensity of reflected light from the halogen light source used in our microscope. On the other hand, an increase in temperature leads to a decrease in the scalar order parameter of the LC, [19] which can decrease the intensity of light reflected from LC emulsions. Consistent with this interpretation, this feature in BPI was not observed in the droplets containing 29.9 wt% chiral dopant (Figure S6, Supporting Information) since the reflection wavelength of the cholesteric was at $\lambda \sim$ 520 nm ($p_0 \sim 330$ nm), close to that of the BP. We note that as the radii of the BP droplets decreased below $R_v = 528 \pm 39$ nm, it was difficult to identify this plateau in reflected light intensity as the reflected (back scattered) intensity was very weak (Figure S7, Supporting Information). Finally, we observed the intensity of reflected light to increase with temperature in the isotropic phase, with the increase being larger for smaller droplets (Figure S7, Supporting Information). Prior studies have reported similar observations with isotropic phase droplets of mesogens. [144] The dependence of scattered intensity on temperature likely arises from changes in refractive index of the isotropic phase. Additionally, because nanoemulsions were prepared with constant volume fraction of mesogens, emul-

sions prepared with small droplets possess a higher number density of droplets, which leads to a more pronounced temperature dependence.

The intensity of transmitted light (forward scattering) in Figure 4.2b shows a temperature-dependence that is distinct from the reflected light measurements (Figure 4.2a): The intensity decreased gradually with increasing temperature from 25.0°C to 39.5°C , then abruptly decreased to zero at 40.0°C , and changed little thereafter with further heating. With reference to Figure 4.2a, it is evident that the cholesteric-to-BP phase transition underlies the abrupt decrease in intensity of transmitted light at 40.0°C . This arises because the BP is (macroscopically) optically isotropic and thus the change in polarization of the light when scattered from the BP droplets is small. [271] This difference in optical rotatory power likely reflects the relative orientations of the optical axes of the cholesteric phase and BPs in the droplets, including the presence of local double or single twists (for BP and cholesteric, respectively). Accordingly, we can readily identify the cholesteric-to-BP transition from the temperature-dependent intensity plot in transmission mode. Overall, the results above, when combined (measurements of the reflected and transmitted intensity), provide the basis of the methodology that we use below to characterize the phase behavior of smaller submicrometer-sized droplets that we cannot image by using optical microscopy.

4.2.3 Size-dependent phase behavior of chiral LC in nanodroplets

Figure 4.3 shows the phase diagrams of the two strongly chiral LC mixtures measured within nanodroplets, as established by using the above-described measurements of the scattering of light (see Figure S6 and S7, Supporting Information). Inspection of Figure 4.3 reveals that the clearing points of the LCs do not measurably change (Table S1, Supporting Information) when the droplet radii decrease from 20 ± 2μm to 200 ± 14 nm. In past studies, [23] the clearing points of BP mixtures in droplets were reported to decrease by

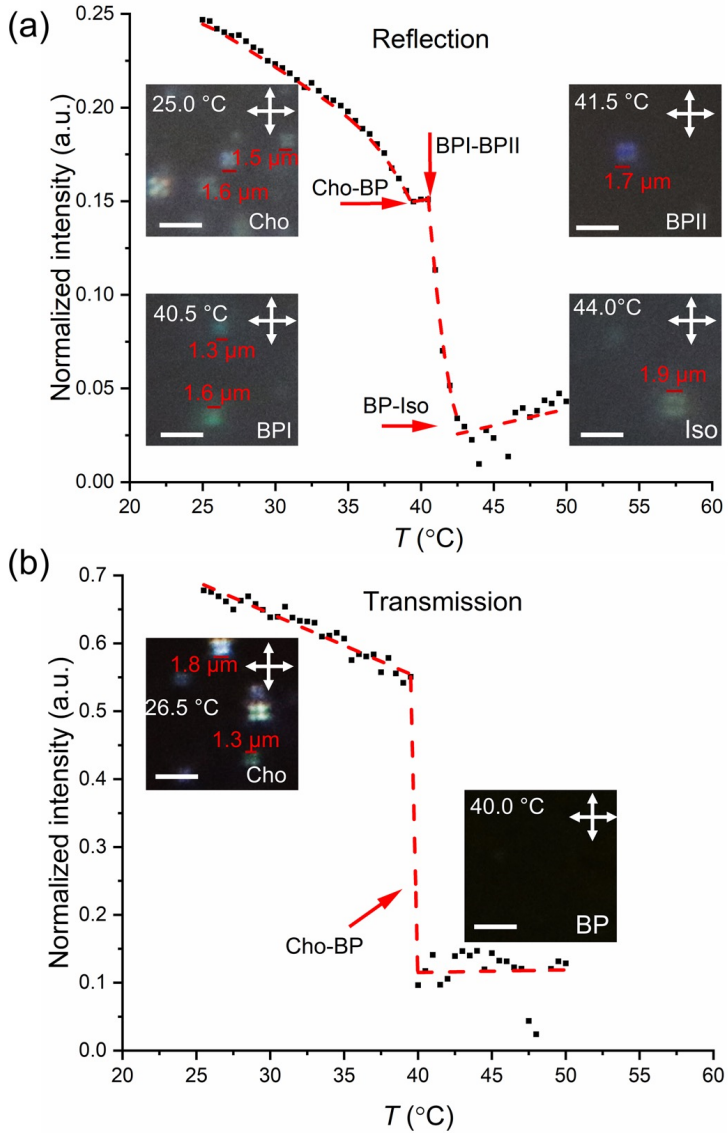

Figure 4.2: Temperature dependence of the intensity of light measured in reflection (a) and transmission (b) modes with an optical microscope. The LC droplets were prepared from 37.4 wt% S-811/MLC 2142 and possess a volume-mean-radius of 528±39 nm. The inserted images are micrographs taken between crossed polars at the indicated temperatures and phases. As shown in Figure S2, the droplets come from a population that is polydisperse in size, and the actual size of the droplets imaged are shown in each image. The scale bar is 5 μm.

0.7 ± 0.3°C as droplet radii decreased from 10μm to 1μm. As detailed below, this small decrease in clearing point of the LC within micrometer-scale droplets lies within the error bars of our measurements performed using submicrometer-scale droplets. In contrast, we measured the clearing point to decrease by 5.2 ± 1.8°C for 37.4 wt% S-811 and 13.5 ± 3.1°C for 29.9 wt% S-811) when the droplet radii decreased from 200±14 nm to 108±6 nm. This result reveals that confinement within droplets with radii that are smaller than the half pitch ($p_0/2$ =140 nm for 37.4 wt% S-811, 165 nm for 29.9 wt% S-811) has a large impact on the LC phase stability, and provides the first hint of the formation of a new LC phase in the highly confined environment of the nanodroplets.

Inspection of Figure 4.3 also reveals that confinement of the LC in nanodroplets with radii (R_v from 526±34 nm to 200±14 nm) larger than half the pitch resulted in a decrease in the temperature of the cholesteric-to-BP transition of 8.9±2.3 °C for 37.4 wt% S-811 and 11.3±2.8 °C for 29.9 wt% S-811. In contrast, the temperature of the cholesteric-to-BP transition changes by only ~0.2°C as the micrometer droplets decreased in size from 5μm to 1.5μm. [24] Our results indicate that confinement in nanodroplets with R_v that is 0.5 to 1 pitch of the chiral LC results in stabilization of the BP over the cholesteric phase. Specifically, the temperature interval over which the confined BP is stabilized (30.6±2.3 °C to 42.9±0.5 °C for 37.4 wt% S-811, 38.1±2.8 °C to 52.8±0.5 °C for 29.9 wt% S-811) exceeds that of the bulk phase BP (38.8±0.1 °C to 41.8±0.1 °C for 37.4 wt% S-811, 48.8±0.1 °C to 52.0±0.2 °C for 29.9 wt% S-811) by a factor of three as R_v decreased to 200±14 nm. Prior studies have reported confinement to enhance supercooling of BPs [173, 168] (which we also observed in preliminary studies with micrometer scale-droplets) but the results reported here were obtained upon heating and thus do not reflect effects of supercooling.

A particularly interesting feature of the phase diagram in Figure 4.3 is the result obtained with nanodroplets with radii (R_v =108±6 nm). A transition in the phase behavior of LCs under confinement occurred between p_0/R_v of 1/3 and 2/3. Specifically, in con-

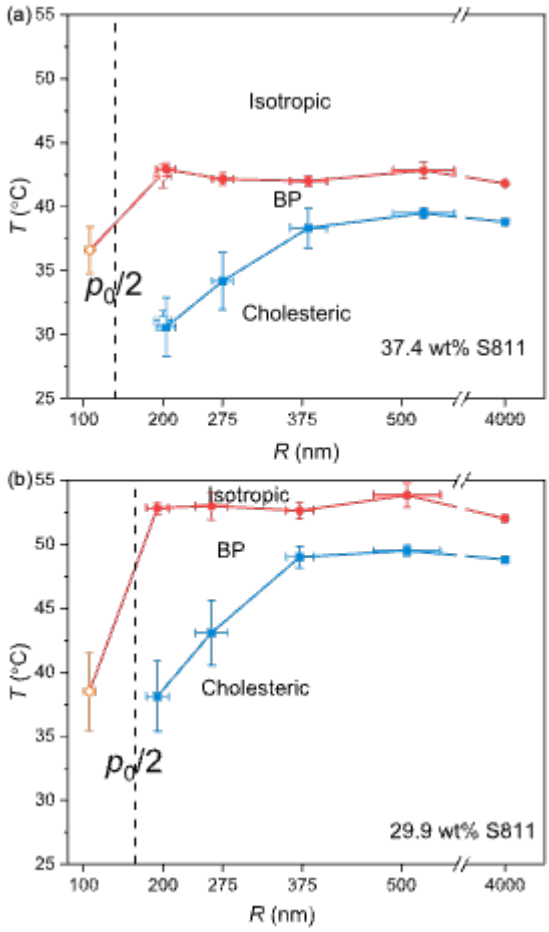

Figure 4.3: Size-dependent phase behavior of LC droplets with chiral dopant (S-811) concentrations of 37.4 wt% (a) or 29.9 wt% (b). Solid symbols: nanoemulsions prepared from PVA (MW 31000 g mol^{-1}, 86.7-88.7% hydrolysis); Open symbols: nanoemulsions prepared from PVA (MW 9000~10000 g mol^{-1}, 80 % hydrolysis). Red circle: BP to isotropic phase transition; Blue square: cholesteric to BP transition; Yellow diamond: LC to isotropic phase transition. Error bars represent standard deviations and $n \geq 3$ for each point.

trast to the larger nanodroplets, we observed no evidence of multiple LC phases below the clearing temperature (the yellow diamond point in Figure 4.3). The structure of this highly confined LC phase is discussed below in the context of numerical simulations and we provide evidence that it arises because a single BP unit cell cannot be accommodated in a nanodroplet with a size smaller than the pitch. Past studies of ultrathin films of chiral LCs have also reported observations of a frustrated BP, which is called a half-skyrmion phase. [171] Finally, we note that the same phase transition temperatures were obtained for nanoemulsions (R_v =204±12 nm) prepared with different aqueous PVA solutions (PVA with MW~31,000 g mol^{-1} and 86.7-88.7% hydrolysis, or with MW 9,000~10,000 g mol^{-1} and 80 % hydrolysis), indicating that the molecular weight and hydrolysis degree of the PVA does not impact the phase behaviors identified in our measurements (open symbols in Figure 4.3a).

4.2.4 Simulations of phase diagrams and structures of chiral LC nanodroplets

To provide additional insight into our experimental measurements of confinement of strongly chiral LCs within nanodroplets, we conducted computer simulations to predict the phase behavior and LC structure within the nanodroplets as a function of temperature and nanodroplet size (Figure 4.4). The free energy functionals used in the simulations follow the Landau-de Gennes formalism and are written in terms of the tensor order parameter **Q**. [229, 45, 7] Minimization of each free energy functional was performed using a simulated annealing technique, as described in previous publications. [9, 253, 115] The simulations were initialized using either a random configuration, the ansatz for BPs, twisted cylinder (TC), or the RSS configuration. We present the results using a reduced temperature, defined as is $T^* = (T - T_{NI})/T_{NI}$, where T is temperature, T_{NI} is clearing point temperature, and dimensionless nanodroplet size $N = 4R/p_0$, which represents

how many π-turns the director can make along the diameter of the nanodroplet. BPI and BPII morphologies can be identified by the type of junctions of the defects. BPI and BPII exhibit different lattice structures, body center cubic structure for BPI, and simple cubic structure for BPII. Because of the different lattice structures, the disclinations formed in BPI are separated from each other, while the disclinations formed in BPII have junctions (Figure 4.1a).

Inspection of Figure 4.4 reveals that the simulations predict a decrease in the cholesteric-to-BP transition temperature with a decrease in droplet radii from 500 nm to 200 nm, a result that agrees closely with our experimental measurements (solid lines in Figure 4.4) for both LC mixture compositions. This size-dependent phase behavior predicted by the simulations supports the conclusion of our experiments that nanoconfinement leads to thermodynamic stabilization of BPs over the cholesteric phase within nanodroplets. For the LC mixture with p_0 = 280 nm (containing 37.4 wt% S-811), the simulated structure of the cholesteric phase for R >275 nm ($N > 3.9$) is the RSS (see inset in Figure 4.4), consistent with our experimental observation in Figure 4.1. However, when the droplet radius decreases below 275 nm ($N < 3.9$), the cholesteric phase transforms into a baseball structure (see inset in Figure 4.4). [115, 29] In contrast, the simulated structures of BPI and BPII did not change with droplet size for droplets with radii larger than 200 nm ($N > 2.9$). As shown in the insets in Figure 4.4, the simulated lattice structure in BPI and BPII form disclinations that bend and intersect with the nanodroplet surface. Overall, the simulations confirm the effects of nanoscale confinement on the stabilization of BPs, as observed in experiments. Similar conclusions were extracted from the simulations performed using the mixture with p_0 = 330 nm (containing 29.9 wt% S-811), with the simulated structure transitioning from RSS to baseball structure in the cholesteric phase at R = 275 nm ($N = 3.3$).

Our simulations also revealed the emergence of a new configuration within nanodroplets

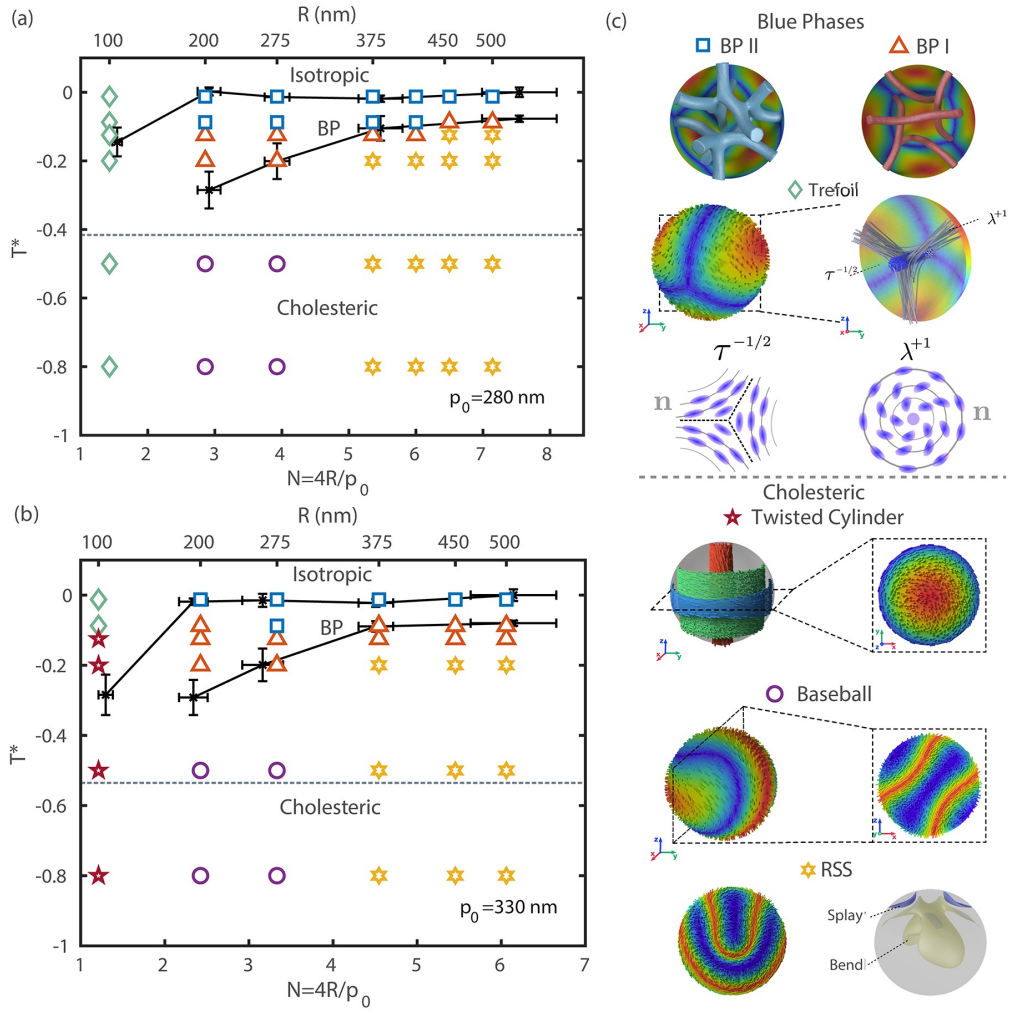

Figure 4.4: Computer simulations of the phase behavior of strongly chiral LCs in nanodroplets for (a) p_0 = 280 nm (b) p_0 = 330 nm, as a function of reduced temperature T^* and chirality parameter $N = 4R/p_0$. Yellow stars: Radial spherical structure (RSS); Purple circles: Baseball structure; Maroon stars: Twisted cylinder (TC); Blue squares: BPII; Red triangles: BPI; Green diamonds: Trefoil structures; corresponding simulated structures are inserted. Director orientations are shown as red when it is oriented perpendicular to the surface and blue for parallel to the surface. Solid lines indicate experimental phase transition data. Gray dash lines indicate 25 °C . Splay-bend isosurface of RSS droplets [279]: the splay deformations (splay-bend parameter $S_{SB} > 0.002$) are shown in blue, and bend deformations ($S_{SB} < -0.002$) are shown in yellow, which reflects the nonsingular disclination of the RSS structure.

with R =100 nm (named as "trefoil structure") that differs from both the BP and cholesteric phase. In the trefoil structure, a $\tau^{-1/2}$ disclination extends across the droplet, dividing it into three regions (see inset in Figure 4.4). For the LC mixture with p_0 = 280 nm (containing 37.4 wt% S-811), the simulated phase diagram in Figure 4.4a shows that only the trefoil structure exists below the clearing point, consistent with our experimental observation. This result suggests that the single phase observed in Figure 4.3a is the trefoil structure. Additionally, we note that the winding numbers of the defects on the droplet surfaces are well defined by the strong planar degenerate anchoring conditions and are consistent with the Poincaré-Hopf theorem, [162] which states that the winding numbers of the surface defects should sum to the Euler characteristic, χ, in this case χ=2. For the case of the trefoil structure, the surface shows two $(-1/2)$ defects and three vortex with winding numbers (+1) resulting in a total topological charge of 2. Similarly, for the cases of BPI and BPII, the surface exhibits a collection of polygons where each vertex has a winding number of $(-1/2)$ and the polygon face has a winding number of +1. Specifically, a droplet of R =200 nm with p_0 = 330 nm and at thermal parameter U =3.2 exhibits a BPI and has eight $(-1/2)$ defects and six (+1) vortices resulting in a total topological charge of 2.

For the mixture with p_0 = 330 nm (containing 29.9 wt% S-811), the simulated phase diagram in Figure 4.4b shows that the nanodroplets at R = 100 nm exhibit both trefoil structure and twisted cylinder [146] (TC, see inset in Figure 4.4, which exhibits a single twist of the director field and no defects, and can be described as a series of concentric cylinders each with a unique director orientation) phases below the clearing point. This observation differs from our experimental observation of a single phase and arises because the simulation does not predict the decrease in the clearing point measured in the experiments. In the temperature interval in which the experiments identify a LC phase, the simulation predicts stabilization of the TC phase. We speculate that the decrease in the

clearing point of LC within nanodroplets with R = 100 nm observed in experiments might be because that the surface anchoring changes as the droplet configuration changes from BP to trefoil/TC structure. Additional simulations are needed to test this hypothesis. In summary, confinement of chiral LC in the droplet at R = 100 nm leads to the emergence of a trefoil structure or TC structure, and the relative stability of the trefoil structure or the TC phase is dependent on the chirality of the LC mixture.

To interpret the simulations, we constructed a surface showing the difference in total free energy between a confined BP (F_{BP}) versus a confined cholesteric phase (F_{Ch}) as a function of N and T^*. Figure 4.5a shows $\Delta F = F_{Ch} - F_{BP}$ for droplets with pitch p_0 = 280 nm. For N = 3, ΔF values become positive for temperatures above T^* ~ -0.3, indicating stabilization of the BP over the cholesteric phase. We also observed that as N decreases, the transition temperature at which ΔF changes from negative to positive decreases, implying that the cholesteric to BP transition temperature decreases as the droplet size decreases, consistent with the phase diagrams from the previous section.

Next, we computed and analyzed the various contributions to the free energy density difference between the BP and cholesteric phase ($\Delta f_{total} = f_{Ch} - f_{BP}$), including the Landau-de Gennes energy density (Δf_{LdG}), the elastic energy density ($\Delta f_{elastic}$), and the surface energy density ($\Delta f_{surface}$). We note that we compared free energy density (f) (calculated as an average over the droplet volume) instead of free energy (F) to eliminate the influence of droplet volume. Figure 4.5b shows Δf as a function of droplet size or parameter N at a reduced temperature of $T^* = -0.125$ and p_0 = 280 nm. We make three key observations using Figure 4.5b. First, the underlying cause of the change in sign of Δf with a decrease in N (and thus stabilization of the BP for values of N less than 6) is the behavior of the elastic energy density. As N decreases from 7 to 6, Δf_{LdG} and $\Delta f_{surface}$ change by ~10 $k_BT/\mu m^3$ whereas $\Delta f_{elastic}$ increases by 250$k_BT/\mu m^3$. Second, for values of N below 6, the contributions to the overall free energy density are only weakly de-

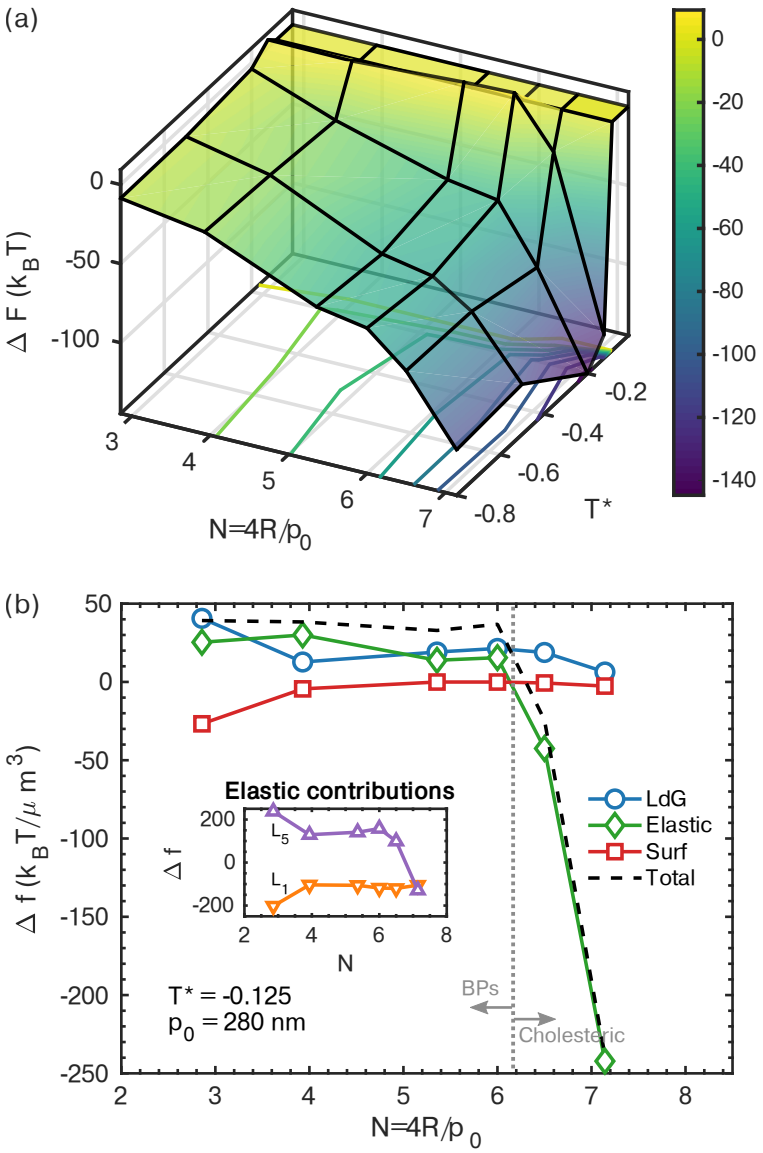

Figure 4.5: (a) Free energy surface corresponding to $\Delta F = F_{Ch} - F_{BP}$ as a function of the reduced temperature T^* and chirality term $N = 4R/p_0$ for droplets of LC with $p_0 = 280$ nm. Contours of ΔF are projected onto the plane as a guide to the eye. (b) Contributions to the free energy density (Total, $\Delta f = f_{Ch} - f_{BP}$) as a function of the droplet size for a reduced temperature of T^* = -0.125 and p_0 = 280 nm under strong planar anchoring conditions $W = 1\times10^{-3} Jm^{-2}$, which include Landau-de Gennes energy density (LdG), elastic energy density (Elastic), surface energy density (Surface). Inserts show the contributions to the elastic energy density from the chiral term ($f(L_5)$) and achiral term ($f(L_1)$).

pendent on size with the small changes in Δf_{LdG} and $\Delta f_{surface}$ compensating each other as N decreases from 4 to 3. The increase in Δf_{LdG} is consistent with a decrease in order within the droplet, which may reflect, in part, the increase in the fraction of the droplet volume that contains defects. It is likely that the compensating decrease in $\Delta f_{surface}$ is also a reflection of disordered LC near the droplet surface. Third, insights into the origins of the dominant role of $\Delta f_{elastic}$ in stabilizing the BP over the cholesteric phase in the nanodroplets can be obtained from a decomposition of the elastic energy into two terms, represented by $f(L_1)$ and $f(L_5)$ as shown in the inset in Figure 4.5b (see equations (3) and (4) in Experimental Section). $f(L_1)$ and $f(L_5)$ are both dependent on the order parameters of the LC. Nevertheless, $f(L_5)$ is also dependent on the pitch, while $f(L_1)$ is an achiral term. Inspection of the inset reveals that as N decreases from 7 to 6, $\Delta f(L_5)$ increases quickly, similar to that of $\Delta f_{elastic}$, but $\Delta f(L_1)$ is invariant. This observation leads to the understanding that the chiral elastic energy dictates the emergence of a BP over a cholesteric phase, and that the effects of confinement-induced chirality (where costly splay elastic energy is relieved by the twist deformation [35]) are distinct for cholesteric and BPs. Overall, we conclude that confinement results in the decrease of the chiral elastic energy of BPs relative to that of the cholesteric phase, which leads to stabilization of BPs in nanodroplets.

4.2.5 Thermal stabilization of BP film by nano-confinement of polymer networks

Next we discuss the relevancy of our observations made using nanodroplets to polymer-stabilized BPs. Past studies have reported that polymer networks can stabilize BPs over a wide range of temperature. [104, 35] The mechanism [104] typically proposed is that polymers accumulate within the cores of the defects and thus replace the energetically costly volume of the defects. This reduces the energy penalty associated with the defect cores,

making the BP stable relative to the cholesteric phase. However, recent studies [39, 83] have shown that polymer networks formed in the isotropic state of mixtures of mesogens can also stabilize BP upon cooling below the clearing temperature. To explore this observation further, we photopolymerized 9.6 wt% reactive monomer (RM257) in the isotropic phase of a mixture (37.4 wt% S-811 in MLC 2142) confined between bare glass surfaces. Figure 4.6 shows the phase diagram that we measured upon heating before and after polymerization. Importantly, we found that the temperature interval over which BPI was stable increased by a factor of three (from 4 K to 12 K) after polymerization (inset in Figure 4.6 shows the platelet texture characteristic of BPI). Inspection of Figure 4.6 also reveals that transition temperatures were all shifted downward after polymerization. This arises because the composition of the mixture changed as the monomer was consumed upon polymerization.

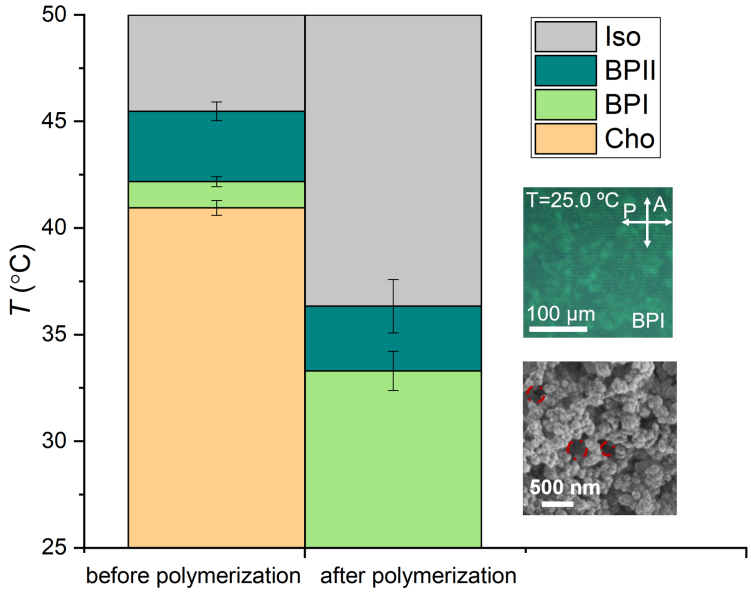

Figure 4.6: Phase behavior of LC mixtures (9.6 wt% RM257 in a mixture of 37.4 wt% S-811/MLC 2142) confined into optical cells before and after photopolymerization in the isotropic phase. Insets show the refection-mode image of BPI (at 25 °C) after polymerization and the SEM image of the shape and morphology of the resulting polymer networks. Error bars represent standard deviations and $n \geq 3$.

A past study [39] has suggested that polymer networks formed in an isotropic phase

can reorganize and diffuse to the cores of the disclinations, thus stabilizing the BP. [148] However, our observations of enhanced stability of BP in nanodroplets (Figure 4.3a) lead us to hypothesize that polymer networks formed in an isotropic phase may confine BPs within submicrometer-scale domains, thus leading to stabilization of the BP. To provide support for our hypothesis, we characterized the polymer networks formed as described above by scanning electron microscope (SEM), which revealed pores with sizes of 250-400 nm (inset in Figure 4.6) comparable to the pitch of the LC (280 nm for 37.4 wt% S-811). Although it is likely that the procedure used to prepare the sample for SEM changed the pore size distribution, when we infused a LC mixture containing 37.4 wt% S-811 into a polymer network prepared for SEM, we observed the BP was stabilized at room temperature (see Figure S8, Supporting Information). This result suggests that some features of the pores were preserved during the SEM sample preparation. Overall, we interpret our observations to suggest that the confinement may dominate the stabilization of BP rather than reorganization of polymers into the cores of disclinations, an interpretation that has not received substantial past consideration in studies that aimed at understanding the stabilization of BPs by polymer networks.

4.3 Conclusions

In summary, this paper describes a study of the phase behavior of strongly chiral LCs in sub-micrometer droplets, a droplet size range that has not been studied extensively in the past due to the inability of conventional optical methods to resolve internal droplet organization at the relevant length scales and the weak enthalpies associated with transitions between LC phases. To enable the characterization of the nanoemulsion droplets, we developed a simple optical method based on measurement of the intensity of forward and back-scattered light (between crossed polars). The method permits characterization of phase transitions between chiral LC phases as well as the isotropic phase and BPs.

Our measurements revealed that the cholesteric phase to BP transition temperature decreased as the droplet diameter decreased into the sub-micrometer scale (larger than the pitch). The stabilization of the BP over the cholesteric phase leads to a three-fold increase in the BP temperature interval. Complementary computational simulations provide insight into the energetics that control the measured effects of nanoconfinement on strongly chiral LCs. The simulated phase diagrams were in good agreement with our experimental results, and a free energy analysis revealed that the chiral contribution to the elastic energy dictates the relative stability of BPs or cholesteric phases. In addition, our results reveal a transition in the effects of nanoconfinement between p_0/R_v of $1/3$ and $2/3$, and support the existence of a new exotic configuration, distinct from the bulk state, when chiral LCs were frustrated in smaller nanodroplets. We further predicted using simulations the emergence of a trefoil structure with a $\tau^{-1/2}$ disclination that goes across the droplet.

The findings in this study suggest a range of directions for additional inquiry. For example, the experimental and simulation results in our manuscript enable us to obtain the phase diagram of chiral LCs in the nanodroplets. However, additional studies are needed to characterize the internal configurations of LCs at various droplet sizes and temperatures, potentially using soft resonant X-ray scattering. [212] Also, our results offer a fresh explanation for why polymer networks can broaden the temperature interval of BPs. Additionally, polymerization in the isotropic phase has the potential to simplify the preparation of PSBP, thus facilitating use in devices. Furthermore, BP LCs with enhanced thermal stability confined in nanodroplets may enable future applications, such as stimuli-responsive sensors or optics based on nanoemulsions. Finally, we speculate that the networks of disclinations formed spontaneously within BP nanodroplets have the potential to serve as nanocarriers for the storage of molecules. When combined with the responsive behavior of LCs, these materials may offer new directions for the design of targeted drug delivery systems using chiral LC nanoemulsions.

4.4 Experimental details

4.4.1 Materials

Nematic Liquid crystal MLC 2142 was purchased from Merck (Darmstadt, Germany). Chiral dopant 4-(1-methylheptyloxycarbonyl)phenyl-4-hexyloxybenzoate (S-811) was purchased from Jiangsu Hecheng Display Technology Co.,Ltd. Reactive mesogenic monomer 2-Methyl-1,4-phenylenebis(4-(3-(acryloyloxy)propoxy)benzoate) (RM257) was purchased from BOC Sciences. Photoinitiator 2,2-Dimethoxy-2-phenylacetophenone (DMPAP) was purchased from Sigma-Aldrich (St. Louis, MO). Poly(vinyl alcohol (Mowiol ®4-88, MW ~ 31000 g mol^{-1}, 86.7-88.7% hydrolysis) and Poly(vinyl alcohol) (MW 9000~10000 g mol^{-1}, 80 % hydrolysis) were purchased from Sigma-Aldrich. Fisher's Finest Premium Grade glass slides and cover glass (22 × 22 mm, 0.13-0.16 mm thick) were obtained from Fisher Scientific (Pittsburgh, PA).

4.4.2 Preparation of LC nanoemulsions

1 wt% PVA (MW~31000 g mol^{-1}, 86.7-88.7% hydrolysis) solution (solution A), 1 wt% PVA (MW 9000~10000 g mol^{-1}, 80 % hydrolysis) solution (solution B), and 0.2 wt% PVA (MW 9000~10000 g mol^{-1}, 80 % hydrolysis) solution (solution C) were prepared in deionized water (Milli-Q water with 18.2 MΩ resistivity). LC mixtures were prepared by mixing the S-811 at 37.4 wt% or 29.9 wt% in MLC 2142.

In order to prepare nanoemulsions with volume mean radii larger than 200 nm, 5 mg of LC mixture was added to the 1995 mg of the solution A and then dispersed by vortex mixer (Model 945415, Fisher Scientific,). Subsequently, the aqueous dispersion of droplets was ultrasonicated (Sonic Dismembrator, Model F60, Fisher Scientific) at a selected power for 8 min to give LC nanoemulsion.

In order to prepare nanoemulsions with the volume mean radius at 104±7 nm, 5 mg of

LC mixture was added to the 1995 mg of solution B and then dispersed by vortex mixer. Subsequently, the aqueous dispersion of droplets was ultrasonicated at 7 watts (RMS) for 12 min to give LC nanoemulsion.

To demonstrate that the molecular weight and hydrolysis degree of PVA do not influence the phase behavior of BP LC in nanodroplets, we also prepared nanoemulsions with the volume mean radius at 200±11 nm using solution C. 5 mg of LC mixture was added to the 1995 mg of the solution C and then dispersed by vortex mixer. Subsequently, the aqueous dispersion of droplets was ultrasonicated at 7 watts (RMS) for 10 min to give LC nanoemulsion. The size distributions of nanodroplets of LCs were measured by Zetasizer Nano 90 (Malvern Panalytical) at 25 °C .

4.4.3 Preparation of optical cells

The purchased glass slides or coverslips were cleaned by first sonicating in detergent solution for 15 min and then rinsing the surfaces with water and ethanol. Finally, the surfaces were dried with a stream of nitrogen gas. One glass slide and a coverslip were spaced apart using a 20 μm-thick plastic film. The cell was glued using 1-min epoxy.

4.4.4 Temperature-dependent reflected or transmitted intensity measurement

Nanoemulsions were introduced into the optical cells, and the cell was then sealed with silicone grease to prevent evaporation. The cells were placed on a hotstage (TMS 94, Linkam Scientific), which was mounted on an optical microscope (BX60, Olympus). Imaging was performed in transmission or reflection mode (crossed polars, white light illumination) with temperature control at a heating rate of 0.5 °C min^{-1}. The illumination intensity of the light source was kept constant during the experiment. The scattered light

intensity was measured based on a series of micrographs and analyzed by ImageJ software (mean gray value). Preparation and characterization of polymer-stabilized BP films: Photopolymerizable LC mixture was prepared by doping reactive monomer RM257 and photoinitiator DMPAP to a mixture of MLC 2142 and S-811 (37.4 wt %) at a concentration of 9.6 wt% and 1.0 wt% respectively. The mixture, heated into the isotropic phase (50 °C), was wicked between two glass substrates spaced by 20 μm plastic spacer. Photopolymerization was carried out by exposing the sample to UV light (2 mW cm^{-2}, 365 nm) for 10 min at 50 °C . After polymerization, the sample was cooled to 25 °C at 0.1 °C min^{-1} and then phase diagrams were measured by subsequent heating towards clearing point at 0.1 °C min^{-1}. For SEM characterization of polymer networks, the non-reacted LCs were extracted by immersing the polymerized films in ethanol for 48 hr and dried under a stream of nitrogen. Following the extraction, imaging of the morphology of the polymer networks was performed by Zeiss Gemini 500 Scanning Electron Microscope.

Chapter 5

Curvature and Confinement Effects on Chiral Liquid Crystal Morphologies

5.1 Introduction

The role of curvature on the ordering and assembly of building blocks is fundamental to the understanding of flexible bilayer membranes, [112, 167] viral capsids, [132, 274, 48] spherical crystallography, [12] quasi-2D materials, [230, 160] and active matter. [55, 277] From a 2D perspective, curvature provides subtle changes to the local order, leading to bistability and a means to manipulate the preferred alignment through the confining geometry. [20, 160, 188] In three dimensions, confinement provides an additional parameter with which to balance bulk elasticity and surface curvature for design of responsive materials. [176, 85, 134, 151, 260, 189]In the context of liquid crystals, orientational order becomes frustrated and defects, regions of low order, emerge as a result of topological constraints. [152, 172, 134, 215, 279]

Past studies have produced stable LC morphologies through geometrical confinement, particularly for chiral liquid crystals (ChLCs) where elongated molecules collectively break rotational symmetry and organize along a main helical path, thereby favoring twist over splay or bending deformations. In spherical cavities, ChLCs' inherent twist conforms to the surface curvature and generate frustrated concentric structures such as the Twisted Bipolar and the Radial Spherical Structure. [273, 215, 69, 25, 129, 279, 182] Highly chiral ChLCs contain disclination lines in the bulk, and curvature can mold them into

hybrid structures. [146, 182, 210, 272] For shells, the inner anchoring conditions generate escaped configurations, and the shell homogeneity and thickness become important parameters to control morphology. [254, 141, 113, 44, 209, 93, 161, 170] More intricate geometries, such as droplets with handles, have been found to guide disclination lines into knots and other non-trivial textures. [181, 239, 96, 31]

Toroidal and cylindrical confinement offer ample grounds for discovery of new phases, as demonstrated in experiments where the ground state of a non-chiral LC is the double twisted morphology, [118, 60, 181, 114, 108] in contrast to the uniform orientation along the main axis of a cylindrical cavity. [99, 95, 162] Under homeotropic confinement, LCs have been shown to exhibit spontaneous twist resulting in escaped radial configurations induced by the curved boundaries. [56, 147] From a computational standpoint, traditional numerical methods are generally limited by the need to formulate an ansatz (or "initial guess") corresponding to each geometry [114, 190], and by the scale of the discretization needed to capture a morphology's nuances. [257]

ChLCs offer several characteristics of interest for photonic and electro-optical devices. They exhibit fast response times and rich optical behaviors. The characteristic length scale of the helical trajectory, or molecular pitch, determine the equilibrium morphology of the system. For long pitches, the material exhibits a cholesteric phase, where molecules can twist uniformly without forming defects. For a sufficiently short pitch, defect lines form spontaneously and self-organize into space filling lattices with cubic symmetry, leading to the so-called Blues Phases (BPs). [52]

However versatile, BPs are only stable over a narrow range of temperature. Furthermore, in the bulk they form polycrystalline domains, posing challenges to applications. [33, 49] External stimuli can help enhance and stabilize morphologies of interest. Lithographic patterns, for example, have been successful in achieving monocrystalline domains of BPII and BPI, where the substrate chemistry is tailored to guide the orien-

tation of the BP unit cells. [**?** 127] Polymerization has also been used to enhance the thermal stability of BPs, by setting the underlying defect network into a permanent scaffold. [104, 102, 82, 211]

More recently, Negro *et al.* reported a detailed analysis of the patterns that appear on the surface of chiral LC shells. These authors relied on lattice Boltzmann simulations to identify the equilibrium morphologies of highly chiral LCs as they transition into an ordered phase from an isotropic state. [164] Building on that work, in this study we examine how geometrical frustration in toroidal and cylindrical cavities can be manipulated to preserve key characteristics of chiral nematics while introducing new geometrical features that do not arise when in bulk. Specifically, curvature is used to engineer new mesophases of ChLCs – curvature couples to defects by screening their topological charge. Recent theoretical reports indicate that strict planar confinement of 2D ChLCs hinders the development of double twist, leading to the formation of a novel chiral structure. [138]

In section 5.2 we outline the details of the phenomenological model adopted here, as well as the numerical methods used to find equilibrium configurations. Section 5.3 introduces our results and discussion by presenting the underlying free energy surface as a function of chirality and cavity size. We continue by presenting phase diagrams at different temperatures, and a more detailed analysis of the surface patterns corresponding to each system. In section 5.4 we provide a short summary of our findings and several remarks about future applications of this work.

5.2 Simulation details

The toroidal and cylindrical cavities shown in Fig. 5.1 ($R = 500\,\text{nm}$ and $r_0 \in [100, 250]\,\text{nm}$) impose planar degenerate alignment with moderate ($W = 1{\times}10^{-4}\,\text{J/m}^2$) to weak ($W = 1{\times}10^{-6}\,\text{J/m}^2$) anchoring strength onto a chiral liquid crystal with pitch $p_o \in [100, 1000]\,\text{nm}$.

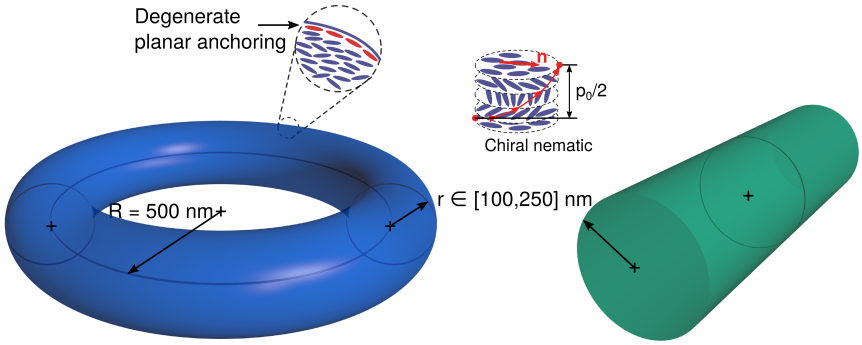

Figure 5.1: Schematic representation of the toroidal and cylindrical cavities used to confine the chiral liquid crystal. The major radius of the toroid is $R = 500\ nm$, while the radius of the cylinder r_0 varies between $100-250\ nm$. Surfaces impose degenerate planar anchoring alignment of the chiral material.

The nematic parameter is close to the IN transition, between $U = 2.7$ and $U = 2.9$, the regime in which BPs are stable in the bulk. The parameters for 4'-pentyl-4-cyanobiphenyl (5CB) are used as the model system with $A = 1 \times 10^5$ J/m^3, $L_1 = 5.11$ pN, and $\xi_N = 7.15$ nm. The free energy minimization requires approximately 4×10^5 Monte Carlo cycles. The system was quenched over five stages through $\hat{T}$. The meshes for these simulations vary in size according to the confinement size r_0; on average, they are comprised of 3×10^5 nodes and 2×10^5 elements for $r_0 = 100$ nm, and up to 9.5×10^5 nodes and 7×10^5 elements for $r_0 = 250$ nm.

5.3 Results

We begin our discussion by exploring the free energy contributions as a function of chirality and confinement, shown in Fig. 5.2a. For convenience, we use the dimensionless group $2q_0r_0$, analog to the chirality, which characterizes the natural twist in the confined system and allows us to collapse our results onto master curves shown in gray.

At low chirality, in the cholesteric (Chol) regime, all components of the free energy are close to zero, meaning that at equilibrium the resulting configuration is uniform and with-

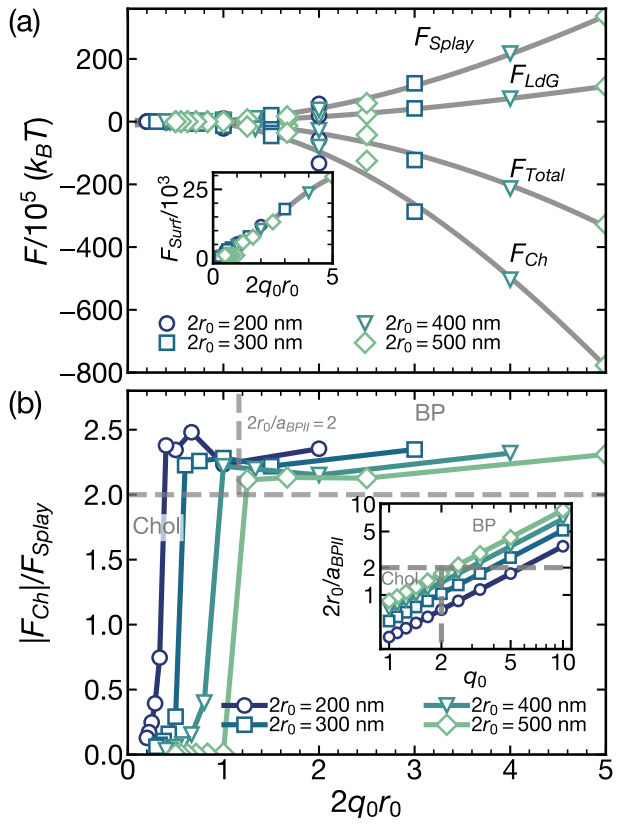

Figure 5.2: (a) Free energy contributions as a function of chirality parameter q_0 scaled by torus inner radius r_0. Markers indicate the radius for the toroidal cavity. The inset shows the surface free energy contribution. Gray curves are polynomial fits of each free energy contribution. (b) Ratio of chiral and splay elastic energies as a function of chirality q_0 scaled by cavity radius r_0. The inset shows the ratio between cavity radius and unit cell size for Blue Phase II a_{BPII} as chirality q_0 increases.

out defects, and the orientation of the LC at the boundary follows its curvature. For higher chirality, the material adopts a double twist configuration that results in a cuboidal defect network (Blue Phases, BP). Their emergence increases the Landau-de Gennes free energy, and the confluence of double twist domains creates regions of high splay, as reflected by the corresponding elastic contribution. At the boundary, the curvature interrupts the cubic symmetry of the defect network and produces a fingerprint pattern, a collection of half-skyrmions that will be described later in our analysis.

The ratio between chiral and splay elastic contributions serves as a proxy for the family of morphologies that arise in these systems, illustrated in Fig. 5.2b as a function of natural twist. Two lines serve to delineate the characteristics of the morphologies at equilibrium. The first is $|F_{Ch}|/F_{Splay} = 2$, and refers to the limiting energy for disclination lines to interweave the bulk of the system. The second line is defined by the balance between the cavity size ($2r_0$) and the Blue Phase unit cell a_{BP}, and plays a crucial role in systems with high chirality. For $2r_0/a_{BP} < 2$, confinement frustrates a fully developed BP cell, and the disclination lines adopt helical features conforming to the geometry. In this case, since $U = 2.7$, the unit cell is that of the Blue Phase II calculated as $a_{BPII} = p_0/1.72$. The inset in Fig. 5.2b shows the ratio $2r_0/a_{BPII}$ as a function of inverse pitch q_0, where a horizontal line delimits the systems in which helical morphologies are favored over fully developed Blue Phases.

The free energy analysis is consistent with the phase diagrams generated in terms of $q_0 = 1/p_0$ and $2r_0$, shown in Fig. 5.3 for a)$U = 2.7$ and b)$U = 2.9$ in a toroidal cavity. Highlighted markers in the phase diagram correspond to the morphologies illustrated in Fig. 5.3c. The first three morphologies occur at low chirality: Double Twist (DT), Twisted Ribbon (TR), and Helical Ribbon (HR). They are best described by the alignment of the director with respect to the major (toroidal) axis. First, the DT is a cholesteric morphology and exhibits a continuous twist in the radial direction. At the core of the cavity, the

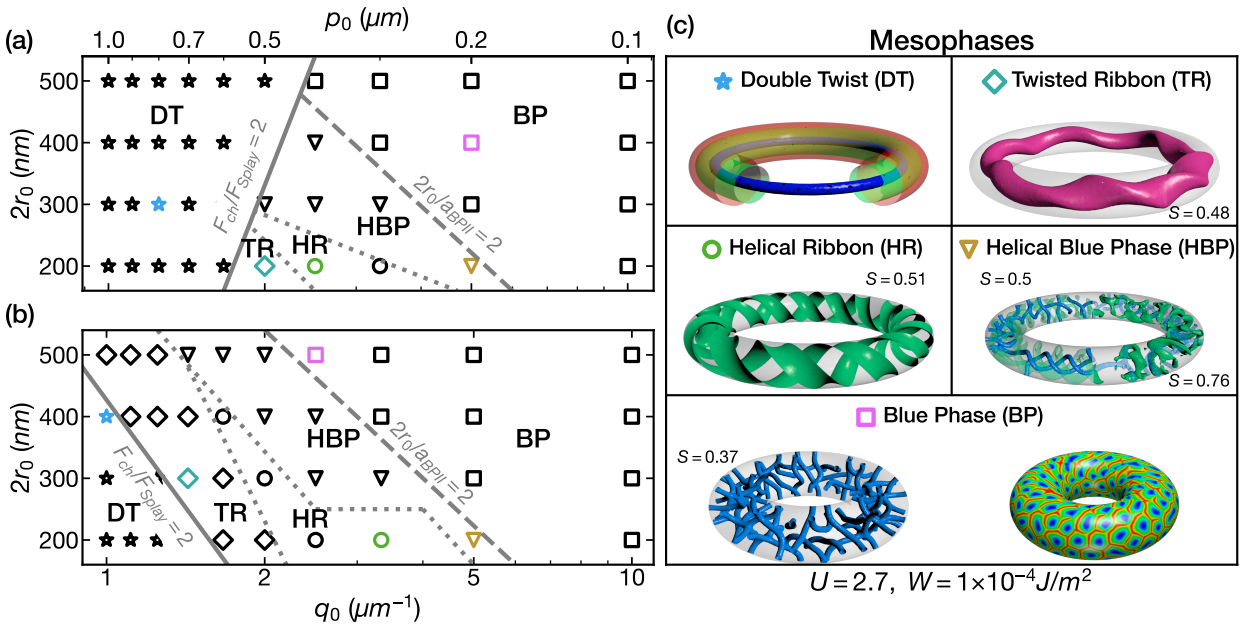

Figure 5.3: Phase diagram and mesophases of a chiral liquid crystal with pitch $p_0 = 1/q_0$ confined in a toroidal cavity of diameter $2r_0$ under moderate planar anchoring ($W = 1 \times 10^{-4} J/m^2$) at (a) $U = 2.7$ and (b) $U = 2.9$. (c) Morphologies corresponding to the highlighted markers in the phase diagrams: Double Twist (DT), Twisted Ribbon (TR), Helical Ribbon (HR), Helical Blue Phase (HBP), Blue Phase (BP).

director is aligned with the toroidal axis such that the midline is straight. At the boundary, the director is tangential to the surface and is tilted with respect to the toroidal axis. The illustration in Fig. 5.3c shows three concentric tubes, each corresponding to regions in which the director tilt with respect to the midline is 0° (blue), 20° (green) and 45° (red).

As chirality increases, a smooth double twist within the torus can no longer be sustained, and each concentric layer of the DT buckles to form a twisted ribbon (TR). Each ribbon retains a straight midline while isosurfaces of the order parameter exhibit saddle-like curvature, as illustrated by the magenta ribbon with $S = 0.48$ in Fig. 5.3c. Additional twisting of the order field requires widening of the ribbon, which is not attainable due to the confining surface. Instead, the ribbon twists on itself forming two Helical Ribbons (HR), in which the midline draws a helix in space and the saddle-like curvature of the ribbon transitions to isosurfaces with zero mean curvature. The HR can also be described as two interlocking torus knot with invariant $T(1, q)$ where q is related to the ratio of the molecular pitch and the major radius of the tori. Previous works on chiral nematic colloids have characterized these type of knots as linkers for colloidal lattices. [243]

Lastly, we examine the region of systems with $2q_0r_0 > 1$ and $|F_{Ch}|/F_{Splay} > 2$, populated with Blue Phase-like defects. In this regime, one can appreciate the pronounced effects of geometrical frustration on the Helical Blue Phase (HBP). For conditions where confinement is smaller than the unit cell of a BP, disclination lines are interwoven with lingering features of the HR morphology. The defects are evenly spaced but do not always grow radially; instead they follow the helical midline, resulting in sections where the defects form a double helix (drawn in blue), and are encased by two helical ribbons (drawn in green).

Under less severe confinement ($2r_0/a_{BPII} > 2$), a BP unit cell is fully circumscribed by the torus, and replicated throughout the toroidal axis. In such a way, the resulting BP morphologies adopt varying crystallographic orientations, thereby affecting the intensity

of the Bragg reflections. In this sense, curvature hinders monocrystallinity but leads to new surface features. For both HBP and BP, the defects are truncated by the curved surface, resulting in a collection of $-1/2$ defects, spaced by double twist cylinders with $+1$ topological charge. These structures are most commonly known as half-skyrmions, or merons, and have been observed as dark spots in microscope images. Half-skyrmions are stable and tend to pack in hexagonal lattices; the $-1/2$ defects form vertices while the $+1$ defects become the faces of the polygon.

The sequence of transitions, critical values of $|F_{Ch}|/F_{Splay}$ and $2q_0r_0$, and the characteristics of each mesophase are identical to those for cylindrical confinement. This indicates that the role of extrinsic curvature is more nuanced and its effect is not localized. On the other hand, the role of temperature, mediated by the thermal parameter U, reduces the stability region of the DT structure. This becomes apparent when comparing the phase diagrams in Fig. 5.3a-b, where the slope of $|F_{Ch}|/F_{Splay} = 2$ changes. At lower temperatures, it is more favorable for defects to nucleate, requiring a lower chirality for the double twist to transform into a chiral ribbon structure.

When packed on the surface of a droplet, "scars" are formed in the lattice and pairs of 5-7 polygons arise. However, the effect of extrinsic curvature on the packing of half-skyrmions is unclear. We seek to quantify the regularity of the half-skyrmion network with the phenomenological surface parameter Ψ_n, illustrated in Fig. 5.4a. For each pair of neighboring edges j that belong to an n-gon, $\Psi_n^j = \theta^j(\mathcal{N}_1^j + \mathcal{N}_2^j)$, where $\mathcal{N}_i^j$ are the number of sides of each neighboring polygon. It follows that, for a regular hexagonal network, only Ψ_6 exists, and its probability distribution function is a Dirac delta centered at 4π. The procedure to calculate Ψ_n is as follows. First, the locations where $\mathbf{n} \cdot \boldsymbol{\nu} \approx 1$ are extracted and grouped by clusters using the k-means algorithm. The clusters are then compared to the original surface to confirm that the correct polygon centroids have been identified. Using Voronoi and Delaunay triangulation, we successfully identify the edges

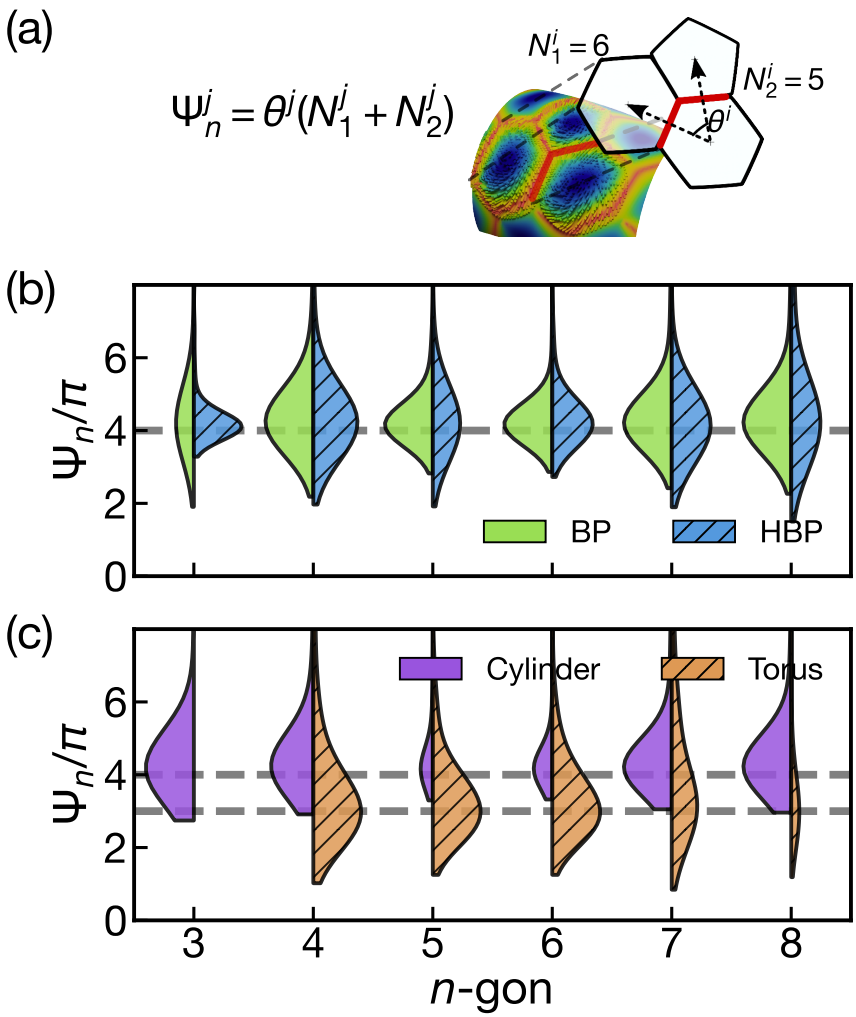

Figure 5.4: (a) Schematic representation of the phenomenological surface parameter Ψ_n for a pair of polygon edges i (highlighted in red) with the surface projection from a BP on a curved surface. The coloring of the curved surface corresponds to the orientation of the director field with respect to the surface normal: blue denotes parallel and red corresponds to perpendicular alignment. (b) Probability distribution of Ψ_n for Blue Phase (left, green) and Helical Blue Phase (right, blue) confined in a cylindrical cavity. (c) Probability distribution of Ψ_n for Blue Phases confined in a cylinder (left, purple) and a torus (right, orange).

of each polygon. Additionally, we compute the total topological charge to ensure morphologies are in equilibrium according to the Poincaré-Hopf theorem. We then proceed to calculate Ψ_n for each n-gon found, and we estimate the normalized probability function. This systematic procedure allows us to characterize the differences between BP and HBP morphologies, as well as the role of confinement.

From the violin plot in Fig. 5.4b, cylindrical confinement broadens the family of polygons expressed on the surface of both BP and HBP. Spherical confinement of a BPII disrupts the regular hexagonal lattice and 5-7 polygon pairs are formed to relieve the stress created by the closed surface. The strict confinement of a cylindrical cavity makes it such that 4-8 pairs of polygons also arise. The probability for Ψ_n in both morphologies is centered around 4π, indicating that all merons are concave polygons. Additionally, the distributions for HBP have a higher variance compared to those of the BP, meaning that the polygons are more irregular in shape. This is a consequence of the helical ribbons interrupting the growth of the defects, and results in the detection of triangular polygons where sections of a ribbon separate merons.

In Fig. 5.4c, we investigate the effect of extrinsic curvature by comparing BP morphologies in cylindrical and toroidal cavities. As a result of the secondary curvature, the polygon lattice experiences additional strain and the average value of Ψ_n shifts to 3π. This implies that besides the polygons being irregular, each polygon has neighbors with different numbers of sides, leading to an amorphous lattice. Recent experimental and computational work has revealed that these are also characteristics of the Blue Phase III, where the authors suggest it is a fluid composed of skyrmions. [193]

We finish our discussion by exploring the stability of the Helical Ribbon morphology. As explained above, the HR is stable for systems with low natural twist ($2q_0r_0 < 1$) and higher thermal parameter ($U = 2.9$). Furthermore, the chiral elastic energy surpasses the limit of purely cholesteric morphologies ($|F_{Ch}|/F_{Splay} > 2$), with a non-negligible

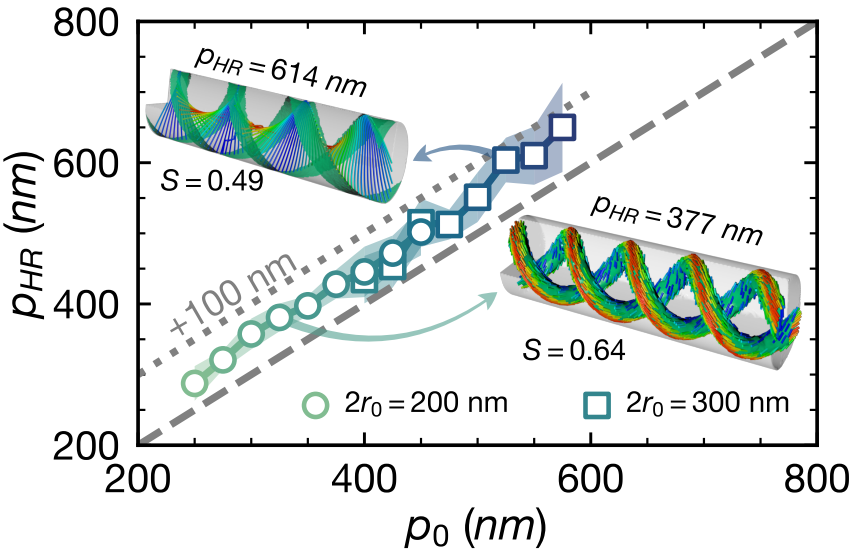

Figure 5.5: Pitch of the Helical Ribbon p_{HR} as a function of the molecular pitch in a cylindrical cavity under moderate anchoring conditions ($W = 1 \times 10^{-4} J/m^2$). Error bars are shown by the shaded region. Different markers correspond to the two confinement radii at which this structure is stable. Two morphologies illustrate this structure: in the lower right $r_0 = 100$ nm and $p_0 = 325$ nm, and in the upper left $r_0 = 150$ nm and $p_0 = 525$ nm. The gray dashed line is the limit for $p_{HR} = p_0$, and the dotted line corresponds to $p_{HR} = p_0 + 100$.

Landau contribution. This indicates that at the center of each ribbon lies a defect core that follows the same helical path. This can be harnessed to drive the assembly of particles into arrays with supramolecular order, since the core of each ribbon will attract particles in order to relieve elastic distortions. Additionally, the helical pattern is imprinted on the surface with tangential orientation of the director, providing an alternative platform for driven assembly of nano or micro particles. Furthermore, the optical properties of LCs and the precise control over the ribbon pitch can be harnessed to engineer optical guides with spiral paths. [219, 200, 195, 40, 1, 54]

To further consider potential applications of HR, we also explored how the pitch of the HR (p_{HR}) is connected related to the molecular pitch (p_0)? We performed additional simulations within the stable HR region for cylindrical cavities ($2r_0 = 200$ nm and $2r_0 = 300$ nm) under moderate anchoring conditions ($W = 1 \times 10^{-4}$ J/m^2) and $U = 2.9$. Fig. 5.5 shows the HR pitch as a function of molecular pitch, including two illustrative HR structures. The pitch was measured from sections throughout the length of each cylinder, and the error bars are represented in the shaded region. There is a linear correlation between both pitches, and the HR pitch is offset by an average of 50 nm from the molecular pitch. The two illustrations represent the helical defect core with $p_{HR} = 377$ nm, as well as the surface helical pattern with $p_{HR} = 614$ nm.

5.4 Conclusions

A theoretical study of chiral liquid crystals confined in cylindrical and toroidal cavities has revealed the existence of new, previously unknown morphologies that arise from the interplay between confining curvature and the inherent twist of the material. These morphologies were generated by relying on a stochastic sampling technique expressed in terms of the five independent components of the order tensor $\mathbf{Q}$, which was mapped onto an orthonormal basis set. These morphologies can be classified in terms of three ratios: (i)

the natural twist, $2q_0r_0$, which captures the two characteristic dimensions of the system and collapses the free energy onto master curves; (ii) the elastic ratio $|F_{Ch}|/F_{Splay} = 2$, which demarcates the limit above which defects emerge in order to minimize the free energy; (iii) the competition between confinement and the BP cell size $2r_0/a_{BP} = 2$, which determines whether a BP cell can develop or instead adopt helical features. Following a progression of chirality, five morphologies are observed in the underlying phase diagrams when expressed in terms of such ratios: Double Twist, Twisted Ribbon, Helical Ribbon, Helical Blue Phase, and Blue Phase.

An in-depth analysis of the patterns that arise on the surface of the cavities for HBP and BP reveals polygonal lattices, in which $-1/2$ defects form the vertices and +1 regions form the faces. Our analysis indicates that the HBP is amorphous, mostly due to sections of chiral ribbons that intersect the lattice. In the case of BP, the defects resemble those of BPII, but the geometry interrupts the cubic symmetry that leads to optical activity in narrow ranges. Finally, we discussed how chiral ribbons, and Helical Ribbons, specifically, can serve as a platform for directed assembly. The nature of the helical defect cores makes them a strong candidate for attracting particles, which alleviate elastic stresses, both in the bulk and adsorbed on the surface. The pitch of the ribbon is tunable and it follows a linear relationship with the cavity size and molecular pitch.

Chapter 6

Reconfigurable multi-compartment emulsion drops formed by nematic liquid crystals and immiscible perfluorocarbon oils

Liquid crystalline (LC) oils offer the basis of stimuli-responsive LC-in-water emulsions. Whereas past studies have explored the properties of single-phase LC emulsions, few studies have focused on complex multi-compartment emulsions containing coexisting isotropic and LC domains. In this paper, we report a study of multiphase emulsions using LCs and immiscible perfluoroalkanes dispersed in water or glycerol (the latter continuous phase is used to enable characterization). We found that the nematogen 4'-pentyl-4-biphenylcarbonitrile (5CB) anchors homeotropically (perpendicularly) and weakly at liquid perfluorononane (F9) interfaces, consistent with smectic-layering of 5CB molecules. The proposed role of smectic layering is supported by experiments performed with 4-(trans-4-pentylcyclohexyl) benzonitrile (PCH5), a nematogen that possesses a cyclohexyl group that frustrates smectic packing and leads to tilted orientations at the F9 interface. By employing perfluorocarbon and hydrocarbon surfactants in combination with multiphase 5CB and F9 emulsion droplets dispersed in a continuous water or glycerol phase, we observe a range of emulsion droplet morphologies to form, including core-shell and Janus structures, with internal organizations that reflect an interplay of interfacial (an-

choring energies; F9 and glycerol) and elastic energies within the confines of the geometry of the emulsion droplet. By comparing experimental observations to simulations of the LC-perfluorocarbon droplets based on a Landau-de Gennes model of the free energy, we place bounds on the orientation-dependent interfacial energies that underlie the internal ordering of these complex emulsions. Additionally, by forming core-shell emulsion droplets from 5CB (shell) and perfluoroheptane (F7; cores), we demonstrate how a liquid-to-vapor phase transition in the perfluorocarbon core can be used to actuate the droplet and rapidly thin the nematic shell. Overall, the results reported in this paper demonstrate that multiphase LC emulsions formed from mixtures of perfluoroalkanes and LCs provide new opportunities to engineer hierarchical and stimuli-responsive emulsion systems.

All experiments and synthesis were performed by Dr. Xin Wang and the computational studies were all developed and performed by me.

6.1 Introduction

Liquid crystals (LCs) are a phase of matter within which the constituent molecules exhibit long-range orientational order and high levels of mobility. [45, 110] Confinement of LCs (e.g., to thin films, [225, 224, 217] emulsions [80, 150, 251, 95, 235, 192] and spherical shells [62, 139, 140, 130, 215, 44]) imposes constraints on the orientational ordering of LCs, leading to mesoscale organizations that reflect a delicate balance of contributions to the free energy arising from orientation-dependent interfacial free energies, elastic strain associated with deformation of LCs, and the presence of singular topological defects. [80, 150, 139, 239, 29, 228, 157, 263, 104, 72, 281, 220] The delicate balance of energetics that controls the ordering of confined LCs have led to their use in a range of contexts, [45, 111] including recently for chemical and biological sensing, [217, 134, 236, 107] in design of autonomous soft matter microsystems [117, 97, 269, 233] and for templating molecular

assemblies. [263, 262] In this manuscript, we explore how immiscible perfluorocarbons can be used to confine LCs, including within domains of emulsion droplets with core-shell and Janus-type morphologies, [94, 235, 166, 264, 276] in ways that are not accessible in conventional single-phase emulsions. [80, 150, 44, 169]

Past studies have reported that a range of organizations of nematic LCs emerge within, for example, thin shells confined between two immiscible aqueous phases as a function of surface orientational ordering (anchoring), thickness of the shells, as well as variation in shell thickness. [251, 62, 140, 215] Topological defects form within the LC shells, depending on the boundary conditions (anchoring) imposed by the two aqueous surfaces. The resulting defects can organize into bipolar, triangular or tetrahedral arrangements, as documented by both experiments and numerical simulations. [62, 139, 140, 215] The exploration of LC ordering within the confines of shells also extends to cholesteric and smectic phases, leading to a rich range of shell textures and defect configurations. [251, 130, 44] In this paper, we reveal that anchoring conditions imposed by immiscible perfluoroalkane phases enable access to LC organizations within shells (and domains defined by Janus morphologies) that have not previously been reported.

Whereas past studies have focused on LCs confined by aqueous phases, including aqueous-glycerol mixtures containing surfactants, [251, 62, 139, 140, 130] we used immiscible perfluorocarbons to confine LCs for three reasons. First, in advance of this study, it was not obvious to us what orientations LCs would adopt at immiscible perfluorocarbon interfaces. Past studies have explored the ordering of LCs at the interfaces of solid perfluorocarbons. [225, 224, 88, 28] The anchoring (easy axis), however, largely depends on the method used to prepare the surfaces. Plasma deposition of perfluorocarbon films induces perpendicular alignment [225, 224] while the anchoring was found to be planar (parallel) on a surface deposited by rubbing a Teflon bar. [88, 28] In this manuscript, we explore LC alignments at liquid perfluoroalkane interfaces using the

nematogens 4'-pentyl-4-biphenylcarbonitrile (5CB) and 4-(trans-4-pentylcyclohexyl) benzonitrile (PCH5) and isotropic perfluorocarbon oils perfluorononane (F9) and perfluoroheptane (F7) (Figure 6.1). We compare the behaviors of 5CB and PCH5 in contact with F9 because 5CB is known to form smectic layering at interfaces whereas the cyclohexyl ring of PCH5 frustrates smectic layering. [163] This comparison thus allows us to probe the role of smectic layering in determining the orientations of LCs at liquid perfluorocarbon interfaces.

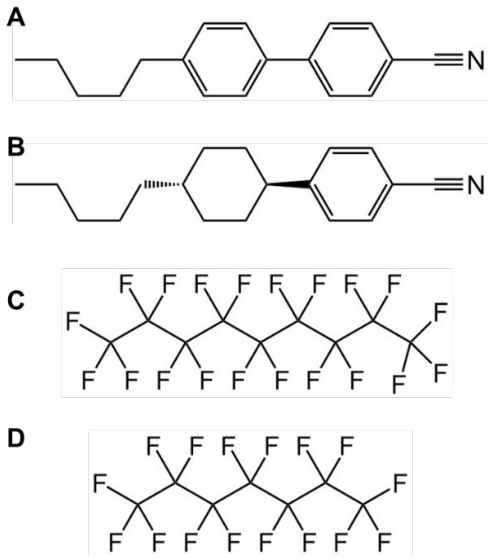

Figure 6.1: Molecular structures of the nematogens (A) 4'-pentyl-4-biphenylcarbonitrile (5CB), (B) 4-(trans-4-pentylcyclohexyl) benzonitrile (PCH5); (C) perfluorononane (F9) and (D) perfluoroheptane (F7).

Second, we used perfluorocarbons to prepare multiphase emulsions because our initial observations revealed that they provide access to a range of LC organizations in emulsion droplets that have not been seen previously. In particular, as detailed below, we found that 5CB molecules anchor weakly at perfluorocarbon interfaces and thus can be readily reoriented by elastic strain of the LC. This yields new configurations of LCs within shells that reflect an interplay between elastic energy, geometry of confinement and anchoring condition. We explored and provide insight into this interplay by comparing our

experimental observations to numerical simulations of multidomain LC droplets using a Landau-de Gennes description of the free energy. The use of perfluorocarbons also provided an opportunity to compare the influence of perfluorocarbon versus hydrocarbon surfactant type on emulsion droplet morphology and internal organization. [264, 275, 75]

The third reason we used perfluorocarbon oils in the experiments reported in this paper was because perfluorocarbons can be readily driven through phase transitions to create vapor-filled cavities within emulsion droplets. [116, 61, 155] We sought to determine if such phase transitions could be used to drive rapid changes in the shapes of the LC domains of the multiphase droplets explored in our study. As described below, we found that it was possible to rapidly thin nematic shells (formed from a high clearing temperature nematic LC called HTW) by thermally driving liquid perfluorocarbon cores (formed from F7) through liquid-to-vapor phase transitions. These results provide fresh ideas for actuation of LC emulsion droplets in ways that may provide insight into the dynamic properties of LCs in confinement. They also hint at new designs of stimuli-responsive LC systems driven far from equilibrium.

6.2 Experimental Methods

6.2.1 Materials

The nematogens, 4'-pentyl-4-biphenylcarbonitrile (5CB, nematic phase from 22.0 °C to 35.5 °C) and HTW45800-000 (HTW, nematic phase from -30 °C to 101 °C), were purchased from HCCH (Jiangsu Hecheng Display Technology Co., LTD). Perfluorononane (97%, F9), the nematogen 4-(trans-4-pentylcyclohexyl) benzonitrile (99%, PCH5, nematic phase from 30 °C to 55 °C), sodium dodecyl sulfate (99.0%, SDS), perfluorooctanoic acid (96%, PFOA), trichloro(1H,1H,2H,2H-perfluorooctyl)silane (97%) and glycerol (≥99.5%) were purchased from Sigma–Aldrich (St. Louis, MO, USA). Perfluoroheptane (mixture of

isomers, 98%, F7) was purchased from Alfa Aesar, Thermo Fisher Scientific (Tewksbury, MA, USA). Fisher Finest Premium Grade glass slides was purchased from Fisher Scientific (Pittsburgh, PA). Polyimide 2555, which was used to induce planar alignment of 5CB when coated on glass substrates, was purchased from HD Microsystems. Purification of water (18.2 MΩ cm resistivity at 25 °C) was performed using a Milli-Q water system (Millipore, Bedford, MA, USA). F9 and F7 were stored and degassed by freezing at -20 °C and -80 °C , respectively, prior to use.

6.2.2 Preparation of Optical Cells

Optical cells were assembled from two glass slides separated from each other by ~100-300 μm-thick spacers. Glass slides used for observation of 5CB droplets in F9 continuous phases were coated with trichloro(1H,1H,2H,2H-perfluorooctyl) silane to make them fluorophilic; glass slides were immersed into trichloro(1H,1H,2H,2H-perfluorooctyl) silane, subsequently rinsed with ethanol, F9 and dried with compressed air. Glass slides used for observations of F9 droplets in 5CB phases were spin-coated with polyimide 2555 using a Laurell spin coater, baked at 250 °C ; the two glass surfaces of cells were rubbed and assembled in an anti-parallel fashion to yield unidirectional tangential alignment of LCs for F9 droplet dispersed in 5CB.

6.2.3 Characterization of Anchoring of Nematic 5CB at interfaces of isotropic F9

We prepared 5CB (or PCH5) droplets in a F9 continuous phase by vortexing 20 μl of 5CB (PCH5) and 200 μl of F9 at 3000 rpm for 30 seconds. The resulting mixture was injected into a 100 μm-thick silane-coated optical glass cell at elevated temperatures (isotropic LCs), and cooled to room temperature for 5CB (or 35 °C for PCH5) for obser-

vation. PCH5 was preheated to isotropic state above 60 °C , and remained fluidic during the preparation process because of supercooling. To prepare F9 droplets in a 5CB-rich continuous phase, 4 μl of F9 and 200 μl of 5CB was homogenized for 10 seconds using a probe ultrasonicator (60 Sonic Dismembrator, Fisher Scientific) with a cold-water bath. The resulting mixture was injected into a 100 μm-thick optical cell, coated with polyimide 2555 on both surfaces to induce a uniform alignment of LCs. We injected the mixture in isotropic state at 40 °C and cooled it to room temperature. The samples were observed using polarized light microscopy.

6.2.4 Preparation of Emulsions using perfluorocaron and LC mixtures

To prepare droplets of F9-5CB, we added 50-100 μl 5CB and 50 μl F9 into glycerol in the absence of surfactants (or aqueous solutions in the presence of surfactants). The mixtures with glycerol were subsequently homogenized using the probe ultrasonicator with a cold water bath. The mixtures with aqueous solutions were vortexed at 3000 rpm for 30 seconds. The resulting mixtures were injected into 100 μm-thick optical cells at room temperature. The samples were heated above the LC clearing temperature (35.5 °C) and cooled to room temperature to equilibrate prior to making observations using optical microscopy. We observed the formation of droplets with core-shell structure as described below. We focused our observations on droplets between 10 and 30 micrometers (external diameter), and 3-10 micrometers (internal).

To prepare F7-HTW droplets, we dispersed 80 μl HTW and 20 μl F7 into glycerol by sonicating the mixture with a cold water bath. 30 μl of the resulting mixtures were diluted into 1000 μl glycerol, subsequently injected into 300 μm-thick optical cells at room temperature and heated to vaporize the F7 cores using a Linkam LTS350 hot stage with an accuracy of 0.1 °C .

6.2.5 Measurements of Interfacial Tensions

The interfacial tensions were measured using the pendant drop method48 performed with an optical tensiometer (Attension Theta T200, Biolin Scientific). Hamilton metal 22-gauge needles (blunt point) were used. The equilibration time was 5 min for each drop. The results presented in this paper were obtained using 5 independent measurements. An environmental chamber heated by a fluid bath was used to control temperature. The densities used to analyze the pendant drop measurements were 1.0258 g cm^{-3} (5CB), 0.9700 g cm^{-3} (PCH5) 1.2613 g cm^{-3} (glycerol, room temperature), 1.2522 g cm^{-3} (glycerol, 35 °C)49, 1.7990 g cm^{-3} (F9, room temperature), 1.7633 g cm^{-3} (F9, 35 °C)50, and 0.9982 g cm^{-3} (aqueous solutions). The density of 5CB was measured to be 1.025753±0.000073 g cm^{-3} using an Anton Paar DSA 5000 M density meter at 20 °C .

6.3 Results and Discussion

6.3.1 Anchoring of 5CB and PCH5 at F9 interfaces

Many perfluoroalkanes and isotropic hydrocarbons are immiscible at low temperatures, and mix above their upper consolute temperatures. [275, 73] Perfluoromethylcyclohexane and hexane, for example, form two phases at 0 °C at a 1:1 volume ratio, but form one phase at room temperature. [73] At the outset of our study, we surveyed a range of perfluoroalkanes for the design of multi-compartment LC emulsions, including perfluorohexane (F6), perfluoroheptane (F7) and perfluorononane (F9). These perfluorocarbons form emulsions with similar morphologies, as described below, but we chose to focus on F9 because it can be readily degassed by freezing at -20 °C . In the absence of degassing, we found that gas bubbles were released from the oils when heating them during studies of phase behaviors.

Unlike mixtures of perfluorocarbons and hydrocarbons described above, we found

that the F9-5CB mixture (1:1 volume ratio) forms two phases over the temperature range 22 °C to 120 °C , which includes the temperature range of the nematic phase of 5CB (22 °C to 34 °C). We also found that a finite amount of F9 can dissolve into 5CB, with the mixture F9:5CB = 1:100 (volume ratio) forming a single phase above 50.5 ± 3 °C . This level of miscibility, although low, has the potential to change the properties (e.g., elastic constants) of the nematic phase. It is noteworthy that the phase behavior of the F9-LC mixtures is different with the mixtures of perfluoroarenes (e.g., hexafluorobenzene, FB) and hydrocarbon liquid crystals (e.g., E7) due to the polarizable nature of perfluoroarenes. [260, 73] The FB-E7 mixture (e.g., 5:100 volume ratio) forms a single nematic phase below a critical temperature and forms coexisting nematic-isotropic phases at elevated temperatures. As described below, in the study reported in this paper, we used the largely immiscible mixtures of F9 and 5CB to form emulsions.

Initially, we prepared emulsions using F9 and 5CB, characterized the morphologies of the F9 or 5CB emulsion drops and inferred the orientational ordering of 5CB at F9 interfaces based on observation of the internal organization of the LC domains. To this end, we examined nematic 5CB droplets dispersed in a continuous phase of F9 (Figures 6.2A-C) as well as droplets of F9 dispersed in continuous phases of nematic 5CB (Figure 6.2D). To make observations of 5CB droplets in F9, we emulsified 10% v/v 5CB into F9 at room temperature, and performed experiments using films of the F9-5CB mixture confined within optical cells with surfaces that were treated to be fluorophilic (see Experimental Methods). Our experiments revealed that nematic phases of 5CB assume a perpendicular (homeotropic) alignment (easy axis) at the interfaces of F9, as indicated by the so-called radial configuration with a point defect at the center of the droplets [134, 51] (Figure 6.2A).

We also examined the influence of 5CB droplet size on LC ordering. The droplet in Figure 6.2B with a 1.4 μm radius generates four brushes under crossed polars (consistent with a radial configuration), while the droplet in Figure 6.2C with a 0.9 μm radius gen-

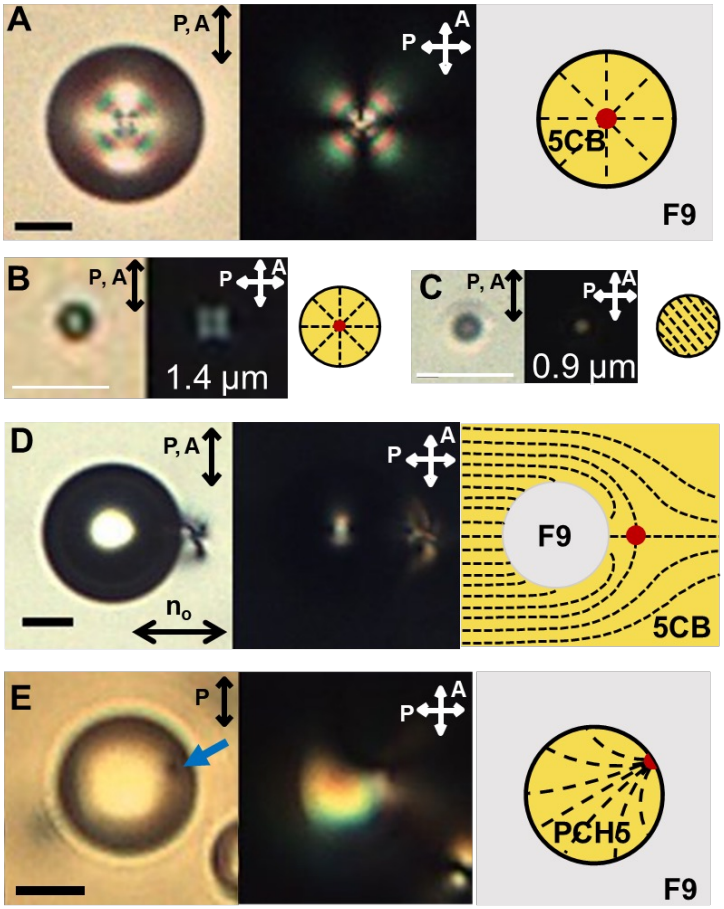

Figure 6.2: Micrographs between parallel polars (left), crossed polars (middle), and schematic illustrations (right) of (A-C) 5CB droplets in a continuous phase of F9 and (D) an F9 droplet dispersed in 5CB at room temperature. (B,C) size-dependence of LC ordering in droplets with radii of 1.4 μm and 0.9 μm, respectively. (E) Single-polar, crossed-polar micrographs and schematic illustration of a PCH5 droplet in F9. The defect denoted by the blue arrow is slightly tilted out of the plane. Scale bars, 10 μm. The double-headed arrows indicate the orientation of the two polarizers. The dash lines show the ordering of 5CB (director). The red dots indicate the defects.

erates a birefringent texture that disappeared periodically during droplet rotation (inconsistent with a radial configuration; Figure S1). The latter result suggests that the smaller droplet has adopted a configuration with a uniform LC orientation. Overall, these observations suggest that a decrease in 5CB droplet radius below a critical value of ~1 μm caused a spontaneous transition from a radial to a uniform director profile within the 5CB domain. Past studies have demonstrated that the elastic energy of a LC droplet scales with the droplet radius ($\sim KR$) and the surface anchoring energy scales with the square of the droplet radius ($\sim WR^2$). [150, 95] These two contributions to the free energy lead to the prediction that droplets with $R \leq K/W$ will exhibit a director profile dominated by elastic energy whereas larger droplets will satisfy the perpendicular anchoring and form the radial configuration. These predictions are consistent with our experimental observations, and permit us to estimate that the anchoring coefficient W of 5CB at F9 interface is 10^{-5} N/m, by using K of 5CB ~ 10^{-11} N [150, 95] and a critical radius of ~ 1μm.

The observation of uniform LC ordering of 5CB droplets in F9 below the critical radius of ~1 μm contrasts with prior reports of 5CB droplets confined within polymeric capsules, where a transition from bipolar (parallel anchoring) to radial configuration was seen below a critical radius of ~400 nm. [80, 150] The transition was attributed to the contribution that k_{24} (saddle-splay elastic constant) makes to the elastic free energy. For the F9-5CB emulsions reported in this manuscript, as noted above, a small amount of F9 dissolves into 5CB. It is possible that the dissolved F9 changes the elastic constants of the 5CB (e.g., to increase the splay and the bend constants more than the twist and the saddle-splay constants), leading to uniform ordering of LC within droplets with radii less than 1 μm. Additionally, we examined the temperature-dependence of LC ordering within the LC droplets but observed no significant difference in director profiles between 25 °C and 34 °C (prior to the nematic to isotropic phase transition of 5CB).

We also observed a perpendicular alignment of 5CB at the F9 interface when droplets

of F9 were dispersed in a continuous phase of nematic 5CB (Figure 6.2D). In these experiments, we emulsified 2% v/v F9 into 5CB and confined films of the mixture between two polymer-coated glass surfaces that induced unidirectional tangential alignment (no) of nematic 5CB. The homeotropic anchoring of 5CB at the F9 droplet interface generates a hyperbolic hedgehog defect [263, 260] accompanying the F9 droplets (Figure 6.2D). A twist deformation can be seen near the point defect in Figure 6.2D. Both clockwise and anticlockwise twisted structures were observed with equal probability. It is possible that the dissolution of F9 into 5CB also plays a role in the observation of the twist in the 5CB (potentially reducing the ratio between twist and splay elastic constants).[51, 196, 10] As noted above, a mixture F9:5CB = 1:100 (volume ratio) forming a single phase above 50.5 ± 3 °C . Upon cooling to room temperature, however, we observed F9 droplets to phase separate from the nematic 5CB and form dimers and chains (Fig. S2). [142]

The observation of homeotropic anchoring of 5CB at perfluoroalkane interfaces contrasts to observations made at interfaces of other immiscible liquids (e.g., water and glycerol, for which the orientations of nematic 5CB are parallel). At least three mechanisms have been proposed to lead to the homeotropic anchoring of 5CB at interfaces. First, at a free surface (air interface), 5CB molecules form a highly ordered smectic-like layer, revealing that an entropic loss is compensated by enthalpic gains arising from layering of the LC molecules. [208] Second, surfactants (e.g., sodium dodecyl sulfate and dodecyltrimethylammonium bromide) can give rise to homeotropic anchoring of 5CB at aqueous interfaces by interdigitating with the tails of 5CB. [150, 95, 139, 130, 51] Third, interfacial disordering can give rise to weak anchoring energies, which allows the LC elastic energy or external fields to dominate the LC orientation at the interface. [45, 51, 22, 165] Because surfactant is absent in the experiments reported above, and because our experiments lead us to conclude that the easy axis of 5CB is perpendicular to the interface to F9, we propose that smectic layering is likely behind the observation of homeotropic ordering of 5CB at

F9 interfaces. Below we explore this proposition.

To probe the possible role of the smectic layering in leading to perpendicular anchoring of 5CB at the F9 interface, we examined the behavior of the nematogen PCH5 at the F9 interface. The molecular structure of PCH5 differs from 5CB in that one aromatic ring of 5CB is replaced by a cyclohexyl group on PCH5 (Figure 6.1B). PCH5 exhibits planar anchoring (parallel to the interface) at free surfaces [163] because the non-planar configuration of the cyclohexyl group of PCH5 frustrates smectic-like layering. We dispersed PCH5 droplets into F9 films at 35 °C , where PCH5 is a nematic LC (5 °C above the crystal-to-nematic transition temperature). In contrast to 5CB, we observed tilted anchoring of nematic PCH5 at the F9 interface. This is indicated by a “pre-radial" configuration of PCH5, with a director profile that radiates from a point defect located near the interface of the nematic droplet (Figure 6.2E). [260, 51] The pre-radial configuration comprises a point hedgehog located near the surface of the droplet with a topological charge of $N = 1$; [256, 123] weak, tilted surface anchoring (so-called weak conic anchoring) prevents formation of defects on the surface of the droplet. The configuration in Figure 6.2E is, therefore, topologically equivalent to a radial droplet. The tilted anchoring is consistent with our hypothesis that the presence of the cyclohexyl group frustrates smectic layering of PCH5. Ongoing molecular-level simulations are being performed to provide additional insight into the ordering of PCH5 and 5CB at F9 interfaces.

6.3.2 Nematic shells with Weak Anchoring

Next we explored how nematic LCs and isotropic perfluorocarbons can be used to design complex multi-compartment emulsions. To form multi-compartment emulsions, we emulsified F9 and 5CB (1:2 volume ratio) mixtures in glycerol at room temperature. Glycerol (more viscous than water) was used to slow the rate of diffusion of the emulsion droplets to enable microscopic observations, although similar results were observed with

water. Because F9 and 5CB are largely immiscible during emulsification at room temperature, the relative volumes of the two phases varied between droplets, providing a means to rapidly screen for possible configurations formed by the two phases.

The morphology of the multi-compartment emulsion droplets explored in this paper are determined by a force balance between three interfacial tensions, [260, 275, 247] namely the interfacial tensions of the F9-glycerol interface, γ_{F9}, the 5CB-glycerol interface, γ_{5CB}, and the F9-5CB interface, γ_{F9-5CB}. To guide our understanding of the morphologies formed by these complex emulsions, we performed measurements of interfacial tensions using a pendant drop tensiometer. In the absence of surfactants, γ_{F9} was measured to be 33.0 ± 0.5 mN/m; γ_{5CB} was 17.2 ± 0.1 mN/m; and γ_{F9-5CB} was measured to be 13.7 ± 0.1 mN/m using pendant drop method. [95, 166, 260, 275, 105] Because $\gamma_{F9} > \gamma_{5CB} + \gamma_{F9-5CB}$, we predicted the formation of morphologies with F9 cores and 5CB shells. [260, 275, 247]

Consistent with these predictions, we observed the formation of core-shell droplets with 5CB shells and F9 cores. We observed three distinct internal organizations of the nematic 5CB shells. First, when the radii of the inner F9 cores (r) were larger than 40% of the droplet radii (R), $r \leq 0.4R$, nematic shells with quadrupolar symmetry were observed (Figure 6.3A). Interestingly, neither Saturn-ring defects [228, 78] (-1/2 disclination rings at the equator) surrounding F9 cores nor boojums [150] (+1 point defects at interface) at 5CB-glycerol interface were observed for the quadrupolar configuration. We hypothesized that the relatively small energetic contribution of surface anchoring compared to elastic strain of the LC (weak anchoring) led to the absence of defects within the 5CB shells. To obtain anchoring energies ($\sim Wl^2$) that are comparable in magnitude to the elastic energy ($\sim Kl$), we estimate the anchoring strength (W) at the both F9 and glycerol interfaces to be of order of $10^{-5} - 10^{-6}$ N/m, where l, the length scale, is $\sim 5\mu$m and K is $\sim 10^{-11}$ N. This estimate of anchoring energy is supported by numerical simulations shown below.

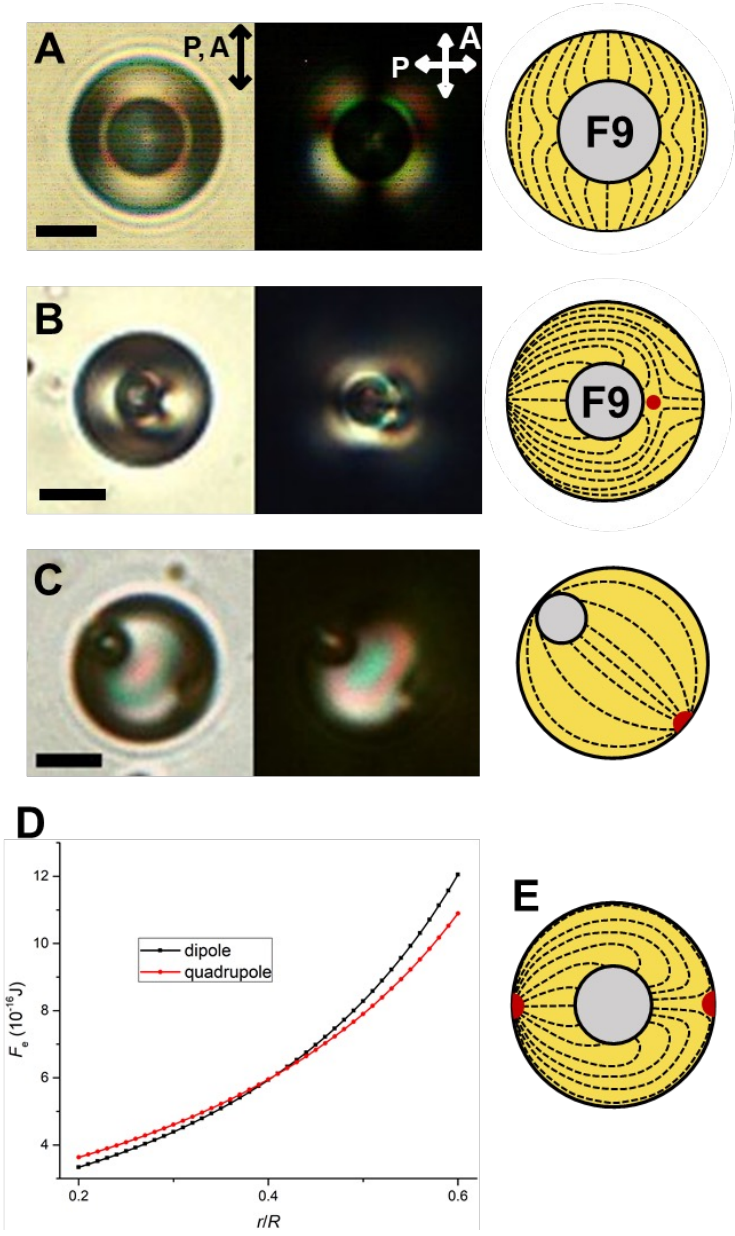

Figure 6.3: (A-C) Polarized-light micrographs (left: parallel-polars; middle: crossed-polars) and schematic illustrations (right) showing internal organizations of double emulsions with nematic 5CB shells and F9 cores of various sizes. Droplets are dispersed in glycerol. Scale bars, 10 μm. The dash lines show the ordering of 5CB (director). The red dots indicate the defects. (D) Estimated elastic free energy Fe as a function of the ratio of core radius to droplet radius 10 μm) for droplets with dipolar and quadrupolar symmetries. (E) Schematic illustration shows the internal organization with strong anchoring at both interfaces (perpendicular inner, planar outer).

Second, for F9 cores with radius $0.4R \geq r \geq 0.3R$, the 5CB shells exhibited a dipolar symmetry (Figure 6.3B). The isotropic F9 inner droplets were accompanied by hyperbolic hedgehogs (-1 point defects). Similar to the quadrupolar symmetry, no boojums were observed at the 5CB-glycerol interface with the dipolar symmetry, indicating a higher anchoring strength at the F9 interface compared to the glycerol interface. Based on the anchoring coefficient estimated above, we inferred at the F9 interface that $W_{inner} = 10^{-5}$N/m and at glycerol interface that $W_{outer} = 10^{-6}$N/m. Our results contrast to nematic 5CB shells with strong anchoring at aqueous interfaces in the presence of surfactants, where the interfacial energy (anchoring energy) dominates the LC elastic energy, and the shells exhibit a dipolar symmetry with two +1 defects (boojums) at the planar interface (Figure 6.3E). [139, 130] Additionally, we note that the F9-5CB emulsions with core-shell morphologies differ from the emulsions formed by the partially miscible perfluorobenzene and LCs, [260] where the mixture only creates emulsion droplets with Janus morphologies.

Third, we observed the F9 inner droplet, when $r < 0.3R$, to be localized to the site of one of the defects of a 5CB droplet in a so-called bipolar configuration [80, 139, 51] (Figure 6.3C). This configuration has been seen before in emulsions with 5CB shells and homeotropic silica particles.68 Defect regions possess a high local free energy density and thus they tend to attract inclusions. Similarly, we interpret our results to indicate that the small F9 droplet replaces the strained LC at and near the defect, [263] consistent with past numerical simulation showing that the free energy is minimized when an isotropic sphere ($r = 0.286R$, where r and R are the inclusion and LC droplet sizes, respectively) with homeotropic anchoring is located at boojums. [209]

To provide insight into the interplay of mechanical confinement and configurational stability that underlies the above-described experiments, we compared the free energies of the LC configurations with quadrupolar and dipolar symmetries. [150, 139, 130,

263] We formulated a simple model to evaluate the free energy of a multi-compartment droplet. (see Figure S3 in Supplemental Material for details.) The elastic free energy F_e, evaluated, as a function of the ratio r/R is shown in Figure 6.3D. Our simple model predicts that the configuration with dipolar symmetry is stable for small inner core sizes, that is $r/R < 0.406$; and quadrupolar symmetry is stable for large cores, $r/R > 0.406$. These predictions agree closely with our experimental observation of a transition between configurations with dipolar and quadrupolar symmetries at $r/R \sim 0.4$, and they are validated further by numerical simulations that are presented below.

6.3.3 Numerical Simulations and Estimates of Anchoring Strengths at Nematic-Perfluorcarbon Oil Interfaces

The scaling arguments presented above provide order of magnitude estimates of the anchoring energies of 5CB at F9 interfaces. To obtain quantitative estimates, we performed numerical simulations to precisely model the detailed orientational ordering of LCs in the confines of the morphologies of the multiphase LC droplets. We used a Landau-de Gennes (LdG) continuum model, calculated optical textures and compared them with experiments. [260, 278] The one elastic constant $K = 4.55$ pN for 5CB was used. We note that the radii of the simulated droplets were of the order of 1 μm, one order smaller than most droplets observed in experiment. To enable comparisons between computation and experiments, we increased the anchoring strength by one order of magnitude to keep the ratio of anchoring energy ($\sim Wl^2$) to elastic energy ($\sim Kl$) comparable in experiment and simulation.

Figures 6.4 and 6.5 reveal that the simulations predicted configurations with quadrupolar and dipolar symmetry by setting $r = 1/2R$ and $r = 1/3R$, respectively, consistent with our experimental results and thermodynamic scaling arguments (Figure 6.3). To aid interpretation of the optical micrographs in Figure 6.3 in terms of the influence of

anchoring strength of LC at the boundaries of the shells, we varied the anchoring coefficient W at the two interfaces, simulated the corresponding optical micrographs, and then compared the simulated light micrographs to our experimental observations. First, we discuss the simulations for the emulsions with quadrupolar symmetry. The use of strong anchoring ($W_{outer} = 10^{-3}$ N/m and 10^{-4} N/m) at the outer interface led to two boojums (Figures 6.4A,B), contrary to our experimental results showing the absence of defects at the outer interface (Figure 6.3A). When $W_{outer} = 10^{-5}$ N/m, defects were absent at the outer interface, in good agreement with experiments (Figures 6.4C-E). Similarly, the use of $W_{inner} = 10^{-3}$ N/m at the inner interface lead to formation of Saturn-ring defects surrounding the inner isotropic cores (Figures 6.4A-C), in contradiction to experimental results. We found that $W_{inner} = 10^{-4}$ N/m for the F9 interface (inner) in Figure 6.4D leads to a defect-free configuration, and the simulated optical micrographs shows four extinction (dark) brushes between crossed polars, in agreement with experiments. When $W_{inner} = 10^{-5}$ N/m (Figure 6.4E), the simulated optical textures are also similar to the experiment. This anchoring strength, however, was found not sufficient to generate dipolar symmetry, as described below. As noted above, the anchoring strength was increased by one order of magnitude in simulations to capture the difference of droplet size between experiments and simulations. The anchoring coefficients of 5CB used in the simulations, $W_{outer} = 10^{-5}$ N/m at outer phase and $W_{inner} = 10^{-4}$ N/m at inner interface, are thus equivalent to the anchoring coefficients estimated from our experiments and scaling arguments ($W_{outer} = 10^{-6}$ N/m at outer glycerol phase and $W_{inner} = 10^{-5}$ N/m at inner F9 core).

The director profiles and polarized images of the emulsion droplets with dipolar symmetry were also simulated (Figure 6.5). We found simulations with $W_{outer} = 10^{-5}$ N/m and $W_{inner} = 10^{-3} - 10^{-4}$ N/m, as shown in Figures 6.5A,B, to capture the key features of experimental results, specifically the formation of hyperbolic hedgehog defects (Fig-

ure 6.3B). In contrast, the use of weak anchoring coefficients ($W = 10^{-5}$ N/m) for both inner and outer interfaces led to the dipolar configuration being unstable (Figure 6.5C). The simulations also revealed that the anchoring strength of nematic 5CB at F9 interface is one order of magnitude larger than that at glycerol interface, consistent with our scaling arguments reported above.

6.3.4 Influence of Surfactant Type and Concentration on Morphologies and Internal Configurations of F9-Nematic Emulsion Droplets

As mentioned in the Introduction, the use of perfluorocarbon oils provides the opportunity to use both perfluorocarbon and hydrocarbon surfactants to tune droplet morphologies and internal organizations via preferential adsorption at interfaces of the two domains of the droplets. [260, 275, 75] To explore this opportunity, similar to the fabrication of nematic shells, F9 and 5CB (1:1-2:1 volume ratio) mixtures were dispersed into aqueous surfactant solutions at room temperature to characterize droplet morphologies.

To guide our understanding of the influence of surfactants on droplet morphology, we measured the interfacial tensions between aqueous phases and oils as a function of the concentration of sodium dodecyl sulfate (SDS), and perfluorooctanoic acid (PFOA) (Figure 6.6A,B). We assume that the interfacial tension at the F9-5CB interface of the emulsion droplets, γ_{F9-5CB} = 13.7 ± 0.1 mN/m, remains unchanged in the presence of the surfactants. In contrast to the surfactant-free emulsions formed by either 5CB and F9, we predicted that in the presence of surfactants (i.e., 2 mM SDS, 1 mM PFOA and 2 mM PFOA), the droplets would all form Janus morphologies, as the three interfacial tensions satisfy the thermodynamic criteria that $\gamma_{jk} - (\gamma_{ij} + \gamma_{ik})$ ($i \neq j \neq k$ = F9, 5CB, F9-5CB) are all negative. [166, 260, 275] This prediction is validated by our experiments (Figures 6.6C-E). We also observed droplets with 5CB cores and F9 shells in 2 mM PFOA solution (Figure 6.6F), but we concluded that this inverted core-shell structure was a metastable morphology be-

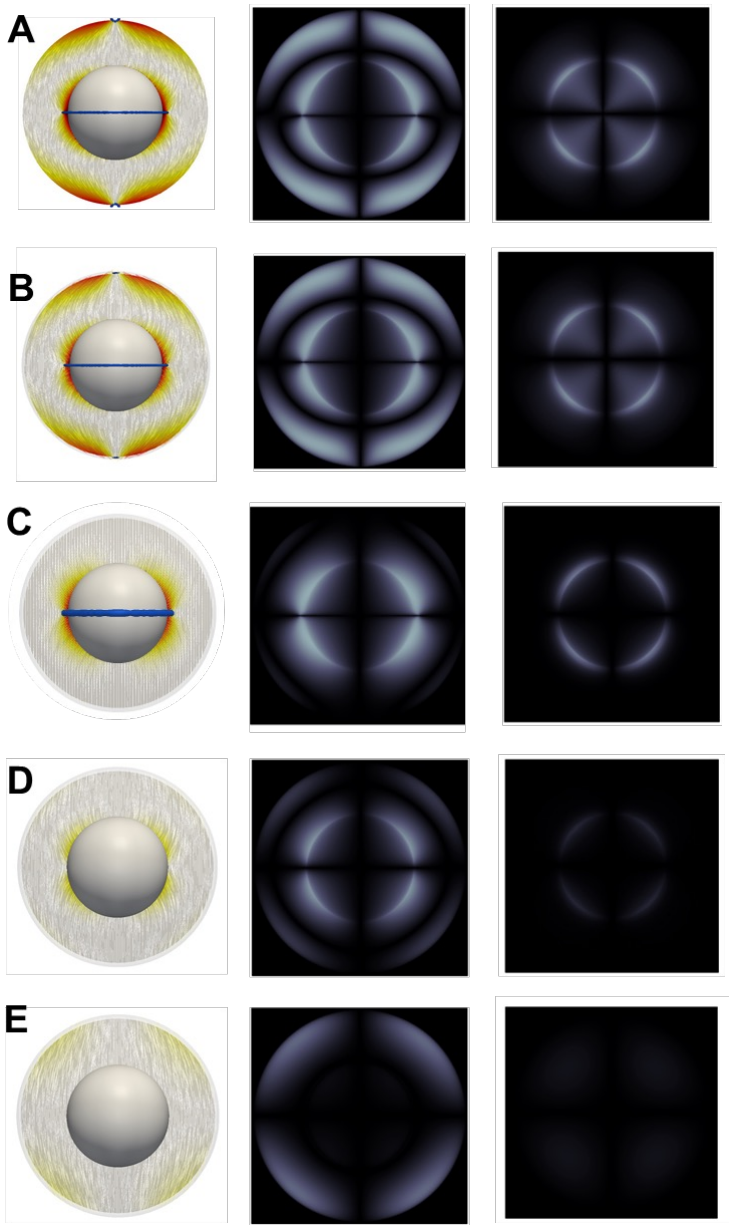

Figure 6.4: Effect of strength of LC anchoring on the organization of core-shell emulsions with F9 core and 5CB shells (quadrupolar symmetry). Simulated director profiles (left) and polarized images from side view (middle) and top-down view (right) of nematic shells with anchoring coefficients W (N/m) = (A) 10^{-3} (inner) and 10^{-3} (outer), (B) 10^{-3} (inner) and 10^{-4} (outer), (C) 10^{-3} (inner) and 10^{-5} (outer), (D) 10^{-4} (inner) and 10^{-5} (outer), and (E) 10^{-5} (inner) and 10^{-5} (outer). Droplet radii in simulations: 1 μm (outer), 0.5 μm (inner). Blue loops indicate defects.

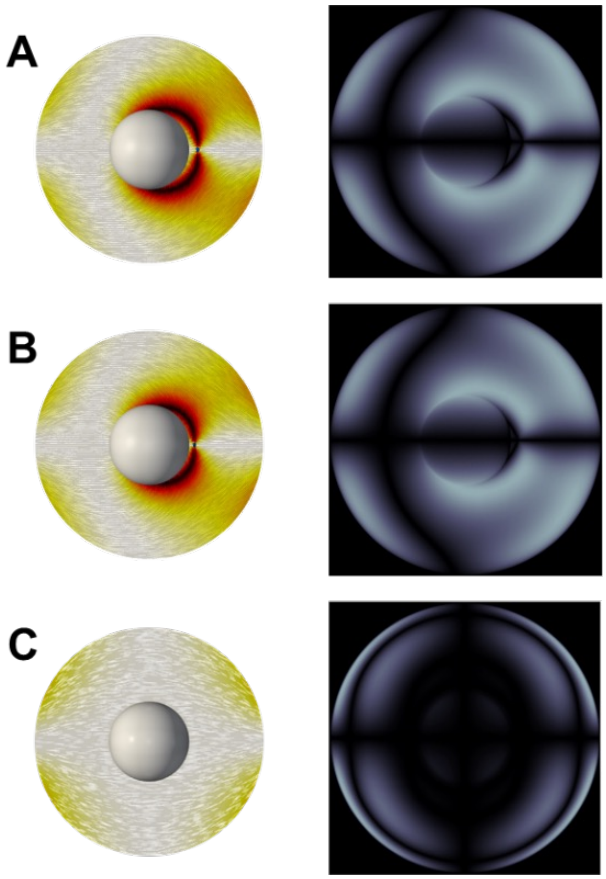

Figure 6.5: Anchoring strength effect on the organizations of a double emulsion with dipolar symmetry. Simulated director profiles (left) and polarized light images (right) of nematic shells with anchoring coefficients W (N/m) = (A) 10^{-3} (inner) and 10^{-5} (outer), (B) 10^{-4} (inner) and 10^{-5} (outer), (C) 10^{-5} (inner) and 10^{-5} (outer). Droplet radii in simulations: 2.25 μm (outer), 0.75 μm (inner).

cause of its small population (less than 5%) and the thermodynamic analyses described above.

Although all surfactants induced the Janus morphology, we observed that the internal organizations depended on the surfactant type and concentration. We elucidated the influence of surfactant type and concentration on the internal organization of the 5CB compartments by comparing experiments to simulations. We assume the anchoring of 5CB at the F9 interface (the inner interface) remains homeotropic in the presence of the surfactants; the anchoring coefficient used in the simulation was unchanged, $W_{inner} = 10^{-4}$ N/m; and, as discussed above, the anchoring coefficients used in the simulations are one order of magnitude larger than the experiments to accommodate the smaller size of droplets in simulations.

When we added 2 mM SDS into aqueous phase, 5CB molecules exhibited homeotropic anchoring at the aqueous interface, confirmed by the radial configuration of nematic single-phase droplet. In the Janus droplets, we observed no defect formation in the nematic compartment (Figure 6.6C). This configuration is in a good agreement with simulations, when strong anchoring $W_{outer} = 10^{-3}$ N/m was used at the aqueous interface. Similar configurations have been seen for droplets formed by partially miscible perfluorobenzene-E7 mixtures in 1 mM SDS solution. [260]

In contrast to 2 mM SDS, 5CB was measured to assume a planar orientation at an interface to 1 mM PFOA. The nematic 5CB compartments of the Janus droplets prepared with 1mM PFOA were found to exhibit a director profile that radiates from a point defect located at the pole (planar anchoring at the aqueous interface, Figure 6.6D). The simulated textures captured the location of the defect and the brushes. Emulsions comprised of poly(dimethylsiloxane) and 5CB in poly(vinyl alcohol) solution also form similar organizations, as reported previously. [95]

When using 2 mM PFOA, 5CB anchors homeotropically, similar to 2 mM SDS. How-

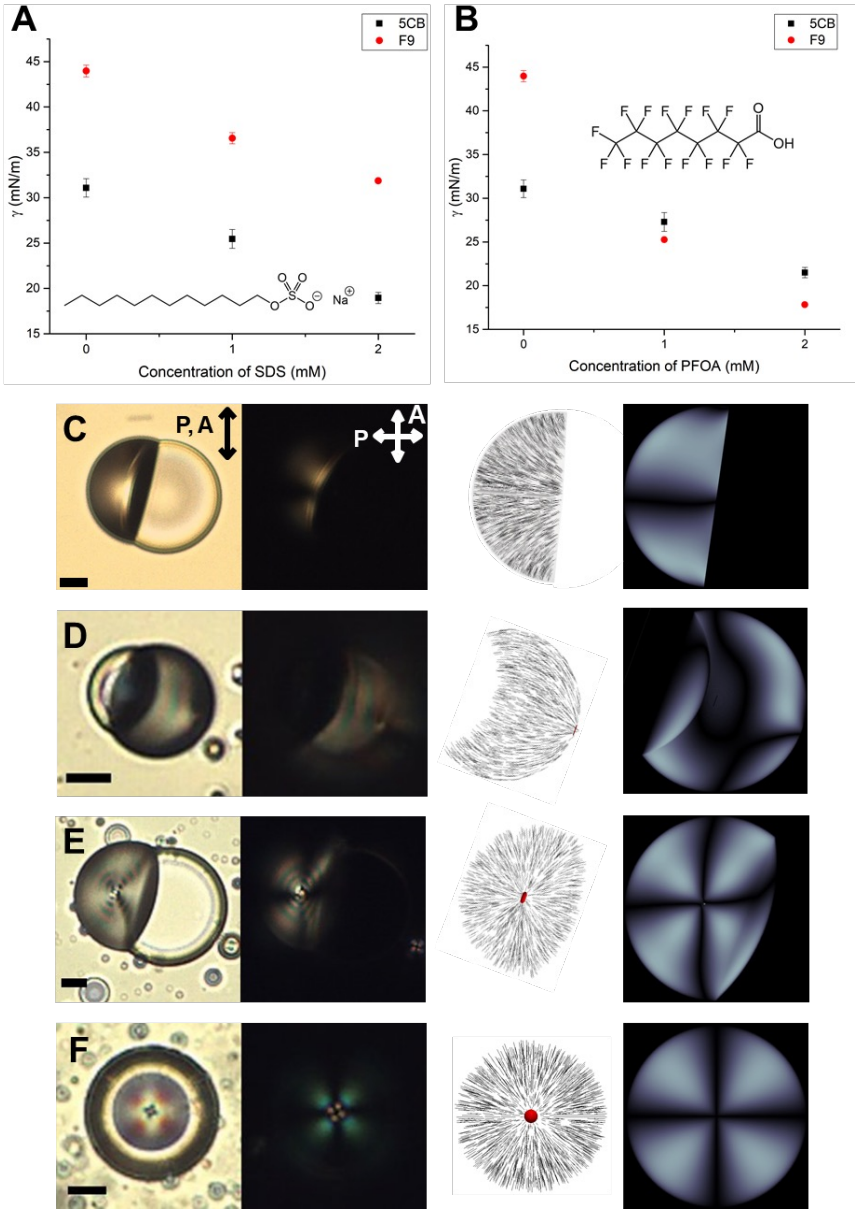

Figure 6.6: (A,B) Interfacial tensions as a function of concentrations of the surfactants. The insets are the molecular structures of (A) the hydrocarbon surfactant, sodium dodecyl sulfate (SDS), and (B) the fluorocarbon surfactant, perfluorooctanoic acid (PFOA). (C-F) Parallel-polar (first column), crossed-polar micrographs (second column), simulated director profiles (third column) and simulated polarized light micrographs (fourth column) show surfactant-dependent morphology and organization of F9-5CB droplet emulsions dispersed in the aqueous phases of (C) 2 mM SDS, (D) 1 mM PFOA and (E,F) 2 mM PFOA, respectively. Scale bars, 10 μm. Adopted boundary conditions in simulations: perpendicular at the 5CB-F9 interface with $W_{inner} = 10^{-4}$ N/m and at the aqueous interfaces: (C) perpendicular with $W_{outer} = 10^{-3}$ N/m ; (D) parallel with $W_{outer} = 10^{-4}$ N/m ; (E) perpendicular with $W_{outer} = 10^{-4}$ N/m . Droplet radii in simulations: 1 μm.

ever, the configuration of the 5CB within the Janus droplet formed with 2 mM PFOA comprises a director profile radiating from a point defect located at the center, which contrasts to the 5CB compartment formed using the 2 mM SDS (Figure 6.6E). We hypothesized that the SDS and the PFOA surfactants provide different anchoring strengths at the aqueous interface. Numerical simulations validated the hypothesis. When $W_{outer} = 10^{-4}$ N/m, the locations of defects and dark brushes were in good agreement with experiments performed with PFOA. We concluded that the PFOA provides an anchoring strength that is one order of magnitude smaller than the SDS surfactant. We note that the configuration of the LC domain within the Janus droplet is a sensitive reporter of changes in surface anchoring energy. We end this section by noting that we observed no visible morphological changes when heating the F9-5CB emulsions above the nematic-isotropic transition temperature of 5CB (35.5 °C), leading to the conclusion that the elasticity and anchoring energy of the LC droplets have a minor impact on droplet morphology.

6.3.5 Liquid-to-Vapor Phase Transitions in the Perfluorocarbon Core of Complex LC Emulsions

Perfluoroalkanes and nematic LCs, as described above, provide access to multicompartment emulsions with morphologies and internal organizations that are not accessible using other systems. In addition, immiscible perfluorocarbons are interesting components of emulsions because they can be driven to undergo liquid-vapor phase transitions in emulsion systems. [116, 61, 155] In contrast, LC shells with aqueous cores are difficult drive through reversible changes because they are generally unstable. [251, 62, 130, 215] In the experiments reported below, we used perfluoroheptane (F7) and the nematogens HTW to form core-shell droplets because the upper part of the nematic temperature range of HTW (-30 °C -101 °C) is above the boiling point of F7 (boiling point (bp) = 82 °C).

In our experiments, F7 and HTW was homogenized into glycerol to form droplets

with core-shell morphology. Figure 6.7 shows the droplet behaviors during one heating and cooling cycle. At 50.0 °C , the F7 core was a liquid phase and the HTW shell was a nematic phase (Figure 6.7A). At 90.0 °C , which is above the boiling point of F7 (82 °C), the morphology and internal organizations of the droplet remained unchanged (Figure 6.7B), indicating the core at this temperature was a superheated liquid phase. At 130.0 °C , the nematic shell turned dark, corresponding to a nematic to isotropic phase transition in the shell while the core remained in the metastable liquid state (Figure 6.7C). Remarkably, it was not until the droplet was heated to 165 °C -170.0 °C did the F7 core rapidly vaporize. Within a period of 0.05 s, we observed the 5CB shell to rapidly expand as the F7 core transformed to a gas (dark micrograph under the crossed polars, Figure 6.7D). We confirmed that the increase in the size of the core was consistent with formation of a gas by using the ideal gas law $pV = nRT$, where p is atmospheric pressure (N/m^2), V is volume to be calculated (m^3), n is the amount of substance (mol), R is the gas constant 8.31 (J mol^{-1} K^{-1}), and T is the temperature (K). We calculated that the volume of the core should expand with the liquid-to-vapor transition by a factor of 133 (factor of 5 in diameter). We measured in our experiments that the core diameter expanded from 9.5 μm to 49.3 μm in Figure 6.7, consistent with the above estimate.

We note that the F7 core was superheated by ~85 °C prior to undergoing the liquid to vapor phase transition and that the phase transition in the nematic shell did not trigger the liquid to vapor transition in the core. Comparable levels of superheating have been reported in prior experiments performed with perfluorocarbons having shorter chain lengths (i.e., perfluoropropane and perfluorobutane). [61, 155] We subsequently cooled the HTW-F7 gas-core emulsion back to 90.0 °C , which is above the bp of F7 but below the clearing temperature of HTW, and we observed the shell to recover its liquid crystalline state as evidenced by the appearance of a bright shell when viewed under crossed polars (Figure 6.7E). We also observed defects to be present within the thin nematic shell,

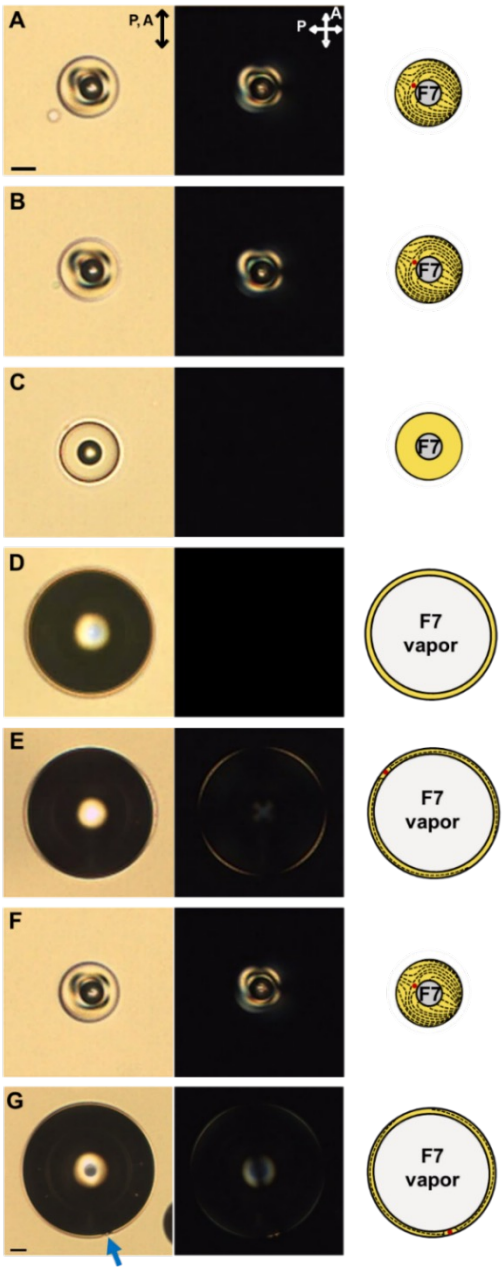

Figure 6.7: Thermal reconfiguration of multiphase LC emulsion droplets with a perfluorocarbon (F7) core and nematic (HTW) shell. Parallel-polar (left), crossed-polar (middle) micrographs and schematic illustrations (right) of a droplet with an F7 core and an HTW shell during heating and cooling cycles; heating to (A) 50.0 °C (liquid core, nematic shell), (B) 90.0 °C (liquid core, nematic shell), (C) 130.0 °C (liquid core, isotropic shell), (D) 170.0 °C (vapor core, isotropic shell), and upon cooling to (E) 90.0 °C (vapor core, nematic shell) and (F) 50.0 °C (liquid core, nematic shell). The defect in (E) (red dot) is not within the focal plane. (G) Droplet with defect evident in the nematic HTW shell. Scale bars, 10 μm.

as shown in Figures 6.7G and S4 (denoted by the blue arrow). We note that the defect is not located at the focal plane for the shell shown in Figure 6.7E. Subsequently, we cooled the system to 50.0 °C . After 30 min, the F7 core was observed to condense into its liquid state and the emulsion droplet returned to its original size (Figure 6.7F). Interestingly, the time scale for expansion (~0.01 s) versus contraction (~10 min) of the gaseous core differed greatly. We hypothesize that the nematic ordering of HTW within the shell slows the contraction process as compared to the expansion during which the HTW is an isotropic phase. Although we observed one defect near the F7 core in both thick and thin shells, thinning of nematic shells can potentially actuate the transform of defects, [62, 139, 215] including elimination of defects if the anchoring extrapolation length becomes larger than the shell thickness. Future studies will explore in more detail the dynamics of these emulsions. Overall, the experiments reported above demonstrate that LC-perfluorocarbon emulsions can be actuated reversibly via heating and cooling of the perfluorocarbon cores through liquid-to-vapor phase transitions.

6.4 Conclusions

This paper reports the formation of complex emulsions from immiscible LCs and isotropic perfluoroalkane oils (F9 and F7). To provide insight into the structures of the emulsion droplets, we characterized the anchoring of two nematic LCs, 5CB and PCH5, at interfaces of isotropic F9 phases. We found that 5CB assumes a perpendicular orientation while PCH5 exhibits a tilted anchoring, consistent with the role of smectic ordering in the perpendicular orientation assumed by 5CB. In the absence of surfactant added to a continuous aqueous/glycerol phase, we found that F9 and 5CB form emulsion droplets with perfluorocarbon cores and nematic shells. Our observations reveal that the anchoring of 5CB at the F9 interface is unusually weak, giving rise to shells of 5CB with either quadrupolar ($r/R > 0.4$) or dipolar symmetry ($r/R < 0.4$), respectively,

a conclusion that is supported by numerical simulations based on a Landau–de Gennes free energy. By dispersing the F9-5CB emulsions into glycerol or aqueous solutions of the surfactants SDS or PFOA, droplets with Janus morphologies were formed, with the internal organization of the nematic domains dependent on the specific surfactant type. Interestingly, under condition for which SDS and PFOA generate the same internal configurations of single phase LC droplets, we observed the LC domains of the multiphase droplets to give rise to distinguishable internal organizations. This result reveals that confinement of LCs within multiphase droplets provides new opportunities to differentiate interfacial phenomena that are not distinguishable in single phase LC droplets. We also showed that LC-perfluorocarbon emulsions provide new opportunity to create thermally actuated and dynamically reconfigurable nematic shells by vaporizing the perfluorocarbon core. More broadly, the results reported in this manuscript demonstrate that perfluoroalkane-nematic two-phase systems provide new opportunities to design stimuli-responsive emulsions

The results reported in this paper also generate a range of unresolved questions. For example, our results suggest that F9 dissolved in 5CB, although low in concentration, may change the elastic constants of 5CB to impact the configurations assumed by 5CB under confinement. Additionally, although our results support the proposal that 5CB assumes smectic ordering at the F9 interface, additional studies are needed to fully understand the molecular-level origins of the LC anchoring observed at liquid perfluorocarbon interfaces. Finally, our studies reveal that the expansion and contraction of the F7 cores within HTW shells differ greatly in dynamics. We do not yet fully understand the factors that control these dynamics.

The results presented in this paper also revealed that the liquid F7 cores of the nematic emulsions were superheated by ~80°C prior to transforming to a vapor phase. We envisage that future studies may exploit this superheated state of the perfluorocarbon core in

a range of potentially useful way, such as in microsensors, e.g., by using the selective dissolution of gases in LCs. [217, 236] We also anticipate that the approach demonstrated in this paper can be extended in future studies to other achiral and chiral LC phases, including smectic, cholesteric and blue phases, as well as other perfluorocarbons. Additionally, the reconfiguration of the LC compartment of the emulsion via vaporization of the perfluorocarbon, as demonstrated in our paper, is not limited to core-shell morphologies, but can also be explored in symmetry-broken morphologies, such as Janus droplets. We predict that the interplay of phase transitions between LCs and perfluorocarbon can also be manipulated to form a range of new non-equilibrium LC organizations that reflect the history of heating and cooling of the emulsion systems.

Chapter 7

Topological dereliction in liquid crystal-mediated nano-particle assembly on spherical droplets

7.1 Introduction

Decorating liquid crystal interfaces is the functional principle of biochemical sensors and hierarchical material design. Fundamentally, these devices rely on elastic forces to mediate the directed-assembly of colloids, that in turn generate an interesting portfolio of patterns and geometric arrangements with extraordinary optical properties. [157, 133, 213, 70, 71, 199, 250, 238] The elastic forces originate at regions with low order, topological defects, in a concerted effort to alleviate distortions of the order field. [125, 222, 255, 266, 221, 71] A canonical example is the bipolar droplet, in which a liquid crystal (LC) confined in a spherical cavity is subject to lie tangential to the surface. This restriction leads the system to find a balance between the bulk and surface free energies and results in the emergence of two antipodal surface defects. [**?** 153**?** , 176**?**]

These morphologies are a product of a thermodynamic minimization of free energy densities – at the bulk and surface – that balance the amount of elastic distortions with the preferred alignment of the LC molecules at the surface [**?** 153**?** **?** **?**]. In addition, these forces mediate the assembly of nano-particles, in bulk or at the surface, because locating the particles at the LC defects alleviate some of the natural elastic distortions of

the nematic field [125, 222, 255, 266, 221, 71].

Using a Landau-de Gennes formalism, previous simulations from our group explored the location and assembly of one, two and three half-submerged nano-particles on planar LC micro–droplets. We generated the thermodynamic rational behind the assembly of homeotropic [136] and weakly (anchoring strength $\sim 10^{-4}$ J/m^2) planar [197] anchored particles. These studies served to delineate the nematic forces, the free energy estimate during a defect annihilation and the penalties that occur once the particles are not located in the global minimum. For completeness and to guide the present research, we wish to summarize our findings for two particles: (i) the global minima configuration for two homeotropic or weakly planar particles is to locate each particle in an opposite boojum; (ii) there is a local minima once the two particles are located in a in single boojum; (iii) the free energy difference between the global and local minima is around 1,000 k_BT for the homeotropic particles and order 100 k_BT for the weakly planar particles; and (iv) to move a particle from the local minima to the global minima, an extra defect around the particle must be created. This additional defect penalizes the free energy by several hundreds of k_BT for homeotropic particles, while several tens of k_BT for the weakly planar particles.

The order of the free energy differences and penalties may lead to always direct the assembly of the particles at the antipodal boojums. Simulations with three particles [136, 197] follow that rational: two particles aggregate at one boojum and the other rests at the opposite pole. Therefore, it is natural to think that multiple particles will agglomerate in the boojums to minimize the free energy and one may think that the global minima should be reached given the large values for the free energy penalization. The particle preference for the boojums has been observed experimentally for half-submerged fluorescent polystyrene (PS) nano-particles in a LC bipolar droplet [261]. However, for a constant particle number, the observed configurations do not follow the permutation rules associated with the global free energy minima. On the contrary, several configurations

are observed for constant particle numbers, which motivates the present work. How is it possible that particles do not assembly according to global free energy minima, giving the fact that the free energy penalties are several k_BT units? We suspect that the underlying feature of this degeneration of particle states is a topological dereliction, similarly observed in glass forming systems where the multitude of diverging pathways open the portfolio of metastable arrays [158, 159]. In addition, this phenomenon is also analog to many self assembly processes in biological systems [280, 249].

In this paper, we aim to describe the underlying physics that drive degenerated particle packing of half-submerged nano-particles in an LC bipolar droplet. Opposite to previous reports, the location of the particles are not fixed, avoiding prdetermined particle configurations. We restrict this study to aplanar anchored droplet, with anchoring strength $W_{\parallel} = 1 \times 10^{-3}$ J/m^2, of size $R = 250$ nm and nano-particles with a size of $r_P = 50$ nm. Figure 7.1 shows schematically some physical details of the system of interest. The figure includes the boojum defect arrangement of a pure bipolar droplet and the defects around the particles. We will use homeotropic (purple) and planar (blue) anchored particles and we will vary their number up to ten particles per droplet. To relax the free energy functional without fixed particle locations, a novel Monte Carlo (MC) sampling algorithm is presented, where a Metropolis sampling criteria for the alignment tensor [8, 6] and the position of the particles is adopted.

7.2 Thermodynamic model and relaxation method

The LC order is described in terms of the local alignment tensor $\mathbf{Q}(\mathbf{x})$, defined as the second moment of the molecular orientational distribution function, $\psi(\mathbf{u}, \mathbf{x}, t)$, $\mathbf{Q}(\mathbf{x}) = \int (\mathbf{uu} - \frac{\delta}{3})\psi(\mathbf{u}, \mathbf{x}, t) d\mathbf{u}$, where $\mathbf{u}(\mathbf{x})$ is the ensemble average of molecular orientations. At each configuration of the alignment tensor field, $\mathbf{Q}(\mathbf{x})$ is assigned a probability proportional to the Boltzmann factor $\exp\left[-\beta F(\mathbf{Q}(\mathbf{x}))\right]$, where $\beta^{-1} = k_B\hat{T}$, k_B is the Boltzmann

constant and $\hat{T}$ is a fluctuating artificial temperature.

The free energy functional is composed of three contributions: a short-range Landau polynomial expansion of the invariants of $\mathbf{Q}(\mathbf{x})$ that describes the isotropic-nematic (IN) transition, a long-range free energy density that penalizes any elastic distortions, and a harmonic potential that imposes a preferred alignment at the interfaces. It is written as,

$$F(\mathbf{Q}) = \int d^3\mathbf{x} \left[\frac{A}{2}\left(1 - \frac{U}{3}\right) \mathrm{tr}(\mathbf{Q}^2) - \frac{AU}{3}\mathrm{tr}(\mathbf{Q}^3) + \frac{AU}{4}\mathrm{tr}(\mathbf{Q}^2)^2 + \frac{L_1}{2}\frac{\partial Q_{ij}}{\partial x_k}\frac{\partial Q_{ij}}{\partial x_k} \right] \tag{7.1}$$
$$+ \oint d^2\mathbf{x} \left[\frac{W}{2}(\mathbf{Q} - \mathbf{Q}_\perp)^2 + \frac{W}{4}\left(\mathbf{Q} : \mathbf{Q} - S^2\right)^2 \right],$$

where A sets the energy density scale, the dimensionless parameter U determines the IN transition, L is the elastic constant related to the material elastic moduli, and W represents the strength of the surface anchoring. Additionally, S is the scalar order parameter, and at the interface $\mathbf{Q}$ is projected to the surface with normal vector $\boldsymbol{\nu}$ through $\bar{\mathbf{Q}}_\perp = \mathbf{p} \cdot \mathbf{Q} \cdot \mathbf{p}$ with $\bar{\mathbf{Q}} = \mathbf{Q} + S\boldsymbol{\delta}/3$ and $\mathbf{p} = \boldsymbol{\delta} - \boldsymbol{\nu}\boldsymbol{\nu}$. Details of the free energy contributions can be found in our previous works [7, 9, 137, 182**?**]. The material parameters define two characteristic length scales: the nematic coherence length $\xi_N = \sqrt{L/A}$ and the surface extrapolation length $\xi_S = L/W$.

To thoroughly explore configuration space, we have devised a technique that incorporates a stochastic approach for uncovering kinetically-trapped states at the continuum scale. This technique combines two relaxation methods: a theoretically-informed Monte Carlo relaxation, and a traditional Ginzburg-Landau relaxation. By integrating these methods, we can efficiently navigate relatively stable regions of configuration space while also considering the potential feasibility of rare configurations. To implement this approach, we first identify suitable variables that facilitate our exploration of configuration space.

The hybrid relaxation requires that the alignment field be sampled uniformly. This is

necessary given that the eigenvalues of $\mathbf{Q}$ are bounded by $S \in [-\frac{1}{2}, 1]$ and $\eta \in [-\frac{1}{3}(1 - S), +\frac{1}{3}(1 - S)]$. Its corresponding eigenvectors, $\mathbf{n}$ and $\mathbf{n'}$, define an orthonormal basis $\{\mathbf{n}, \mathbf{n'}, (\mathbf{n} \times \mathbf{n'})\}$ for the LC orientations. Therefore, attempting to form Markov chains for changes in S, η, $\mathbf{n}$ or $\mathbf{n'}$ would require cumbersome schemes that can break the detailed balance. We thereby express $\mathbf{Q}$ in terms of an orthonormal basis that obeys its symmetric and traceless characteristics. [98, 16, 17]

The $\mathbf{Q}$ tensor can then be rewritten as:

$$\mathbf{Q}(\mathbf{x}, t) = \sum_{\nu}^{5} a_\nu(\mathbf{x}, t)\, \mathbf{T}^\nu, \tag{7.2}$$

where the orthonormal basis is defined by five tensors:

$$\begin{aligned}
\mathbf{T}^1 &= \sqrt{3/2}\,[\mathbf{zz}]^{\mathrm{ST}} = \sqrt{3/2}\left(\delta_{i3}\delta_{j3} - \delta_{ij}/3\right), \\
\mathbf{T}^2 &= \sqrt{2}\,[\mathbf{xy}]^{\mathrm{ST}} = \sqrt{2}\left(\delta_{1i}\delta_{2j} + \delta_{2i}\delta_{1j}\right)/2, \\
\mathbf{T}^3 &= \sqrt{2}\,[\mathbf{xz}]^{\mathrm{ST}} = \sqrt{2}\left(\delta_{1i}\delta_{3j} + \delta_{3i}\delta_{1j}\right)/2, \\
\mathbf{T}^4 &= \sqrt{1/2}\,(\mathbf{xx} - \mathbf{yy}) = \sqrt{1/2}\left(\delta_{1i}\delta_{1j} - \delta_{2i}\delta_{2j}\right), \\
\mathbf{T}^5 &= \sqrt{2}\,[\mathbf{yz}]^{\mathrm{ST}} = \sqrt{2}\left(\delta_{2i}\delta_{3j} + \delta_{3i}\delta_{2j}\right)/2,
\end{aligned} \tag{7.3}$$

where $\mathbf{x}$, $\mathbf{y}$ and $\mathbf{z}$ form the $\mathfrak{R}^3$ basis, δ_{ij} is the Kronecker delta and $[\mathbf{A}]^{\mathrm{ST}}$ is the symmetric-traceless projection operation. Because the $\{\mathbf{T}^m\}$ basis is orthonormal, it ensures that the five scalar components a_ν of the alignment tensor are simple projections: $a_\nu = \mathrm{tr}(\mathbf{Q}\mathbf{T}^\nu)$. In this way, the $\mathbf{a}$ set is linearly independent and equivalent to $\mathbf{Q}$ in such a way that eq. 7.1 can be rewritten in terms of five independent scalars a_ν.

The LC domain is discretized into a uniform mesh with M nodes. A tensor $\mathbf{Q}_i$ is assigned to each i-th node and the free energy functional is calculated numerically from approximate values of $\mathbf{a}(\mathbf{x})$ and $\nabla\mathbf{a}(\mathbf{x})$. A second-order finite difference scheme is used to approximate gradients and to integrate the free energy functional; the mesh is selected in

such a way that the LC characteristic length scales, ξ_N and ξ_S, are resolved.

The first component of our hybrid relaxation is the artificial annealing akin to the method from our previous works. [9, 7, 182**?**] In this instance, updates to the **Q** tensor and the NP positions are proposed and accepted according to a Metropolis criteria [**? ?**]. During the relaxation, we propose a new configuration "n" from an old configuration "o" with a probability $P_{\text{prop}}(\text{o} \rightarrow \text{n})$, which is accepted according to:

$$P_{\text{acc}}(\text{o} \rightarrow \text{n}) = \min\left[1, \exp(-\beta \Delta F)\right], \tag{7.4}$$

where $\Delta F = F(\mathbf{Q}(\text{n})) - F(\mathbf{Q}(\text{o}))$ is the energy difference between the new and the old configuration.

During the relaxation of the alignment tensor, a node is selected at random, in the bulk or on the interface, and an MC move is attempted by changing $\mathbf{a}(\mathbf{x})$ according to:

$$a_{\mu,\text{n}}(\mathbf{x}) = a_{\mu,\text{o}}(\mathbf{x}) + \bar{\delta}_{\mu}(\lambda - 0.5), \tag{7.5}$$

where "n" and "o" indicate the new and old configurations, μ is chosen randomly from 1 to 5 and λ is a uniform random number between $[0, 1]$. $\bar{\delta}_{\mu}$ is the maximum allowed change of a_{μ} and it is adjusted periodically during the minimization to achieve a 30% average acceptance rate. For each MC move, the bounds of **Q** are enforced. Details of the MC relaxation can be found in our previous publications [7, 9].

The geometrical features of the NP cluster are not known *a priori*. Modeling these events and assemblies requires changing the position of each NP $\mathbf{x_p}$ along the relaxation of **Q**. In the occurrence of a NP displacement, a localized Ginzburg-Landau (GL) relaxation is carried out in the vicinity of the new and old particle locations. The intention is to avoid quenched configurations, and prevent premature rejection of the trial move. We use the fact that a GL relaxation is characterized by a "quick" adjustment of the eigen-

values of **Q**, aiding the relocation of the particles. After the localized GL has converged, typically after several LC relaxation times, the “new" particle position is fixed, and the Metropolis criteria is computed before carrying on with the next Monte Carlo cycle.

Two modes for NP relocation are proposed: a short-range and a long-range particle relocation (see Fig. **??**). The particle is subject to be half-submerged on the droplet surface, and its position is defined by $\mathbf{x}(r_p, \theta_p, \phi_p)$. Therefore, a randomly selected particle, p, is displaced over a spherical shell according to:

$$\begin{aligned} \theta_{p,\mathrm{n}} &= \theta_{p,\mathrm{o}} + \delta_\theta(\xi_1 - 0.5), \\ \phi_{p,\mathrm{n}} &= \phi_{p,\mathrm{o}} + \delta_\phi(\xi_2 - 0.5), \end{aligned} \tag{7.6}$$

where “n" and “o" indicate the new and old particle locations and where ξ_1 and ξ_2 are uniformly distributed random numbers between $[0, 1]$. Accordingly, δ_θ and δ_ϕ are the maximum allowed angular displacements, fixed to be $\delta_\theta \approx 0.11\pi$ and $\delta_\phi \approx 0.11\pi$. We determined that the localized GL relaxation must be done for nodes that are inside a sphere with a cut off radius R_c from the particle. We found heuristically that $R_c = 1.5r_P$ is enough to create acceptable configurations.

For the “long-range" particle displacement, attempting configurations that would otherwise will not be observed, the entire range for $\theta \in [0, \pi]$ and $\phi \in [0, 2\pi]$ are explored. The new position is obtained randomly from the θ_p and ϕ_p domains according to:

$$\theta_{p,n} = \pi\xi_4, \quad \phi_{p,n} = 2\pi\xi_5, \tag{7.7}$$

where ξ_4 and ξ_5 are uniformly distributed random numbers between $[0, 1]$. During a “long-range" relocation, we check for overlapping particles as well.

For completeness, recall that the Ginzburg-Landau relaxation consists on minimizing

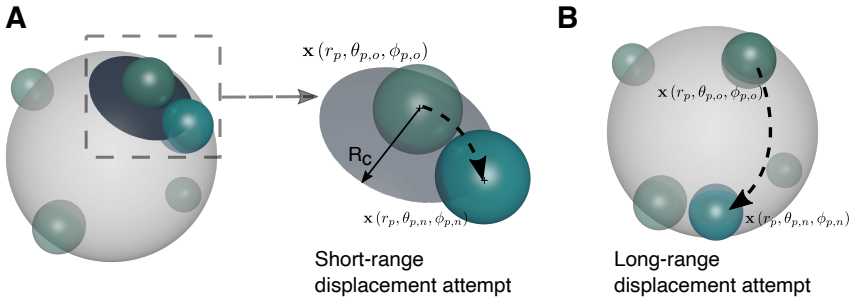

Figure 7.1: Schematic for the relocation of NP on the LC droplet surface.

the free energy by solving the evolution equation for $\mathbf{Q}$,

$$\frac{\partial \mathbf{Q}}{\partial t} = -\frac{1}{\gamma}\left[\frac{\delta F}{\delta \mathbf{Q}}\right]^{\mathrm{ST}}, \tag{7.8}$$

where γ is the LC rotational diffusion coefficient, and defines the LC relaxation time as $\tau = \gamma \xi_N / L$. The Volterra derivatives are defined as follows,

$$\frac{\delta F}{\delta \mathbf{Q}} = \frac{\partial F}{\partial \mathbf{Q}} - \frac{\partial}{\partial \mathbf{x}} \cdot \frac{\partial F}{\partial \nabla \mathbf{Q}}. \tag{7.9}$$

The model system employed in this study consists of a bipolar droplet with a radius of $R = 250$ nm, adorned with nanoparticles (NPs) of radius $r_P = 0.2R = 50$ nm. The material properties utilized correspond to 4'-pentyl-4-cyanobiphenyl (5CB), where $A \approx 1 \times 10^5$ J/m^3 and $L = 5.11$ pN, yielding $\xi_N = 7.15$ nm. The droplet surface exhibits strong degenerate planar anchoring characterized by a strength of $W = 1 \times 10^{-3}$ J/m^2. In the Landau-de Gennes framework, isotropic to nematic phase transitions occur in bulk systems at $U = 8/3$. For these simulations $U = 5$, resulting in a bulk scalar order parameter $S \approx 0.76$. The approximation of all order fields and their gradients is achieved using a finite differences scheme, with uniform meshes accommodating the spheres of sizes r_P. The typical meshes employed in these simulations range from $1 - 2 \times 10^6$ nodes. Artificial annealing is performed over an average of 1×10^6 MC cycles. [7, 9].

7.3 Results

To begin, we determine the energetic barrier associated with the assembly of two particles are partially submerged in an LC droplet surface. As previously established, the boojums situated at the poles of the bipolar droplet represent regions of elevated elastic energy, which attract NPs to alleviate spatial distortions of the order field. The system's symmetry simplifies the calculation of the free energy since it only depends on the angle θ between the two NPs. Through Ginzburg-Landau relaxations, we compute the free energy contributions as one particle remains fixed on one pole, while the second particle approaches, and the interparticle distance is the arc length θR. At $\theta = 180°$each particle resides at one pole, serving as the reference state. At $\theta = 30°$, the particles have assembled. Figure 7.2A illustrates the total free energy as a function of the particle separation (θ) for homeotropic and planar anchored particles.

The results presented in Fig. 7.2A for homeotropic particles align with previous computational and experimental reports. [136, 197] These investigations have demonstrated that strong homeotropic anchoring prompts the assembly of NPs at the poles of the bipolar droplet. In this scenario, the LC orientation near the NP mirrors the order field at the boojum's center. When the NP occupies the boojum position ($\theta = °, 180°$), the defect is substituted by the NP, minimizing the elastic energy. The energetic barrier for an NP to transition from one pole to the other is approximately 1×10^3 k_BT and occurs at $\theta = 90°$. This energetic cost is associated with the regeneration of one boojum at the pole, while a half-Saturn ring defect envelops the particle at the equator (see Fig. 7.1). The same behavior occurs for weaker anchoring conditions, resulting in a reduced energetic barrier of 300 k_BT.

In contrast to homeotropic NPs, which exhibit equivalence to hedgehog defects possessing a topological charge of +1, planar NPs with degenerate anchoring resembling an isotropic region. They induce orientations within the plane without incurring energetic

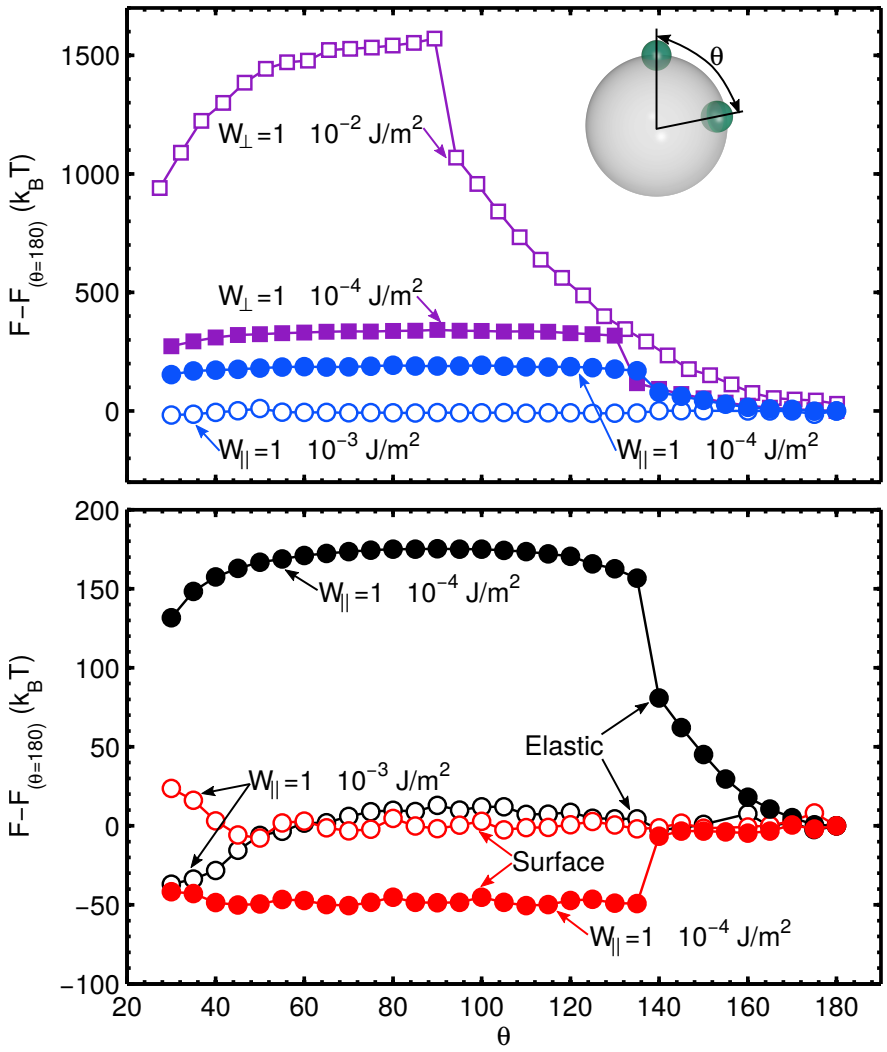

Figure 7.2: Free energy difference as a function of the angle θ between two NPs on the surface of a bipolar droplet. A) Total free energy for planar particles (blue circles) and homeotropic particles (purple squares) with anchoring strength $W = 1\times10^{-2}$ J/m^2 (open symbols) and $W = 1\times10^{-4}$ J/m^2 (closed symbols). B) Elastic (black) and surface (red) free energy for planar particles with anchoring strength $W = 1\times10^{-3}$ J/m^2 (open symbols) and $W = 1\times10^{-4}$ J/m^2 (closed symbols).

penalties for in-plane rotation.

Planar NPs with strong anchoring experience minimal penalties when moving across the droplet's surface, whereas weakly anchored NPs encounter an energetic barrier of approximately $\sim$ 150 k_BT. Figure 7.2B provides an analysis of the elastic and surface free energies associated with planar NPs, offering deeper insights. The matching anchoring strength between planar NPs and the droplet surface ensures that the NP's presence in various locations has minimal disruption on the order field. Irrespective of their position relative to the boojums, the NP is consistently encapsulated by a hemisphere defect. However, when the NP anchoring is lower, roughly one order of magnitude less than that of the droplet surface, the NP's presence introduces local order disturbances, akin to an isotropic inclusion with an energetic penalty.

Based on the results from Fig. 7.2, we have established that, in general, NPs tend to reside on the poles to minimize the global free energy. This observation supports the notion that bipolar droplets serve as a good platform to detect the presence of colloidal units and amplify the response up to the visible scale. With the consideration of larger NP ensembles, we incorporate the conditions derived from experimental results [261] to perform hybrid relaxations of the computational systems.

Simulations were set up for a bipolar droplet with N homeotropic particles on the surface with anchoring strength $W = 1{\times}10^{-2}\,\mathrm{J/m^2}$, and the results are reported in Fig. 7.3. The liquid crystal (LC) system was initialized in an isotropic configuration, while the non-overlapping random placement of the NPs was ensured across the surface. Through the implementation of hybrid relaxation, both the development of nematic order and the assembly of NPs were observed. To capture a diverse range of configurations and emulate realistic scenarios, we employed 20 replicas of each system and quantified the frequency of observed geometric arrays.

Figure 7.3A shows the free energy difference for each scenario with N nanoparticles,

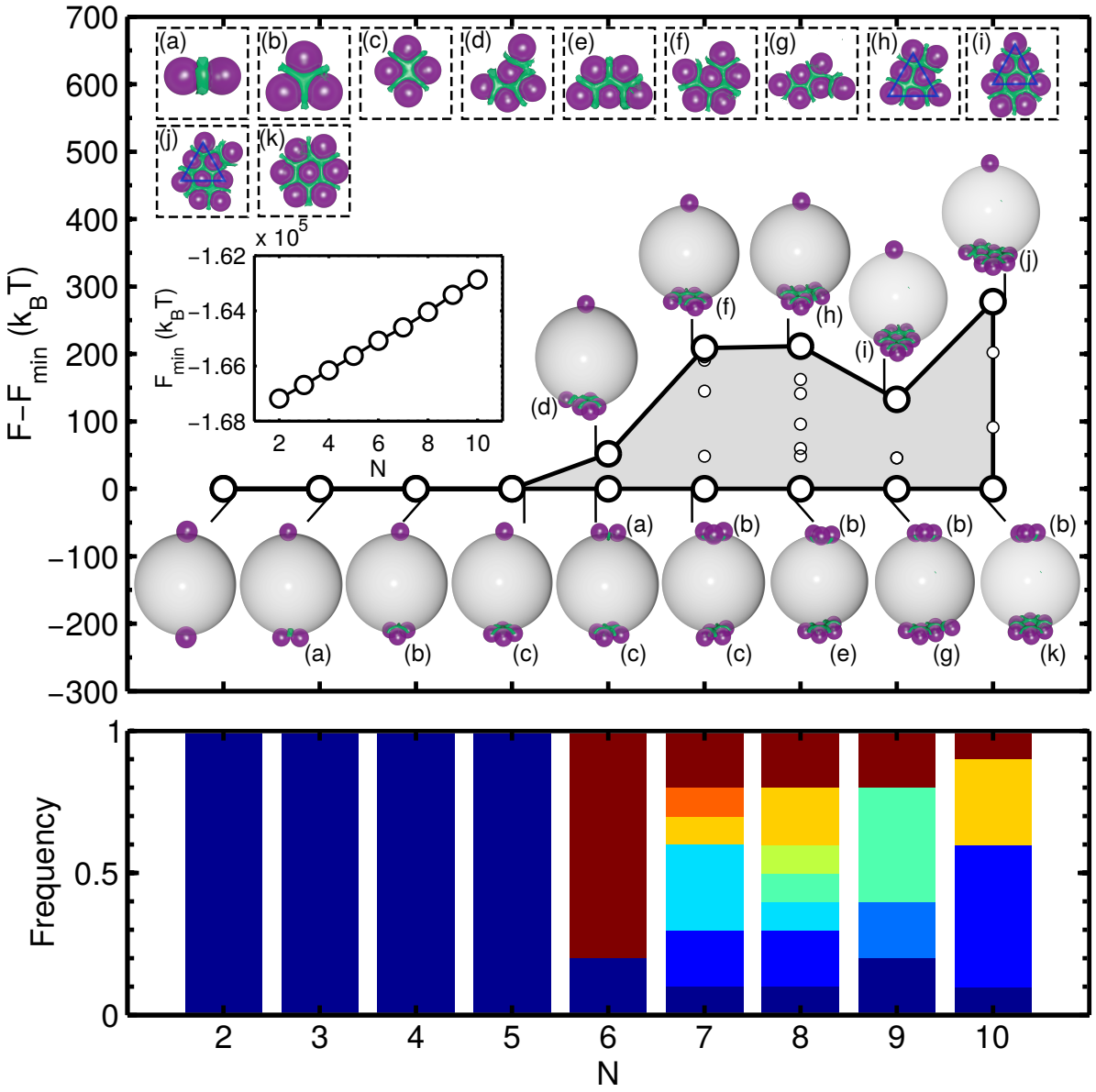

Figure 7.3: Free energy difference for homeotropic particles with $W = 1 \times 10^{-2}$ J/m^2 on a bipolar droplet as a function of the number of particles N. The reference values are the minimum free energy for each N, included in the insert. Small round markers indicate metastable configurations, while big markers represent configurations with the maximum and minimum free energies. Labels (a)-(k) correspond to the inserts that show the different geometrical arrays observed. The frequency of appearance for each configuration is shown in the color bar at the bottom. The blue color corresponds to the global minima while the red is for the maximum energy configuration. Intermediate colors are for the configurations in between and the size of the color stripe is proportional to the frequency.

taking as reference the minima for each case as depicted in the inset. The baseline for the free energy follows a linear trend with the number of NPs, consistent with the volume displaced by the half-submerged particle and the addition of half-Saturn ring defects when the particles assemble. Notably, for the case of $N = 2$, our hybrid relaxation approach confirms the previous findings [136] that each particle occupies a boojum position at equilibrium. Moving to $N = 3$, a $2:1$ distribution of particles on the poles is observed, with the dimer stabilized by a half-Saturn ring defect. As the number of nanoparticles increases, the pole distribution deviates from equal partitioning, following an $N-1:1$ pattern. The most populated pole exhibits closed-packing arrangements accompanied by a nematic defect at the junction.

We also observe that for $N \leq 5$ all configurations are non-degenerate. For these cases, one particle rests at a boojum while the other ones show a tendency to aggregate at the opposite pole, forming a close-packed-like structure and a new LC defect. These arrangements are shown in the insets of Figure 7.3, where the green isosurfaces represent the LC defects. Once two homeotropic particles encounter, a half Saturn ring forms between them, as shown for $N = 3$ in insert (a). As more particles aggregate, the defect takes a shape according to the particles junctures and fills the empty spaces between them.

For systems with $N > 5$, the sheer multitude of potential geometric arrangements prevents the clusters from converging to a single conformation when allowed to assemble from a random configuration. In fact, the free energy surface is bifurcated, and energetic barriers of the orders of $\sim 10 - 100$ k_BT that effectively separate distinct metastable states. In light of the relaxation process employed, we aptly categorize these assemblies as kinetically-trapped states. Notably, unlike traditional relaxation techniques employed at the continuum scale, the formation of nanoparticle (NP) clusters is not predetermined at the start of the simulation. Additionally, we compute the frequency with which these clusters appear and capture their diversity, as depicted in Figure 7.3B. In this representa-

tion, each bar's color corresponds to the magnitude of the energy difference (ΔF), where blue denotes the global minima for the given system size N, while red represents the configuration with the maximum energy. Intermediate colors reflect the configurations in between, and the width of each stripe signifies the frequency of occurrence, as ordered by their appearance as denoted by the small markers in Figure 7.3A. For a more detailed exploration of the different particle arrangements associated with these kinetically-trapped states, we provide close-up views in the Supplementary Information (SI).

Notice that for the degenerate states, the configuration of maximum free energy is that one with a particle in one boojum and $N-1$ particles in the opposite side. These particles form hexagonal, triangular or diamond-shaped structures, as labelled and drawn in the inserts. On the other hand, in the states of minimum energy, the particles tend to arrange more equitably with more than 2 particles in each pole. Intermediate local minima configurations consist of redistributed arrays of particles, *e.g.* for $N = 10$ particles sort in the following proportions: $9:1, 8:2, 7:3$, where the triangular or hexagonal patterns are a determining factor of its frequency of occurrence.

The results for homeotropic particle sets yields significant insights into the underlying rationale for topological dereliction. It becomes evident that only a limited number of particles conform to the energetic principles governing defect relaxation within the LC system. It is important to recall that the energies associated with defect annihilation are on the order of $\sim$ 1000 k_BT units, as illustrated in Figure 7.2. However, as the particle count increases, elastic distortions alone cannot solely dictate the self-assembly of particles. The role of entropy becomes increasingly prominent, driving local entrapment phenomena. During the minimization process, if a particle becomes "trapped" on one side of the droplet, the energy cost of relocating it to the opposite pole amounts to approximately $\sim$ 500 k_BT. Consequently, the expanding array of particle arrangements across the droplet surface during minimization engenders an entropic frustration that deviates from

the global minima, resulting in different particle arrangements. Through our simulations, we quantify the energy gaps between these arrangements, which amount to several k_BT units, rendering them impervious to particle diffusion or thermal fluctuations that would otherwise disrupt their stability.

While our findings successfully capture the diverse range of NP arrangements on the surface of the droplets, it is evident that not all conceivable arrays have been thoroughly explored. For instance, when considering $N = 6$, an equilibrium configuration with an even distribution of 3 : 3 NPs was not attained. Instead, the packing of 3 and 4 NPs gave rise to hexagonal structures. Interestingly, the formation of linear NP chains at the poles, as reported in experimental studies [261], eluded observation in our continuum simulations. It is crucial to acknowledge that the computational expense associated with hybrid relaxation renders it impractical to exhaustively explore all possible arrays. Rather, this approach offers valuable insights into the accessibility of specific configurations. Notably, the global minima, representing the least frequently observed state, underscores the roughness of the free energy landscape for large NP clusters.

Based on the insights gained from our continuum simulations, we put forth effective potentials aimed at enhancing our exploration of the NP assembly landscape. In this particular scenario, it is evident that the NPs experience two distinct interactions when residing on the droplet's surface. The first interaction is anisotropic in nature, governing their attraction towards the poles with the purpose of annihilating the boojum defect. Subsequently, once one particle becomes adsorbed at the defect, the remaining particles undergo a short-range interaction driven by the concerted effort to minimize the size of the half-Saturn ring defect formed between them. To capture the essence of these interactions, we devise a simplified model, leveraging Molecular Dynamics simulations and employing enhanced sampling techniques to characterize the barriers impeding the efficient packing of NPs.

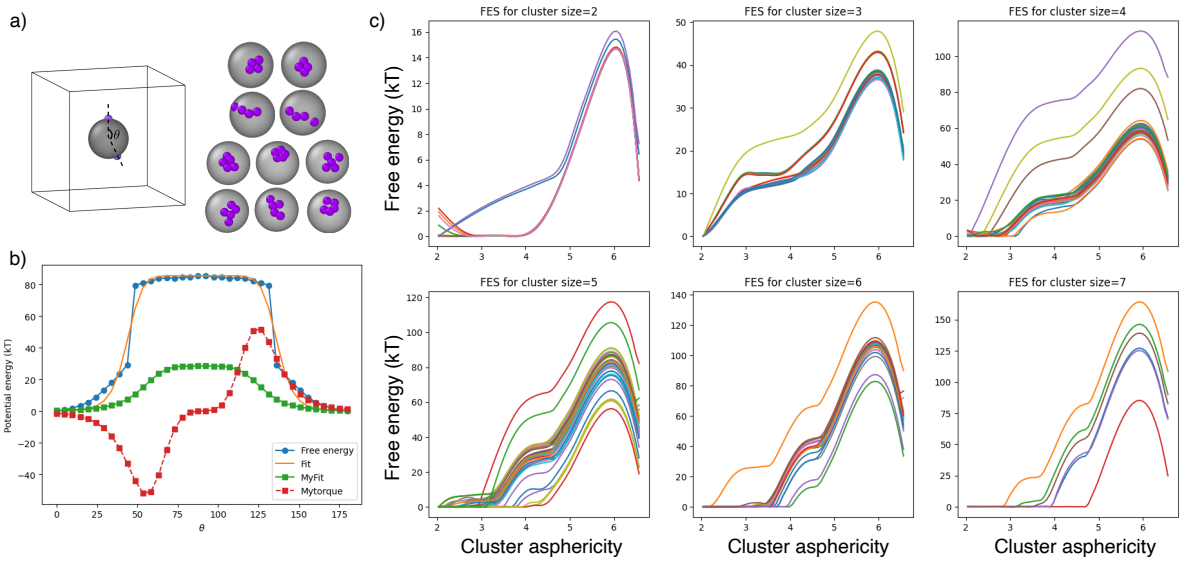

Figure 7.4: Simplified representation of the assembly of homeotropic colloids on the surface of a bipolar droplets. a) Different geometrical packing of particles on the pole of the droplet as the cluster size is bigger. b) Potential energy extracted from continuum simulations, and the effective potential implemented in the molecular simulations. c) Free energy surface as a function of cluster asphericity, as reported by PySAGES.

The simplified system comprises particles of size σ, exhibiting an attractive interaction with a larger particle of size 2.5σ through a Gaussian wall potential. Additionally, two ghost particles are strategically placed at the poles, enforcing an angular potential interpolated from the free energy landscape depicted in Fig. 7.2A. To account for the interparticle interactions, we harness the information amassed from our continuum simulations. Specifically, we extract the positions of the NPs within the clusters and compute the radial distribution function. By performing a Boltzmann inversion, we obtain an effective interparticle potential, from which we determine the depth and location necessary to implement a Morse potential. Following this parametrization, we conduct accelerated simulations utilizing HOOMD-blue and Adaptive Biasing Force (ABF), implemented in PySAGES. This concerted approach allows us to efficiently explore the underlying free energy surface and unravel the fundamental aspects of NP assembly in terms of the asphericity of the cluster. Results from this simplified model can be found in fig. 7.4

We continue our exploration of NP assembly by following the hybrid relaxation of planar NPs on a bipolar droplet. As we introduced in Fig. 7.2B, planar NPs have a reverse effect when it comes to altering the nematic order field in the droplet. In that manner, strongly anchored NPs ($W = 1{\times}10^{-3}\,\mathrm{J/m^2}$) encounter minimal penalties when displacing across the droplet surface whereas moderately anchored NPs ($W = 1 \times 10^{-4}\,\mathrm{J/m^2}$) have a preference to staying at the poles without annihilating the defects.

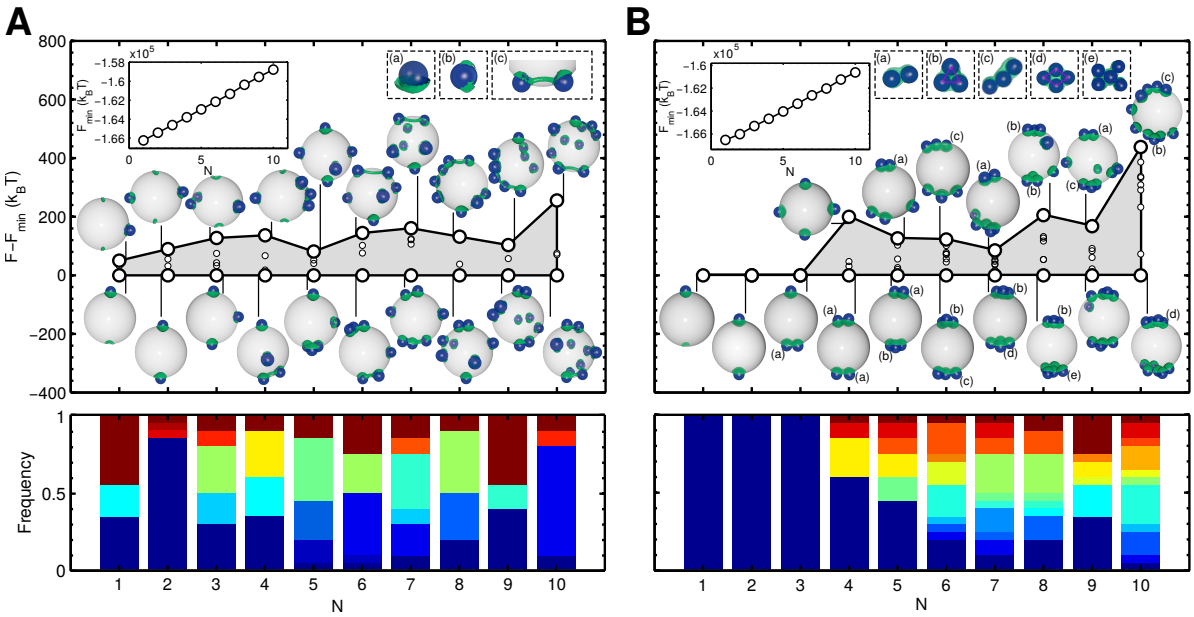

Figure 7.5: Free energy difference for planar particles with anchoring strengths: (A) $W = 1{\times}10^{-3}\,\mathrm{J/m^2}$ and (B) $W = 1{\times}10^{-4}\,\mathrm{J/m^2}$. The reference values are the minimum free energy for each N, included in the insert. Small round markers indicate metastable configurations, while big markers represent configurations with the maximum and minimum free energy. For (A), the inserts show the defect structure exhibited by nanoparticles positioned on (a) the boojum, (b) the equator and (c) a bridge defect between two nanoparticles near the boojum. For (B), the labels (a) to (e) are assigned to the most characteristic assembly of nanoparticles pictured in the inserts.

Figure 7.5A shows the free energy difference, the frequency of appearance and representative particle arrangements for strongly anchored NPs $W = 1 \times 10^{-3}\,\mathrm{J/m^2}$. The anchoring strength matches that of the LC-droplet interface, effectively freeing the particles from assembling at a predetermined site. As a consequence, the range of possible particle arrangements becomes more limited. We observe three distinct scenarios: (i) the

planar particle may be located at the boojum, generating a half-shell defect (insert (a) in Fig. 7.5(A)); (ii) the particle is located anywhere else on the surface and the defect does not surround the complete hemisphere that is submerged but instead forms two bands that surround the particle (insert (b) in Fig. 7.5(A)), and (iii) when two particles aggregate near the boojum, there is a bridging defect between the two shell defects that join both particles (insert (c) in Fig. 7.5(A)). This bridge is more notorious in configurations with higher free energy. It is worth noting that configurations with maximum free energy correspond to scenarios where particles are dispersed throughout the droplet surface, lacking any discernible order or clustering. Additionally, the wide variety of arrays is evidenced by the different bands obtained in the frequency of observation in Fig. 7.5A. A detailed table of the configurations observed and their corresponding ΔF are provided in the SI.

For the case of lower anchoring strength, see Fig. 7.5B, the behavior resembles that of the homeotropic particles. Small sets of particles are found to assemble near the boojums, and once there, the particles form close-packed arrays. The bridge-like defect is no longer observed. Moreover, the free energy surface bifurcates at $N = 4$ indicating that the onset of entropic frustration hampers the system from finding the global free energy minima. These observations correspond to previous findings using traditional Ginzburg-Landau relaxations. [197] A remarkable difference, however, is that in the states of maximum energy, some particles can be found at the equator or near it. For the intermediate states, particles form close-packed-like structures as well, and the full table of geometric arrays can be found in the SI. The large sets become increasingly difficult to sample and differentiate due to the large number of possible geometric arrays. This is evidenced in the increasing number of metastable states, as represented in the frequency plot.

The development of a simplified MD model proved challenging for the case of planar particles, primarily due to anomalous behaviors observed during continuum simulations. Notably, the interparticle interactions exhibited a longer range only when the particles

were in close proximity to the poles, resulting in the formation of the bridge defect. Conversely, when the particles were positioned near the equator, a distinct repulsive behavior was observed, hindering their assembly.

Furthermore, the clusters that formed at the poles exhibited a relatively smaller size, rendering it difficult to accumulate sufficient statistical data for precise Boltzmann inversions that could faithfully reproduce the results obtained from continuum simulations. This stood in contrast to the case of homeotropic particles, where this approach was successfully employed. These peculiarities highlight the intricate nature of planar NP assembly on bipolar droplets, necessitating further investigations and refinements to capture the nuanced interparticle interactions and dynamics accurately.

Following our results on the assembly of homogeneous sets of nanoparticles, we continue the discussion with the assembly of mixed sets decorating the bipolar droplet. First, we present the assembly of NP sets composed by the ratio between homeotropic and planarly anchored particles $N_{\mathrm{H}} : N_{\mathrm{P}} = [2:2, 2:3, 3:3, 3:4, 4:4, 4:5, 5:5]$ with anchoring conditions $W = 1 \times 10^{-3}$ J/m^2 and $W = 1 \times 10^{-4}$ J/m^2. Figure 7.6 shows the free energy difference, the frequency of appearance and the particle configurations at the global and higher energy local minima.

In systems with strong anchoring conditions, $W = 1 \times 10^{-3}$ J/m^2, (Fig. 7.6(A)) bifurcation of the free energy landscape emerges as a result of the assembly dynamics of the homeotropic particles. Energetically driven, these particles exhibit a strong propensity to accumulate at the poles of the droplet, while the planar particles remain around the equatorial region, avoiding assembly. This intriguing behavior represents a juxtaposition of the two assembly scenarios discussed previously, offering a pathway to engineer particle segregation through the deliberate design of anchoring conditions.

Furthermore, the clusters formed by the homeotropic particles display intriguing hexagonal packing arrangements, reminiscent of the patterns observed in the homogeneous

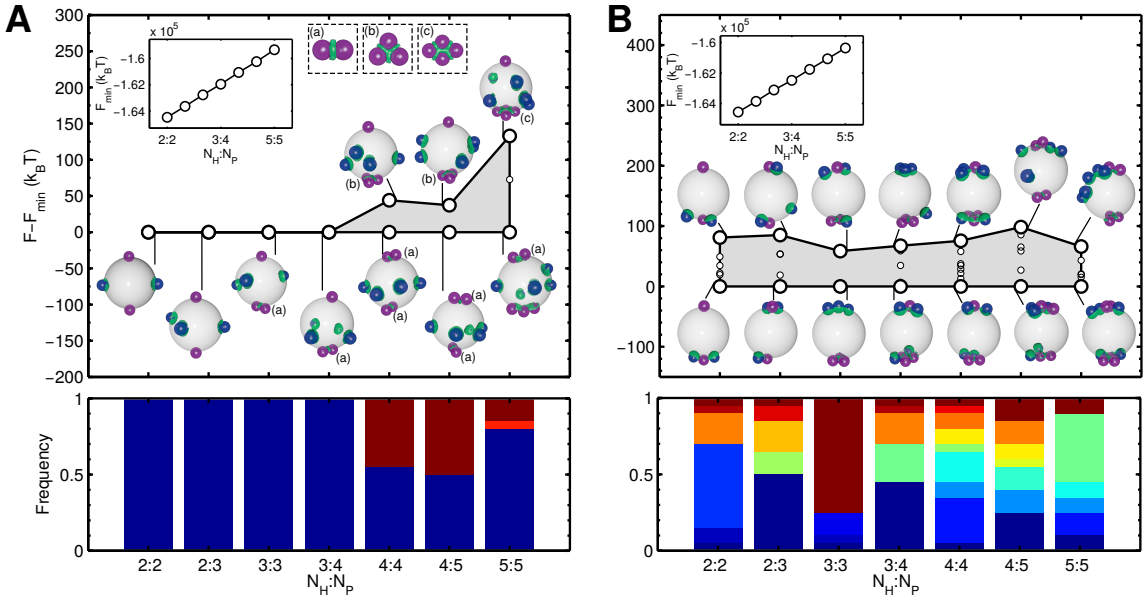

Figure 7.6: Free energy density difference for a heterogeneous set of particles with anchoring strength (A) $W = 1 \times 10^{-3}$ J/m^2 and (B) $W = 1 \times 10^{-4}$ J/m^2, as a function of the number ratio of homeotropic (N_H, in purple) to planar (N_P, in blue) particles. For (A), the labels (a)-(c) indicate the configuration adapted by homeotropic particles and each is zoomed in the inserts where defects (green) are observed. The frequency of appearance for each configuration is shown in the color bar at the bottom. The blue color corresponds to the global minima while the red is for the maximum energy configuration. Intermediate colors are for the configurations in between and the size of the color stripe indicates the frequency.

particle sets. These kinetically trapped states, characterized by energetic barriers of approximately $\sim 10 - 100\ k_BT$, mirror the robustness and complexity exhibited in the previous cases.

When we decrease the anchoring strength of the NPs to $W = 1\times10^{-4}\ J/m^2$ (Fig. 7.6(B)) a notable shift in the assembly behavior occurs, hindering the clear segregation of nanoparticles based on their anchoring type. Instead, both types of nanoparticles become attracted to the pole region. In these systems, the configurations with the lowest energy exhibit clusters where the homeotropic particles occupy the central region, while the planar particles surround them. On the other hand, systems with higher free energy showcase a scattered distribution of planar nanoparticles across the surface of the droplet. This observation highlights the diverse array of nanoparticle clusters that can emerge under these conditions. Furthermore, the relatively small magnitude of the free energy difference (ΔF) suggests that planar particles possess higher mobility and play a significant role in the observed topological dereliction phenomena.

Our last scenario involves varying the proportion of homeotropic to planar particles in a set of 10 NPs, from $N_H : N_P = 1 : 9$ to $N_H : N_P = 9 : 1$. As seen in Fig. 7.7, the energetic gap between the most stable and least stable configuration varies. For systems with a greater number of planar particles, the energetic gap is between 300 k_BT and 480 k_BT. States with greater free energy involve the localization of all planar particles at one pole, while minimum free energy is achieved by planar particles surrounding the assembled homeotropic particles. Intermediate states often exhibit planar particles roaming around the equator. For systems with a majority of homeotropic particles, we notice that the energetic gap is reduced and varies between 80 k_BT and 200 k_BT. The difference between intermediate states is related to the multiple assemblies of the homeotropic particles at the two boojums with planar particles surrounding them. It suggests that the homeotropic particle shifting and rearrangement is enhanced by the presence of planar particles. A

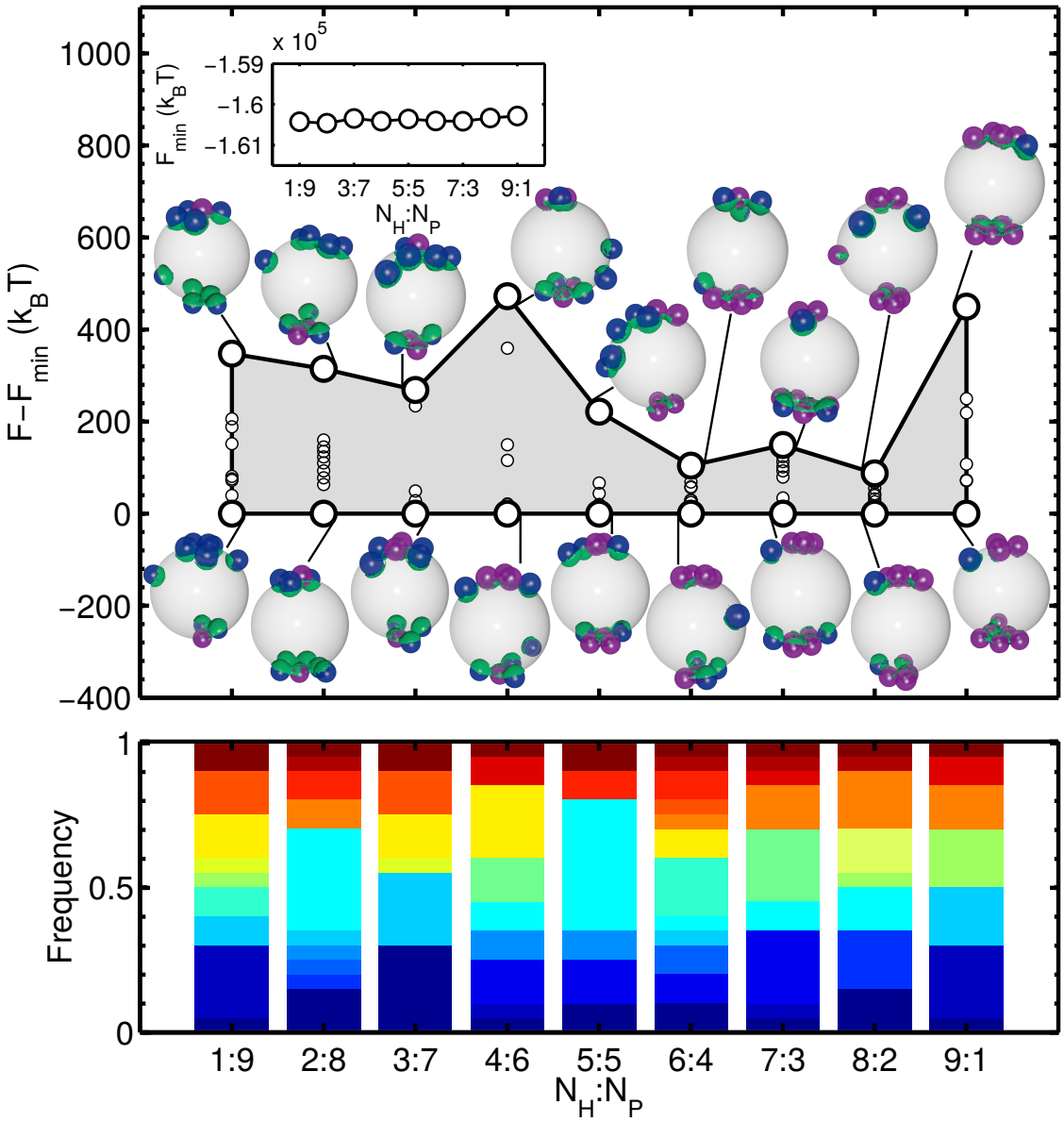

Figure 7.7: Free energy density difference for $N = 10$ varying the number ratio of homeotropic (N_H, in purple) to planar (N_P, in blue) particles, with anchoring strength $W = 1 \times 10^{-4}$ J/m^2. Droplet inserts correspond to the states with maximum and minimum free energy density states, with the defects drawn in green. Small round markers indicate the free energy density of metastable states. The frequency of appearance for each configuration is shown in the color bar at the bottom. The blue color corresponds to the global minima while the red is for the maximum energy configuration. Intermediate colors are for the configurations in between and the size of the color stripe indicates the frequency.

considerable increase in the free energy difference is observed for the case $N_H = 9$. The behavior of homeotropic particles in the states pictured in Fig. 7.7 follow the same assembles as exhibited by configurations with the minimum and maximum free energy in Fig. 7.3.

7.4 Conclusions

In this work, we present a study on the assembly of nanoparticles, homeotropic and planarly anchored, adsorbed on bipolar liquid crystalline droplets. The bipolar droplet offers a precise platform to direct the NP packing, since its two anitpodal defects attract NPs and enable the formation of closely-packed clusters of NPs. Building upon previous studies, [137, 197, 263, 261] we present a hybrid relaxation scheme that allows to minimize the LC free energy while introducing a stochastic feature that allows for the NPs to arrange freely. We demonstrate that the multitude of pathways available for NP assembly yields a bifurcation in the free energy landscape, thus creating kinetically-trapped states that are more accessible than the global free energy minima when being relaxed from an isotropic state. The energetic cost for the particles to rearrange locally to optimize their packing is of the order of ~ 100 k_BT, while the cost to traverse and achieve equipartition between the two poles is of the order of ~ 1000 k_BT. In this sense, the onset of entropic frustration causes rare conformations to be observed, in agreement with previous experimental observations.

A simplified model is also introduced with effective potentials calculated from the continuum simulations. This approach allows us to use enhanced sampling techniques to efficiently explore configuration space, and quantify the energetic barriers encountered by the NPs in terms of the cluster asphericity. The results reproduce the behavior from the continuum model in terms of variability in the shape of the clusters, as well as explore the key parameters needed to control the NP assembly. By increasing the interparticle inter-

action, which translated in continuum to higher anchoring strength, the metastable states are far and fewer until only closed-packed and linearly arranged clusters are observed.

With the insights from homogeneous sets, we also present an exploration of mixed sets of NPs. Simulations indicate that each type of particle behaves independently of the other type, where homeotropic particles assemble at the poles and planar particles either stay at the equator or surround the cluster.

This study encompasses different scenarios that are feasible to design and control the assembly of NPs through LC order. Additionally, we introduce a simulation technique that enables the computational exploration and discovery of kinetic traps at the continuum scale. Albeit computationally expensive, this method is versatile and yields vast results that can be used to parametrize simplified modes, as well as providing enough information to involve machine learning techniques into molecular systems design.

Chapter 8

Bayesian Optimization for parameter space exploration

8.1 Introduction

The key for inverse design of material applications lies in the formulation of powerful computational methods that are able to model the relevant phenomena of experimental systems. In general, mean-field simulations of LCs aim to study systems of micron-sized dimensions while attempting to resolve events in the scale of the nematic coherence length $\xi_n \sim 10$ nm. Motivated by the disparity in length scales, several approaches have attempted to optimize solution methods.

One approach involves non-uniform meshing, in which a finer discretization is achieved near the defects and coarser discretization is done in the far-field. This requires *a priori* knowledge of the equilibrium configuration of the system. Additionally, it does not necessarily apply to confined systems, in which the balance between surface and bulk interactions play a crucial role in determining the convergence of the simulation. Alternatively, while using a uniform mesh ξ_n, simulations can start at a coarser resolution and perform refining of the mesh as the relaxation carries on. This approach is akin to those used in coarse-grained simulations, and have been proven to speed up calculations considerably.

Manipulating the spatial discretization to optimize the computation time is not the only route to create efficient computational frameworks. Other strategies include hybrid relaxation of the order field, and using optimized libraries for solving the resulting PDE.

These approaches significantly speed up the simulations. However, they do not solve the issue of achieving qualitative agreement with experimental observations.

One limitation lies on understanding the relationship between order field and optical signature. From the experimental side, the optical signature from Polarized Optical Microscopy (POM) is often accompanied by vibrant colors, but it is a projection of the three dimensional structure which leads to uncertainty when inferring the order field in complex systems. From the simulations side, calculating the POM from an order field is only possible under the assumption of a monochromatic plane wave and it neglects the optical response across the entire visible spectrum.

Reaching a combination of phenomenological coefficients that yields the best approximate POM comes at great computational expense. In this work we present a methodology informed by comparisons with experimental observations to guide the choice of phenomenological parameters. First, we introduce an efficient relaxation method that allows for accurate representation of complex geometries, and numerically stable to resolve non-linear behavior. The relaxation method is followed by a general description of Bayesian optimization and Gaussian processes. The combination of these two achieves good efficiency when optimizing the anchoring strength to observe a radial and bipolar droplet. Furthermore, optimizing the shape of a nematic colloid allows for the exploration of efficient colloidal assembly in a nematic bulk.

8.2 Numerical Methods

8.2.1 Dissipative dynamics for the Ginzburg–Landau relaxation

A typical Ginzburg–Landau relaxation (section 2.2.1) for a micrometer sized system will most certainly yield a metastable configuration. To prevent that, we want to adopt a non-equilibrium relaxation as presented by Tucker and Halperin [248], and explicitly

for the GL case by Binder [18]. This formalism is a generalization to continuous fields of the Langevin equation for velocity, where a noise source, $\mathcal{D}(\mathbf{x}, t)$, is introduced as a phenomenological representation of faster degrees of freedom not captured by $\mathbf{Q}$ [37]. We can rewrite our evolution equation as,

$$\frac{\partial \mathbf{Q}}{\partial t} = \nabla^2 \mathbf{Q} + \mathbf{f}'(\mathbf{Q}, \nabla \mathbf{Q}) + \mathcal{D}(\mathbf{x}, t) \tag{8.1}$$

where $\mathcal{D}$ is a symmetric and traceless Gaussian noise source and must satisfy the fluctuation–dissipation theorem by holding the following,

$$\begin{gathered} \langle \mathcal{D}(\mathbf{x}, t) \rangle = 0, \\ \left\langle \mathcal{D}(\mathbf{x}, t) : \mathcal{D}\left(\mathbf{x}', t'\right) \right\rangle = 2 k_B \hat{T} \delta\left(\mathbf{x} - \mathbf{x}'\right) \delta\left(t - t'\right) \end{gathered} \tag{8.2}$$

An Îto integration is performed for $\mathcal{D}$, through which we impose a similar annealing as in the MC relaxation. With this proposed relaxation we attempt to include thermal fluctuations that help the system overcome energetic barriers that prevent the method to find the global free energy minima.

8.2.2 Parallelized Finite Element Method implementation

For the Ginzburg–Landau relaxation we propose the use of the Galerkin method of weighted residuals, where a variational formulation of the evolution equation is proposed. The variational form is expressed in terms of basis functions ψ, which transform the problem into solving a linear system of equations $\mathbf{A} \cdot \mathbf{x} = \mathbf{b}$. The Ginzburg–Landau relaxation, from section 2.2.1, can be rewritten as,

$$\begin{gathered} \mathbf{D} \cdot \frac{\partial \mathbf{Q}}{\partial t} = -\mathbf{E} \cdot \mathbf{Q} + \mathbf{D} \cdot \mathbf{f}' + \mathbf{R} \cdot \mathbf{f}'' \\ \mathbf{D} = \int \mathrm{d}^3 \mathbf{x} \psi \psi \qquad \mathbf{E} = \int \mathrm{d}^3 \mathbf{x} \nabla \psi \nabla \psi \qquad \mathbf{R} = \oint \mathrm{d}^2 \mathbf{x} \psi \psi \end{gathered} \tag{8.3}$$

The time discretization will be done with a semi-implicit Euler scheme [43], which is known to provide a better stability and allows for larger time steps than explicit schemes. The first version of this method is built as a serial implementation with the help of libMesh [109] for mesh optimization, and the SuperLU library [128] that performs a LU factorization required to solve the system of equations. Although this version is numerically robust, it is computationally inefficient due to the CPU time required to perform said factorization.

The parallelization approach for the GL relaxation is implemented for the most critical step of the solution process: the factorization. The software is being built using open source libraries like libMesh [109] which has SuperLU for distributed memory built-in for systems with less than one million degrees of freedom. It has been found that for systems with a greater number of degrees of freedom, an iterative solver is required. This also calls for introducing a preconditioning step into the solving process, which is problem-dependent.

8.2.3 Bayesian optimization and Gaussian processes

The simplest way of searching through parameter space is by performing a grid search, in which each combination of parameters can be imagined to be a point on a grid spanned by the values each parameter can take. This approach can be extremely computationally expensive, especially when the model includes non-linear terms. Grid search is a deterministic approach, in which we consider each resulting configuration independently. A key point to note is that often times, the free energy surface of a LC system is continuous and well-behaved. So if instead we take a probabilistic approach to surveying parameter space, this might result in using far fewer simulations to converge to a system that compares quantitatively to experimental observations.

Bayes rule allows us to consider that if we have some *prior* knowledge about the error

between the simulation results and the experimental observations, we can gather more *evidence* and update the error using newly gathered evidence to find a *posterior estimate* of the optimal parameters. The first hypothesis is that the validation error is a function of the phenomenological parameters without assuming the form this function takes. We can assume at the beginning that the error is uniformly distributed, and the approximation of the error at each point is represented by a Gaussian processes. An alternative interpretation of a Gaussian process is a fractional Brownian motion whose covariance function follows that of the Wiener process. In it, every collection of variables is represented as a multivariate normal distribution.

The main advantage of using a Gaussian process lies in the ability to estimate the function and provide information about its respective uncertainty. The uncertainty information is fundamental to Bayesian optimization, since will allow us to strike a balance between exploration and exploitation of the parameter search. We want to explore areas of the free energy surface that we haven't explored yet (where the model is highly uncertain), but we also want to exploit areas where we're more certain that the precision is good, because those areas are more likely to be where the best parameter combination lies.

To determine what point to sample next, we can find the hyperparameters which maximize an "acquisition function". The acquisition function is a function that when evaluated at x (some combination of hyperparameters), tells us how advantageous it would be to evaluate our expensive function at that point. That way, we can use the acquisition function to find the next combination of hyperparameters to try.

In that sense, the procedure to implement Bayesian optimization in the context of a Ginzburg-Landau relaxation is as follows. First, we evaluate the equilibrium configuration for seed points across the optimization domain, the range of the phenomenological coefficients of interest, and compute the similarity metric between experimental observa-

tion and simulation results. We use these evaluations to regress a function that approximates the similarity metric across the domain and calculate the uncertainties, variances, and standard deviations associated with the regressed function. The uncertainty is used to estimate which point in the optimization domain is most likely to improve the similarity metric. Once the next set of points is evaluated, the regressed function is updated and the iteration continues.

8.2.4 Jones representation of polarization states

The description of the polarizing behavior of an optical field in terms of amplitudes was one of the great contributions of the wave theory of light. The solution of the wave equation in terms of transverse components leads to elliptically polarized light and its degenerate linear and circular forms. However, even using the amplitude formulations, the propagation of the optical field through several polarizing components is challenging to simulate.

In 1941, R. Clark Jones developed a matrix calculus for addressing these problems, in which the Jones vector allows to represent a plane wave in terms of its amplitudes (A_x, A_y) and the phase angles (δ_x, δ_y). In such a way, a monochromatic plane wave is represented by the Jones vector by $\vec{E} = A_k e^{i\delta_k}$. The total intensity I of the optical field is given by, $I = E^{\dagger}E$, the product between the Jones vector and its complex transpose.

In this case, the polarizing components are considered to be discretized sections of the nematic system. The components of a light beam E' emerging from each polarizing element J are linearly related to the incident light beam E. This is better expressed by the product $E' = JE$, where J represents the transforming factors of the polarizing element.

Ondris-Crawford *et al.*[176] implemented the calculation of Jones calculus for nematic systems, in which the polarizing elements J are related to the birefringence of the LC material and its local degree of order. As a result, each discretized layer of the system

accumulates the phase shift, and the result is a projection of the intensity map when a single beam of polarized light travels throughout the material. Conventionally, the result is an optical texture that indicates the average orientation of the LC with respect to the vertical or horizontal axis of the plane. We will use this approximation to calculate the similarity metric between crossed polarizer images from experimental observations and those calculated using equilibrium configurations.

8.3 Results

In this section, we first demonstrate the computational efficiency of the FEM implementation of the Ginzburg-Landau relaxation, followed by a brief discussion on the implications of using stochastic integration to solve the linear system of equations. The first proof of concept for the Bayesian Optimization technique is able to capture the influence of anchoring strength in the equilibrium morphology of LC droplets with homeotropic and planar anchoring. Furthermore, comparison with POM experimental images of nematic colloids yields the optimal shape parameter that allows us to explore the energetic barriers for assembly of cuboidal particles in a nematic bulk.

8.3.1 Numerical analysis

Computational efficiency is paramount to the applicability of novel relaxation techniques. The efficiency of GL-pFEM is compared against other numerical methods (Finite Differences) and relaxation techniques (artificial annealing). In order to test the robustness of this method, we model a system that involves confinement and chirality. A highly chiral LC is confined in a droplet with strong degenerate planar anchoring. At equilibirium, the system exhibits Blue Phase II, a morphology characterized by the presence of a network of defects. An illustration of the defects is included in figure 8.1.

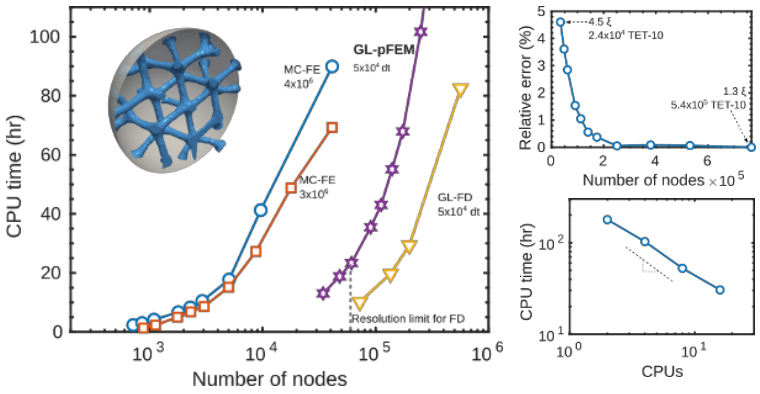

Figure 8.1: Computational efficiency of the parallelized FEM Ginzubrg-Landau relaxation, compared to other conventional relaxation techniques and numerical approximations, as a function of mesh size. Approximation error as a function of mesh resolution, and scalability as the FEM relaxation runs in multiple processors.

The CPU time utilized by the GL-pFEM scheme is shown as a function of mesh size discretized into quadratic tetrahedral elements. The GL-pFEM method proves to be competitive with other techniques, and follows the same trend. One thing to note is that the MC-FE relaxations were carried out with linear elements, which results in smaller mesh sizes. The advantage of the FEM, in general, is its ability to resolve non-linear behavior with a coarser resolution than FDM. This is evident in the case of small meshes for FD, in which the resolution limit impedes the coarseninng of the mesh before incurring in instabilities in the time integration scheme.

Additionally, we report the relative error in the approximation of the total free energy as a function of mesh size. Taking the finest mesh as the true value, the FE is able to reach equilibrium and only incur in a relative error of 4%. This provides grounds to explore a method that adapts the mesh size as the relaxation carries on. In this sense, taking advantage of the speed up reported for coarser meshes. Additionally, the method scales close to linearly for a small number of processors owing to the use of optimized libraries for performing linear algebra operations, and mesh discretization.

As we mentioned previously, the Ginzburg-Landau relaxation is prone to yield quenched configurations. In order to circumvent this, the relaxation is solved with stochastic inte-

gration. In this section we will demonstrate that the white noise is related to the order of the system, and by tuning the fluctuation strength $\hat{\mathcal{D}}_R$, we can obtain fluctuations that are physical and no longer connected to an artificial temperature.

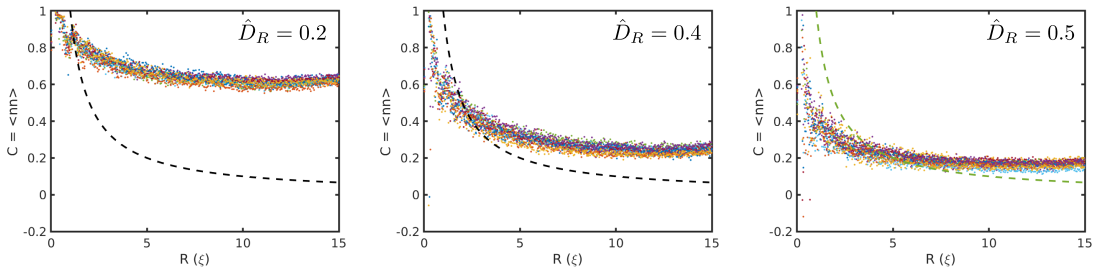

Figure 8.2: Correlation of the director field as a function of distance R for different fluctuation strength $\mathcal{D}$ during the relaxation of a nematic bulk.

8.3.2 Nematic droplets: Uniaxial-Radial and Uniaxial-Bipolar transition

As proof of concept, we wish to capture the transition from uniaxial to radial configuration or bipolar configuration, depending on the anchoring strength. The metric that we are using to guide the optimization is the Feature Similarity Index Measurement (FSIM). Through this metric, we are able to identify general domains in the POM images, instead of comparing pixel to pixel. Additionally, this index eliminates the need to compare images that are only centered, with similar resolution, and captures rotational symmetries.

The first data point provided to the optimization is a dark image that results from a uniaxial droplet. The range of optimization is the anchoring strength $W \in \left[10^{-6}, 10^{-3}\right]$ J/m^2. The optimization converges in under 7 iterations.

8.3.3 Optimizing colloidal shape for self-assembly

In this section, we investigate the structure of topological defects at superballs immersed in a bulk nematic phase and the means for particle assembly. The theoretical

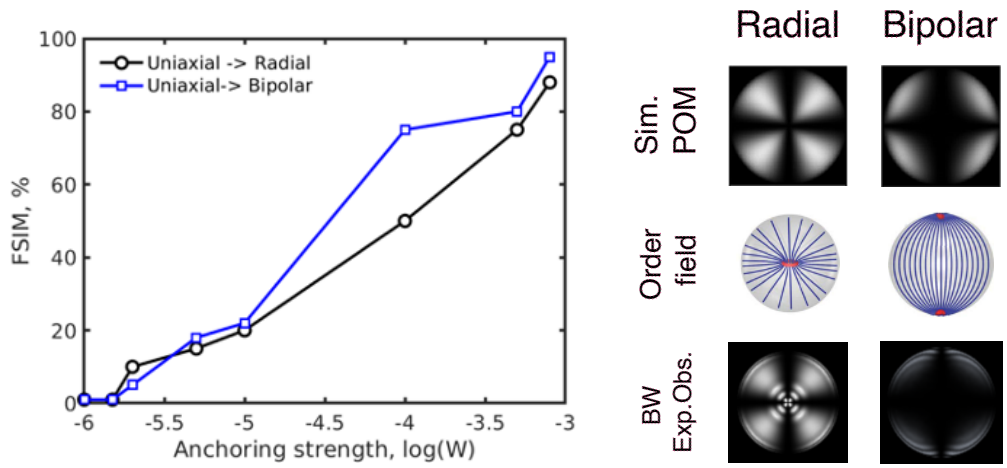

Figure 8.3: Percentage of feature similarity index measurement as a function of anchoring strength for two droplets with homeotropic and planar anchoring conditions.

predictions are then corroborated by experiments. Furthermore, we study the forces on the particles for different separations and orientations with respect to the nematic director. We focus primarily on the case of colloids with strong homeotropic anchoring. In all cases, the stability of the systems is determined by free energy calculations. The geometry of the cuboids is defined by

$$x^m + y^m + z^m \leq R^m, \tag{8.4}$$

where R is the particle size and $m \geq 0$ is the shape parameter. It indicates to what extent the particle shape is deformed from a spherical particle, i.e. $m = 2$. For $m > 2$ this equation describes a family of convex superballs with cubic-like shapes with rounded corners. If $m \to \infty$, the superball becomes a cube wit sharp edges.

Experimental setup

The 4-Pentyl-4'-Cyanobiphenyl (5CB) liquid crystal was purchased from Sigma–Aldrich. Silica cuboids with a shape parameter of $m = 3.9$ and a size of 1.4 μm were synthesized according to Sugimoto *et al.* and Rossi *et al.* [205, 234, 204]. Briefly, an iron oxide cube was used as a template, which was then coated with a layer of amorphous silica. The iron

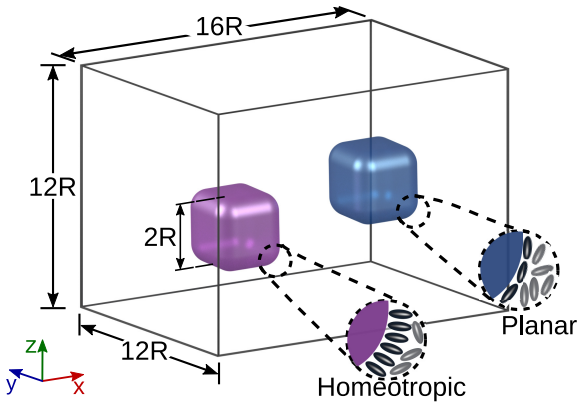

Figure 8.4: Schematic representation of two superballs with shape parameter $m = 6.26$ suspended in a nematic liquid crystal, each particle shows a specific type of anchoring: purple for homeotropic (perpendicular) anchoring, and blue for planar (parallel) anchoring. Periodic boundary conditions are applied in the x, y and z directions.

oxide core is dissolved in hydrochloric acid to create hollow silica cuboids. To induce homeotropic anchoring, the surface of the silica particles was treated with a 3 wt% solution of DMOAP (N, N-dimethyl-N-octadecyl-3-aminopropyltrimethoxysilyl chloride, Sigma-Aldrich) in mQ-water.

To create a sample cell with homeotropic alignment surfaces, 50 μm thick $\times$1 mm wide $\times$25 mm long rectangular capillaries (VitroCom) are used. The inner surface of the capillary was functionalized by exposing it to oxygen plasma at 200 W for 30 min and 0.65 mbar pressure. The rectangular capillaries were then immediately immersed in a 3 wt% solution of DMOAP in mQ-water for 10 min, rinsed with ethanol and mQ-water 3 times and dried with nitrogen.

The liquid crystal sample cell with a planar surface anchoring was fabricated by coating two glass slides with a rubbed polyvinyl alcohol (PVA) layer. To do so, a 1% wt solution of polyvinyl alcohol (PVA, average Mw=35k-50k, 87-89% hydrolyzed, Sigma-Aldrich) in a mixture of ethanol and water (5: 95 %wt ethanol/water) was spin coated on the glass slides for 30 s at 1200 rpm. After baking at 110°C for 2 hours, the coated glass surfaces were rubbed along one direction to control the planar LC alignment. A 1% wt

solution of silica cuboidal particles was dispersed in 5CB liquid crystal and loaded into cells via capillary force. The experiment was performed at room temperature, where 5CB is in the nematic phase. An Olympus BX51 and a Nikon Eclipse Ti-U optical microscopes equipped with crossed polarizers were utilized to image the topological defects formed in the presence of cuboidal particles and the emerging colloidal assembly.

Defect structure on a single cuboid

In order to inspect the defect structure that forms around a cuboid, different geometries are studied by varying the shape parameter m. We selected a smooth progression from spherical ($m = 2$) to a cubic shape ($m = 66$). Two geometrical parameters aid the understanding of the evolution of the defect. Firstly, the orientation of the elastic dipole, $\boldsymbol{\mu}_E$, with respect to the far-field director field $\mathbf{n}$, which is defined by $\theta = \cos^{-1}(\boldsymbol{\mu}_E \cdot \boldsymbol{n})$. The elastic dipole $\boldsymbol{\mu}_E$ is determined to be a vector in the plane that contains the furthest points of the defect. The far-field director field was calculated as the average of the director field that lies on a sphere of radius $6R$. The second parameter, α, describes the aperture of the defect. It is calculated by the angle between the plane that contains the furthest points of the defect and the plane that contains two opposite edges of the defect. For a sphere, $\alpha = 0°$because both planes are parallel, and for a cube, $\alpha = 66.6°$. Schematics of these descriptions can be seen in the insert of Figure 8.5a.

As expected, the shape of the particle has a strong influence on the defect structure, as shown in Figure 8.5b. For $m = 2$, we obtain a Saturn ring defect consistent with previous observations [78]. In this case, the plane containing the ring defect is perpendicular to the far–field director which leads to a value of $\theta = 90°$, and the defect is contained in a single plane so $\alpha = 0°$. As m increases, the new edges of the particle induce strong elastic deformations of the director field, thereby affecting the symmetry of the ring defect. It starts with a slight twist of the ring until it fully evolves to form a chair-like defect. In

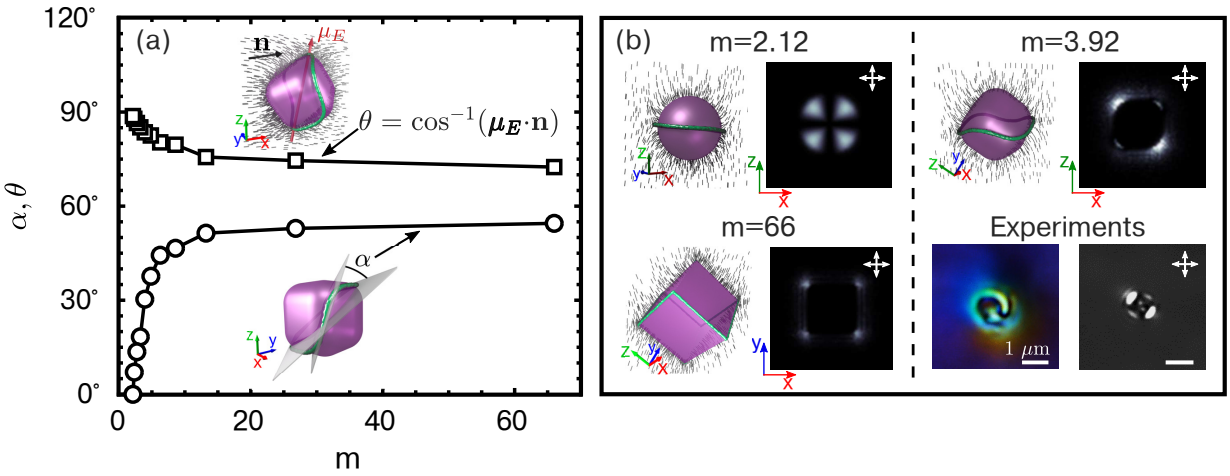

Figure 8.5: (a) Geometrical parameters α and θ, as illustrated in the inserts, as a function of the shape parameter m for a single particle with strong homeotropic anchoring. This shows the gradual transformation of the ring defect into a chair defect. (b) Defect configurations and simulated crossed polarizer images for three cuboidal particles. Defects are shown in green and correspond to an isosurface of $S = 0.42$. The black lines illustrate the orientation of the director field $\mathbf{n}$ surrounding the particle. For $m = 3.92$, bright field microscopy (left bottom) and crossed polarizer (right bottom) images show the corresponding defect structure. Scale bar is $1\mu m$.

all cases, the defect wraps around the colloid. Similar defect configurations were found by Hung and Bale [89] for smaller cubic nanoparticles of side length 40 nm, by Beller *et al.* [13] for superballs of side length 540 nm, and experimentally in a system with magnetic interactions by Sudhakaran *et al.* [232]. The theoretical predictions are compared to experimental micrographs using optical polarized textures. The simulated images are shown in Figure 8.5b next to the corresponding defect configurations. For the case of $m = 3.92$, a direct comparison from simulations to experiments is included.

Self-assembly of a pair of cuboids.

In order to analyze liquid crystal–mediated interactions between cuboids, the Potential of Mean Force (PMF) between two superballs, with shape parameter $m = 6.26$, and side length of 500 nm and $R = 250$ nm, is calculated. The PMF, $\psi = F - F_0$, provides a measure of the effective difference in free energy between two states as a function of one

or more degrees of freedom. We focus on three scenarios for assembly using the surface-to-surface distance d, and relative orientation with respect to each other β as parameters.

In the first set of simulations, two particles, in a face-to-face orientation, are separated in the x–direction and one of the particles is rotated with respect to the same x–axis. The PMF values are summarized in Figure 8.6. The inset in Figure 8.6a shows how the two cuboids exhibit chair–like defects when separated by a large distance and adopt the same configuration as if they were single particles. As the particles approach, the PMF decreases abruptly independent of the orientation of the particles. This indicates that the particles experience an attractive force that drives their assembly, and become arrested at a critical distance. When the separation between the particles is of the same order of magnitude as the nematic coherence length, the defects interact and rearrange to accommodate the distorted director field around them. The result of this is a new defect structure: T–ring defect. A similar disclination has been observed before on spherical colloids, where a three-ring structure forms once the pair of particles are arrested [81, 244].

The PMF indicates that assembled particles are more stable when they are not perfectly aligned and they are oriented with $\beta = 15°$. The free energy minima results in $\Delta F \approx 800\ k_B T$ as shown in Figure 8.6b. In the PMF curve as a function of the particle separation, the critical distance, d_{critic}, for assemble is defined as the distance where the PMF becomes approximately flat. It is plotted in Figure 8.6c as a function of the particle orientation β. The results indicate that the attractive force has a shorter range for particles that are not perfectly aligned with each other. This is quantified by a difference of approximately 60 nm when $\beta = 45°$. The inset shows the configuration for two particles with $\beta = 0°$. The gray lines represent the orientation of the director field, which shows slight distortions in the space between the particles. The average far-field orientation, depicted by the pink arrow, shows how the director field is tilted with respect to the orientation of the particles.

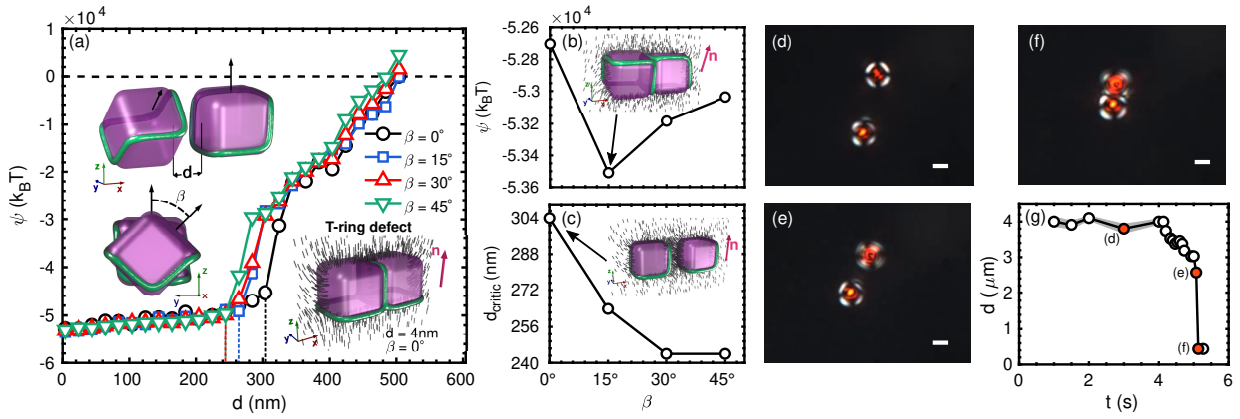

Figure 8.6: Hometropic cuboids ($m = 6.26$) with strong anchoring conditions ($W = 1\times10^{-3}$ J/m^2) immersed in a nematic LC induce the formation of defects, shown in green as isosurfaces of $S = 0.42$. (a) Potential of mean force surface $\psi = F - F_0$ between two particles in terms of their separation distance d and mismatching orientation with respect to the x-axis by an angle β. The reference free energy, $F_0 = -1.075\times10^7 k_BT$, is defined at the longest separation ($d = 500$ nm) for $\beta = 0°$. The inset on the left shows the schematic for measuring d and β, and on the right is the configuration corresponding to the T–ring defect, where the defects are shown in green, the gray lines indicate the orientation of the director field surrounding the particles, and the pink arrow illustrates the orientation of the far-field. (b) PMF as a function of β for the shortest separation distance $d \approx 4$ nm. (c) Critical distance as a function of β. (d)-(f) POM snapshots of two cuboids as they assemble. Scale bar is 1μm. (g) Tracking of inter-particle distance as a function of time. Error bars are represented by the shaded region. Highlighted points correspond to the snapshots in (d)-(f).

The critical distance for assembly, and the sharpness of the PMF for two particles is confirmed in experimental observations (see Fig. 8.6d-g, and Movie 1 in SI), where the interparticle distance is measured as a function of time. The particles attract each other and become arrested in the span of 1 second. Because of the hematite core in each particle, the assembly could be caused by the magnetic forces between them. However, the magnetic energy decays as $\sim 1/r^4$, and considering the magnetization of hematite is $M = 2.2 \times 10^3$ A/m the cuboids experience a magnetic interaction of the order of 10^2 k_BT, which is four orders of magnitude smaller than the bulk elastic free energy.

To complete the paths for assembly, the PMF was calculated with the particles' approach from different directions. Thus, two cuboids were distanced with their main diagonals aligned with the x–axis, while the director field $\mathbf{n}$ is initially aligned with the z–axis. The PMF countour in Figure 8.7 is built as a function of the distance between the particles d, measured from corner to corner, and the orientation with respect to the x–axis with the angle β.

The PMF surface is relatively flat with a maximum energetic barrier of $\sim 1000 k_B T$. The PMF minima corresponds to particles oriented with $\beta = 20°$which is consistent with the minima with mismatching orientations in Figure 8.6. The defects around the particles keep their chair configuration, even when the particles are close to each other. There is no remarkable feature in this PMF that indicates this is the optimum route for assembly, and leads us to believe that the particles would move freely until they achieve an orientation similar to Figure 8.5. Experimental evidence confirms that the assembly on this case is a smooth process without any abrupt behavior, as shown in Figure 8.7b-e. The evolution of the inter-particle distance indicates that particles hover and slowly approach each other.

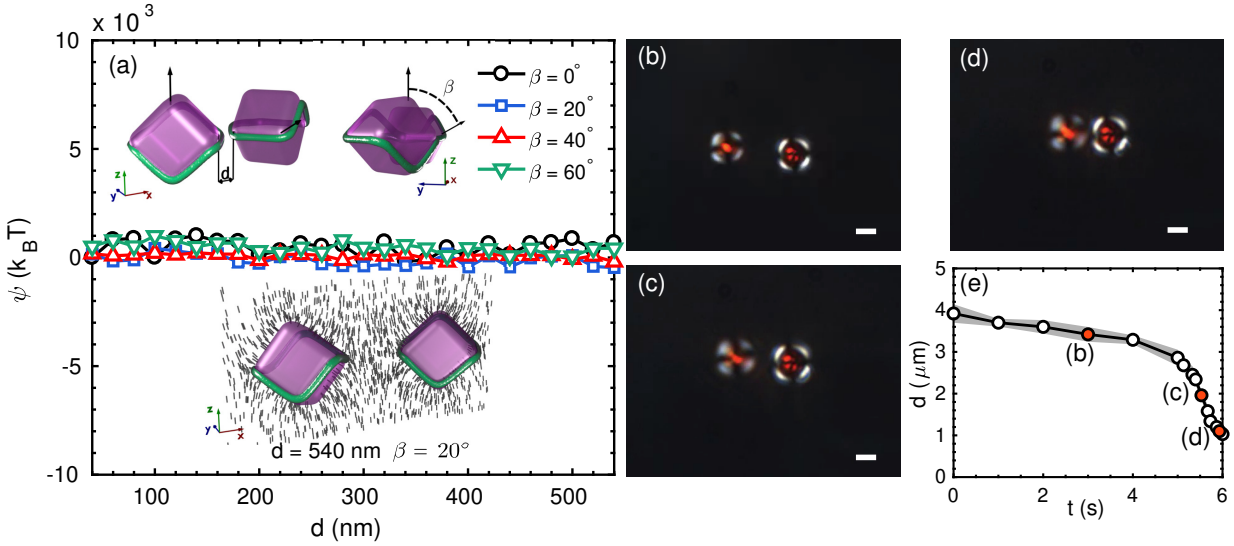

Figure 8.7: Two cuboidal particles oriented corner-to-corner with strong homeotropic anchoring ($W = 1 \times 10^{-3}$ J/m^2). Defects of isosurfaces of $S = 0.42$ are shown in green and the black lines represent the director field $\mathbf{n}$. (a) Potential of mean force surface as a function of inter-particle distance d and relative d the x-axis by an angle β. The reference free energy, F_0, is defined as the energy for the largest separation distance and for $\beta = 20°$, $F_0 = -1.0744 \times 10^7 k_B T$. The inset on the top shows the schematics for the corner-to-corner orientation and measurement of d and β, and on the bottom is the configuration of the reference state with two superballs at $d = 540$ nm and $\beta = 20°$. (b)-(d) POM snapshots of two cuboids oriented corner-to-corner as they assemble. Scale bar is 1μm. (e) Tracking of inter-particle distance as a function of time. Error bars are represented by the shaded region. Highlighted points correspond to the snapshots in (b)-(d).

8.4 Conclusions

In this work, we have introduced a methodology that allows us to explore parameter space and achieve qualitative comparison between simulation results and experimental observations. This methodology can be adapted to different numerical relaxations and metrics that relate order fields to lab measurements. First, we developed an efficient simulation method that represents complex geometries and makes use of stochastic integration to prevent quenched configurations. In this instance, the comparison between simulations and experiments is done through the feature similarity between POM images.

The first demonstration of this methodology is the stability of radial and bipolar droplets as a function of anchoring strength. This system demonstrates the fundamental balance between bulk and surface elasticity, and produces unique optical signatures. In under 10 iterations, the new methodology is able to optimize the anchoring strength to reproduce the radial and bipolar morphologies, when the starting point was a dark image produced by a uniaxial droplet. The second example compares POM images of aspherical nematic colloids. We elucidate the dependence of colloidal shape in the resulting defect structure, which has consequences in the assembly of a pair of cuboids. Because of the geometry, the assembly occurs in a preferred direction, in which the defect structure is offset from the far-field.

The use of Bayesian optimization allows for a fast examination of possible combinations of phenomenological parameters, such as anchoring strength and colloidal shape. In this sense, using stochastic principles for guiding the exploration of parameter space enhances our understanding of the LC model and opens the possibilities of inverse design without incurring in the computational cost of training large Machine Learning models.

Chapter 9

Future work

9.1 Hydrodynamics and Nematic Ordering

Under far-from-equilibrium conditions, the nematic order of an LC is coupled to the hydrodynamic field. Traditionally, such systems have been modeled using the Leslie-Ericksen (LE) [58, 124] theory and equations, where the LC is represented through a vectorial order field, $\mathbf{n}$. Unfortunately, the LE approach is restricted to systems where the nematic order is continuous, thereby excluding the hydrodynamics at topological defects. To fully capture LC defects, a tensorial representation is required.

Popular formulations include the Beris-Edwards equations [14] and the Olmsted-Goldbart formulation [174]. In this work, we adopt the Stark-Lubensky (SL) formulation for liquid crystal hydrodynamics [227] that employs a general Poisson-bracket formalism for a molecular theory of the structure and dynamics of LCs. The SL model differs from previous formulations [174, 14, 86, 120, 194] in the values of kinetic coefficients, the closure in the equations –given by a differentiation between molecular and continuum time scales–, and in the form of the non-linear coupling terms between the velocity and the LC order fields. Nevertheless, the SL formulation is equivalent to the LE equations when considering an uniaxial LC.

The molecular ordering of the nematic liquid crystal is characterized by the tensor order parameter $\mathbf{Q}$ [14]. This description contains the information of the scalar order parameter S, biaxiality η, and director fields $\mathbf{n}$ and $\mathbf{n'}$. For an uniaxial LC, the tensor order parameter is reduced to $\mathbf{Q} = S\,(\mathbf{nn} - \boldsymbol{\delta}/3)$. The material properties of the LC include the

elastic constant L, the thermal energy scale A, and the rotational viscosity γ. They define an LC characteristic length scale $\xi = \sqrt{L/A}$, the nematic coherence length, and a characteristic time scale $t_{LC} = \xi^2\gamma/L$. For a full description, we refer the reader to [9, 253]. On the other hand, a velocity gradient $\nabla\mathbf{v}$, given by the vorticity tensor $\mathbf{\Omega} = \left(\nabla\mathbf{v} - \nabla\mathbf{v}^T\right)/2$, and/or the deformation tensor $\mathbf{\Gamma} = \left(\nabla\mathbf{v} + \nabla\mathbf{v}^T\right)/2$ sets a characteristic velocity $v_c = L_c/t_c$ where L_c is the the characteristic "flow" length scale and t_c the characteristic "flow" time. The ratio between the viscous and elastic time scales determines the Ericksen number,

$$Er = \frac{t_{LC}}{t_c} = \frac{\gamma\xi v_c}{L}. \tag{9.1}$$

where the flow length scale is assumed to be equal to the nematic coherence length. In consequence, $Er \leq 1$, all responses are related to the elastic forces of the LC, while for $Er > 1$ the dynamics involves a competition between the viscous and elastic responses.

In this work, the momentum, the constitutive and the evolution equations for the tensor order parameter are written in dimensionless form and denoted by $\hat{}$. The factors and dimensionless numbers of interest are listed in Table 9.1. The Poisson-bracket evolution equation for the order parameter is given by,

$$\frac{D\mathbf{Q}}{D\hat{t}} = \boldsymbol{\lambda} : \hat{\nabla}\hat{\mathbf{v}} - \frac{1}{Er}\mathbf{H}, \tag{9.2}$$

where $D/D\hat{t} = \left(\partial/\partial\hat{t} + \mathbf{v}\cdot\hat{\nabla}\right)$. The fourth order tensor $\boldsymbol{\lambda}(\mathbf{Q})$ describes the alignment and rotation of the molecular orientations with velocity. This leads to a coupling term between $\mathbf{Q}$ and $\hat{\mathbf{v}}$ as follows:

$$\begin{aligned}\boldsymbol{\lambda} : \hat{\nabla}\hat{\mathbf{v}} =& \mathbf{Q}\cdot\hat{\mathbf{\Omega}} - \hat{\mathbf{\Omega}}\cdot\mathbf{Q} + \frac{1}{3}\frac{I}{\Delta I}\left[\hat{\mathbf{\Gamma}}\right]^{ST} - \frac{2}{3}\mathrm{tr}\left(\hat{\mathbf{\Gamma}}\right)\mathbf{Q} \\ &+ 2\left[\mathbf{Q}\hat{\mathbf{\Gamma}}\right]^{ST} - \left(1 + \frac{I}{\Delta I}\right)\left(\mathbf{Q} : \hat{\mathbf{\Gamma}}\right)\mathbf{Q},\end{aligned} \tag{9.3}$$

where $I/\Delta I$ is the parameter related to the anisotropy of the LC molecule, and $[\mathbf{B}]^{ST} = \left(\mathbf{B} + \mathbf{B}^T\right)/2 - \mathrm{tr}\left(\mathbf{B}\right)\boldsymbol{\delta}/3$ is a symmetric-traceless projection operator for any tensor $\mathbf{B}$. The last term, $\mathbf{H}$, is the free energy gradient with respect to $\mathbf{Q}$,

$$\mathbf{H} = \left[\frac{\delta \hat{F}}{\delta \mathbf{Q}}\right]^{ST} \tag{9.4}$$

where $\delta/\delta\mathbf{Q}$ represents the functional derivative of the potential.

Table 9.1: Characteristic scales and dimensionless numbers

Quantity	**Symbol**	**Factor**
Ericksen number	Er	$\gamma\xi v_c/L$
Reynolds number	Re	$\rho v_c \xi/\eta_2$
Free energy	F	$A\xi^3$
Anchoring strength	$W_\perp, W_\parallel$	$L\xi$
Pressure	p	$\eta_2 v_c/\xi$
Viscous stress	$\boldsymbol{\sigma}^V$	$\eta_2 v_c/\xi$
Elastic stress	$\boldsymbol{\sigma}^E$	L/ξ^2

The free energy of the nematic LC is defined within the Landau-de Gennes formalism [47] with bulk and surface contributions. The bulk contribution includes a Landau short-range density that captures the isotropic-nematic transition and a long-range density that penalizes elastic distortions from a completely ordered state. The surface contribution imposes a preferred molecular orientation at the surface. The total free energy in terms of $\mathbf{Q}$ is then written as,

$$F\left(\mathbf{Q}, \nabla\mathbf{Q}\right) = \int f_B\left(\mathbf{Q}, \nabla\mathbf{Q}\right) \mathrm{d}^3\mathbf{x} + \oint f_S\left(\mathbf{Q}\right) \mathrm{d}^2\mathbf{x} \tag{9.5}$$

The bulk contribution contains the Landau free energy density, expressed as a polynomial expansion of the $\mathbf{Q}$ tensor invariants [14, 50], and the Frank-Oseen elastic free energy

[179, 65, 154]

$$f_B(\mathbf{Q}, \nabla\mathbf{Q}) = \frac{A}{2}\left(1 - \frac{U}{3}\right)\mathrm{tr}(\mathbf{Q}^2) - \frac{AU}{3}\mathrm{tr}(\mathbf{Q}^3) + \frac{AU}{4}\mathrm{tr}(\mathbf{Q}^2)^2 + \frac{L}{2}\frac{\partial Q_{ij}}{\partial x_k}\frac{\partial Q_{ij}}{\partial x_k}, \tag{9.6}$$

where A and U are material-dependent phenomenological coefficients. The energy scale of the model is controlled by A, while U controls the isotropic-nematic transition [14] and the equilibrium scalar order parameter S. The elastic constant L is related to the elastic moduli for a uniaxial LC through $K = 2LS^2$.

The interaction between the LC and a surface is described by the surface free energy. The two canonical cases are homeotropic and planar anchoring, in which the preferred molecular orientation is perpendicular or parallel to the surface with normal vector $\boldsymbol{\nu}$. These two cases are modeled with the second order Rapini-Papoular potential for homeotropic anchoring [185] or with the fourth order degenerate potential proposed by Fournier and Galatola [64] for planar anchoring. They are defined as follows,

$$f_{S,\perp}(\mathbf{Q}) = \frac{W_\perp}{2}(\mathbf{Q} - \mathbf{Q}_\perp)^2, \tag{9.7}$$

$$f_{S,\parallel}(\mathbf{Q}) = \frac{W_\parallel}{2}(\mathbf{Q} - \mathbf{Q}_\perp)^2 + \frac{W_\parallel}{4}\left(\mathbf{Q} : \mathbf{Q} - S^2\right)^2, \tag{9.8}$$

where $W_\perp, W_\parallel$ is the anchoring strength, $\mathbf{Q}_\perp = S(\boldsymbol{\nu}\boldsymbol{\nu} - \boldsymbol{\delta}/3)$ is the equilibrium tensor for homeotropic anchoring, and $\bar{\mathbf{Q}}_\perp = \mathbf{p}\cdot\mathbf{Q}\cdot\mathbf{p}$ is the tensor projection onto the surface for planar anchoring with $\bar{\mathbf{Q}} = \mathbf{Q} + S\boldsymbol{\delta}/3$ and $\mathbf{p} = \boldsymbol{\delta} - \boldsymbol{\nu}\boldsymbol{\nu}$.

The evolution of the order field in Eqn. (9.2) is coupled with the momentum balance. In the SL theory, the momentum equation is given by,

$$Re\frac{D\mathbf{v}}{D\hat{t}} = -\hat{\nabla}\hat{p} + \hat{\nabla}\cdot\hat{\boldsymbol{\sigma}}^V + \frac{\hat{\gamma}}{Er}\left[\hat{\nabla}\cdot\hat{\boldsymbol{\sigma}}^E + \hat{\nabla}\cdot(\mathbf{H}:\boldsymbol{\lambda})\right], \tag{9.9}$$

where $\hat{p}$ is the pressure field, $\hat{\boldsymbol{\sigma}}^V$ is the viscous stress, $\hat{\boldsymbol{\sigma}}^E$ is the elastic stress, and $\mathbf{H}\colon\boldsymbol{\lambda}$ is an additional reactive stress related to gradients of the free energy. The viscous stress $\hat{\boldsymbol{\sigma}}^V$ is defined by,

$$\begin{aligned}\hat{\boldsymbol{\sigma}}^V =&\hat{\eta}_1 \mathrm{tr}\left(\hat{\boldsymbol{\Gamma}}\right)\boldsymbol{\delta} + 2\hat{\eta}_2\hat{\boldsymbol{\Gamma}} + \hat{\eta}_3\left[\left(\mathbf{Q}\colon\hat{\boldsymbol{\Gamma}}\right)\boldsymbol{\delta} + \mathrm{tr}\left(\hat{\boldsymbol{\Gamma}}\right)\mathbf{Q}\right]\\ &+ 2\hat{\eta}_4\left[\mathbf{Q}\cdot\hat{\boldsymbol{\Gamma}} + \hat{\boldsymbol{\Gamma}}\cdot\mathbf{Q}\right] + \hat{\eta}_5\left(\mathbf{Q}\colon\hat{\boldsymbol{\Gamma}}\right)\mathbf{Q},\end{aligned} \tag{9.10}$$

where $\hat{\eta}_i = \eta_i/\eta_2$ are the viscosity coefficients, related to Leslie-Ericksen parameters [47, 227]. These coefficients satisfy the Onsager relations [47] and the Parodi relation [186]. The elastic stress $\hat{\boldsymbol{\sigma}}^E$, under the one-elastic constant approximation, takes the form

$$\hat{\boldsymbol{\sigma}}^E = -\frac{\partial \hat{F}_B}{\partial\hat{\nabla}\mathbf{Q}} = \hat{\nabla}\mathbf{Q} : \hat{\nabla}\mathbf{Q}. \tag{9.11}$$

The Landau-de Gennes stress $\left(\hat{\mathbf{H}}\colon\boldsymbol{\lambda}\right)$ vanishes as the system reaches a minimum in the free energy ($\partial\hat{F}/\partial\mathbf{Q} = 0$). This stress is given by,

$$\begin{aligned}\mathbf{H}\colon\boldsymbol{\lambda} =& -\frac{2}{3}\left(\mathbf{Q}\colon\hat{\mathbf{H}}\right)\boldsymbol{\delta} + 2\mathbf{Q}\cdot\hat{\mathbf{H}} + \frac{1}{3}\frac{I}{\Delta I}\hat{\mathbf{H}}\\ &-\left(1+\frac{I}{2\Delta I}\right)\left(\mathbf{Q} : \hat{\mathbf{H}}\right)\mathbf{Q}.\end{aligned} \tag{9.12}$$

In this work, we considered the LC media incompressible; therefore, the pressure field p becomes a "Lagrangian" multiplier with no connection to the thermodynamic pressure [180], and the continuity equation must hold,

$$\hat{\nabla}\cdot\hat{\mathbf{v}} = 0. \tag{9.13}$$

The $\mathbf{Q}$ tensor is mapped onto an orthonormal tensor basis $\{\mathbf{T}^m\}$ [86, 223, 203] such that $\mathbf{Q} = \sum_{\mu=1}^{5} a_\mu\mathbf{T}^\mu$, where the coefficients $a_\mu = \mathrm{tr}\left(\mathbf{Q}\mathbf{T}^\mu\right)$ are projections over the tensorial

basis. In this way, the alignment tensor **Q** is represented in terms of five independent scalar components. This allows for an unbiased representation of the inherent biaxiality of defects, and at the same time eases the computational cost by substituting slow tensor operations with fast scalar ones.

Chapter 10

Concluding Remarks

This thesis is focused on the formulation of new computational approaches that study the behavior and equilibrium configurations of liquid crystalline systems. While great advancements have been made in terms of computational efficiency and numerical approximations, several challenges remain when involving non-linear behaviors and complex geometries. The central motivation of this work is the development of simulation methods; the resulting tools serve to demonstrate the effective use of confinement and geometry to control and design emerging morphologies and nematic-mediated assembly of nanoparticles. Mainly, the addition of stochastic elements to classical simulation techniques provides insight into the emergence of kinetic traps and a general understanding of the role of balance between the bulk and surface elasticity of LC media.

We began (Chapters 3, 4, and 5) by probing the resulting morphologies of cholesteric and highly chiral LCs when confined in droplets, cylinders, and toroids. In the second part (Chapters 6 and 7), we consider the interaction of the order field with non-LC inclusions. Advancing the capabilities of our methods, we optimize phenomenological parameters to reproduce experimental observations (Chapter 8). Finally, we expand our formulation by adapting the Stark-Lubensky theory into a Finite Element discretization to account for hydrodynamic effects in anisotropic fields (Chapter 9).

The first part of this dissertation focused on probing the resulting morphologies of confined cholesteric and highly chiral liquid crystals (LCs) in different geometries such as droplets, cylinders, and toroids. The addition of stochastic elements to classical simulation techniques allowed for a deeper understanding of the emergence of kinetic traps

and the role of the balance between bulk and surface elasticity in LC media. Geometric frustration was found to play a crucial role in stabilizing and generating new morphologies, leading to the discovery of hybrid blue phases with distinct optical responses and tunable chiral ribbon-like defects.

The second part of this thesis investigated the interaction between the LC order field and non-LC inclusions, particularly focusing on the assembly of nanoparticles on bipolar liquid crystalline droplets. A hybrid relaxation scheme incorporating stochastic features was developed, revealing the presence of kinetically trapped states and providing insights into the energetics and pathways of nanoparticle assembly. Simplified models based on continuum simulations were also introduced, allowing for efficient exploration of configuration space and the quantification of energetic barriers. Additionally, the study explored the assembly of mixed sets of nanoparticles, highlighting the independent behavior of each particle type.

Furthermore, this work addressed the optimization of phenomenological parameters through Bayesian optimization, enabling qualitative comparisons between simulation results and experimental observations. The developed methodology facilitated the exploration of parameter space and provided insights into the balance between bulk and surface elasticity, as well as the dependence of defect structures on colloidal shape. The use of stochastic principles in guiding parameter exploration enhanced the understanding of the liquid crystal model and opened possibilities for inverse design without the computational cost of training large machine learning models.

In summary, the studies presented in this dissertation attempt to study systems as close to the experimental description without compromising computational efficiency. At the same time, these tools provide insights into the nature of the balance between confinement and elasticity in the search for system parameters that can be used to control and design new morphologies and assembly mechanisms. This thesis has contributed to the

field of computational modeling of liquid crystalline systems by developing new simulation approaches and exploring their applications in controlling and designing emerging morphologies and nanoparticle assembly.

References

1. Hamed Abbaszadeh, Michel Fruchart, Wim van Saarloos, and Vincenzo Vitelli. Liquid-crystal-based topological photonics. *Proceedings of the National Academy of Sciences*, 118:e2020525118, 6 2021. ISSN 1091-6490. doi:10.1073/PNAS.2020525118.

2. Paul J Ackerman, Timothy Boyle, and Ivan I Smalyukh. Squirming motion of baby skyrmions in nematic fluids. *Nature Communications*, 8:673, 9 2017. doi:10.1038/s41467-017-00659-5.

3. D. W. Allender, G. P. Crawford, and J. W. Doane. Determination of the liquid-crystal surface elastic constant k_{24}. *Physical Review Letters*, 67(11):1442–45, jun 1991. ISSN 1538-8670. doi:10.1097/01.NUMA.0000430408.88453.4f. URL http://www.ncbi.nlm.nih.gov/pubmed/23706050.

4. Anatoliy Andrushchak, Zenon Hotra, Zinoviy Mykytyuk, Taras Prystay, Orest Sushynskyi, and Maria Vistak. Nanostructures on the basis of porous alumina with intercalated with cholesteric liquid crystal. *Molecular Crystals and Liquid Crystals*, 611 (1):132–38, 2015. doi:10.1080/15421406.2015.1030201. URL https://doi.org/10.1080/15421406.2015.1030201.

5. Nicolas Anton and Thierry F. Vandamme. Nano-emulsions and micro-emulsions: Clarifications of the critical differences. *Pharmaceutical Research*, 28(5):978–85, 2011. doi:10.1007/s11095-010-0309-1. URL https://doi.org/10.1007/s11095-010-0309-1.

6. Julio C. Armas-Pérez, Juan P. Hernández-Ortiz, and Juan J. de Pablo. Liquid crystal free energy relaxation by a theoretically informed Monte Carlo method using a finite element quadrature approach. *The Journal of Chemical Physics*, 143(24):243157, 2015. ISSN 0021-9606. doi:10.1063/1.4937628. URL http://scitation.aip.org/content/aip/journal/jcp/143/24/10.1063/1.4937628.

7. Julio C Armas-Pérez, Juan P Hernández-Ortiz, and Juan J de Pablo. Liquid crystal free energy relaxation by a theoretically informed monte carlo method using a finite element quadrature approach. *The Journal of Chemical Physics*, 143:243157, 2015. ISSN 0021-9606. doi:10.1063/1.4937628.

8. Julio C. Armas-Pérez, Alejandro Londono-Hurtado, Orlando Guzmán, Juan P. Hernández-Ortiz, and Juan J. de Pablo. Theoretically informed Monte Carlo simulation of liquid crystals by sampling of alignment-tensor fields. *The Journal of Chemical Physics*, 143(4):044107, 2015. ISSN 0021-9606. doi:10.1063/1.4926790. URL http://scitation.aip.org/content/aip/journal/jcp/143/4/10.1063/1.4926790.

9. Julio C Armas-Pérez, Alejandro Londoño-Hurtado, Orlando Guzmán, Juan P Hernández-Ortiz, and Juan J de Pablo. Theoretically informed monte carlo simulation of liquid crystals by sampling of alignment-tensor fields. *Journal of Chemical Physics*, 143:44107, 2015. ISSN 0021-9606. doi:10.1063/1.4926790.

10. Bahadur. B. ed. *Liquid Crystals: Applications and Uses.Vol*, 1.

11. J Bajc, P P Crooker, and S Zumer. Chiral nematic liquid crystal droplets. *Liquid Crystals Today*, 7:1–6, 1997. ISSN 1358-314X. doi:10.1080/13583149708047675.

12. A R Bausch, M J Bowick, A Cacciuto, A D Dinsmore, M F Hsu, D R Nelson, M G Nikolaides, A Travesset, and D A Weitz. Grain boundary scars and spherical crystallography. *Science*, 299:1716–1718, 6 2003. ISSN 0036-8075. doi:10.1126/SCIENCE.1081160.

13. Daniel A. Beller, Mohamed Amine Gharbi, and Iris Liu. Shape-controlled orientation and assembly of colloids with sharp edges in nematic liquid crystals. *Soft Matter*, 11: 1078–1086, 2015. ISSN 1744-683X. doi:10.1039/C4SM01910E.

14. A N Beris and B J Edwards. *Thermodynamics of flowing systems: with internal microstructure*. Oxford Engineering Science Series. Oxford Science Publications, New York, 1994. ISBN 019507694X.

15. Antony N. Beris and Hans Christian Öttinger. Bracket formulation of nonequilibrium thermodynamics for systems interacting with the environment. *Journal of Non-Newtonian Fluid Mechanics*, 152(1-3):2–11, jun 2008. ISSN 03770257. doi:10.1016/j.jnnfm.2007.10.017. URL `http://linkinghub.elsevier.com/retrieve/pii/S037702570700218 2http://www.sciencedirect.com/science/article/pii/S0377025707002182`.

16. A. K. Bhattacharjee, Gautam I. Menon, and R. Adhikari. Numerical method of lines for the relaxational dynamics of nematic liquid crystals. *Physical Review E*, 78(2): 026707, aug 2008. ISSN 1539-3755. doi:10.1103/PhysRevE.78.026707. URL `http://link.aps.org/doi/10.1103/PhysRevE.78.026707`.

17. A. K. Bhattacharjee, Gautam I. Menon, and R. Adhikari. Fluctuating dynamics of nematic liquid crystals using the stochastic method of lines. *The Journal of Chemical Physics*, 133(4):044112, aug 2010. ISSN 00219606. doi:10.1063/1.3455206. URL `http://link.aps.org/doi/10.1103/PhysRevE.78.026707http://scitation.aip.org/content/aip/journal/jcp/133/4/10.1063/1.3455206`.

18. K Binder. Time-dependent Ginzburg-Landau theory of nonequilibrium relaxation. *Physical Review B*, 8(7):3423–3438, 1973. ISSN 01631829. doi:10.1103/PhysRevB.8.3423. URL `https://journals.aps.org/prb/pdf/10.1103/PhysRevB.8.3423`.

19. S. Bono, Y. Takanishi, and J. Yamamoto. Isotropic-to-nematic phase transition of liquid crystals confined in nanoemulsion droplets. *EPL*, 109(2):26004, 2015. doi:10.1209/0295-5075/109/26004. URL https://doi.org/10.1209/0295-5075/109/26004.

20. Mark J Bowick and Luca Giomi. Two-dimensional matter: order, curvature and defects. *Advances in Physics*, 58:449–563, 6 2009. ISSN 0001-8732. doi:10.1080/00018730903043166.

21. J M Brake, M K Daschner, Y Y Luk, and N L Abbott. Biomolecular interactions at phospholipid-decorated surfaces of liquid crystals. *Science*, 302:2094–2097, 12 2003. ISSN 1095-9203. doi:10.1126/science.1091749.

22. G. P. Bryan-Brown, E. L. Wood, and I. C. Sage. Weak surface anchoring of liquid crystals. *Nature*, 399:338–340, 5 1999. ISSN 0028-0836. doi:10.1038/20646.

23. Emre Bukusoglu, Xiaoguang Wang, Jose a. Martinez-Gonzalez, Juan J de Pablo, and Nicholas L Abbott. Stimuli-responsive cubosomes formed from blue phase liquid crystals. *Advanced Materials*, 27:6892–6898, 11 2015. ISSN 0935-9648. doi:10.1002/adma.201503484.

24. Emre Bukusoglu, Xiaoguang Wang, Jose A. Martinez-Gonzalez, Juan J. Pablo, and Nicholas L. Abbott. Stimuli-responsive cubosomes formed from blue phase liquid crystals. *Advanced Materials*, 27(43):6892–98, 2015. doi:10.1002/adma.201503484. URL https://doi.org/10.1002/adma.201503484.

25. Emre Bukusoglu, Xiaoguang Wang, Ye Zhou, Jose Adrian Martinez-Gonzalez, Mohammad Rahimi, Qi Wang, Juan J de Pablo, and Nicholas L Abbott. Positioning colloids at the surfaces of cholesteric liquid crystal droplets. *Soft Matter*, pages 8781–8789, 2016. ISSN 1744-683X. doi:10.1039/C6SM01661H.

26. Emre Bukusoglu, Jose A. Martinez-Gonzalez, Xiaoguang Wang, Ye Zhou, Juan J. Pablo, and Nicholas L. Abbott. Strain-induced alignment and phase behavior of blue phase liquid crystals confined to thin films. *Soft Matter*, 13(47):8999–9006, 2017. doi:10.1039/C7SM01755C. URL https://doi.org/10.1039/C7SM01755C.

27. Agata Bąk and Wioletta Podgórska. Influence of poly(vinyl alcohol) molecular weight on drop coalescence and breakage rate. *Chemical Engineering Research and Design*, 108:88–100, 2016. doi:10.1016/j.cherd.2015.10.027. URL https://doi.org/https://doi.org/10.1016/j.cherd.2015.10.027.

28. E. Campanelli, S. Faetti, and M. Nobili. Azimuthal anchoring energy at the interface between a nematic liquid crystal and a ptfe substrate. *The European Physical Journal E - Soft Matter*, 11:199–209, 6 2003. ISSN 1292-8941. doi:10.1140/epje/i2002-10156-3.

29. Michael G Campbell, Mykola Tasinkevych, and Ivan I Smalyukh. Topological polymer dispersed liquid crystals with bulk nematic defect lines pinned to handlebody surfaces. *Physical Review Letters*, 112:197801, 6 2014. ISSN 1079-7114. doi:10.1103/PHYSREVLETT.112.197801/FIGURES/4/MEDIUM.

30. Wenyi Cao, Antonio Muñoz, Peter Palffy-Muhoray, and Bahman Taheri. Lasing in a three-dimensional photonic crystal of the liquid crystal blue phase ii. *Nature Materials*, 1:111–113, 10 2002. ISSN 1476-1122. doi:10.1038/nmat727.

31. L N Carenza, G Gonnella, D Marenduzzo, G Negro, and E Orlandini. Cholesteric shells: Two-dimensional blue fog and finite quasicrystals. *Physical Review Letters*, 128:27801, 6 2022. ISSN 1079-7114. doi:10.1103/PHYSREVLETT.128.027801/FIGURES/3/MEDIUM.

32. F Castles. A model for the pockels effect in distorted liquid crystal blue phases. *Applied Physics Letters*, 107:101106, 9 2015. ISSN 0003-6951. doi:10.1063/1.4930579.

33. F Castles, S M Morris, E M Terentjev, and H J Coles. Thermodynamically stable blue phases. *Physical Review Letters*, 104:157801, 4 2010. ISSN 0031-9007. doi:10.1103/PhysRevLett.104.157801.

34. F Castles, F V Day, S M Morris, D-H. Ko, D J Gardiner, M M Qasim, S Nosheen, P J W Hands, S S Choi, R H Friend, and H J Coles. Blue-phase templated fabrication of three-dimensional nanostructures for photonic applications. *Nature Materials*, 11: 599–603, 2012. ISSN 1476-1122. doi:10.1038/nmat3330.

35. F Castles, S M Morris, J M C Hung, M M Qasim, A D Wright, S Nosheen, S S Choi, B I Outram, S J Elston, C Burgess, L Hill, T D Wilkinson, and H J Coles. Stretchable liquid-crystal blue-phase gels. *Nature Materials*, 13:817–821, 6 2014. ISSN 1476-1122. doi:10.1038/nmat3993.

36. M. Cestari. *Atomistic modelling of liquid crystal materials properties: theoretical and computatonal methodoly.* Tesis doctoral, Scuola di Dottorato in Scienze Molecolari, Universit a Degli Studi di Padova., 2008.

37. Paul M. Chaikin and Tom C. Lubensky. *Principles of Condensed Matter Physics*. Cambridge University Press, 2000. ISBN 9780521794503.

38. E.G. Chatzi and C. Kiparissides. Drop size distributions in high holdup fraction dispersion systems: Effect of the degree of hydrolysis of pva stabilizer. *Chemical Engineering Science*, 49(24, Part 2):5039–52, 1994. doi:10.1016/0009-2509(94)00359-9. URL `https://doi.org/https://doi.org/10.1016/0009-2509(94)00359-9.`

39. Hui-Yu Chen, Che-Kai Wu, Fang-Chi Chen, and Chia-Sheng Chen. Investigation on morphology of polymer structure in polymer-stabilized blue phase. *Liquid Crystals*, 43:1351–1358, 8 2016. ISSN 0267-8292. doi:10.1080/02678292.2016.1173244.

40. M G Clerc, G González-Cortés, and S Echeverría-Alar. Localized dissipative vortices in chiral nematic liquid crystal cells. *Physical Review Research*, 4:L022021, 6 2022. ISSN 2643-1564. doi:10.1103/PHYSREVRESEARCH.4.L022021/FIGURES/5/MEDIUM.

41. H. J. Coles. Laser and electric field induced birefringence studies on the cyanobiphenyl homologues. *Molecular Crystals and Liquid Crystals*, 49(3):67–74, 1978. doi:10.1080/00268947808070330.

42. Harry J Coles and Mikhail N Pivnenko. Liquid crystal 'blue phases' with a wide temperature range. *Nature*, 436:997–1000, 2005. ISSN 1476-4687. doi:10.1038/nature03932.

43. J Crank and P. Nicolson. A practical method for numerical evaluation of solutions of partial differential equations of the heat-conduction type. *Mathematical Proceedings of the Cambridge Philosophical Society*, 43(1):50–67, 1947. ISSN 14698064. doi:10.1017/S0305004100023197. URL `https://link.springer.com/content/pdf/10.1007{%}2FBF02127704.pdf`.

44. Alexandre Darmon, Michael Benzaquen, David Seč, Simon Čopar, Olivier Dauchot, and Teresa Lopez-Leon. Waltzing route toward double-helix formation in cholesteric shells. *Proceedings of the National Academy of Sciences*, 113:9469–9474, 8 2016. ISSN 0027-8424. doi:10.1073/pnas.1525059113.

45. P. de Gennes and J Prost. *The Physics of Liquid Crystals*. Oxford University Press, 2nd edition, 1995. ISBN 0-19-852024-7.

46. P. G. de Gennes. Phenomenology of short-range-order effect in the isotropic phase of nematic materials. *Physics Letters*, 30(8):454–455, 1969.

47. P. G. de Gennes and J. Prost. *The Physics of Liquid Crystals*. Clarendon Press, Oxford, 2nd edition, 1993.

48. Sanjay Dharmavaram, Fangming Xie, William Klug, Joseph Rudnick, and Robijn Bruinsma. Orientational phase transitions and the assembly of viral capsids. *Physical Review E*, 062402:1–19, 6 2017. doi:10.1103/PhysRevE.95.062402.

49. Ingo Dierking, W Blenkhorn, E Credland, W Drake, R Kociuruba, B Kayser, and T Michael. Stabilising liquid crystalline blue phases. *Soft Matter*, 8:4355, 2012. ISSN 1744-683X. doi:10.1039/c2sm07155j.

50. Masao Doi. Molecular dynamics and rheological properties of concentrated solutions of rodlike polymers in isotropic and liquid crystalline phases. *Journal of Polymer Science: Polymer Physics Edition*, 19:229–243, 2 1981. ISSN 0098-1273. doi:10.1002/pol.1981.180190205.

51. P S Drzaic. *Liquid Crystal Dispersions*. World Scientific.

52. E Dubois-violette and B Pansu. Frustration and related topology of blue phases. *Molecular Crystals and Liquid Crystals Incorporating Nonlinear Optics*, 165:151–182, 1988. doi:10.1080/00268948808082200.

53. A Dupuis, D Marenduzzo, and J M Yeomans. Numerical calculations of the phase diagram of cubic blue phases in cholesteric liquid crystals. *Physical Review E*, 71: 11703, 1 2005. ISSN 1539-3755. doi:10.1103/PhysRevE.71.011703.

54. Sebastián Echeverría-Alar, Marcel G Clerc, and Ignacio Bordeu. Emergence of disordered branching patterns in confined chiral nematic liquid crystals. *Proceedings of the National Academy of Sciences*, 120:e2221000120, 6 2023. ISSN 1091-6490. doi:10.1073/PNAS.2221000120.

55. Perry W Ellis, Daniel J G Pearce, Ya Wen Chang, Guillermo Goldsztein, Luca Giomi, and Alberto Fernandez-Nieves. Curvature-induced defect unbinding and dynamics in active nematic toroids. *Nature Physics 2017 14:1*, 14:85–90, 6 2017. ISSN 1745-2481. doi:10.1038/nphys4276.

56. Perry W Ellis, Karthik Nayani, James P McInerney, D Zeb Rocklin, Jung Ok Park, Mohan Srinivasarao, Elisabetta A Matsumoto, and Alberto Fernandez-Nieves. Curvature-induced twist in homeotropic nematic tori. *Physical Review Letters*, 121:247803, 6 2018. ISSN 1079-7114. doi:10.1103/PHYSREVLETT.121.247803/FIGURES/4/MEDIUM.

57. John H. Erdmann, Slobodan Žumer, and J.William Doane. Configuration transition in a nematic liquid crystal confined to a small spherical cavity. *Physical Review Letters*, 64(16):1907–10, 1990. doi:10.1103/PhysRevLett.64.1907. URL `https://doi.org/10.1103/PhysRevLett.64.1907.`

58. J. L. Ericksen. Anisotropic fluids. *Archive for Rational Mechanics and Analysis*, 4(1): 231–237, January 1959. doi:10.1007/bf00281389.

59. P Etchegoin. Blue phases of cholesteric liquid crystals as thermotropic photonic crystals. *Physical Review E*, 62:1435–1437, 7 2000. ISSN 1063-651X. doi:10.1103/PhysRevE.62.1435.

60. Julian S Evans, Paul J Ackerman, Dirk J Broer, Jao van de Lagemaat, and Ivan I Smalyukh. Optical generation, templating, and polymerization of three-dimensional arrays of liquid-crystal defects decorated by plasmonic nanoparticles. *Physical Review E*, 87:32503, 3 2013. ISSN 1539-3755. doi:10.1103/PhysRevE.87.032503.

61. Mario L. Fabiilli, Kevin J. Haworth, Oliver D. Kripfgans, Paul L. Carson, and J. Brian Fowlkes. The role of inertial cavitation in acoustic droplet vaporization. volume 56, pages 768–771. IEEE, 11 2008. ISBN 978-1-4244-2428-3. doi:10.1109/ULTSYM.2008.0184.

62. A. Fernández-Nieves, V. Vitelli, A. S. Utada, D. R. Link, M. Márquez, D. R. Nelson, and D. A. Weitz. Novel defect structures in nematic liquid crystal shells. *Physical Review Letters*, 99:157801, 10 2007. ISSN 0031-9007. doi:10.1103/PhysRevLett.99.157801.

63. J. B. Fournier and P. Galatola. Modeling planar degenerate wetting and anchoring in nematic liquid crystals. *Europhysics Letters (EPL)*, 72(3):403–409, nov 2005. ISSN 0295-5075. doi:10.1209/epl/i2005-10253-5. URL http://stacks.iop.org/0295-5075/72/i=3/a=403?key=crossref.4fea3b19126763e6f41a2eee18491612.

64. J.-B Fournier and P Galatola. Modeling planar degenerate wetting and anchoring in nematic liquid crystals. *Europhysics Letters (EPL)*, 72:403–409, 11 2005. ISSN 0295-5075. doi:10.1209/epl/i2005-10253-5.

65. F C Frank. On the theory of liquid crystals. *Discussions of the Faraday Society*, 25: 19–28, 1958.

66. Jun Ichi Fukuda. Stabilization of blue phases by the variation of elastic constants. *Physical Review E*, 85:20701, 2 2012. ISSN 1539-3755. doi:10.1103/PhysRevE.85.020701.

67. Jun Ichi Fukuda and Slobodan Žumer. Novel defect structures in a strongly confined liquid-crystalline blue phase. *Physical Review Letters*, 104:1–4, 2010. ISSN 0031-9007. doi:10.1103/PhysRevLett.104.017801.

68. Jun Ichi Fukuda and Slobodan Žumer. Quasi-two-dimensional skyrmion lattices in a chiral nematic liquid crystal. *Nature Communications*, 2:246, 3 2011. ISSN 2041-1723. doi:10.1038/ncomms1250.

69. Y Geng, D Seč, P L Almeida, O D Lavrentovich, S Žumer, and M H Godinho. Liquid crystal necklaces: Cholesteric drops threaded by thin cellulose fibres. *Soft Matter*, 9: 7928–7933, 2013. ISSN 1744-683X. doi:10.1039/c3sm50900a.

70. Mohamed Amine Gharbi, Maurizio Nobili, Martin In, G Prevot, Paolo Galatola, J B Fournier, and Christophe Blanc. Behavior of colloidal particles at a nematic liquid crystal interface. *Soft Matter*, 7(4):1467–1471, 2011. ISSN 1744-683X. doi:10.1039/C0SM00863J. URL http://arxiv.org/abs/1007.0585$\backslash$n{\T1\textless}GotoISI{\T1\textgreater}://WOS:000287091600027$\backslash$nhttp://pubs.rsc.org/en/content/articlepdf/2011/sm/c0sm00863j.

71. Mohamed Amine Gharbi, Maurizio Nobili, and Christophe Blanc. Use of topological defects as templates to direct assembly of colloidal particles at nematic interfaces. *Journal of colloid and interface science*, 417:250–5, mar 2014. ISSN 1095-7103. doi:10.1016/j.jcis.2013.11.051. URL http://www.ncbi.nlm.nih.gov/pubmed/24407684.

72. Mohamed Amine Gharbi, Sabine Manet, Julien Lhermitte, Sarah Brown, Jonathan Milette, Violeta Toader, Mark Sutton, and Linda Reven. Reversible nanoparticle cubic lattices in blue phase liquid crystals. *ACS Nano*, 10:3410–3415, 3 2016. ISSN 1936-0851. doi:10.1021/acsnano.5b07379.

73. J A Gladysz, D P Curran, and I Horváth. *Handbook of Fluorous Chemistry*. Wiley, 7 2004. ISBN 9783527306176. doi:10.1002/3527603905.

74. A. Golemme, S. Zumer, D.W. Allender, and J.W. Doane. Continuous nematic-isotropic transition in submicron-size liquid-crystal droplets. *Physical Review Letters*, 61(26):2937–40, 1988. doi:10.1103/PhysRevLett.61.2937. URL https://doi.org/10.1103/PhysRevLett.61.2937.

75. Amy E. Goodling, Sara Nagelberg, Bryan Kaehr, Caleb H. Meredith, Seong Ik Cheon, Ashley P. Saunders, Mathias Kolle, and Lauren D. Zarzar. Colouration by total internal reflection and interference at microscale concave interfaces. *Nature*, 566:523–527, 2 2019. ISSN 0028-0836. doi:10.1038/s41586-019-0946-4.

76. EF Gramsbergen, L Longa, and WH de Jeu. Landau theory of the nematic-isotropic phase transition. *Physics Reports*, 4(4):195–257, 1986. URL http://www.sciencedirect.com/science/article/pii/0370157386900074.

77. T Gruhn and S Hess. Monte Carlo simulation of the director field of a nematic liquid crystal with three elastic coefficients. *Zeitschrift fur Naturforschung - Section A Journal of Physical Sciences*, 51(1-2):1–9, 1996. ISSN 09320784. URL https://www.degruyter.com/downloadpdf/j/zna.1996.51.issue-1-2/zna-1996-1-201/zna-1996-1-201.pdf.

78. Yuedong Gu and Nicholas L. Abbott. Observation of saturn-ring defects around solid microspheres in nematic liquid crystals. *Physical Review Letters*, 85:4719–4722, 11 2000. ISSN 0031-9007. doi:10.1103/PhysRevLett.85.4719.

79. Ankur Gupta, H.Burak Eral, T.Alan Hatton, and Patrick S. Doyle. Nanoemulsions: Formation, properties and applications. *Soft Matter*, 12(11):2826–41, 2016. doi:10.1039/C5SM02958A. URL https://doi.org/10.1039/C5SM02958A.

80. Jugal K. Gupta, Sri Sivakumar, Frank Caruso, and Nicholas L. Abbott. Size-dependent ordering of liquid crystals observed in polymeric capsules with micrometer and smaller diameters. *Angewandte Chemie - International Edition*, 48(9):1652–55, 2009. doi:10.1002/anie.200804500. URL https://doi.org/10.1002/anie.200804500.

81. O. Guzmán, E. B. Kim, S. Grollau, N. L. Abbott, and J. J. de Pablo. Defect structure around two colloids in a liquid crystal. *Physical Review Letters*, 91(23):235507, December 2003. doi:10.1103/physrevlett.91.235507.

82. Igor Gvozdovskyy. 'blue phases' of highly chiral thermotropic liquid crystals with a wide range of near-room temperature. *Liquid Crystals*, 42:1391–1404, 6 2015. ISSN 0267-8292. doi:10.1080/02678292.2015.1053001.

83. Igor Gvozdovskyy. Role of the photopolymerisation conditions in the broadening of the temperature range of the 'blue phases'. *Liquid Crystals*, 43:1813–1830, 9 2016. ISSN 0267-8292. doi:10.1080/02678292.2016.1213431.

84. O Henrich, K Stratford, D Marenduzzo, P V Coveney, and M E Cates. Confined cubic blue phases under shear. *Journal of Physics: Condensed Matter*, 24:284127, 7 2012. ISSN 0953-8984. doi:10.1088/0953-8984/24/28/284127.

85. S I Hernández, J A Moreno-Razo, A Ramírez-Hernández, E Díaz-Herrera, J P Hernández-Ortiz, and Juan J de Pablo. Liquid crystal nanodroplets, and the balance between bulk and interfacial interactions. *Soft Matter*, 8:1443–1450, 2012. ISSN 1744-683X. doi:10.1039/c1sm06425h.

86. Siegfried Hess. Irreversible thermodynamics of nonequilibrium alignment phenomena in molecular liquids and in liquid crystals. *Zeitschrift für Naturforschung A*, 30 (10):1224–1232, January 1975. doi:10.1515/zna-1975-1002.

87. Y. Hisakado, H. Kikuchi, T. Nagamura, and T. Kajiyama. Large electro-optic kerr effect in polymer-stabilized liquid-crystalline blue phases. *Advanced Materials*, 17(1): 96–98, 2005. doi:10.1002/adma.200400639. URL https://doi.org/10.1002/adma.200400639.

88. Pascal Hubert, Hanna Dreyfus, Daniel Guillon, and Yves Galerne. Anchoring orientation of nematic and smectic a liquid crystals on ptfe treated plates. *Journal de Physique II*, 5:1371–1383, 9 1995. ISSN 1155-4312. doi:10.1051/jp2:1995188.

89. Francisco R. Hung and Shivkumar Bale. Faceted nanoparticles in a nematic liquid crystal: defect structures and potentials of mean force. *Molecular Simulation*, 35(10-11):822–834, 2009. ISSN 0892-7022. doi:10.1080/08927020902801563.

90. Germano S. Iannacchione and Daniele Finotello. Calorimetric study of phase transitions in confined liquid crystals. *Physical Review Letters*, 69(14):2094–97, 1992. doi:10.1103/PhysRevLett.69.2094. URL https://doi.org/10.1103/PhysRevLett.69.2094.

91. G.S. Iannacchione, G.P. Crawford, S. Žumer, J.W. Doane, and D. Finotello. Randomly constrained orientational order in porous glass. *Physical Review Letters*, 71 (16):2595–98, 1993. doi:10.1103/PhysRevLett.71.2595. URL https://doi.org/10.1103/PhysRevLett.71.2595.

92. Michele Invernizzi, Omar Valsson, and Michele Parrinello. Coarse graining from variationally enhanced sampling applied to the Ginzburg–Landau model. *Proceedings of the National Academy of Sciences*, page 201618455, mar 2017. ISSN 0027-8424.

doi:10.1073/pnas.1618455114. URL http://www.pnas.org/lookup/doi/10.1073/pnas.1618455114.

93. Arman Javadi, Jonghee Eun, and Joonwoo Jeong. Cylindrical nematic liquid crystal shell: effect of saddle-splay elasticity. *Soft Matter*, 14:9005–9011, 2018. ISSN 1744-6848. doi:10.1039/c8sm01829d.

94. Joonwoo Jeong, Adam Gross, Wei-Shao Wei, Fuquan Tu, Daeyeon Lee, Peter J. Collings, and A. G. Yodh. Liquid crystal janus emulsion droplets: preparation, tumbling, and swimming. *Soft Matter*, 11:6747–6754, 2015. ISSN 1744-683X. doi:10.1039/C5SM01053E.

95. Joonwoo Jeong, Louis Kang, Zoey S Davidson, Peter J Collings, Tom C Lubensky, and A G Yodh. Chiral structures from achiral liquid crystals in cylindrical capillaries. *Proceedings of the National Academy of Sciences*, 112:E1837–E1884, 6 2015. ISSN 1091-6490. doi:10.1073/PNAS.1423220112/VIDEO-1.

96. Dalija Jesenek, Samo Kralj, Riccardo Rosso, and Epifanio G Virga. Defect unbinding on a toroidal nematic shell. *Soft Matter*, 11:2434–2444, 6 2015. ISSN 1744-6848. doi:10.1039/C4SM02540G.

97. Chenyu Jin, Carsten Krüger, and Corinna C. Maass. Chemotaxis and autochemotaxis of self-propelling droplet swimmers. *Proceedings of the National Academy of Sciences*, 114:5089–5094, 5 2017. ISSN 0027-8424. doi:10.1073/pnas.1619783114.

98. P Kaiser, W Wiese, and S Hess. Stability and instability of an uniaxial alignment against biaxial distortions in the isotropic and nematic phases of liquid crystals. *Journal of Non-Equilibrium Thermodynamics*, 17:153–170, 1992. ISSN 0340-0204. doi:10.1515/jnet.1992.17.2.153.

99. Randall D Kamien and Thomas R Powers. Determining the anchoring strength in a capillary using topological defects. *Liquid Crystals*, 23:213–216, 8 1997. ISSN 0267-8292. doi:10.1080/026782997208460.

100. Randall D Kamien and Jonathan V Selinger. Order and frustration in chiral liquid crystals. *Journal of Physics: Condensed Matter*, 13:R1–R22, 1 2001. ISSN 0953-8984. doi:10.1088/0953-8984/13/3/201.

101. A. V. Kaznacheev, M. M. Bogdanov, and A. S. Sonin. The influence of anchoring energy on the prolate shape of tactoids in lyotropic inorganic liquid crystals. *Journal of Experimental and Theoretical Physics*, 97(6):1159–1167, dec 2003. ISSN 1063-7761. doi:10.1134/1.1641899.

102. Emine Kemiklioglu and Liang chy Chien. Polymer-encapsulated blue phase liquid crystal droplets. *Applied Physics Express*, 7:91701, 9 2014. ISSN 1882-0778. doi:10.7567/APEX.7.091701.

103. Ibrahim Khan, Khalid Saeed, and Idrees Khan. Nanoparticles: Properties, applications and toxicities. *Arabian Journal of Chemistry*, 12(7):908–31, 2019. doi:10.1016/J.ARABJC.2017.05.011. URL https://doi.org/10.1016/J.ARABJC.2017.05.011.

104. H Kikuchi, M Yokota, Y Hisakado, H Yang, and T Kajiyama. Polymer-stabilized liquid crystal blue phases. *Nature Materials*, 1:64–68, 9 2002. ISSN 1476-1122. doi:10.1038/nmat712.

105. Jung-Whan Kim, Hojin Kim, Myoungbae Lee, and Jules J. Magda. Interfacial tension of a nematic liquid crystal/water interface with homeotropic surface alignment. *Langmuir*, 20:8110–8113, 9 2004. ISSN 0743-7463. doi:10.1021/la049843k.

106. Young-Ki Kim, Sergij V Shiyanovskii, and Oleg D Lavrentovich. Morphogenesis of defects and tactoids during isotropic-nematic phase transition in self-assembled lyotropic chromonic liquid crystals. *Journal of Physics: Condensed Matter*, 25:404202, 2013. ISSN 1361-648X. doi:10.1088/0953-8984/25/40/404202.

107. Young-Ki Kim, Xiaoguang Wang, Pranati Mondkar, Emre Bukusoglu, and Nicholas L. Abbott. Self-reporting and self-regulating liquid crystals. *Nature*, 557: 539–544, 5 2018. ISSN 0028-0836. doi:10.1038/s41586-018-0098-y.

108. Yun Ho Kim, Min-Jun Gim, Hee-Tae Jung, and Dong Ki Yoon. Periodic arrays of liquid crystalline torons in microchannels. *RSC Advances*, 5:19279–19283, 2015. ISSN 2046-2069. doi:10.1039/c4ra16883f.

109. Benjamin S. Kirk, John W. Peterson, Roy H. Stogner, and Graham F. Carey. libmesh : a c++ library for parallel adaptive mesh refinement/coarsening simulations. *Engineering with Computers*, 22:237–254, 12 2006. ISSN 0177-0667. doi:10.1007/s00366-006-0049-3.

110. M Kleman and O D Lavrentovich. *Soft Matter Physics : An Introduction*. Springer.

111. M Kleman and O D Lavrentovich. Topological point defects in nematic liquid crystals. *Philosophical Magazine*, 86:4117–4137, 9 2006. ISSN 1478-6435. doi:10.1080/14786430600593016.

112. T Kohyama, D M Kroll, and G Gompper. Budding of crystalline domains in fluid membranes. *Physical Review E*, 68:61905, 6 2003. ISSN 1063-651X. doi:10.1103/PhysRevE.68.061905.

113. Vinzenz Koning, Teresa Lopez-Leon, Alberto Fernandez-Nieves, and Vincenzo Vitelli. Bivalent defect configurations in inhomogeneous nematic shells. *Soft Matter*, 9:4993, 2013. ISSN 1744-683X. doi:10.1039/c3sm27671f.

114. Vinzenz Koning, Benjamin C van Zuiden, Randall D Kamien, and Vincenzo Vitelli. Saddle-splay screening and chiral symmetry breaking in toroidal nematics. *Soft Matter*, 10:4192, 2014. ISSN 1744-683X. doi:10.1039/c4sm00076e.

115. Mikhail N. Krakhalev, Anna P. Gardymova, Oxana O. Prishchepa, Vladimir Yu Rudyak, Alexander V. Emelyanenko, Jui-Hsiang Liu, and Victor Ya Zyryanov. Bipolar configuration with twisted loop defect in chiral nematic droplets under homeotropic surface anchoring. *Scientific Reports*, 7(1):14582, 2017. doi:10.1038/s41598-017-15049-6. URL https://doi.org/10.1038/s41598-017-15049-6.

116. Oliver D. Kripfgans, J.Brian Fowlkes, Douglas L. Miller, O.Petter Eldevik, and Paul L. Carson. Acoustic droplet vaporization for therapeutic and diagnostic applications. *Ultrasound in Medicine Biology*, 26:1177–1189, 9 2000. ISSN 0301-5629. doi:10.1016/S0301-5629(00)00262-3.

117. Carsten Krüger, Gunnar Klös, Christian Bahr, and Corinna C. Maass. Curling liquid crystal microswimmers: A cascade of spontaneous symmetry breaking. *Physical Review Letters*, 117:048003, 7 2016. ISSN 0031-9007. doi:10.1103/PhysRevLett.117.048003.

118. I M Kulić, D Andrienko, and M Deserno. Twist-bend instability for toroidal dna condensates. *Europhysics Letters (EPL)*, 67:418–424, 8 2004. ISSN 0295-5075. doi:10.1209/epl/i2004-10076-x.

119. Zdravko Kutnjak, George Cordoyiannis, George Nounesis, Andrija Lebar, Boštjan Zalar, and Slobodan Žumer. Calorimetric study of phase transitions in a liquid-crystal-based microemulsion. *The Journal of Chemical Physics*, 122(22):224709, 2005. doi:10.1063/1.1927516. URL https://doi.org/10.1063/1.1927516.

120. Nobu Kuzuu and Masao Doi. Constitutive equation for nematic liquid crystals under weak velocity gradient derived from a molecular kinetic equation. *Journal of the Physical Society of Japan*, 52(10):3486–3494, October 1983. doi:10.1143/jpsj.52.3486.

121. Sandia National Laboratories. Cubit v14.1, 2014.

122. L. D. Landau. The Theory of Phase Transitions. *Nature*, 138:840–841, 1936.

123. O. D. Lavrentovich. Topological defects in dispersed words and worlds around liquid crystals, or liquid crystal drops. *Liquid Crystals*, 24:117–126, 1 1998. ISSN 0267-8292. doi:10.1080/026782998207640.

124. F. M. Leslie. Some constitutive equations for anisotropic fluids. *The Quarterly Journal of Mechanics and Applied Mathematics*, 19(3):357–370, jan 1966. doi:10.1093/qjmam/19.3.357. URL https://academic.oup.com/qjmam/article-lookup/doi/10.1093/qjmam/19.3.357.

125. B. I. Lev, H. Yokoyama, S. B. Chernyshuk, and P. M. Tomchuk. Symmetry Breaking, Elastic Interaction and Structures in Nematic Colloids. *Molecular Crystals and Liquid Crystals*, 409(1):99–109, jan 2004. ISSN 1542-1406. doi:10.1080/15421400490435819. URL http://www.tandfonline.com/doi/abs/10.1080/15421400490435819.

126. Xiao Li, José A Mart{ı}nez-González, Juan P Hernández-Ortiz, Abelardo Ram{ı}rez-Hernández, Ye Zhou, Monirosadat Sadati, Rui Zhang, Paul F Nealey, and Juan J de Pablo. Mesoscale martensitic transformation in single crystals of topological defects. *Proceedings of the National Academy of Sciences*, 114:10011–10016, 9 2017. doi:10.1073/pnas.1711207114.

127. Xiao Li, José A Martínez-González, Orlando Guzmán, Xuedan Ma, Kangho Park, Chun Zhou, Yu Kambe, Hyeong Min Jin, James A Dolan, Paul F Nealey, and Juan J de Pablo. Sculpted grain boundaries in soft crystals. *Science Advances*, 5:9112–9141, 6 2019. ISSN 2375-2548. doi:10.1126/SCIADV.AAX9112/SUPPL_FILE/AAX9112_SM.PDF.

128. Xiaoye S Li. An overview of SuperLU: Algorithms, implementation, and user interface. *ACM Trans. Math. Softw.*, 31(3):302–325, 2005. ISSN 0098-3500. doi:10.1145/1089014.1089017. URL http://delivery.acm.org/10.1145/1090000/1089017/p302-li.pdf?ip=128.135.132.183{&}id=1089017{&}acc=ACTIVESERVICE{&}key=06A6A3A8AFB87403.37E789C11FBE2C91.4D4702B0C3E38B35.4D4702B0C3E38B35{&}{_}{_}acm{_}{_}=1517379952{_}176f69046a8063ec3cc7472296e86e78http://portal.acm.org/.

129. Yunfeng Li, Jeffrey Jun yan Suen, Elisabeth Prince, Egor M Larin, Anna Klinkova, Héloïse Thérien-Aubin, Shoujun Zhu, Bai Yang, Oleg D Lavrentovich, and Eugenia Kumacheva. Colloidal cholesteric liquid crystal in spherical confinement. *Nature Communications*, 7:12520, 2016. ISSN 2041-1723. doi:10.1038/ncomms12520.

130. Hsin-Ling Liang, Rudolf Zentel, Per Rudquist, and Jan Lagerwall. Towards tunable defect arrangements in smectic liquid crystal shells utilizing the nematic–smectic transition in hybrid-aligned geometries. *Soft Matter*, 8:5443, 2012. ISSN 1744-683X. doi:10.1039/c2sm07415j.

131. E. Liberty, F. Woolfe, P.-G. Martinsson, V. Rokhlin, and M. Tygert. Randomized algorithms for the low-rank approximation of matrices. *Proceedings of the National Academy of Sciences*, 104(51):20167–20172, dec 2007. ISSN 0027-8424. doi:10.1073/pnas.0709640104. URL http://www.pnas.org/cgi/doi/10.1073/pnas.0709640104.

132. Jack Lidmar, Leonid Mirny, and David R Nelson. Virus shapes and buckling transitions in spherical shells. *Physical Review E*, 68:51910, 6 2003. ISSN 1063-651X. doi:10.1103/PhysRevE.68.051910.

133. I-Hsin Lin, Gary M Koenig, Juan J de Pablo, and Nicholas L Abbott. Ordering of solid microparticles at liquid crystal-water interfaces. *The journal of physical chemistry. B*, 112(51):16552–8, dec 2008. ISSN 1520-6106. doi:10.1021/jp807286s. URL http://www.ncbi.nlm.nih.gov/pubmed/19049270.

134. I-Hsin Lin, Daniel S. Miller, Paul J. Bertics, Christopher J. Murphy, Juan J. de Pablo, and Nicholas L. Abbott. Endotoxin-induced structural transformations in liquid crystalline droplets. *Science*, 332:1297–1300, 6 2011. ISSN 0036-8075. doi:10.1126/science.1195639.

135. Tsung-Hsien Lin, Yannian Li, Chun-Ta Wang, Hung-Chang Jau, Chun-Wei Chen, Cheng-Chung Li, Hari Krishna Bisoyi, Timothy J Bunning, and Quan Li. Red, green and blue reflections enabled in an optically tunable self-organized 3d cubic nanostructured thin film. *Advanced Materials*, 25:5050–5054, 2013. ISSN 0935-9648. doi:10.1002/adma.201300798.

136. Alejandro Londoño-Hurtado, Julio C. Armas-Pérez, Juan P. Hernández-Ortiz, and Juan J. de Pablo. Homeotropic nano-particle assembly on degenerate planar nematic interfaces: films and droplets. *Soft Matter*, 11(25):5067–5076, 2015. ISSN 1744-683X. doi:10.1039/C5SM00940E. URL `http://pubs.rsc.org/en/Content/ArticleLanding/2015/SM/C5SM00940Ehttp://xlink.rsc.org/?DOI=C5SM00940E`.

137. Alejandro Londoño-Hurtado, Julio C Armas-Pérez, Juan P Hernández-Ortiz, and Juan J de Pablo. Homeotropic nano-particle assembly on degenerate planar nematic interfaces: films and droplets. *Soft Matter*, 11:5067–5076, 2015. ISSN 1744-683X. doi:10.1039/C5SM00940E.

138. Cheng Long and Jonathan V Selinger. Explicit demonstration of geometric frustration in chiral liquid crystals. *Soft Matter*, 19:519–529, 6 2022. ISSN 1744-6848. doi:10.1039/d2sm01420c.

139. T. Lopez-Leon and A. Fernandez-Nieves. Topological transformations in bipolar shells of nematic liquid crystals. *Physical Review E*, 79:021707, 2 2009. ISSN 1539-3755. doi:10.1103/PhysRevE.79.021707.

140. T. Lopez-Leon, V. Koning, K. B. S. Devaiah, V. Vitelli, and A. Fernandez-Nieves. Frustrated nematic order in spherical geometries. *Nature Physics*, 7:391–394, 5 2011. ISSN 1745-2473. doi:10.1038/nphys1920.

141. Teresa Lopez-Leon, Martin A Bates, and Alberto Fernandez-Nieves. Defect coalescence in spherical nematic shells. *Physical Review E - Statistical, Nonlinear, and Soft Matter Physics*, 86:1–4, 2012. ISSN 1539-3755. doi:10.1103/PhysRevE.86.030702.

142. Jean-Christophe Loudet, Philippe Barois, and Philippe Poulin. Colloidal ordering from phase separation in a liquid- crystalline continuous phase. *Nature*, 407:611–613, 10 2000. ISSN 0028-0836. doi:10.1038/35036539.

143. W. Maier and A. Saupe. Eine einfache molekulare Theorie des nematischen kristallinflüssigen Zustandes. *Zeitschrift Naturforschung Teil A*, 13:564–70, 1958.

144. G.I. Maksimochkin, S.V. Pasechnik, and A.G. Maksimochkin. Ultrasonic studies of structural transformations and phase transitions in liquid crystal emulsions. *Acoustical Physics*, 57(2):264–70, 2011. doi:10.1134/S1063771011020126. URL https://doi.org/10.1134/S1063771011020126.

145. Alexandra Manka, Harshad Pathak, Shinobu Tanimura, Judith Wölk, Reinhard Strey, and Barbara E. Wyslouzil. Freezing water in no-man's land. *Physical Chemistry Chemical Physics*, 14(13):4505–16, 2012. doi:10.1039/C2CP23116F. URL https://doi.org/10.1039/C2CP23116F.

146. José A Martínez-González, Ye Zhou, Mohammad Rahimi, Emre Bukusoglu, Nicholas L Abbott, and Juan J de Pablo. Blue-phase liquid crystal droplets. *Proceedings of the National Academy of Sciences*, 112:13195–13200, 10 2015. ISSN 0027-8424. doi:10.1073/pnas.1514251112.

147. James P McInerney, Perry W Ellis, D Zeb Rocklin, Alberto Fernandez-Nieves, and Elisabetta A Matsumoto. Curved boundaries and chiral instabilities – two sources of twist in homeotropic nematic tori. *Soft Matter*, 15:1210–1214, 6 2019. ISSN 1744-6848. doi:10.1039/C8SM02055H.

148. S. Meiboom, James P. Sethna, P.W. Anderson, and W.F. Brinkman. Theory of the blue phase of cholesteric liquid crystals. *Physical Review Letters*, 46(18):1216–19, 1981. doi:10.1103/PhysRevLett.46.1216. URL https://doi.org/10.1103/PhysRevLett.46.1216.

149. Michael Melle, Madlona Theile, Carol K Hall, and Martin Schoen. Nanoconfinement-induced structures in chiral liquid crystals. *International Journal of Molecular Sciences*, 14:17584–17607, 2013. ISSN 1661-6596. doi:10.3390/ijms140917584.

150. Daniel S. Miller, Xiaoguang Wang, and Nicholas L. Abbott. Design of functional materials based on liquid crystalline droplets. *Chemistry of Materials*, 26:496–506, 1 2014. ISSN 0897-4756. doi:10.1021/cm4025028.

151. DS Miller, Xiaoguang Wang, and NL Abbott. Design of Functional Materials Based on Liquid Crystalline Droplets. *Chemistry of Materials*, 26(1):496–506, 2013. URL http://pubs.acs.org/doi/abs/10.1021/cm4025028.

152. John W Milnor and David W Weaver. *Topology from the Differentiable Viewpoint*. Univ of Virginia Press, 1965.

153. J. a. Moreno-Razo, E. J. Sambriski, G. M. Koenig, E. Díaz-Herrera, N. L. Abbott, and J. J. de Pablo. Effects of anchoring strength on the diffusivity of nanoparticles in model liquid-crystalline fluids. *Soft Matter*, 7(15):6828, 2011. ISSN 1744-683X. doi:10.1039/c0sm01506g. URL http://xlink.rsc.org/?DOI=c0sm01506g.

154. Hiroyuki Mori, Eugene C Gartland, Jack R Kelly, and Philip J Bos. Multidimensional director modeling using the q tensor representation in a liquid crystal cell and its application to the it cell with patterned electrodes. *Japanese Journal of Applied Physics, Part 1: Regular Papers and Short Notes and Review Papers*, 38:135–146, 1999. ISSN 0021-4922. doi:10.1143/JJAP.38.135.

155. Paul A. Mountford, Alec N. Thomas, and Mark A. Borden. Thermal activation of superheated lipid-coated perfluorocarbon drops. *Langmuir*, 31:4627–4634, 4 2015. ISSN 0743-7463. doi:10.1021/acs.langmuir.5b00399.

156. I Musevic. Nematic colloids, topology and photonics. *Philosophical transactions. Series A, Mathematical, physical, and engineering sciences*, 371:20120266, 2013. ISSN 1364-503X. doi:10.1098/rsta.2012.0266.

157. Igor Muševič, Miha Škarabot, Uroš Tkalec, Miha Ravnik, and Slobodan Žumer. Two-dimensional nematic colloidal crystals self-assembled by topological defects. *Science*, 313:954–958, 8 2006. ISSN 0036-8075. doi:10.1126/science.1129660.

158. M. Muthukumar. Topological dereliction in polymers. *Computational Materials Science*, 4(4):370–372, nov 1995. ISSN 09270256. doi:10.1016/0927-0256(95)00043-7. URL `http://linkinghub.elsevier.com/retrieve/pii/0927025695000437`.

159. M Muthukumar. Chain entropy: Spoiler or benefactor in pattern recognition? *Proceedings of the National Academy of Sciences*, 96(21):11690–11692, oct 1999. ISSN 0027-8424. doi:10.1073/pnas.96.21.11690. URL `http://www.pubmedcentral.nih.gov/articlerender.fcgi?artid=33788{&}tool=pmcentrez{&}rendertype=abstracthttp://www.pnas.org/cgi/doi/10.1073/pnas.96.21.11690`.

160. Gaetano Napoli and Luigi Vergori. Influence of the extrinsic curvature on two-dimensional nematic films. *Physical Review E*, 97:52705, 2018. doi:10.1103/PhysRevE.97.052705.

161. Gaetano Napoli, Oleksandr V Pylypovskyi, Denis D Sheka, and Luigi Vergori. Nematic shells: new insights in topology- and curvature-induced effects. *Soft Matter*, 17:10322–10333, 6 2021. ISSN 1744-6848. doi:10.1039/D1SM00719J.

162. Karthik Nayani, Rui Chang, Jinxin Fu, Perry W Ellis, Alberto Fernandez-Nieves, Jung Ok Park, and Mohan Srinivasarao. Spontaneous emergence of chirality in achiral lyotropic chromonic liquid crystals confined to cylinders. *Nature Communications 2015 6:1*, 6:1–7, 6 2015. ISSN 2041-1723. doi:10.1038/ncomms9067.

163. Karthik Nayani, Prabin Rai, Nanqi Bao, Huaizhe Yu, Manos Mavrikakis, Robert J. Twieg, and Nicholas L. Abbott. Liquid crystals with interfacial ordering that enhances responsiveness to chemical targets. *Advanced Materials*, 30:1706707, 7 2018. ISSN 0935-9648. doi:10.1002/adma.201706707.

164. G Negro, L N Carenza, G Gonnella, D Marenduzzo, and E Orlandini. Topological phases and curvature-driven pattern formation in cholesteric shells. *Soft Matter*, 19: 1987–2000, 2023. doi:10.1039/d2sm01347a.

165. Xiangyi Nie, Ruibo Lu, Haiqing Xianyu, Thomas X. Wu, and Shin-Tson Wu. Anchoring energy and cell gap effects on liquid crystal response time. *Journal of Applied Physics*, 101:103110, 5 2007. ISSN 0021-8979. doi:10.1063/1.2734870.

166. Takasi Nisisako. Recent advances in microfluidic production of janus droplets and particles. *Current Opinion in Colloid Interface Science*, 25:1–12, 10 2016. ISSN 1359-0294. doi:10.1016/j.cocis.2016.05.003.

167. Hiroshi Noguchi, Caterina Tozzi, and Marino Arroyo. Binding of anisotropic curvature-inducing proteins onto membrane tubes. *Soft Matter*, 2022. ISSN 1744-6848. doi:10.1039/D2SM00274D.

168. Takeshi Noma, Masayoshi Ojima, Hiroaki Asagi, Yuichi Kawahira, Akihiko Fujii, Masanori Ozaki, and Hirotsugu Kikuchi. Effects of polymer network surfaces on expansion of cholesteric blue phases temperature. *E-Journal of Surface Science and Nanotechnology*, 6:17–20, 2008. doi:10.1380/ejssnt.2008.17. URL `https://doi.org/10.1380/ejssnt.2008.17.`

169. Emma M. Nomena, Caroline Remijn, Faranaaz Rogier, Micah van der Vaart, Panayiotis Voudouris, and Krassimir P. Velikov. Unravelling the mechanism of stabilization and microstructure of oil-in-water emulsions by native cellulose microfibrils in primary plant cells dispersions. *ACS Applied Bio Materials*, 1:1440–1447, 11 2018. ISSN 2576-6422. doi:10.1021/acsabm.8b00385.

170. Sepideh Norouzi, Antonio Tavera-Vazquez, Johanan Ramirez-De Arellano, Dae Seok Kim, Teresa Lopez-Leon, Juan J de Pablo, Jose A Martinez-Gonzalez, and Monirosadat Sadati. Elastic instability of cubic blue phase nano crystals in curved shells. *ACS Nano*, 16:15894–15906, 6 2022. ISSN 1936-086X. doi:10.1021/ACSNANO.2C02799/ASSET/IMAGES/MEDIUM/NN2C02799_M021.GIF.

171. Andriy Nych, Jun-ichi Fukuda, Uliana Ognysta, Slobodan Žumer, and Igor Muševič. Spontaneous formation and dynamics of half-skyrmions in a chiral liquid-crystal film. *Nature Physics*, 13, 2017.

172. Patrick W Oakes, Jorge Viamontes, and Jay X Tang. Growth of tactoidal droplets during the first-order isotropic to nematic phase transition of f-actin. *Physical Review E*, 75:1–11, 2007. ISSN 1539-3755. doi:10.1103/PhysRevE.75.061902.

173. Masayoshi Ojima, Takeshi Noma, Hiroaki Asagi, Akihiko Fujii, Masanori Ozaki, and Hirotsugu Kikuchi. Pinning effect of mixed cellulose ester membrane on appearance of cholesteric blue phases. *Applied Physics Express*, 2(2):7–10, 2009. doi:10.1143/APEX.2.021502. URL `https://doi.org/10.1143/APEX.2.021502.`

174. Peter D. Olmsted and Paul Goldbart. Theory of the nonequilibrium phase transition for nematic liquid crystals under shear flow. *Physical Review A*, 41(8):4578–4581, April 1990. doi:10.1103/physreva.41.4578.

175. R. J. Ondris-Crawford, G. P. Crawford, Slobodan Žumer, and J. W. Doane. Curvature-induced configuration transition in confined nematic liquid crystals. *Physical Review Letters*, 70(2):194–198, 1993. URL `http://link.aps.org/doi/10.1103/PhysRevLett.70.194`.

176. R J Ondris-Crawford, G P Crawford, Slobodan Žumer, and J W Doane. Curvature-induced configuration transition in confined nematic liquid crystals. *Physical Review Letters*, 70:194–198, 1993. doi:10.1103/PhysRevLett.70.194.

177. L. Onsager. The effects of shape on the interaction of colloidal particles. *Annals of the New York Academy of Sciences*, 51:627–59, 1949.

178. Tetiana Orlova, Sarah Jane Aßhoff, Tadatsugu Yamaguchi, Nathalie Katsonis, and Etienne Brasselet. Creation and manipulation of topological states in chiral nematic microspheres. *Nature Communications*, 6:7603, 2015. ISSN 2041-1723. doi:10.1038/ncomms8603.

179. C W Oseen. The theory of liquid crystals. *Transactions of the Faraday Society*, 29: 883–899, 1933.

180. Tim Osswald and Juan P. Hernández-Ortiz. *Polymer processing : modeling and simulation*. Hanser Publishers, Munich Cincinnati, 2006. ISBN 978-3-446-40381-9.

181. Ekapop Pairam, Jayalakshmi Vallamkondu, Vinzenz Koning, Benjamin C van Zuiden, Perry W Ellis, Martin A Bates, Vincenzo Vitelli, and Alberto Fernandez-Nieves. Stable nematic droplets with handles. *Proceedings of the National Academy of Sciences*, 110:9295–9300, 6 2013. ISSN 0027-8424. doi:10.1073/pnas.1221380110.

182. V Palacio-Betancur, J C Armas-Pérez, S Villada-Gil, N L Abbott, J P Hernández-Ortiz, and J J de Pablo. Cuboidal liquid crystal phases under multiaxial geometrical frustration. *Soft Matter*, 16:870–880, 2020. ISSN 1744-6848. doi:10.1039/c9sm02021g.

183. M B Pandey, P J Ackerman, A Burkart, T Porenta, S Žumer, and I Smalyukh. Topology and self-assembly of defect-colloidal superstructure in confined chiral nematic liquid crystals. *Physical Review E*, 91:12501, 2015. doi:10.1103/PhysRevE.91.012501.

184. Marco A. Bedolla Pantoja, Yu Yang, and Nicholas L. Abbott. Toluene-induced phase transitions in blue phase liquid crystals. *Liquid Crystals*, 46:1925–1936, 11 2019. ISSN 0267-8292. doi:10.1080/02678292.2019.1633432.

185. M Papoular and A Rapini. Surface waves in nematic liquid crystals. *Solid State Communications*, 7:1639–1641, 1969. ISSN 0038-1098. doi:10.1016/0038-1098(69)90045-3.

186. O. Parodi. Stress tensor for a nematic liquid crystal. *Journal de Physique*, 31(7):581–584, 1970. doi:10.1051/jphys:01970003107058100.

187. Kamla Pathak, Satyanarayan Pattnaik, and Kalpana Swain. Chapter 13 - application of nanoemulsions in drug delivery. In Seid Mahdi Jafari and David Julian B. T, editors, *Nanoemusions- Formulations, Applications and Characterization*. 2018. doi:10.1016/B978-0-12-811838-2.00013-8. URL https://doi.org/https://doi.org/10.1016/B978-0-12-811838-2.00013-8. - Nanoemulsions McClements, 415–33. Academic Press.

188. D J G Pearce. Coupling the topological defect phase to the extrinsic curvature in nematic shells. *Soft Matter*, 18:5082–5088, 6 2022. ISSN 1744-6848. doi:10.1039/D2SM00602B.

189. Karthik Peddireddy, Simon Čopar, Khoa V Le, Igor Muševič, Christian Bahr, and Venkata S R Jampani. Self-shaping liquid crystal droplets by balancing bulk elasticity and interfacial tension. *Proceedings of the National Academy of Sciences*, 118:e2011174118, 6 2021. ISSN 1091-6490. doi:10.1073/PNAS.2011174118/SUPPL_FILE/PNAS.2011174118.SM04.MP4.

190. Andrea Pedrini and Epifanio G Virga. Instability of toroidal nematics. *https://doi.org/10.1080/02678292.2018.1495771*, 45:2054–2064, 6 2018. ISSN 1366-5855. doi:10.1080/02678292.2018.1495771.

191. Chenhui Peng and Oleg D Lavrentovich. Chirality amplification and detection by tactoids of lyotropic chromonic liquid crystals. *Soft Matter*, 11:7257–7263, 2015. doi:10.1039/c5sm01632k.

192. Haiyan Peng, Wenhong Jiang, Qingkun Liu, Guannan Chen, Mingli Ni, Fuxin Liang, Yonggui Liao, Xiaolin Xie, and Ivan I. Smalyukh. Liquid crystals under confinement in submicrometer capsules. *Langmuir*, 34(37):10955–63, 2018. doi:10.1021/acs.langmuir.8b01056. URL https://doi.org/10.1021/acs.langmuir.8b01056.

193. J Pišljar, S Ghosh, S Turlapati, N V S Rao, M Škarabot, A Mertelj, A Petelin, A Nych, M Marinčič, A Pusovnik, M Ravnik, and I Muševič. Blue phase iii: Topological fluid of skyrmions. *Physical Review X*, 12, 6 2022. ISSN 2160-3308. doi:10.1103/PhysRevX.12.011003.

194. Harald Pleiner, Mario Liu, and Helmut R. Brand. Convective nonlinearities for the orientational tensor order parameter in polymeric systems. *Rheologica Acta*, 41(4): 375–382, January 2002. doi:10.1007/s00397-002-0237-z.

195. Guilhem Poy, Andrew J Hess, Andrew J Seracuse, Michael Paul, Slobodan Žumer, and Ivan I Smalyukh. Interaction and co-assembly of optical and topological solitons. *Nature Photonics*, 16:454–461, 6 2022. ISSN 1749-4885. doi:10.1038/s41566-022-01002-1.

196. M. J. Press and A. S. Arrott. Theory and experiments on configurations with cylindrical symmetry in liquid-crystal droplets. *Physical Review Letters*, 33:403–406, 8 1974. ISSN 0031-9007. doi:10.1103/PhysRevLett.33.403.

197. Mohammad Rahimi, Tyler F Roberts, Julio C Armas-Pérez, Xiaoguang Wang, Emre Bukusoglu, Nicholas L Abbott, and Juan J de Pablo. Nanoparticle self-assembly at the interface of liquid crystal droplets. *Proceedings of the National Academy of Sciences*, 112:5297–5302, 2015. ISSN 0027-8424, 1091-6490. doi:10.1073/pnas.1422785112.

198. M D Asiqur Rahman, Suhana Mohd Said, and S Balamurugan. Blue phase liquid crystal: strategies for phase stabilization and device development. *Science and Technology of Advanced Materials*, 16:033501, 6 2015. ISSN 1468-6996. doi:10.1088/1468-6996/16/3/033501.

199. Miha Ravnik and Jun ichi Fukuda. Templated blue phases. *Soft Matter*, 4:1166–1169, 2015. ISSN 1744-683X. doi:10.1039/C5SM01878A.

200. Miha Ravnik and Jaka Pišljar. Lensing and waveguiding in birefringent double-twist cylinders demonstrated using fdtd simulations. *Optics Express, Vol. 26, Issue 20, pp. 26327-26338*, 26:26327–26338, 6 2018. ISSN 1094-4087. doi:10.1364/OE.26.026327.

201. Miha Ravnik and Slobodan Zumer. Landau–de Gennes modelling of nematic liquid crystal colloids. *Liquid Crystals*, 36(10-11):1201–1214, 2009. doi:10.1080/02678290903056095.

202. Miha Ravnik, Gareth P Alexander, Julia M Yeomans, and Slobodan Žumer. Three-dimensional colloidal crystals in liquid crystalline blue phases. *Proceedings of the National Academy of Sciences of the United States of America*, 108:5188–5192, 2011. ISSN 0027-8424. doi:10.1073/pnas.1015831108.

203. G. Rienäcker, M. Kröger, and S. Hess. Chaotic and regular shear-induced orientational dynamics of nematic liquid crystals. *Physica A: Statistical Mechanics and its Applications*, 315(3-4):537–568, 2002. ISSN 0378-4371. doi:10.1016/S0378-4371(02)01008-7.

204. Laura Rossi, Stefano Sacanna, William T. M. Irvine, Paul M. Chaikin, David J. Pine, and Albert P. Philipse. Cubic crystals from cubic colloids. *Soft Matter*, 7(9):4139–4142, 2011. doi:10.1039/c0sm01246g.

205. Laura Rossi, Vishal Soni, Douglas J. Ashton, David J. Pine, Albert P. Philipse, Paul M. Chaikin, Marjolein Dijkstra, Stefano Sacanna, and William T. M. Irvine. Shape-sensitive crystallization in colloidal superball fluids. *Proceedings of the National Academy of Sciences*, 112(17):5286–5290, April 2015. doi:10.1073/pnas.1415467112.

206. R W Ruhwandl and E M Terentjev. Monte Carlo simulation of topological defects in the nematic liquid crystal matrix around a spherical colloid particle. *Physical Review*

E - Statistical Physics, Plasmas, Fluids, and Related Interdisciplinary Topics, 56(5):5561–5565, 1997. ISSN 1063651X. doi:10.1103/PhysRevE.56.5561. URL https://journals.aps.org/pre/pdf/10.1103/PhysRevE.56.5561.

207. Monirosadat Sadati, Aslin Izmitli Apik, Julio C Armas-Pérez, José A Martínez-González, Juan P Hernández-Ortiz, Nicholas L Abbott, and Juan J de Pablo. Liquid crystal enabled early stage detection of beta amyloid formation on lipid monolayers. *Advanced Functional Materials*, 25:6050–6060, 2015. ISSN 1616-3028. doi:10.1002/adfm.201502830.

208. Monirosadat Sadati, Hadi Ramezani-Dakhel, Wei Bu, Emre Sevgen, Zhu Liang, Cem Erol, Mohammad Rahimi, Nader Taheri Qazvini, Binhua Lin, Nicholas L. Abbott, Benoı
t Roux, Mark L. Schlossman, and Juan J. de Pablo. Molecular structure of canonical liquid crystal interfaces. *Journal of the American Chemical Society*, 139(10):3841–3850, March 2017. doi:10.1021/jacs.7b00167. URL https://doi.org/10.1021/jacs.7b00167.

209. Monirosadat Sadati, Ye Zhou, Drew Melchert, Ashley Guo, Jose A. Martinez-Gonzalez, Tyler F. Roberts, Rui Zhang, and Juan J. de Pablo. Spherical nematic shells with a prolate ellipsoidal core. *Soft Matter*, 13:7465–7472, 2017. ISSN 1744-683X. doi:10.1039/C7SM01403A.

210. Monirosadat Sadati, Jose A Martinez-Gonzalez, Ye Zhou, Nader Taheri Qazvini, Khia Kurtenbach, Xiao Li, Emre Bukusoglu, Rui Zhang, Nicholas L Abbott, Juan Pablo Hernandez-Ortiz, and Juan J DePablo. Prolate and oblate chiral liquid crystal spheroids. *Science Advances*, 6, 6 2020. ISSN 2375-2548. doi:10.1126/SCIADV.ABA6728.

211. Monirosadat Sadati, Jose A Martinez-Gonzalez, Alexander Cohen, Sepideh Norouzi, Orlando Guzmán, and Juan J de Pablo. Control of monodomain polymer-stabilized cuboidal nanocrystals of chiral nematics by confinement. *ACS Nano*, 15:15972–15981, 6 2021. ISSN 1936-0851. doi:10.1021/acsnano.1c04231.

212. Mirosław Salamończyk, Nataša Vaupotič, Damian Pociecha, Cheng Wang, Chenhui Zhu, and Ewa Gorecka. Structure of nanoscale-pitch helical phases: Blue phase and twist-bend nematic phase resolved by resonant soft x-ray scattering. *Soft Matter*, 13 (38):6694–99, 2017. doi:10.1039/C7SM00967D. URL https://doi.org/10.1039/C7SM00967D.

213. Sadaki Samitsu, Yoichi Takanishi, and Jun Yamamoto. Molecular manipulator driven by spatial variation of liquid-crystalline order. *Nature Materials*, 9(10):816–820, oct 2010. ISSN 1476-1122. doi:10.1038/nmat2853. URL http://dx.doi.org/10.1038/nmat2853http://www.nature.com/doifinder/10.1038/nmat2853.

214. Alfred Saupe. On Molecular Structure and Physical Properties of Thermotropic Liquid Crystals. *Molecular Crystals*, 7(1):59–74, jun 1969. ISSN 0369-1152. doi:10.1080/15421406908084865. URL http://www.tandfonline.com/doi/abs/10.1080/15421406908084865{#}.VMffvWjF830.

215. David Seč, Teresa Lopez-Leon, Maurizio Nobili, Christophe Blanc, Alberto Fernandez-Nieves, Miha Ravnik, and Slobodan Žumer. Defect trajectories in nematic shells: Role of elastic anisotropy and thickness heterogeneity. *Physical Review E*, 86:020705, 8 2012. ISSN 1539-3755. doi:10.1103/PhysRevE.86.020705.

216. David Seč, Simon Copar, and Slobodan Zumer. Topological zoo of free-standing knots in confined chiral nematic fluids. *Nature communications*, 5:3057, 2014. ISSN 2041-1723. doi:10.1038/ncomms4057.

217. Rahul R. Shah and Nicholas L. Abbott. Principles for measurement of chemical exposure based on recognition-driven anchoring transitions in liquid crystals. *Science*, 293:1296–1299, 8 2001. ISSN 0036-8075. doi:10.1126/science.1062293.

218. Arshdeep Singh, Praveen Malik, and Divya Jayoti. Observation of blue phase in chiral nematic liquid crystal and its stabilization by silica nanoparticles. *International Journal of Modern Physics B*, 30:1650011, 2 2016. ISSN 0217-9792. doi:10.1142/S0217979216500119.

219. Sergei Slussarenko, Alessandro Alberucci, Chandroth P Jisha, Bruno Piccirillo, Enrico Santamato, Gaetano Assanto, and Lorenzo Marrucci. Guiding light via geometric phases. *Nature Photonics 2016 10:9*, 10:571–575, 6 2016. ISSN 1749-4893. doi:10.1038/nphoton.2016.138.

220. Kostyantyn Slyusarenko, Christophe Blanc, Yuriy Reznikov, and Maurizio Nobili. Quenched disorder of a nematic liquid crystal under a magnetic field. *Journal of Molecular Liquids*, 267:100–108, 10 2018. ISSN 0167-7322. doi:10.1016/j.molliq.2018.02.055.

221. I. I. Smalyukh, S. Chernyshuk, B. I. Lev, A. B. Nych, U. Ognysta, V. G. Nazarenko, and O. D. Lavrentovich. Ordered droplet structures at the liquid crystal surface and elastic-capillary colloidal interactions. *Physical review letters*, 93:117801, September 2004. doi:10.1103/PhysRevLett.93.117801.

222. I. I. Smalyukh, O. D. Lavrentovich, A. N. Kuzmin, A. V. Kachynski, and P. N. Prasad. Elasticity-Mediated Self-Organization and Colloidal Interactions of Solid Spheres with Tangential Anchoring in a Nematic Liquid Crystal. *Physical Review Letters*, 95 (15):157801, oct 2005. ISSN 0031-9007. doi:10.1103/PhysRevLett.95.157801. URL http://link.aps.org/doi/10.1103/PhysRevLett.95.157801.

223. A. Sonnet, A. Kilian, and S. Hess. Alignment tensor versus director: Description of defects in nematic liquid crystals. *Phys. Rev. E*, 52:718–722, July 1995. doi:10.1103/PhysRevE.52.718.

224. G. J. Sprokel. Molecular order induced by cell walls: Part i, experimental results. *Molecular Crystals and Liquid Crystals*, 42:233–248, 1 1977. ISSN 0026-8941. doi:10.1080/15421407708084510.

225. G. J. Sprokel and R. M. Gibson. Liquid crystal alignment produced by rf plasma deposited films. *Journal of The Electrochemical Society*, 124:557–561, 4 1977. ISSN 0013-4651. doi:10.1149/1.2133350.

226. Christopher M. Stafford, Bryan D. Vogt, Christopher Harrison, Duangrut Julthongpiput, and Rui Huang. Elastic moduli of ultrathin amorphous polymer films. *Macromolecules*, 39(15):5095–99, 2006. doi:10.1021/ma060790i. URL https://doi.org/10.1021/ma060790i.

227. H. Stark and T. C. Lubensky. Poisson-bracket approach to the dynamics of nematic liquid crystals. *Physical Review E*, pages 1–11, 2003. doi:10.1103/PhysRevE.67.061709. URL http://pre.aps.org/abstract/PRE/v67/i6/e061709.

228. Holger Stark. Saturn-ring defects around microspheres suspended in nematic liquid crystals: An analogy between confined geometries and magnetic fields. *Physical Review E*, 66:032701, 9 2002. ISSN 1063-651X. doi:10.1103/PhysRevE.66.032701.

229. Michael J Stephen and Joseph P Straley. Physics of liquid crystals. *Reviews of Modern Physics*, 46:617–704, 1974. ISSN 0034-6861. doi:10.1103/RevModPhys.46.617.

230. Norbert Stoop and Jörn Dunkel. Defect formation dynamics in curved elastic surface crystals. *Soft Matter*, 14:2329–2338, 2018. ISSN 1744-6848. doi:10.1039/c7sm02233f.

231. A. Strigazzi. On the surface-type elastic constant k24 in nematics. *Molecular Crystals and Liquid Crystals*, 152:435–45, 1987.

232. Devika Venkuzhy Sudhakaran, Ravi Kumar Pujala, and Surajit Dhara. Orientation dependent interaction and self-assembly of cubic magnetic colloids in a nematic liquid crystal. *Advanced Optical Materials*, page 1901585, January 2020. doi:10.1002/adom.201901585. URL https://doi.org/10.1002/adom.201901585.

233. Mariko Suga, Saori Suda, Masatoshi Ichikawa, and Yasuyuki Kimura. Self-propelled motion switching in nematic liquid crystal droplets in aqueous surfactant solutions. *Physical Review E*, 97:062703, 6 2018. ISSN 2470-0045. doi:10.1103/PhysRevE.97.062703.

234. Tadao Sugimoto, Mohammad M. Khan, and Atsushi Muramatsu. Preparation of monodisperse peanut-type α-fe2o3 particles from condensed ferric hydroxide gel. *Colloids and Surfaces A: Physicochemical and Engineering Aspects*, 70(2):167–169, March 1993. doi:10.1016/0927-7757(93)80285-m.

235. Toyoko Suzuki, Yunfeng Li, Albert Gevorkian, and Eugenia Kumacheva. Compound droplets derived from a cholesteric suspension of cellulose nanocrystals. *Soft Matter*, 14:9713–9719, 2018. ISSN 1744-683X. doi:10.1039/C8SM01716F.

236. Tibor Szilvási, Nanqi Bao, Karthik Nayani, Huaizhe Yu, Prabin Rai, Robert J. Twieg, Manos Mavrikakis, and Nicholas L. Abbott. Redox-triggered orientational responses of liquid crystals to chlorine gas. *Angewandte Chemie*, 130:9813–9817, 7 2018. ISSN 0044-8249. doi:10.1002/ange.201803194.

237. Tharwat Tadros, P Izquierdo, J Esquena, and C Solans. Formation and stability of nano-emulsions. *Advances in Colloid and Interface Science*, 108-109:303–318, 5 2004. ISSN 0001-8686. doi:10.1016/j.cis.2003.10.023.

238. Yuta Tamura and Yasuyuki Kimura. Fabrication of ring assemblies of nematic colloids and their electric response. *Applied Physics Letters*, 108(1):011903, jan 2016. ISSN 0003-6951. doi:10.1063/1.4939627. URL `http://scitation.aip.org/content/aip/journal/apl/108/1/10.1063/1.4939627`.

239. Mykola Tasinkevych, Michael G Campbell, and Ivan I Smalyukh. Splitting, linking, knotting, and solitonic escape of topological defects in nematic drops with handles. *Proceedings of the National Academy of Sciences*, 111:16268–16273, 11 2014. ISSN 0027-8424. doi:10.1073/pnas.1405928111.

240. J. Thoen. Adiabatic scanning calorimetric results for the blue phases of cholesteryl nonanoate. *Physical Review A*, 37(5):1754–59, 1988. doi:10.1103/PhysRevA.37.1754. URL `https://doi.org/10.1103/PhysRevA.37.1754.`

241. A. Tiribocchi, G. Gonnella, D. Marenduzzo, and E. Orlandini. Switching dynamics in cholesteric blue phases. *Soft Matter*, 7:3295, 2011. ISSN 1744-683X. doi:10.1039/c0sm00979b.

242. A. Tiribocchi, M. E. Cates, G. Gonnella, D. Marenduzzo, and E. Orlandini. Flexoelectric switching in cholesteric blue phases. *Soft Matter*, 9:4831, 2013. ISSN 1744-683X. doi:10.1039/c3sm50317h.

243. Uroš Tkalec, Miha Ravnik, Simon Čopar, Slobodan Žumer, and Igor Muševič. Reconfigurable knots and links in chiral nematic colloids. *Science*, 333:62–65, 6 2011. ISSN 0036-8075. doi:10.1126/SCIENCE.1205705/SUPPL_FILE/TKALEC-SOM.PDF.

244. V. Tomar, S.I. Hernández, N.L. Abbott, J.P. Hernández-Ortiz, and J.J. Pablo. Morphological transitions in liquid crystal nanodroplets. *Soft Matter*, 8(33):8679, 2012. doi:10.1039/c2sm25383f. URL `https://doi.org/10.1039/c2sm25383f.`

245. Oychai Tongcher, Reinhard Sigel, and Katharina Landfester. Liquid crystal nanoparticles prepared as miniemulsions. *Langmuir*, 22(10):4504–11, 2006. doi:10.1021/la052857l. URL `https://doi.org/10.1021/la052857l.`

246. Luana Tortora and Oleg D. Lavrentovich. Chiral symmetry breaking by spatial confinement in tactoidal droplets of lyotropic chromonic liquid crystals. *Proceedings of the National Academy of Sciences*, 108:5163–5168, 3 2011. ISSN 0027-8424. doi:10.1073/pnas.1100087108.

247. S. Torza and S. G. Mason. Coalescence of two immiscible liquid drops. *Science*, 163: 813–814, 2 1969. ISSN 0036-8075. doi:10.1126/science.163.3869.813.

248. J. R. Tucker and B. I. Halperin. Onset of Superconductivity in One-Dimensional Systems. *Physical Review B*, 4(11):369–249, 1966. URL `https://journals.aps.org/prb/pdf/10.1103/PhysRevB.3.3768`.

249. Reidun Twarock. Mathematical virology: a novel approach to the structure and assembly of viruses. *Philosophical transactions. Series A, Mathematical, physical, and engineering sciences*, 364(1849):3357–3373, 2006. ISSN 1364-503X. doi:10.1098/rsta.2006.1900.

250. Martin Urbanski. On the impact of nanoparticle doping on the electro-optic response of nematic hosts. *Liquid Crystals Today*, 24(4):102–115, oct 2015. ISSN 1358-314X. doi:10.1080/1358314X.2015.1059586. URL `http://www.tandfonline.com/doi/full/10.1080/1358314X.2015.1059586`.

251. Martin Urbanski, Catherine G Reyes, JungHyun Noh, Anshul Sharma, Yong Geng, Venkata Subba Rao Jampani, and Jan P F Lagerwall. Liquid crystals in micron-scale droplets, shells and fibers. *Journal of Physics: Condensed Matter*, 29:133003, 4 2017. ISSN 0953-8984. doi:10.1088/1361-648X/aa5706.

252. Davide Vanzo, Matteo Ricci, Roberto Berardi, and Claudio Zannoni. Shape, chirality and internal order of freely suspended nematic nanodroplets. *Soft Matter*, 8:11790, 2012. ISSN 1744-683X. doi:10.1039/c2sm27114a.

253. Stiven Villada-Gil, Viviana Palacio-Betancur, Julio C Armas-Pérez, Juan J de Pablo, and Juan P Hernández-Ortiz. Fluctuations and phase transitions of uniaxial and biaxial liquid crystals using a theoretically informed monte carlo and a landau free energy density. *Journal of Physics: Condensed Matter*, 31:175101, 5 2019. ISSN 0953-8984. doi:10.1088/1361-648X/ab0394.

254. Vincenzo Vitelli, J B Lucks, and D R Nelson. Crystallography on curved surfaces. *Proceedings of the National Academy of Sciences*, 103:12323–12328, 6 2006. ISSN 0027-8424. doi:10.1073/pnas.0602755103.

255. D. Voloschenko, O. P. Pishnyak, S. V. Shiyanovskii, and O. D. Lavrentovich. Effect of director distortions on morphologies of phase separation in liquid crystals. *Physical Review E*, 65(6):060701, jun 2002. ISSN 1063-651X. doi:10.1103/PhysRevE.65.060701. URL `http://link.aps.org/doi/10.1103/PhysRevE.65.060701`.

256. G E Volovik and O D Lavrentovich. Topological dynamics of defects: Boojums in nematic drops. *Sov. Phys. JETP*, 58:1159–1166.

257. Charlie R Wand and Martin A Bates. Chiral nematic liquid crystals in torus-shaped and cylindrical cavities. *Physical Review E*, 100, 6 2019. ISSN 2470-0053. doi:10.1103/PhysRevE.100.052702.

258. Pei-Xi Wang and Mark J. MacLachlan. Liquid crystalline tactoids: ordered structure, defective coalescence and evolution in confined geometries. *Philosophical Transactions of the Royal Society A: Mathematical, Physical and Engineering Sciences*, 376: 20170042, 2 2018. ISSN 1364-503X. doi:10.1098/rsta.2017.0042.

259. Pei-Xi Wang, Wadood Y. Hamad, and Mark J. MacLachlan. Size-selective exclusion effects of liquid crystalline tactoids on nanoparticles: A separation method. *Angewandte Chemie International Edition*, 57:3360–3365, 3 2018. ISSN 1433-7851. doi:10.1002/anie.201712158.

260. X Wang, Y Zhou, V Palacio-Betancur, Y.-K. Kim, L Delalande, M Tsuei, Y Yang, J J de Pablo, and N L Abbott. Reconfigurable multicompartment emulsion drops formed by nematic liquid crystals and immiscible perfluorocarbon oils. *Langmuir*, 35:16312–16323, 2019. ISSN 1520-5827. doi:10.1021/acs.langmuir.9b02864.

261. Xiaoguang Wang, Daniel S Miller, Juan J de Pablo, Nicholas L Abbott, J De Pablo, and Nicholas L Abbott. Organized assemblies of colloids formed at the poles of micrometer-sized droplets of liquid crystal. *Soft matter*, 10(44):8821–8, 2014. ISSN 1744-6848. doi:10.1039/c4sm01784f. URL `http://pubs.rsc.org/en/content/articlehtml/2014/sm/c4sm01784f`.

262. Xiaoguang Wang, Young-Ki Kim, Emre Bukusoglu, Bo Zhang, Daniel S. Miller, and Nicholas L. Abbott. Experimental insights into the nanostructure of the cores of topological defects in liquid crystals. *Physical Review Letters*, 116:147801, 4 2016. ISSN 0031-9007. doi:10.1103/PhysRevLett.116.147801.

263. Xiaoguang Wang, Daniel S. Miller, Emre Bukusoglu, Juan J. de Pablo, and Nicholas L. Abbott. Topological defects in liquid crystals as templates for molecular self-assembly. *Nature Materials*, 15:106–112, 1 2016. ISSN 1476-1122. doi:10.1038/nmat4421.

264. Xin Wang, Ye Zhou, Young-Ki Kim, Michael Tsuei, Yu Yang, Juan J. de Pablo, and Nicholas L. Abbott. Thermally reconfigurable janus droplets with nematic liquid crystalline and isotropic perfluorocarbon oil compartments. *Soft Matter*, 15:2580–2590, 2019. ISSN 1744-683X. doi:10.1039/C8SM02600A.

265. Chong-Lun Wei, Te-Cheng Chen, Putikam Raghunath, Ming-Chang Lin, and Hong-Cheu Lin. Novel asymmetrical single- and double-chiral liquid crystal diads with wide blue phase ranges. *RSC Advances*, 5:4615–4622, 2015. ISSN 2046-2069. doi:10.1039/C4RA13943G.

266. G. M. Whitesides. Self-Assembly at All Scales. *Science*, 295(5564):2418–2421, mar 2002. ISSN 00368075. doi:10.1126/science.1070821. URL http://www.sciencemag.org/cgi/doi/10.1126/science.1070821.

267. F. Xu and P. P. Crooker. Chiral nematic droplets with parallel surface anchoring. *Physical Review E*, 56:6853–6860, 12 1997. ISSN 1063-651X. doi:10.1103/PhysRevE.56.6853.

268. Jun Yamamoto and Hajime Tanaka. Transparent nematic phase in a liquid-crystal-based microemulsion. *Nature*, 409(6818):321–25, 2001. doi:10.1038/35053035. URL https://doi.org/10.1038/35053035.

269. Takaki Yamamoto and Masaki Sano. Chirality-induced helical self-propulsion of cholesteric liquid crystal droplets. *Soft Matter*, 13:3328–3333, 2017. ISSN 1744-683X. doi:10.1039/C7SM00337D.

270. Jin Yan, Yan Li, and Shin-Tson Wu. High-efficiency and fast-response tunable phase grating using a blue phase liquid crystal. *Optics Letters*, 36(8):1404–6, 2011. doi:10.1364/OL.36.001404. URL https://doi.org/10.1364/OL.36.001404.

271. Deng-Ke Yang and Shin-Tson Wu. Blue phases of chiral liquid crystals. In *Fundamentals of Liquid Crystal Devices*, page 445–76. John Wiley Sons, Ltd, 2014. doi:10.1002/9781118751992.ch13. URL https://doi.org/10.1002/9781118751992.ch13.

272. Yu Yang, Viviana Palacio-Betancur, Xin Wang, Juan J de Pablo, and Nicholas L Abbott. Strongly chiral liquid crystals in nanoemulsions. *Small*, 18, 6 2022. ISSN 1613-6829. doi:10.1002/SMLL.202105835.

273. H Yoshida, Y Tanaka, K Kawamoto, H Kubo, Tsuda, A Fujii, S Kuwabata, H Kikuchi, and M Ozaki. Nanoparticle-stabilized cholesteric blue phases. *Applied physics express*, 2(12):121501, nov 2009. doi:10.1143/apex.2.121501.

274. Roya Zandi, David Reguera, Robijn F Bruinsma, William M Gelbart, and Joseph Rudnick. Origin of icosahedral symmetry in viruses. *Proceedings of the National Academy of Sciences*, 101:15556–15560, 6 2004. ISSN 0027-8424. doi:10.1073/PNAS.0405844101.

275. Lauren D. Zarzar, Vishnu Sresht, Ellen M. Sletten, Julia A. Kalow, Daniel Blankschtein, and Timothy M. Swager. Dynamically reconfigurable complex emulsions via tunable interfacial tensions. *Nature*, 518:520–524, 2 2015. ISSN 0028-0836. doi:10.1038/nature14168.

276. Mengwen Zhang, Patrick T. Corona, Nino Ruocco, David Alvarez, Paula Malo de Molina, Samir Mitragotri, and Matthew E. Helgeson. Controlling complex nanoemulsion morphology using asymmetric cosurfactants for the preparation of polymer nanocapsules. *Langmuir*, 34:978–990, 1 2018. ISSN 0743-7463. doi:10.1021/acs.langmuir.7b02843.

277. Rui Zhang, Ye Zhou, Mohammad Rahimi, and Juan J de Pablo. Dynamic structure of active nematic shells. *Nature Communications*, 7:13483, 2016. ISSN 2041-1723. doi:10.1038/ncomms13483.

278. Y Zhou, B Senyuk, R Zhang, I I Smalyukh, and J J Pablo. Degenerate conic anchoring and colloidal elastic dipole-hexadecapole transformations. *Nature Communications*, 10(1):1000, mar 2019. doi:10.1038/s41467-019-08645-9.

279. Ye Zhou, Emre Bukusoglu, Jose A Martinez-Gonzalez, Mohammad Rahimi, Tyler F Roberts, Rui Zhang, Xiaoguang Wang, Nicholas L Abbott, and Juan J de Pablo. Structural transitions in cholesteric liquid crystal droplets. *ACS Nano*, 10(7): acsnano.6b01088, 2016. ISSN 1936-0851. doi:10.1021/acsnano.6b01088. URL `https://doi.org/10.1021/acsnano.6b01088.`

280. Adam Zlotnick. Viruses and the physics of soft condensed matter. *Proceedings of the National Academy of Sciences of the United States of America*, 101(44):15549–50, 2004. ISSN 0027-8424. doi:10.1073/pnas.0406935101. URL `http://www.pubmedcentral.nih.gov/articlerender.fcgi?artid=524855{&}tool=pmcentrez{&}rendertype=abstract`.

281. Jianhua Zou and Jiyu Fang. Director configuration of liquid-crystal droplets encapsulated by polyelectrolytes. *Langmuir*, 26:7025–7028, 5 2010. ISSN 0743-7463. doi:10.1021/la904257j.